TARDEC

---TECHNICAL REPORT---

THE NATION'S LABORATORY FOR ADVANCED AUTOMOTIVE TECHNOLOGY

No. 13770

WINNER OF THE 1995 PRESIDENTIAL AWARD FOR QUALITY

BEHAVIOR OF MATERIALS IN A DYNAMIC ENVIRONMENT: SUMMARY OF PHASE II RESULTS

By
M. El-Raheb
The Dow Chemical Company
K. Weber
V. Hohler
EMI
Freiburg, Germany

Approve for public release, distribution unlimited

U.S. Army Tank-Automotive Research,
Development, and Engineering Center
Detroit Arsenal
Warren, Michigan 48397-5000

REPORT DOCUMENTATION PAGE

Form Approved
OMB No. 074-0188

1. AGENCY USE ONLY (Leave blank)

2. REPORT DATE
July, 1999

3. REPORT TYPE AND DATES COVERED
Final

4. TITLE AND SUBTITLE
Behavior of Materials in a Dynamic Environment: Phase II Results

5. FUNDING NUMBERS
Contract Number
DAEE07-95-C-X0-60

6. AUTHOR(S)
M. El-Raheb; K. Weber*; V. Hohler*

7. PERFORMING ORGANIZATION NAME(S) AND ADDRESS(ES)
The Dow Chemical Company
Midland, MI 48674

*EMI Institut
Frieberg, Germany

8. PERFORMING ORGANIZATION REPORT NUMBER
TARDEC Technical Report
13770

9. SPONSORING / MONITORING AGENCY NAME(S) AND ADDRESS(ES)

10. SPONSORING / MONITORING AGENCY REPORT NUMBER

11. SUPPLEMENTARY NOTES

12a. DISTRIBUTION / AVAILABILITY STATEMENT
Approved for public release, distribution unlimited

12b. DISTRIBUTION CODE

13. ABSTRACT *(Maximum 200 Words)*

A theoretical and experimental study was conducted on stress waves and ballistic performance of weakly coupled stacks of AlN tiles bonded by thin polyurethane films. The cylindrical projectile was made of tungsten alloy with L/D = 6 weighing 61g at a velocity close to 1170 m/s striking the stack centrally. Total thickness of the stack ranged between 3" and 1.5", and with individual tile thicknesses of 1.5", 0.75", 0.5" and 0.25". Ballistic performance was evaluated by the DOP method into an aluminum block. For the 1.5" unconfined stack, DOP of the monolith was highest with substantial scatter, while DOP of the 0.75" layer stack was lowest with reduced scatter. DOP then rises smoothly for the 0.5" and 0.25" layer stacks while scatter is reduced further. Trends of this behavior is partly explained by analysis valid up to crack initiation. An important feature of all DOP results is the dominance of self-confinement.

14. SUBJECT TERMS
ballistic, ceramic, armor, impact, test, penetration, DOP

15. NUMBER OF PAGES

16. PRICE CODE

17. SECURITY CLASSIFICATION OF REPORT	18. SECURITY CLASSIFICATION OF THIS PAGE	19. SECURITY CLASSIFICATION OF ABSTRACT	20. LIMITATION OF ABSTRACT
UNCLASSIFIED	UNCLASSIFIED	UNCLASSIFIED	UL

NSN 7540-01-280-5500

Standard Form 298 (Rev. 2-89)
Prescribed by ANSI Std. Z39-18
298-102

BEHAVIOR OF MATERIALS IN A DYNAMIC ENVIRONMENT: PHASE II RESULTS

July 1999

Contract #DAEE07-95-C-X0-60

Period Covered by Report: 1995-1999

M. El-Raheb
The Dow Chemical Company
Midland, MI

K. Weber
V. Hohler
EMI Institut
Frieberg, Germany

TABLE OF CONTENTS

ABSTRACT

A theoretical and experimental study was conducted on stress waves and ballistic performances of weakly coupled attacks of aluminum nitrite (AlN) tiles bonded by thin polyurethane films. The cylindrical projectile was made of tungsten alloy with length/diameter (L/D=6) weighing 61g at a velocity close to 1170 m/s striking the stack centrally. Total thickness of the stack ranged between 3″ and 1.5″, and with individual tile thickness of 1.5″, 0.75″, 0.5″ and 0.25″. Ballistic performance was evaluated by the depth of penetration (DOP) method into an aluminum block. For the 1.5″ unconfined stack, DOP of the monolith was highest with substantial scatter, while DOP of the 0.75″ layer stack was lowest with reduced scatter. DOP then rises smoothly for the 0.5″ and 0.25″ layer stacks while scatter is reduced further. Trends of this behavior are partly explained by analysis valid up to crack initiation. An important feature of all DOP results is the dominance of self-confinement.

INTRODUCTION

This constitutes a summary report of the accomplishments and meaningful experience gained in Phase II. Phase II focused on three activities:

(1) Analysis of stress waves in a composite of a bi-periodic layered system of ceramic tiles bonded by thin polymer layers adopting plate flexure theory. The intent was to develop an approximation to the 2-D axisymmetric analysis in Phase I, and evaluate its accuracy. This procedure yielded insight into the various key parameters controlling propagation of elastic waves in weakly coupled bi-periodic stacks.

(2) Controlled ballistic experiments on center impact at EMI aimed at understanding the penetration process, and its sensitivity to various elements in the experimental set-up: layer thickness, crack initiation, lateral confinement and cover plate.

(3) Controlled ballistic experiments on center impact at California Institute of Technology (CalTech) aimed at correlating with and confirming results from Ernst Mach Institute (EMI).

A summary of importance results in the three activities appears below. Activities (2) and (3) are discussed together, since they are closely related.

All references are included at the end of the report as Appendices.

(1) *STRESS WAVES IN A PERIODIC STACK "PLATE FLEXURE MODEL"*

Approximate equations incorporating flexure of plates bonded elastically by thin polymer layers were derived [Ref. 2]. This is equivalent to the first propagating group of modes in the exact 2-D axisymmetric theory in Part I [Ref. 1], but excludes all high frequency groups relating to extensional & shear motions in the ceramic layers. Also, the plate flexure model is equivalent to the mass-spring chain in the 1-D model which includes only the first propagation zone.

Transient response histories of the stack of 5 periodic sets computed by the simplified plate flexure model [Ref. 2] were compared to the 2-D model [Ref. 1]. Radial stress on top of the struck tile was 30% less than that of the 2-D model. The reason is that stress from the volumetric component of normal traction under the footprint raises stress over the equivoluminal (flexure) state, an effect neglected by the plate flexure model. Stresses and displacements elsewhere along the stack were within 15-20% of those of the 2-D model. This difference is caused principally by the distortion of the cross-section, because the assumption that plane sections remain plane after deformation is not accurate for tiles thicker than 0.25". Nevertheless, the plate flexure model is sufficiently accurate when comparing various designs of stacks and parametric studies.

Parametric study, using the 2-D model [Ref. 1] excluding inertia of the weak layer, revealed no difference in response histories. This fact was exploited to reduce the number of modes included in the modal analysis for transient response, which increased computational speed greatly. Also, a study of phase and group velocities of both 2-D and plate flexure models revealed that low frequency modes or large wave lengths are essential contributors to these characteristic speeds. Indeed, these coincide very closely with phase velocity across the stack in the 1-D model [Ref. 3]. Consequently, the 1-D approximation to these characteristic speeds is sufficiently accurate in evaluating propagation including the effect of flexure.

Computed histories of the 5-layer stack were compared with experiment conducted at EMI using flyer plate impact. The calculated stress histories agree closely with measurement [Ref. 4].

In preparation of the work in Phase III treating wave propagation in layered stacks struck by an off-center projectile, a plate flexure model was adapted to treat asymmetric waves. This analysis also considered the square tile to evaluate how the difference in geometry affects propagation. Also considered is the effect of boundary constraint. Simple supports, clamped and free edges were considered. The difference in edge constraint becomes important in the vicinity of the boundary [Ref. 5].

(2) CONTROLLED BALLISTIC EXPERIMENTS AT EMI & CALTECH

Three experimental Series on center impact were conducted at EMI:

Series 1 [Ref. 6]used unconfined stacks with total thickness of 3″ and 4″ x 4″ or 6″ x 6″ AlN tiles with tile thickness ranging between 1.5″ and 1/4″ but no monolith. The ceramic was bonded by PMMA thin layers 0.4mm to 1.4mm thick (see Figure 1a). The projectile was Tungsten Alloy L/D=6 weighing 110 grams at a speed of 2.1 km/sec and zero obliquity. Flash X-rays were used before impact and at two stages of the penetration to evaluate yaw. The yaw angle did not exceed 4 degrees. X-rays revealed that yaw angle was reduced during penetration indicating stabilization. Also, X-rays showed that the stack does not shatter globally, while the penetrator is eroding and advancing through the stack. Only after the penetration process is over, the stack bursts into pulverized ceramic powder. Table I, summarizes the results. Figure 1b, shows depth of penetration of the residual projectile into the backing steel block for different stack configurations and with bond line thickness as a parameter: 1.4mm, 0.9mm, and 0.4mm. The line of 0.4mm bond yielded the lowest penetration. This line shows that penetration diminishes with increasing layer thickness. Lines of thicker bonds show that a minimum penetration exists when the layer thickness is 1/2″. These results can be understood in the following way. Kinetic energy of the penetrator was too high and its velocity was close to the phase velocity c_p along the stack (2.3 km/sec). This allowed little time for the waves to propagate radically and disperse. In this way, propagation was confined to the immediate vicinity of the projectile's footprint as in a 1-D situation. Phase velocity in 1-D is approximately equal to

$$c_p \sim Sqrt\left\{\left(E_b h_c\right)/\left(\rho_c h_b\right)\right\} \tag{1}$$

where E_b is bond modulus, ρ_c is ceramic density, and (h_b, h_c) are bond and ceramic thickness. Fixing all parameters except h_b, c_p diminishes with h_b like Sqrt ($1/h_b$). This means that c_p for the stack with 1.4mm bond is almost half that of the same stack with 0.4 mm bond. Consequently, dynamic coupling of the layers bonded by 1.4 mm is reduced to half that of the layers bonded with 0.4mm. Reducing coupling by thickening the bond reduces transmission along the stack which raises flexural stress of the ceramic layers. The difference in c_p between 0.4mm & 1.4mm bonds is magnified for thicker tiles because of the factor Sqrt (h_c) in equation (1).

Although PMMA was chosen for bond material, because of its linearity in a wide pressure range, it lacks the important visco-elastic property of stiffening at high strain rate and weakening at low strain rate. The stiffening is needed, during early times when the pulse of first arrival is transmitted to the next layer, while the softening is needed at later times to reduce intensity of reflecting tensile waves. Although, PMMA is stiffer than polyurethane at low strain rates, it is much softer at the high strain rates, when polyurethane becomes glassy.

This experimental Series has demonstrated that the utility of weakly coupled periodic stacks is limited to projectile velocities sufficiently lower than phase velocity along the stack. It also confirmed the importance of the weak bond and its spatial uniformity on ballistic performance. This is clearly evident from tests performed at EMI in 1990 on stacks of 2 or 3 layers of 2″ to 2.5″ thick stacks confined laterally including cover plates with a projectile similar to that in the present experiments. These results are depicted in Figure 2. The scatter in depth of penetration for the same configuration, and inconsistency in results comparing different stacks was caused by not recognizing the importance of the weak layer and failing to control its uniformity.

Series 2 [Ref. 7] consisted of 6″ x 6″ stacks 2.5″ thick made of tiles ranging in thickness between 1.5″ and 1/4″ but no monolith, and bonded by 10 mil polyurethane adhesive. The stacks were highly confined laterally and with a cover plate (see Figure 3a). The projectile was Tungsten alloy L/D=10 weighing 67.5 grams and speed of 1.5 km/sec. This Series was intended to reproduce a 1989 Dow experiment at UDRL (Univ. of Dayton) on 60mm AlN stacks composed of a monolith, 5 x 12mm layers, and 10 x 6mm layers, bonded by 10 mil polyurethene adhesive. These limited experiments demonstrated the ballistic advantage of the 10 layer stack over the monolith. Table II lists results and Figure 3b shows depth of penetration for the different stack configurations of **Series 2**. The average line indicates a slight advantage by thinning the layers yet the results cannot be trusted because of the stiff confinement which, as was discovered in **Series 3** experiments, has a paramount effect on penetration.

Series 3a,b [Ref. 8] were aimed at correlating results with experiments at CalTech. These experiments consisted of 1.5″ stacks made of a 1.5″ monolith, 2 x 3/4″ layers, 3 x 1/2″ layers and 6 x 1/4″ layers, bonded by 10 mil sheets of very uniform polyurethene, adhering to the ceramic tiles by heating to 375 degrees F. The stacks were confined laterally and with cover plates (see Figure 4a). The projectile was Tungsten alloy with L/D=6 weighing 50 grams with velocity near 1170 m/sec. This is the first Series that included a monolith. At first, the result of EMI did not match those of CalTech. CalTech measured depth of penetration p_r = 30 mm for the 1.5″ monolith, and almost no penetration for the 1/2″ stack. EMI measured p_r = 0 mm for the 1.5″ monolith and 6mm for the 1/2″ stack (see Tables III and IV).

After reviewing CalTech's experimental setup more closely, it became clear that CalTech's lateral confinement was so weak that it was failing at the corner welds, and the confining plates were ejected laterally. In essence, the CalTech stack was unconfined. Also, the sabot separated from the projectile by arresting it by the cover plate, which was in direct contact with the top surface of the stack. This separation pre-shocked the stack since the mass of the sabot, 35 grams, is comparable to that of the projectile. The pre-shocking initiated micro-cracks in the monolith or in the top layer of the stack, weakening it from its virgin stage. The two layers beneath the top layer of the 1/2″ stack were shielded from the shock by the polyurethene bond, preserving their unshocked properties (see Table III). This experimental mismatch clarified the following points:

(a) Lateral and cover plate confinement increases ballistic performance substantially. This is an accepted fact among researchers in ballistics. Yet the way it works is not by reducing tensile waves from boundary reflections, but by keeping the cominuted material in the path of the projectile, increasing its erosion and consuming its energy.

(b) Crack initiation controls ballistic performance of ceramic material. This strengthens the role that linear analysis plays in evaluating ballistic performance, since it is valid up to the stage of crack initiation.

Having recognized the differences in the CalTech setup, it was redesigned so that, after sabot separation by the cover plate, the projectile is sufficiently distant from the top surface of the stack, avoiding pre-shocking. Also the confining box was designed with a clearance of 5 mm around the stack to permit lateral expansion of the damaged ceramic without interference from the plates forming the box (see Figure 5). The same procedure was applied to the setup of EMI (**Series 3c**): no lateral confinement and a cover plate distant from the top face of the stack by 3 mm (see Figure 6).

Series 3c [Ref. 8] experiments were performed at CalTech and EMI expecting that results from the two would now match. Results for the 1/2″ stack agreed: EMI measured p_r of 20mm and 23mm, and CalTech measured 20 mm and 26 mm. Yet results for the 1.5″ monolith were still quite different: EMI measured p_r of 6.8mm and 0mm, and CalTech measured 30mm and 34mm (see Tables V and VI). The consistency of the latest CalTech results pointed this time to a possible deficiency in the EMI setup. EMI repeated 3 more tests on the 1.5″ monolith which yielded 11mm, 33mm and 46mm (see Table VI). This large scatter among the EMI results for the 1.5″ confirmed that a fundamental difference existed between the two setups meriting a closer look at the EMI setup. Examining the cover plates of these last three EMI tests revealed that the cover plate corresponding to p_r = 11mm case suffered substantial plastic deformation, while that of the p_r = 46mm case had very little plastic deformation. This suggested that the large scatter in p_r was caused by the degree of confining ejecta in the direction of impact by the 3mm thick cover plate which was not even touching the stack. The 3mm gap between cover plate and stack was small enough to confine ejecta at times when they did not escape through the central hole in the cover plate. When ejecta did not escape through the cover plate hole, they remained in the path of the projectile increasing resistance, reducing p_r and causing the cover plate to yield. When ejecta escaped through the hole, the penetrator encountered less resistance increasing p_r and keeping the cover plate intact. These results shed new light on how the cover plate increases ballistic performance. Its function is not to reduce reflected tensile waves but to keep cominuted material from ejecta in the path of the projectile, increasing its erosion and consuming its energy.

An explanation was still needed to account for the reduced scatter in EMI's **Series 3c** results for the stacked configurations in spite of the cover plate's closeness. That explanation lies in the concept of phase velocity c_p. For the monolith, the rate of formation of cominuted material in ejecta is approximately the compressional speed of sound which for AlN is 10 km/sec. In the stack, c_p is given by equation (1). For material properties of polyurethene and 1/2" layers, $c_p \sim 2.3$ km/sec. The reduction in c_p from the weak coupling reduces the rate of ejecta formation by a factor of 4. This enables ejecta to escape from the cover plate hole more often, diminishing the scatter. In fact, the scatter is reduced for thinner tiles consistent with the corresponding reduction in c_p given by equation (1).

To bring the two setups into equivalence now required adjusting the EMI setup by increasing the distance between cover plate and stack from 3mm to 50mm (see Figure 7). This allowed sufficient space for the ejecta to expand without restriction from confinement. Experiments with this final setup **Series 3d** measured a higher p_r in two tests with the 1.5" monolith: 29mm and 41mm (see Table VI).

Figure 8 shows EMI results of **Series 3c and 3d** and CalTech results for all stacks tested. Note the large scatter in p_r for the monolith when gap between cover plate and stack was 3mm, and the reduced scatter from CalTech and EMI data when that gap was increased to 50mm. The scatter diminishes as layer thickness in the stack is reduced.

Experiments at Caltech on 4" x 4" AlN tiles, 3/4" thick, and stacks made of 7 x 0.11" thick tiles bonded to 10 mil polyurethene sheets, struck by a 50 cal projectile at 3,000 ft/sec, revealed that the stack failed to stop the projectile. Analysis adopting the 2-D model on a single 3/4" monolith, 2 x 3/8" stack, 3 x 1/4" stack and 5 x 0.15" stack, explained this experimental result. The 2 layer case showed a reduction in tensile stress integrated throughout the stack, while the 5 layer case showed a magnification in that stress. This numerical experiment and the test demonstrate that layering does not scale. Starting with some thickness of monolith, layering may be effective depending on the absolute thickness of the monolith. For thick targets, ballistic performance is enhanced by thinning the layer down to a minimum thickness beyond which further thinning reduces performance because of magnification of tensile stress from flexure.

In conclusion, weakly coupled periodic stacks may enhance ballistic performance depending on stack thickness, number of layers, and impulse characteristics. Three distinct mechanisms each play a role in the penetration process, two favorable and one adverse:

(1) Attenuation of stress wave of first arrival as it propagates along the stack, by transmission loss across the weak layer. This produces crack initiation in a zone described by an inverse conoid, provided projectile velocity is sufficiently smaller than phase velocity along the stack. The comminuted zone creates a self-confining funnel that increases projectile erosion.

(2) Arrest of crack propagation in the stack across weak layers, a mechanism lacking in the monolith.

(4) The adverse effect of layering is that thinner tiles magnify tensile flexural stress promoting failure sooner and counteracting the positive effects above.

(3a) References:

Reports, external publications and computer programs produced in the course of research in Phase II which also constitute deliverable are listed below. A descriptive title and objective is listed.

1. Transient elastic waves in finite layered media: two-dimensional axisymmetric analysis (J.Acoust.Soc.Am. 99 (6) June 1996)
2. Simplified models of transient elastic waves in finite axisymmetric layered media (J.Acoust.Soc.Am. 104 (6) December 1998)
3. Simplified analytical models for transient uniaxial waves in a layered periodic stack (Int.J. Solids Structures, 23, 1997)
4. Transient waves in a periodic stack: experiments and comparison with analysis (J.Acoust.Soc.Am. 101 (2) February 1997)
5. Transient flexural waves in a disk and square plate from off-center impact (Preliminary copy, March 1999)
6. Protection efficiency of layered AIN ceramic targets bonded with PMMA, K. Weber, V. Hohler, (EMI Report E 11/96 January 1997)
7. EMI Report E 19/97
8. Results of the 1998 center and off-center impact tests with 4″ x 4″ and 6″ x 6″ AIN ceramic targets (November 1998)

(3b) Computer Programs Developed:

(1) "STACK1D": Transient response of simply supported stack of layered Mindlin plates using a plate flexure model

(2) "STACK2D": Transient response of simply supported stack of layered tiles using a 2-D axisymmetric model

(3) "HDISK": Transient waves in a disk and square plate from off-center impact adopting plate flexure theory, with simply support, clamped and free boundaries

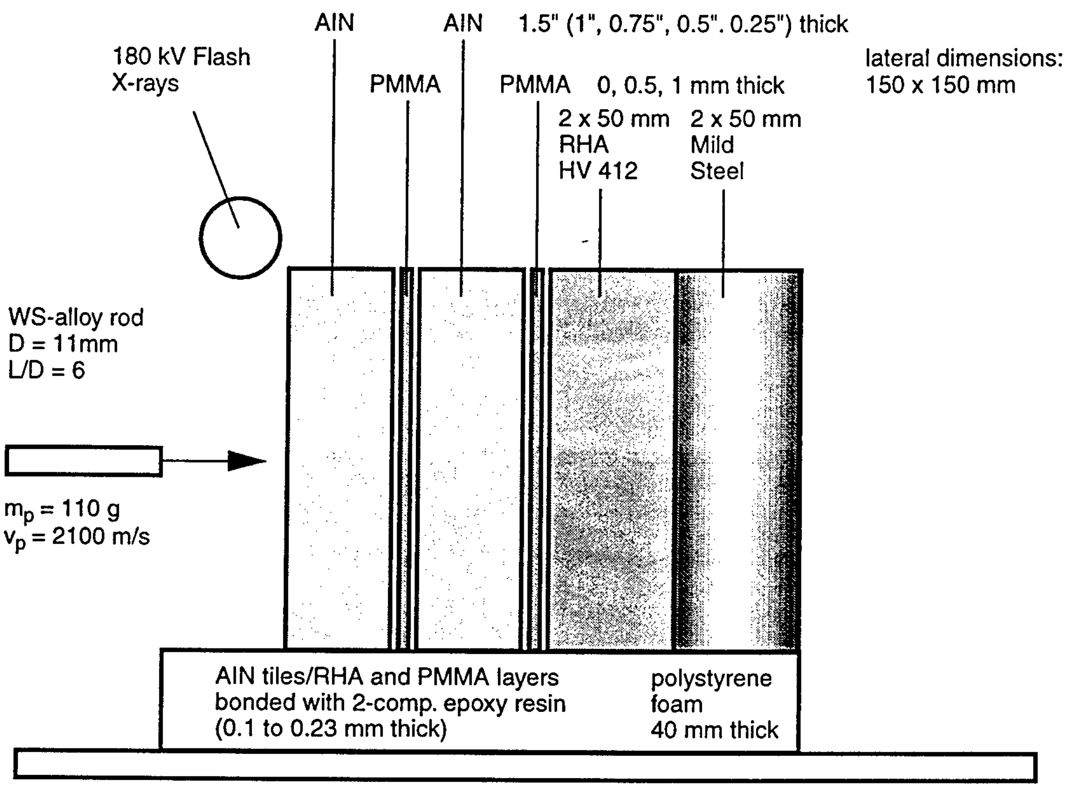

Figure 1a. Test set-up (series 1)

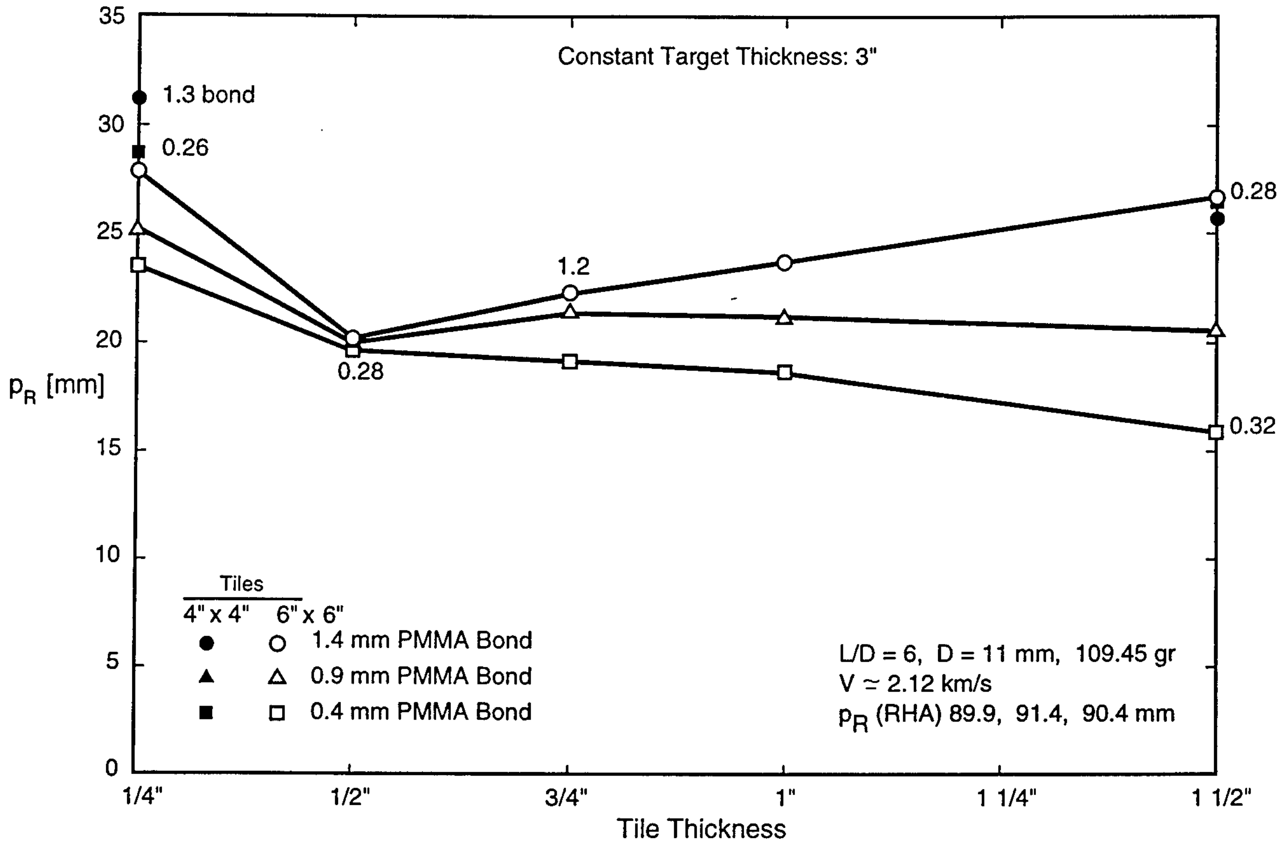

Figure 1b. Penetration depth in ceramic stacks (series 1)

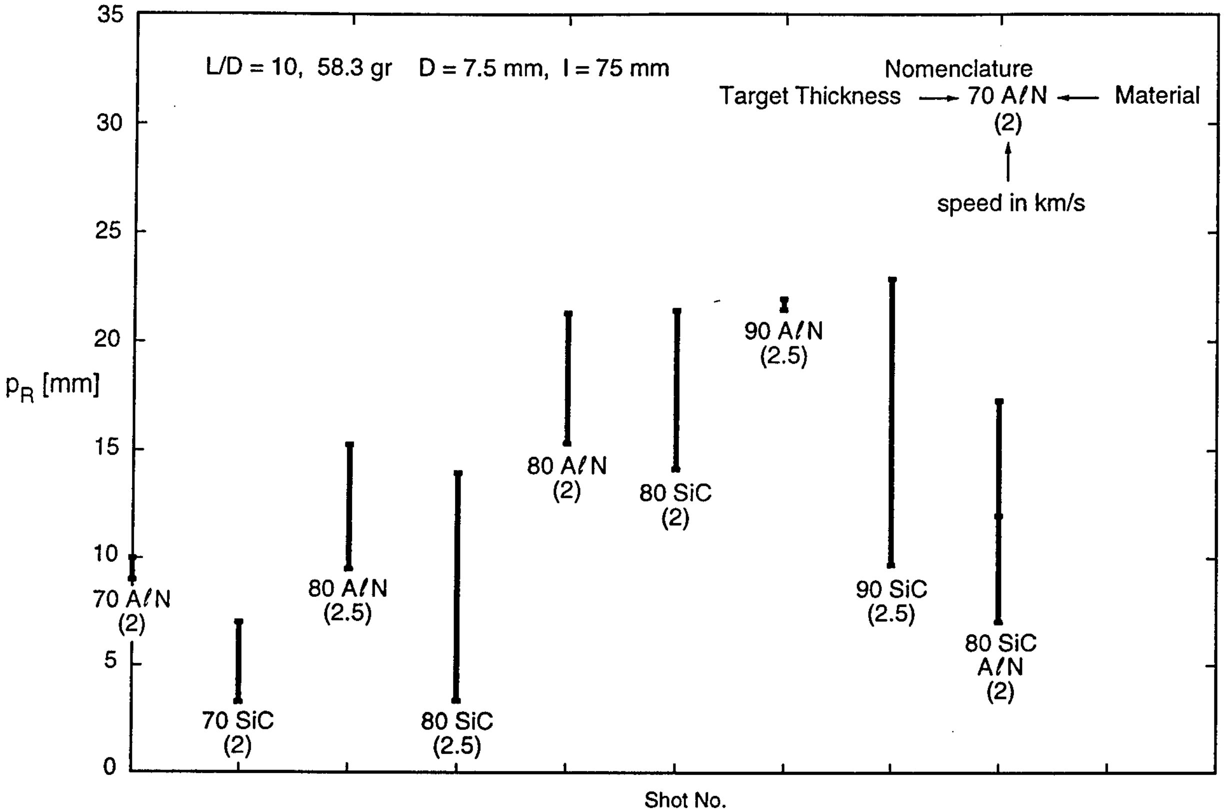

Figure 2 Penetration depth in ceramic stacks (1990 experiments)

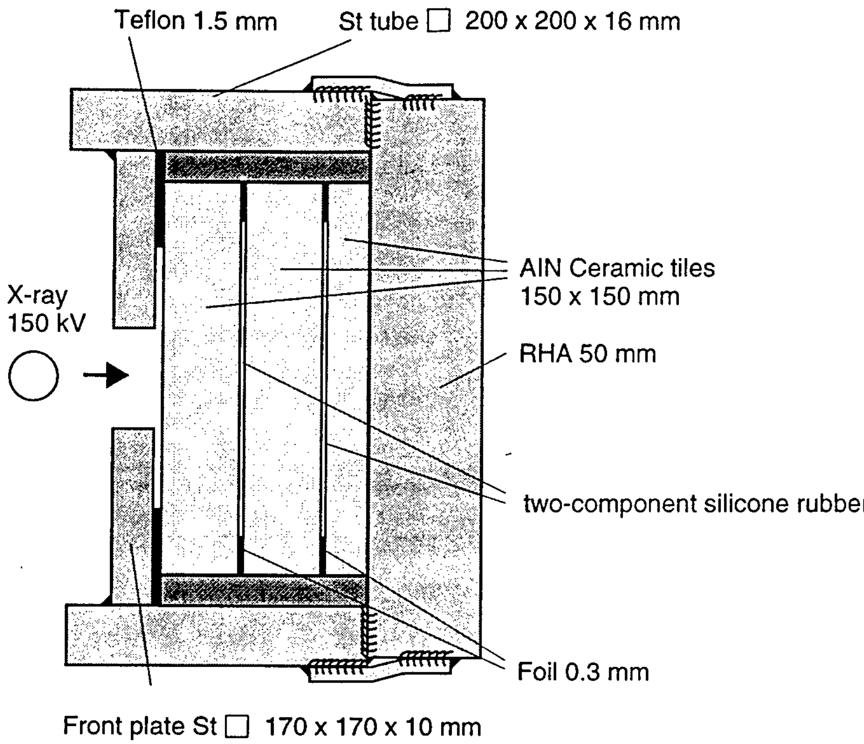

Projectile: D = 7.87 mm, L/D = 10, $m_p \approx 70$ g, $v_p = 1550$ m/s, hemispherical nose

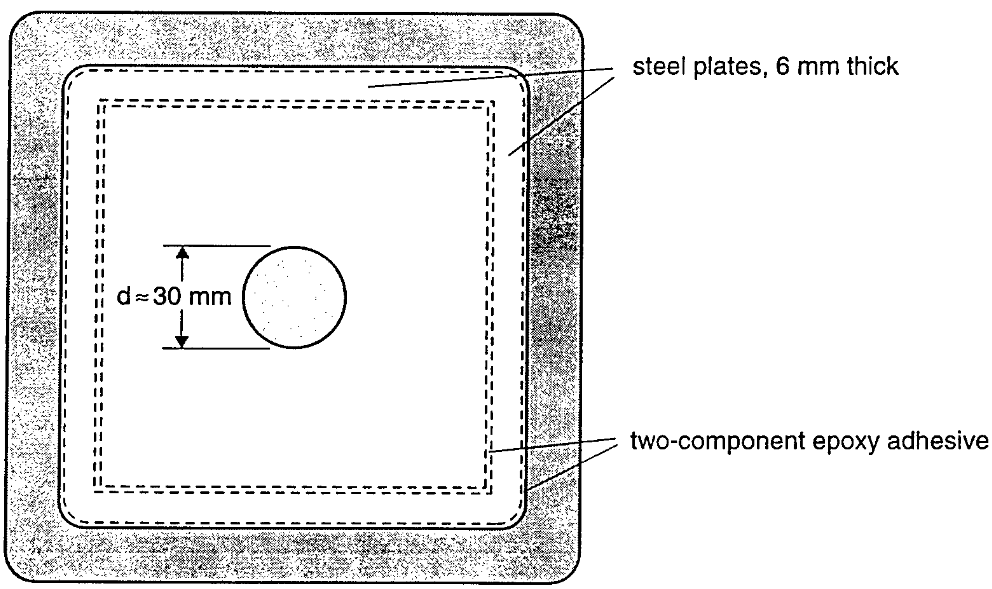

Figure 3a. EMI test set-up (series 2)

3199 7/30/98

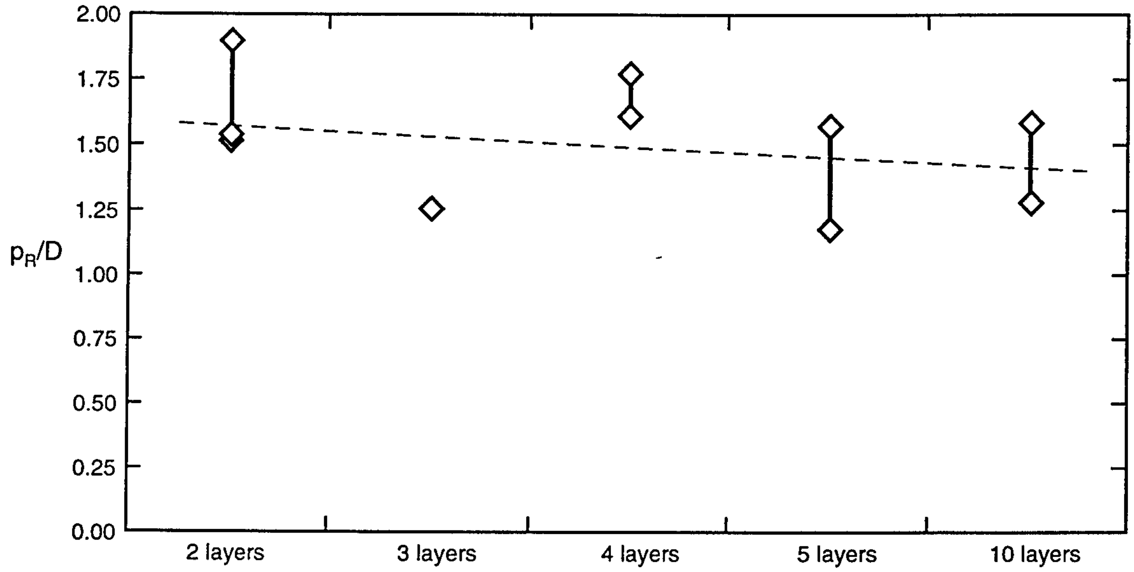

Figure 3b. Normalized penetraton depth p_R vs. AlN layer number (series 2)

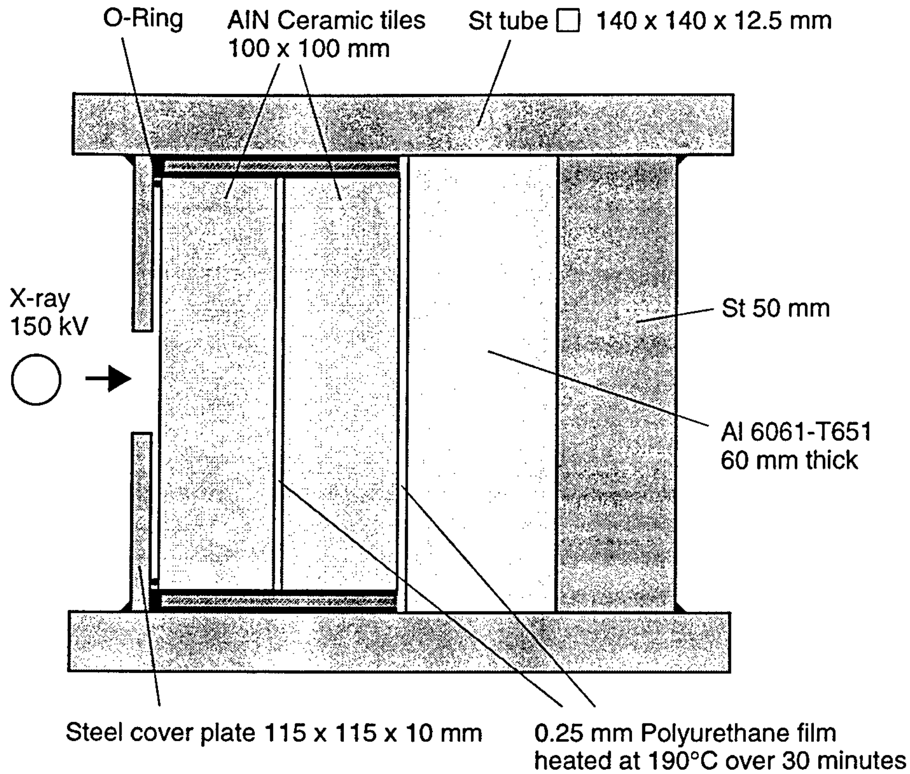

Projectile: D = 8.33 mm, L/D = 6, $m_p \approx 50$ g, $v_p = 1150$ m/s, flat nose

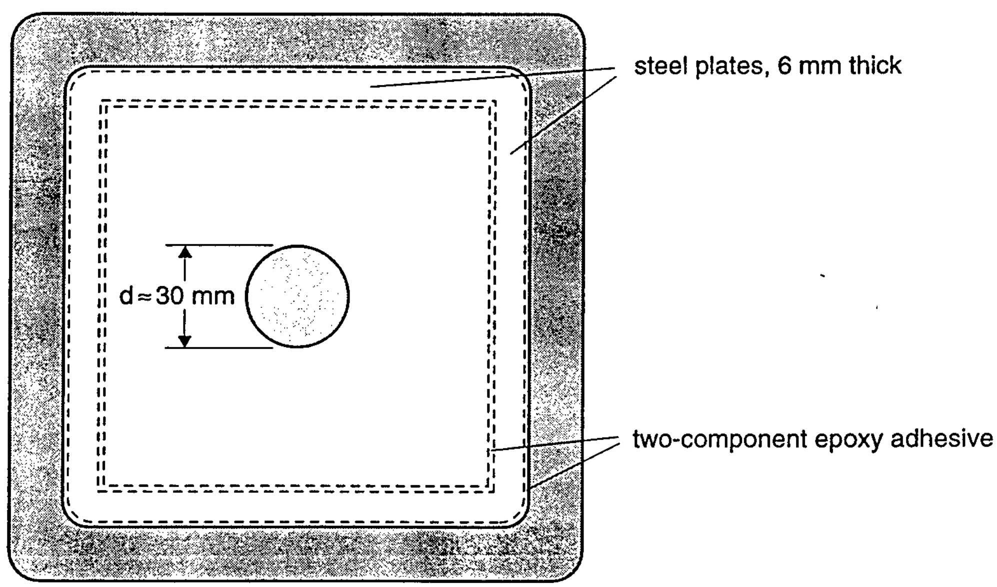

Figure 4a. EMI test set-up (series 3a)

8199 5/19/98

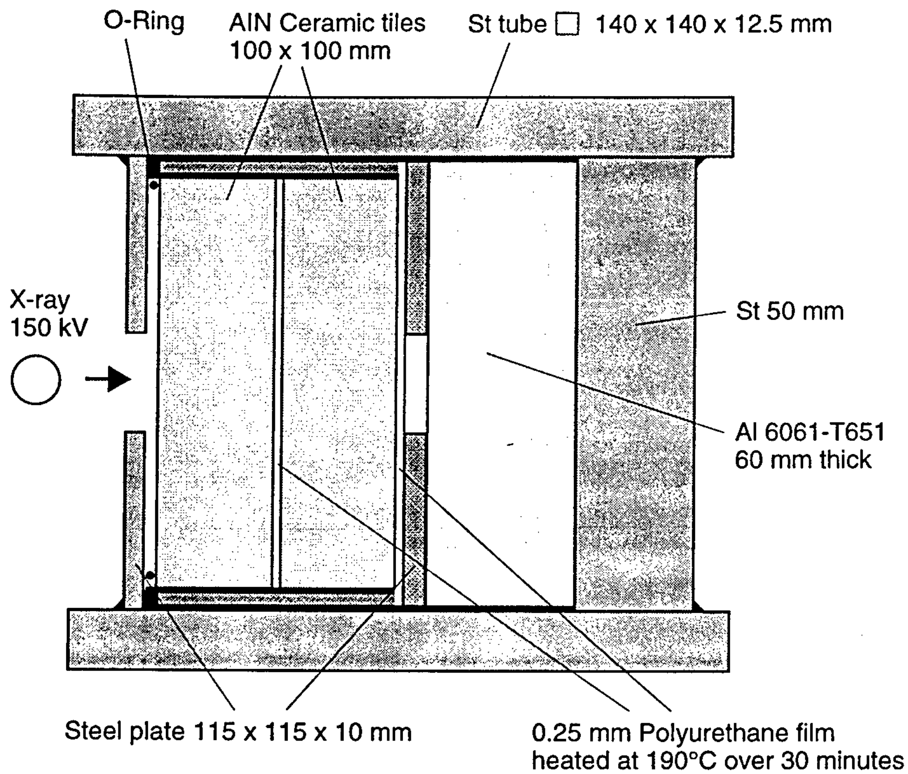

Projectile: D = 8.33 mm, L/D = 6, $m_p \approx 50$ g, $v_p = 1150$ m/s, flat nose

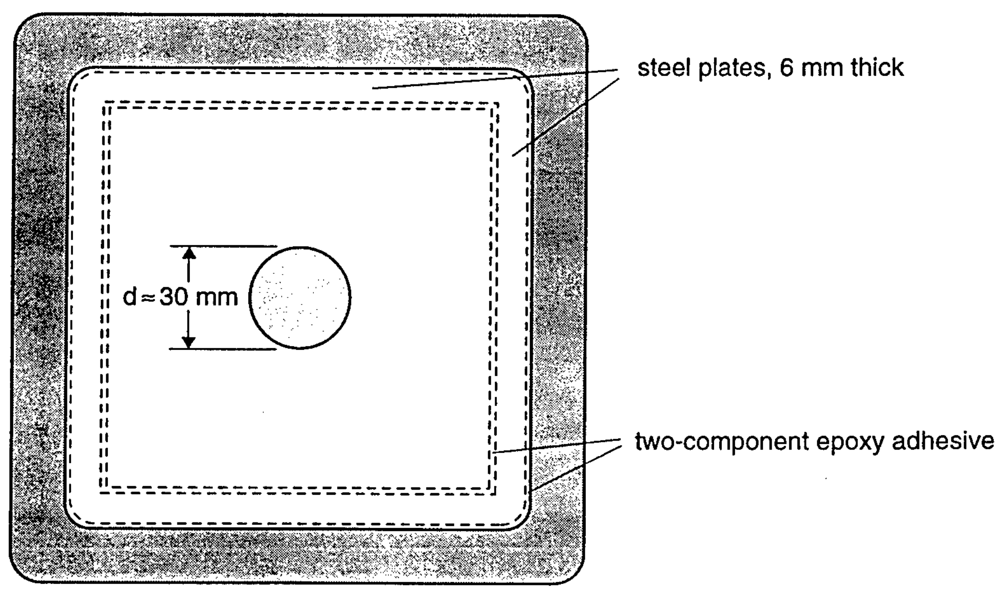

Figure 4b. EMI test set-up (series 3b)

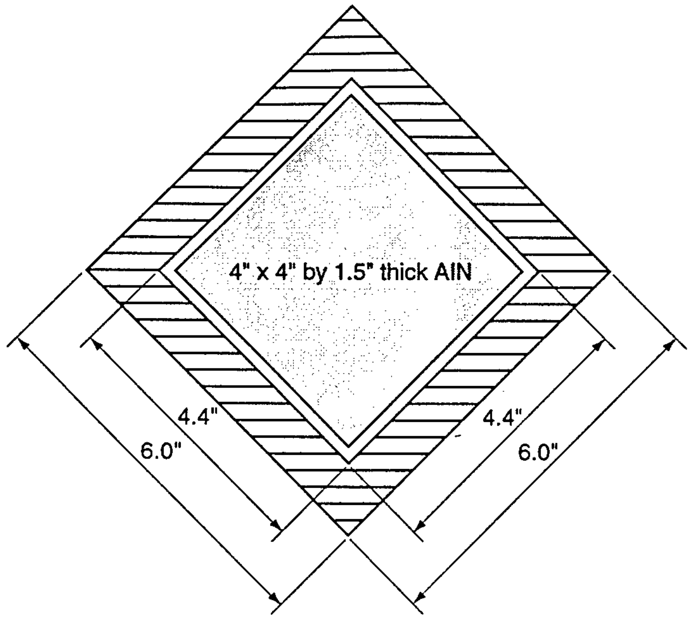

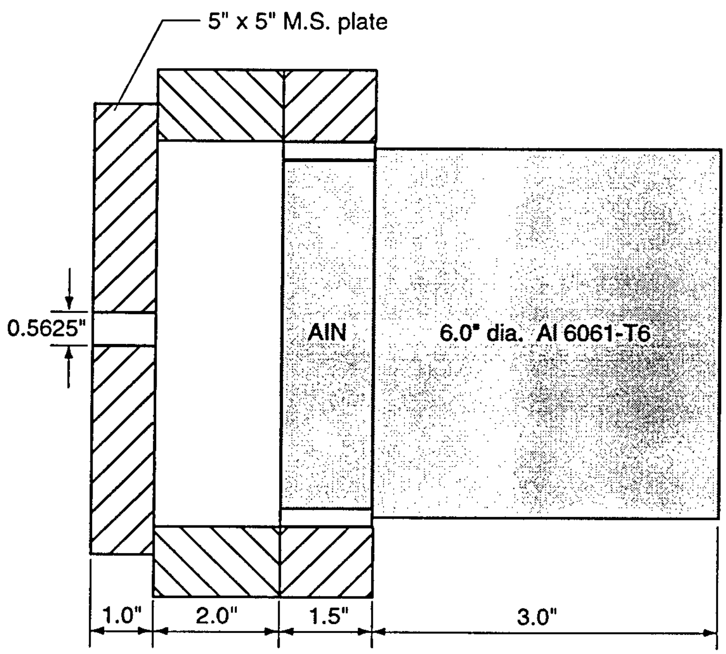

Figure 5. Caltech test set-up

8199 5/19/98

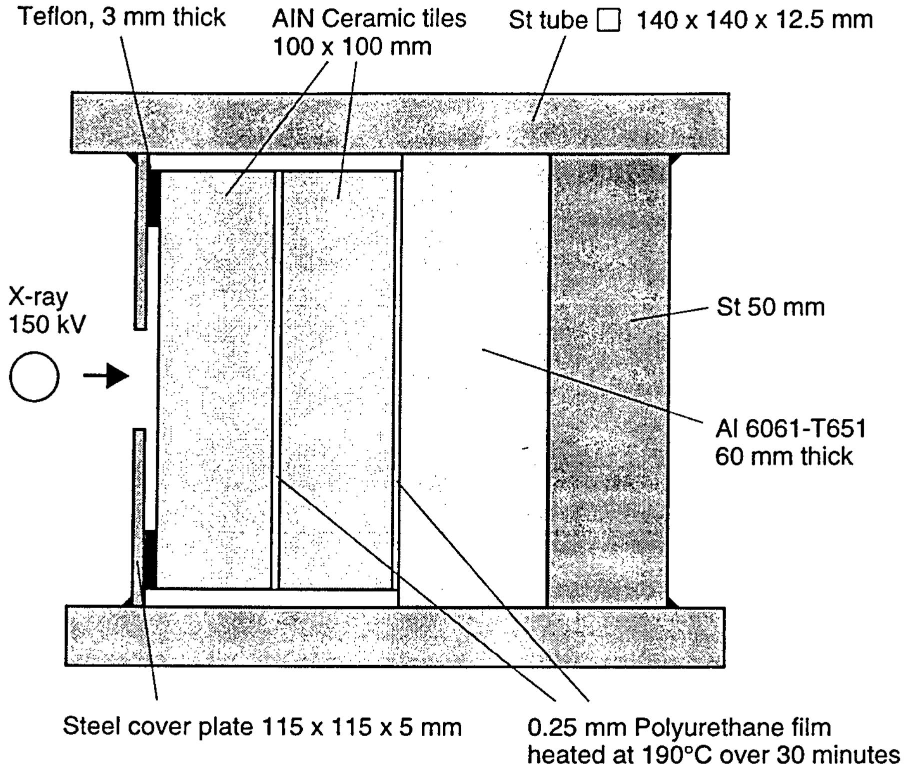

Projectile: D = 8.33 mm, L/D = 6, $m_p \approx 50$ g, $v_p = 1150$ m/s, flat nose

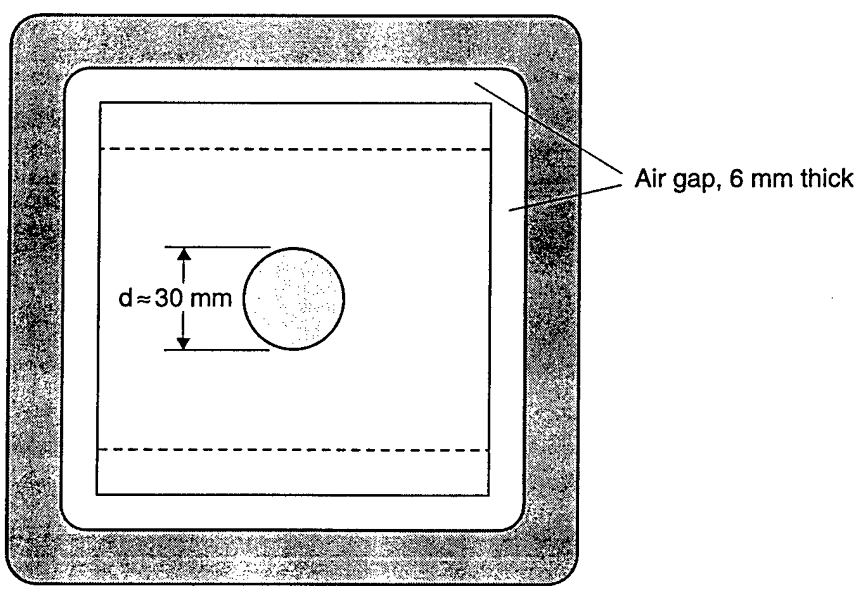

Figure 6a. EMI test set-up (series 3c)

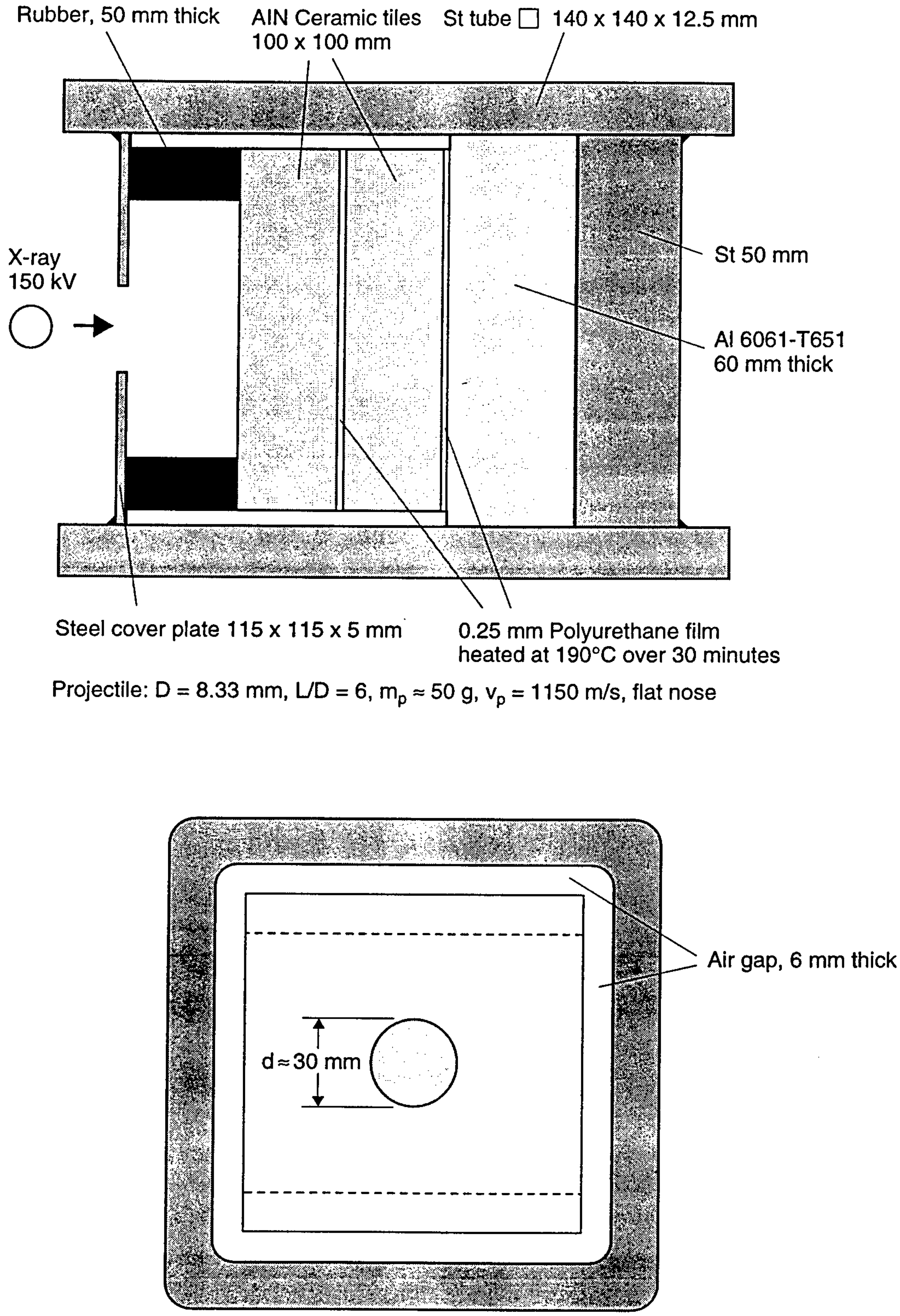

Figure 6b. EMI test set-up (series 3d)

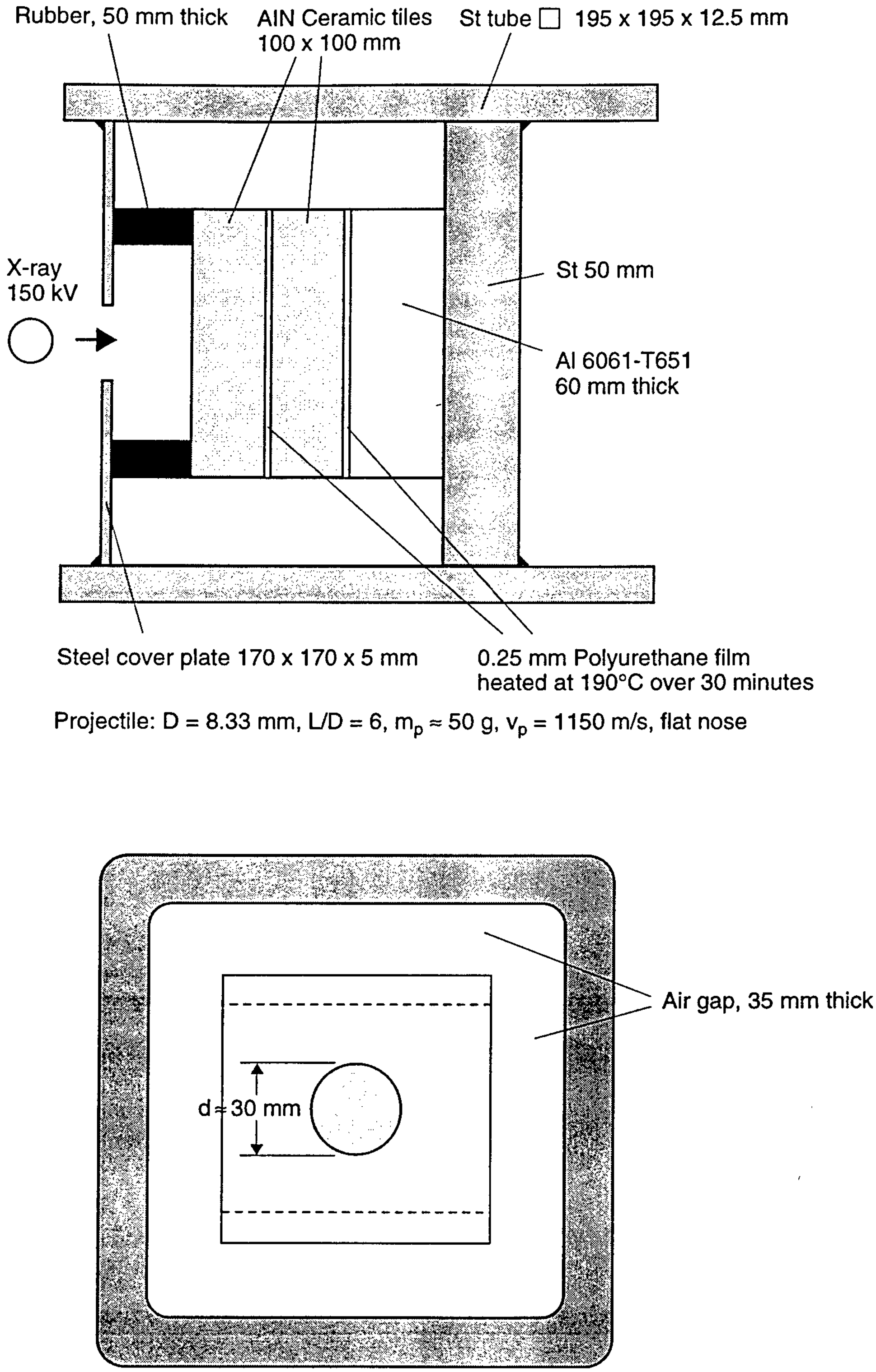

Figure 7. EMI test set-up (series 3e)

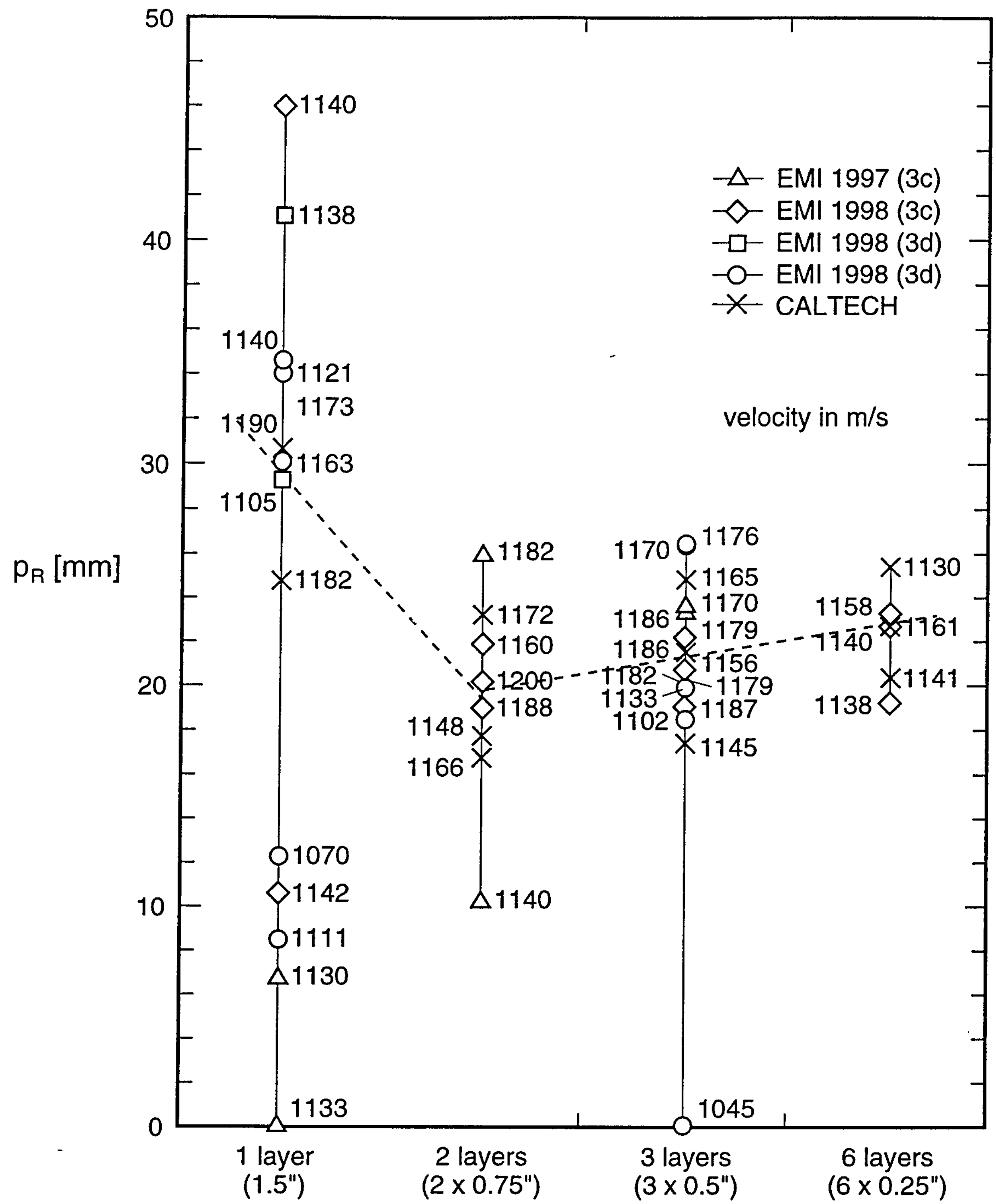

Figure 8. Residual penetration depth vs. AIN layer numbers

8199 7/30/98

Projectile: Rod (Material: WSA rod), D = 11 mm, L/D = 6, m_p = 109.45 g, ρ = 17.55 g/cm^3, R_m =1550 ± 9 MPa, A_5 = 8.2 ± 1.9%, flat nose

RHA-Catcher: Vickers hardness number HV20 = 412

Exp. no.	v_p [m/s]	α_1 / α_7 [deg]	Lateral target dimensions [mm]	No. of tiles	AIN average tile thickness [mm]	PMMA average sheet thickness [mm]	Adhesive average layer thickness [mm]	RHA thick-ness [mm]	p_R [mm]
8401	2130	+1.5/---	150 x 150	12	6.36	0.99	0.20	50.06	27.9
8402	2132	+3.5/-1.0	150 x 150	12	6.35	0.49	0.17	49.73	25.4
8403	2133	+1.5/-0.5	150 x 150	12	6.35	0	0.16	50.05	23.5
8413	2129	+4.0/-1.0	150 x 150	6	12.77	0.97	0.23	50.24	20.1
8412	2134	+2.0/-0.5	150 x 150	6	12.80	0	0.14	50.33	19.8
8405	2120	+2.0/-0.5	150 x 150	4	19.31	0.98	0.10	49.87	22.2
8406	2128	+0.5/-0.5	150 x 150	4	19.10	0.48	0.21	50.06	21.6
8407	2120	0/-0.5	150 x 150	4	19.12	0	0.21	50.22	19.2
8411	2131	+2.0/-0.5	150 x 150	3	25.43	0.99	0.21	50.07	23.8
8408	2129	+2.0/-0.5	150 x 150	2	38.12	0.97	0.22	50.17	26.7
8409	2124	+3.0/-0.5	150 x 150	2	38.10	0.50	0.23	50.19	20.6
8410	2118	+2.5/-1.0	150 X 150	2	38.07	0	0.19	50.16	16.0
8399	1975	+1.5/---	150 x 150	---	---	---	---	3 x 50	89.8
8400	1996	+2.5/-0.5	150 x 150	---	---	---	---	3 x 50	91.4
8414	2120	-0.5/-0.5	150 x 150	---	---	---	---	3 x 50	90.4
8418	2108	+1.0/0	100 x 100	12	6.32	0.97	0.16	50.15	31.1
8417	2123	+1.0/-0.5	100 x 100	12	6.35	0	0.13	49.92	28.6
8416	2119	+1.0/-0.5	100 x 100	2	38.11	1.0	0.20	50.12	25.7
8415	2116	+0.5/-0.5	100 x 100	2	38.20	0	0.14	50.00	26.4

Table I Results of test series 1

Projectile: WSA rod, D = 7.87 mm, L/D = 10, m_p = 69 g; hemispherical nose;
Backing Plate: RHA, 50 mm thick, HV20 = 280;
Cover Plate: steel, 10 mm thick

Exp. no.	v_p [m/s]	α_1 [deg]	Lateral target dimensions [mm]	No. of tiles	AlN tile thickness [mm]	RHA thickness [mm]	p_R [mm]
8627	1498	-3	150 x 150	-	-	100	70.5
8628	1500	-3	150 x 150	-	-	100	72.8
8629	1501	-1	150 x 150	-	-	100	71.9
8630	1493	-2	150 x 150	2	38.1 + 25.4	50	12.0
8631	1554	+0.5	150 x 150	2	38.1 + 25.4	50	12.2
8632	1541	-2	150 x 150	2	38.1 + 25.4	50	15.0
8633	1543	-1	150 x 150	3	2 x 25.4 + 12.7	50	10.0
8634	1548	0	150 x 150	3	2 x 25.4 + 12.7	50	10.0
8635	1564	-1	150 x 150	4	3 x 19.05 + 6.35	50	12.7
8636	1560	-2	150 x 150	4	3 x 19.05 + 6.35	50	14.0
8637	1562	-0.5	150 x 150	5	5 x 12.7	50	9.3
8638	1543	-0.5	150 X 150	5	5 x 12.7	50	12.4
8639	1546	+1.5	150 x 150	10	10 x 6.35	50	12.5
8640	1546	+1	150 x 150	10	10 x 6.35	50	10.1

Table II Results of test series 2

Shot no.	AlN layers	Velocity [m/s]	DOP	Qualifying remarks
MONOLITHIC AlN – 1.5" thick				
S14	1 x 1.5"	1082	1.17"	Ceramic pre-shocking + Al containment
S19	1 x 1.5"	1137	1.28"	No confinement but pre-shocking of the ceramic
S17	1 x 1.5"	1166	1.17"	Mild steel confinement, ceramic pre-shocking, 1/4" thick steel rear plate with 1" diameter hole
LAYERED AlN – 3 x 0.5" thick				
S20	3 x 0.5"	1035	0.6"	No confinement but pre-shocking of the ceramic
S18	3 x 0.5"	1140	0	Mild steel confinement, pre-shocking of the ceramic

Table III Summary of earlier CalTech experiments

Projectile: WSA rod, D = 8.33 mm, L/D = 6, m_p = 51 g; flat nose;
Backing Plate: Al6061-T651, 60 mm thick;
Cover Plate: steel, 10 mm thick

Exp. no.	Test series	v_p [km/s]	AlN layers	Yaw angle [deg]	St plate thickness [mm]	p_R [mm]
8715	3a	1223	Al6061-T651 5 x 40 mm	-2.0	--	123.0
8716	3a	1192	1 x 1.5"	0	--	0
8718	3a	1145	1 x 1.5"	-1.0	--	0
8717	3a	1174	3 x 0.5"	-1.5	--	6.2
8719	3a	1161	3 x 0.5"	+0.5	--	6.0
8725	3b	1167	1 x 1.5"	+1.0	9.75	--
8726	3b	1125	1 x 1.5"	+0.5	9.75	--
8724	3b	1203	3 x 0.5"	+3.5	9.75	8.2
8727	3b	1169	3 x 0.5"	-2.0	9.75	20.5
8733	3c	1130	1 x 1.5"	+2.0	--	6.8
8738	3c	1133	1 x 1.5"	+1.0	--	0
8734	3c	1140	2 X 0.75"	0	--	10.3
8739	3c	1182	2 X 0.75"	+2.0	--	26.0
8735	3c	1186	3 x 0.5"	-4.0	--	23.3
8740	3c	1170	3 x 0.5"	+0.5	--	23.5

Table IV Results of test series 3a, b, c

8199 7/30/98

Shot no.	AIN layers	Velocity [m/s]	DOP	Remarks
MONOLITHIC AIN – 1.5" thick				
S32	1 x 1.5"	1070	0.48"	
S40	1 x 1.5"	1121	1.34"	EMI material
S38	1 x 1.5"	1140	1.36"	
A41	1 x 1.5"	1163	1.18"	EMI material
LAYERED AIN – 3 x 0.5" thick				
S31	3 x 0.5"	1045	0	
S37	3 x 0.5"	1102	0.72"	
S43	3 x 0.5"	1133	0.78"	
S45	3 x 0.5"	1170	1.03"	EMI material
S44	3 x 0.5"	1176	1.03"	
LAYERED AIN – 6 x 0.25" thick				
S42	6 x 0.25"	1170	1.54"	

Table V Summary of recent CalTech experiments

Projectile: WSA rod, D = 8.33 mm, L/D = 6, m_p = 51 g; flat nose;
Backing Plate: Al6061-T651, 60 mm thick;
Cover Plate: steel, 10 mm thick

Exp. No.	v_p [m/s]	α_1 / α_2 [deg]	Test set-up	Lateral tile dimensions [mm]	No. of tiles	p_R [mm]	Projectile used from
8733*	1130	+2.0/--	3c	100 x 100	1 x 1.5"	6.8	EMI
8738*	1133	+1.0/--	3c	100 x 100	1 x 1.5"	0	EMI
8850	1142	0/-1	3c	100 x 100	1 x 1.5"	10.60	EMI
8853	1173	-4/-2	3c	100 x 100	1 x 1.5"	33.00	EMI
8857	1140	-1/-4	3c	100 x 100	1 x 1.5"	45.90	EMI
8874	1111	0/-1.5	3c	100 x 100	1 x 1.5"	8.5	CALTECH
8875	1105	-3/0	3d	100 x 100	1 x 1.5"	29.3	EMI
8876**	1138	0/-3	3d	100 x 100	1 x 1.5"	20.5/41**	EMI
8734*	1140	0/--	3c	100 x 100	2 x 0.75"	10.3	EMI
8739*	1182	+2.0/--	3c	100 x 100	2 x 0.75"	26.0	EMI
8851	1200	-0.5/-2.5	3c	100 x 100	2 x 0.75"	20.05	EMI
8854	1160	+2/-1	3c	100 x 100	2 x 0.75"	21.75	EMI
8858	1188	+1/0	3c	100 x 100	2 x 0.75"	18.85	EMI
8735*	1186	-4/--	3c	100 x 100	3 x 0.5"	23.3	EMI
8740*	1170	+0.5/--	3c	100 x 100	3 x 0.5"	23.5	EMI
8852	1179	-0.5/+3.0	3c	100 x 100	3 x 0.5"	19.80	EMI
8856	1187	-1/-1.5	3c	100 x 100	3 x 0.5"	18.90	EMI
8859	1182	-1/-3	3c	100 x 100	3 x 0.5"	19.90	EMI
8871	1179	-1/+0.5	3c	100 x 100	3 x 0.5"	22.0	CALTECH
8872	1156	+0.5/0	3c	100 x 100	3 x 0.5"	20.5	CALTECH
8855	1140	-1/-1	3c	100 x 100	6 x 0.25"	22.50	EMI
8860	1138	-1.5/-1.5	3c	100 x 100	6 x 0.25"	19.00	EMI
8861	1158	+0.5/+0.5	3c	100 x 100	6 x 0.25"	23.00	EMI

*1997 experiments
**In experiment 8876 strong deflection of the residual projectile during the penetration into the ceramic; therefore, ricocheting of the rod in the Al backing plate.
p_R' = 20.5 mm (deepest point of the crater)
$p_R \approx 2 \times p_R'$ = 41 mm (estimated residual penetration depth)

Table VI EMI experiments of test series 3c and 3d

Reference [1]

Transient Elastic Waves in Finite Layered Media: Two-Dimensional Axisymmetric Analysis

Transient elastic waves in finite layered media: Two-dimensional axisymmetric analysis

Michael El-Raheb
Central Research, The Dow Chemical Company, Midland, Michigan 48674

Paul Wagner
1020 Crestview Drive, Pasadena, California 91107

(Received 28 April 1995; revised 15 December 1995; accepted 23 February 1996)

The analysis of transient linear elastic waves in Ref. 1 [J. Acoust. Soc. Am. **94**, 172–184 (1993)] is extended to 2-D axisymmetric finite layered periodic and weakly coupled media. Two essential features distinguishing 2-D propagation are flexure and increased dispersion. To allow separation of z and r eigenproblems, a boundary condition that approximates simple supports is adopted that yields nonorthogonal eigenfunctions in the modal analysis. © *1996 Acoustical Society of America.*

PACS numbers: 43.40.Ph, 43.20.Gp

INTRODUCTION

Before understanding propagation of elastic waves in weakly coupled finite two-dimensional periodic media, a good understanding of its one-dimensional counterpart[1,2] is necessary. Transient uniaxial wave propagation in a weakly coupled periodic stack of m_c hard ceramic layers A bonded by (m_c-1) weak polymer layers B exhibits the following characteristics:

(a) In the frequency domain, response is divided into narrow propagation zones termed PZ and wider attenuation zones termed AZ. The first PZ includes a cluster of (m_c-1) resonances, where the hard layers move as rigid masses against the springlike weak layers. The width of the first PZ is $\Delta\omega_{pz1}\simeq 2c_A/h_A(\tilde{z}\,\tilde{\tau})^{-1/2}$, where (c_A, h_A) are speed of sound and thickness of the hard layer, $\tilde{z}=(\rho_A c_A)/(\rho_B c_B)$ is ratio of acoustic impedances, and $\tilde{\tau}=(h_B/c_B)/(h_A/c_A)$ is ratio of travel times. All PZ's after the first belong to one of two groups; one group includes clusters of m_c axial elastic resonances of an unconstrained hard layer, and the other group includes clusters of (m_c-1) axial elastic resonances of a constrained weak layer. Including these groups in the response causes high-frequency oscillations.

(b) In transient response, peak stress of first arrival changes its shape quickly within the first hard layer from the trapezoidal input shape of magnitude σ_0 to a fully dispersed bell shape. At interfaces between layers, peak stress is magnified or attenuated depending on the wave transmissibility $\mathfrak{T}$, which is the product of $\Delta\omega_{pz1}$ and time interval t_f of the equivalent rectangular forcing pulse that conserves impulse divided by π, i.e., $\mathfrak{T}=\Delta\omega_{pz1}t_f/\pi$. When $\mathfrak{T}<1$ peak stress is attenuated, varying as $t_a^{-1/3}$, where t_a is time of first arrival, but when $\mathfrak{T}>1$ peak stress is magnified in the first layers, reaching a maximum not exceeding 1.2 σ_0, then falls off asymptotically. $\mathfrak{T}$ is the single parameter that determines whether transient peak stress grows or declines as the wave moves through the stack.

(c) Except for high-frequency oscillations, wave propagation is controlled by the first PZ, and can be modeled accurately by a simple finite periodic chain of masses and springs. The wavefront moves at the phase velocity c_p corresponding to the frequency of the repeated set in the chain, while peak stress moves at the group velocity c_g evaluated at that same frequency. Both c_p and c_g diminish with frequency from a maximum of $c_0\simeq c_A(\tilde{z}\,\tilde{\tau})^{-1/2}$ at zero frequency.

Understanding uniaxial propagation and how it is coupled to radial waves forms the basis of understanding 2-D propagation. A chronology of events in 2D now follows. A forcing pulse is applied on top of a periodic stack. A compressive normal stress wave is generated under the footprint, which disperses as it propagates across the thickness of the first hard layer. The difference in σ_{zz} between top and bottom faces of a hard layer $\Delta\sigma_{zz}$, induces flexure in the form of antisymmetric radial and circumferential stresses $\sigma_{rr}, \sigma_{\theta\theta}$. At an interface, the wave is partly reflected and partly transmitted depending on $\tilde{z}$. Obviously, in 2D, σ_{zz} at an interface is smaller than in 1D because of spreading from radial propagation into undisturbed material. A stiffer weak layer, i.e., smaller $\tilde{z}$, increases transmission and reduces $\Delta\sigma_{zz}$ which reduces flexure of a hard layer. A weaker weak layer, i.e., larger $\tilde{z}$, decreases transmission and reduces coupling between hard layers allowing more flexure of the top layers. In the limit of a weak layer without stiffness, the case of the lone hard layer is recovered when flexure is greatest on the first layer. The process is repeated for all other layers, while intensity of all stress components is further reduced from dispersion and radial spreading.

Section I develops the modal analysis adopting transfer matrices to treat wave propagation in a 2-D axisymmetric biperiodic stack of disks with radius a. The governing linear differential equations of elastodynamics are separable. Solution of the separated equations is found in terms of primitives in cylindrical coordinates. The product of the axial and radial solutions is expressed in terms of a transfer matrix relating state vectors at the two faces of a layer. Radial wave number is selected to satisfy traction conditions on the lateral boundary $r=a$. A traction-free condition does not yield a

 0001-4966/96/99(6)/3513/15/$6.00

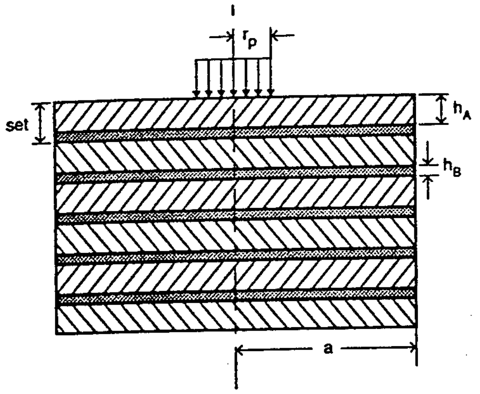

FIG. 1. Geometry of 2-D axisymmetric periodic stack.

unique dispersion relation for this wave number. One natural boundary yielding this condition is for shear stress and radial displacement to vanish. Numerical experiments adopting Mindlin plate flexure theory[3] show that with this constraint, the stress after reflection from the lateral boundary is much greater than with the traction-free condition. An alternate condition is a vanishing gradient of radial displacement, $\partial u/\partial r=0$. Radial wave numbers with this constraint asymptotically approach those with vanishing axial displacement, $w=0$, and radial stress $\sigma_{rr}=0$ for higher wave numbers. In plate theory, this constraint is termed simple supports since a vanishing radial stress across the thickness is equivalent to a vanishing radial moment. Unfortunately, with $\partial\tau_{rz}/\partial r=\partial u/\partial r=0$ at $r=a$, the problem is not self-adjoint and yields nonorthogonal eigenfunctions.

Section II discusses results of the basic stack subjected to a trapezoidal pulse. The first part studies the dispersion characteristics by observing modal groups in the frequency-radial wave number domain. Identification of the dominant motion in each group enables the exclusion of eigenfunctions with negligible generalized acceleration from the modal expansion. The second part presents transient histories of the basic stack and compares results to other numerical methods.

I. ANALYSIS

Consider the axisymmetric biperiodic layered stack in Fig. 1. Each periodic set in the stack consists of a thick hard disk A bonded to a thin weak disk B, where (E,ρ,ν) denote

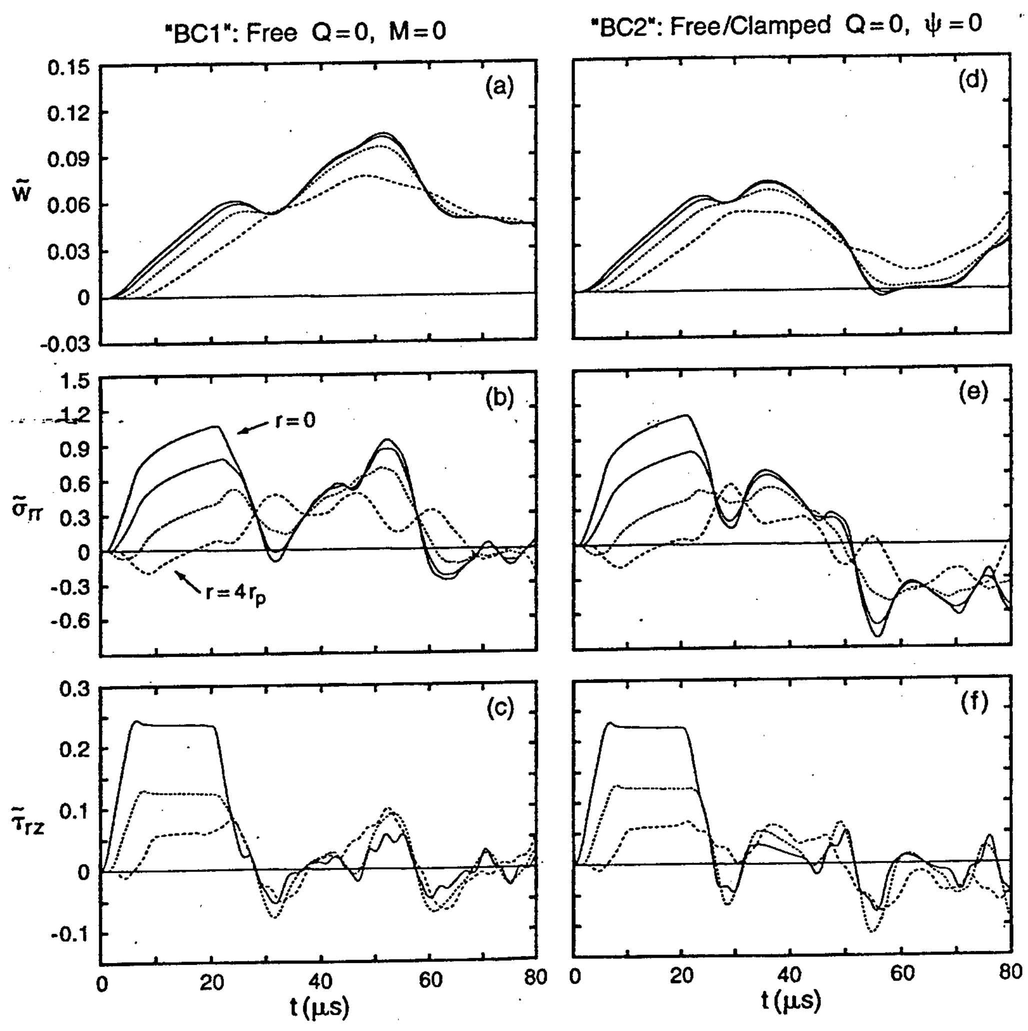

FIG. 2. Histories of normalized displacement $\bar{w}$ (microinch), and stresses $\bar{\sigma}_{rr}, \bar{\tau}_{rz}$ for boundary condition: (a)–(c) free; (d)–(f) free/clamped at — $r=0$, ---- r_p, ------ $2r_p$, –·–· $4r_p$.

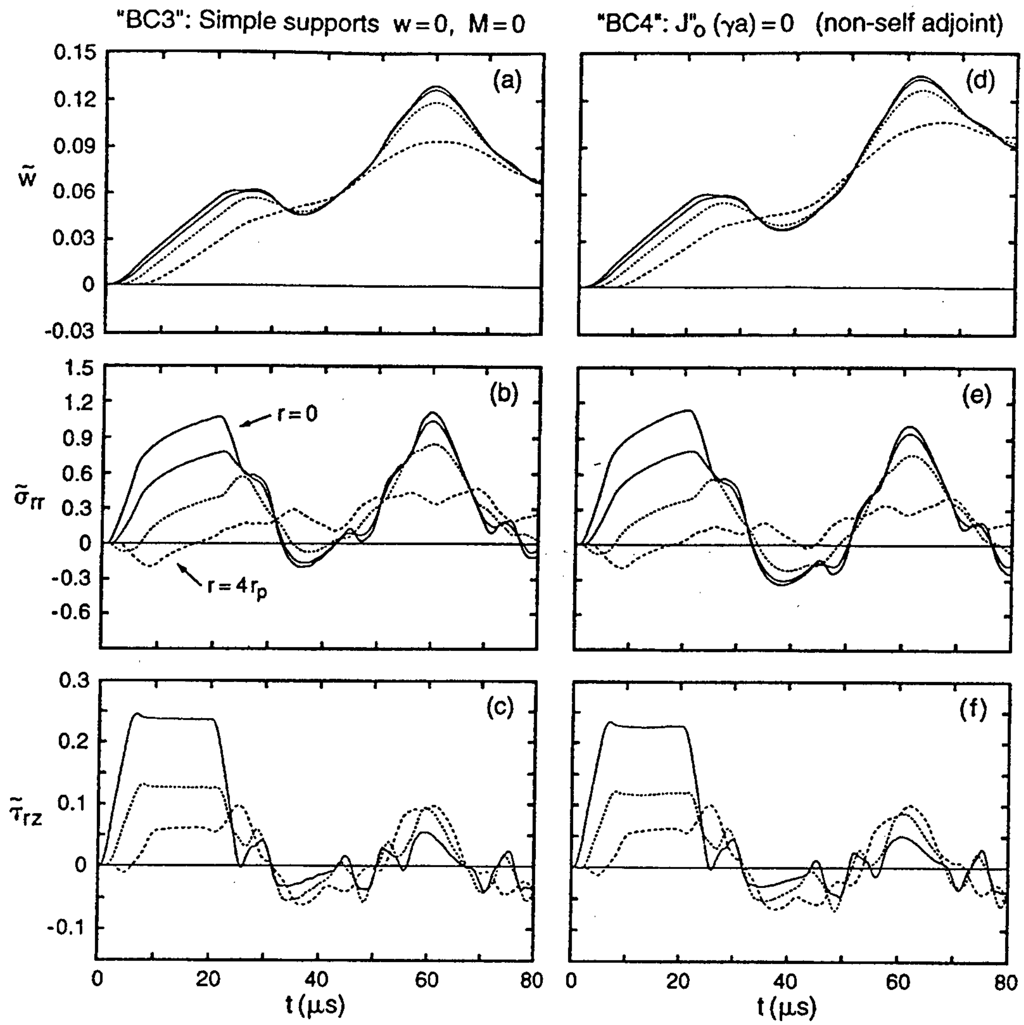

FIG. 3. Histories of normalized displacement $\tilde{w}$ (microinch), and stresses $\tilde{\sigma}_{rr}, \tilde{\tau}_{rz}$ for boundary conditions: (a)–(c). Simple supports; (d)–(f) $J_0''(\gamma a)=0$ (nonself-adjoint); at — $r=0$, ----- r_p, -------- $2r_p$, ------ $4r_p$.

modulus of elasticity, density and Poisson ratio, and h is thickness. All disks in the stack have the same radius a.

Start with the axisymmetric Navier equations of linear elastodynamics in the time domain[4]

$$(\lambda+\mu)\nabla(\nabla\cdot\mathbf{u})+\mu\nabla\cdot(\nabla\mathbf{u})+\rho\,\frac{\partial^2}{\partial t^2}\,\mathbf{u}=0, \tag{1}$$

where $\mathbf{u}(r,z)=\{u,w\}$ is the displacement vector with radial and axial components u and w, (λ,μ) are Lame's constants of the material

$$\lambda=\frac{E\nu}{(1+\nu)(1-2\nu)},\quad \mu=\frac{E}{2(1+\nu)}, \tag{1a}$$

and ∇ is the gradient operator. For an axisymmetric geometry $\mathbf{u}$ can be expressed in terms of scalar potentials φ and η[4]

$$\mathbf{u}=\nabla\varphi+\nabla\times\nabla\times(\eta\bar{\mathbf{e}}_z), \tag{2}$$

where $\bar{\mathbf{e}}_z$ is the unit vector along z. Expanding (2) yields

$$u=\frac{\partial\varphi}{\partial r}+\frac{\partial^2\eta}{\partial r\,\partial z},$$
$$w=\frac{\partial\varphi}{\partial z}-\frac{1}{r}\frac{\partial}{\partial r}\left(r\,\frac{\partial\eta}{\partial r}\right). \tag{3}$$

Substituting (2) in (1) assuming periodic motions in time with frequency ω

$$\nabla^2\varphi+k_L^2\varphi=0,\quad \nabla^2\eta+k_T^2\eta=0, \tag{4a}$$

$$k_L=\frac{\omega}{c_L},\quad c_L^2=\frac{\lambda+2\mu}{\rho},$$
$$k_T=\frac{\omega}{c_T},\quad c_T^2=\frac{\mu}{\rho}. \tag{4b}$$

The constitutive equations are

$$\sigma_{ij}=\lambda\,\delta_{ij}+2\mu\epsilon_{ij},$$
$$\delta_{ii}=\epsilon_{rr}+\epsilon_{\theta\theta}+\epsilon_{zz},$$
$$\epsilon_{rr}=\frac{\partial u}{\partial r},\quad \epsilon_{\theta\theta}=\frac{u}{r},\quad \epsilon_{zz}=\frac{\partial w}{\partial z},\quad \epsilon_{rz}=\frac{\partial u}{\partial z}+\frac{\partial w}{\partial r}. \tag{5}$$

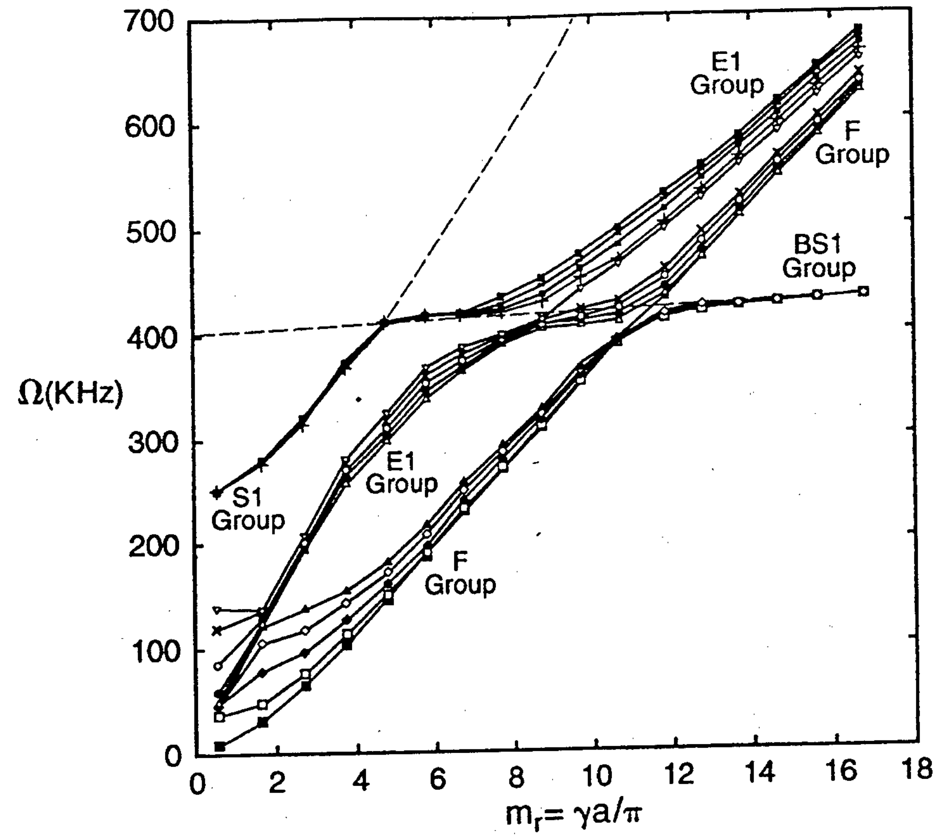

FIG. 4. Circular frequency Ω versus radial wave number m_r.

Solutions satisfying (4) are

$$\varphi(r,z)=J_0(\gamma r)(Ae^{-\alpha z}+Be^{\alpha z}),$$
$$\eta(r,z)=J_0(\delta r)(Ce^{-\beta z}+De^{\beta z}), \tag{6a}$$
$$\alpha^2=\gamma^2-k_L^2, \quad \beta^2=\delta^2-k_T^2, \tag{6b}$$

where γ and δ are roots of the dispersion relations to follow. Admissible constraints at the lateral boundary $r=a$ are $BC1\Rightarrow$traction free: $\tau_{rz}(a,z)=0$, $\sigma_{rr}(a,z)=0$

$$\tau_{rz}(a,z)\equiv 2\mu\alpha\gamma(-Ae^{-\alpha z}+Be^{\alpha z})J_0'(\gamma a)+\mu\delta(\beta^2+\delta^2)(Ce^{-\beta z}+De^{\beta z})J_0'(\delta a)=0, \tag{7a}$$
$$\sigma_{rr}(a,z)\equiv[-\lambda(\gamma^2-\alpha^2)J_0(\gamma a)+2\mu\gamma^2J_0''(\gamma a)]\times(Ae^{-\alpha z}+Be^{\alpha z})+2\mu\beta\delta^2J_0''(\delta a)\times(-Ce^{-\beta z}+De^{\beta z})=0. \tag{7b}$$

$BC1$ does not yield a z-independent dispersion relation for γ or δ. $BC2\Rightarrow$Shear-free with radial restraint: $\tau_{rz}(a,z)=0$, $u(a,z)=0$

$$\tau_{rz}(a,z)=0\Rightarrow[\text{same as (7a)}], \tag{8a}$$
$$u(a,z)\equiv J_0'(\gamma a)\gamma(Ae^{-\alpha z}+Be^{\alpha z})+J_0'(\delta a)\beta\delta\times(-Ce^{-\beta z}+De^{\beta z})=0. \tag{8b}$$

$BC2$ is identically satisfied if $\gamma=\delta$ and a dispersion relation for radial wave number γ in the form

$$J_0'(\gamma a)=0. \tag{8c}$$

$BC3\Rightarrow$Simple supports: $\sigma_{rr}(a,z)=0$, $w(a,z)=0$

$$\sigma_{rr}(a,z)=0\Rightarrow[\text{same as (7b)}], \tag{9a}$$
$$w(a,z)\equiv J_0(\gamma a)\alpha(-Ae^{-\alpha z}+Be^{\alpha z})+J_0(\delta a)\delta^2(Ce^{-\beta z}+De^{\beta z})=0. \tag{9b}$$

$BC3$ is as awkward to satisfy as $BC1$. However, it can be satisfied approximately if $\gamma=\delta$ and

$$J_0''(\gamma a)=0. \tag{10}$$

This constraint will be termed $BC4$, and it exactly satisfies $\partial\tau_{rz}/\partial r=\partial u/\partial r=0$. Note that for $\gamma a>8.65$, roots of (10) approximate roots of $J_0(\gamma a)=0$ with a difference less than 1%.[5]

Since the goal is to approximate $BC1$, selection among $BC2$, $BC3$, or $BC4$ depends on how close the corresponding response is to that of $BC1$. A numerical test adopting Mindlin's plate theory[3] to a lone disk with properties:

$E=45\times10^6$ lb/in.^{2}; $a=3$ in.

$\rho=3\times10^{-4}$ lb s^2/in.^{4}; $h=0.5$ in.

$\nu=0.25$; $r_p=0.25$ in.

compares histories of w, σ_{rr}, and τ_{rz} at $r=0$, r_p, $2r_p$, $4r_p$ in Figs. 2 and 3 for each of the four constraints $BC1$ through $BC4$. The disk is forced by a trapezoidal pressure pulse of unit magnitude, 25-μs duration and 5-μs rise and fall times, acting concentrically over a circular area of radius r_p. After reflection from the boundary $r=a$, histories of $BC2$ [Fig.

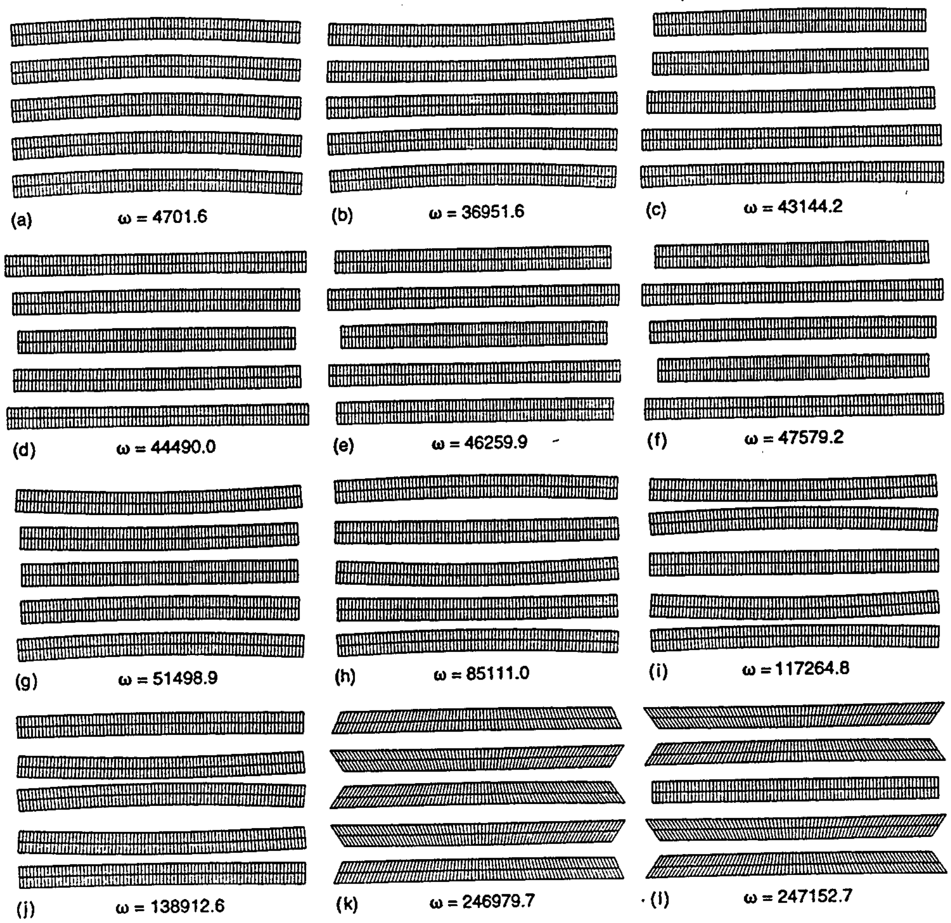

FIG. 5. Eigen modes of 2-D basic stack for radial wave number $m_r=0.58607$.

2(d),(e),(f)] are different from those of $BC1$ [Fig. 2(a),(b),(c)]. However, histories of $BC3$ almost coincide with those of $BC4$ (Fig. 3) and both agree well in magnitude and shape with histories of $BC1$ except for a shift in time of reflection caused by the difference in period of the fundamental resonance. Therefore, $BC4$ and Eq. (10) will be used throughout the analysis since, added to its convenient dispersion relation, it is physically acceptable, as it produces histories closest to those of $BC3$. Unfortunately, with (10) self-adjointness is lost, yielding nonorthogonal eigenfunctions which slightly offsets the ease of computing response.

Define the state vector at one face of a layer as

$$\mathbf{s}=\{u,\sigma_{zz},w,\tau_{rz}\}^{\mathrm{T}}. \tag{11}$$

Let $\bar{\mathbf{s}}$ be a function of z only after normalization by the radial dependence

$$\begin{aligned}&\bar{s}=\{\bar{u},\bar{\sigma}_{zz},\bar{w},\bar{\tau}_{rz}\}^T,\\ &\bar{u}=u/J_0'(\gamma r),\quad \bar{\tau}_{rz}=\tau_{rz}/J_0'(\gamma r)\\ &\bar{w}=w/J_0(\gamma r),\quad \bar{\sigma}_{zz}=\sigma_{zz}/J_0(\gamma r).\end{aligned} \tag{12}$$

Expressing $\bar{\mathbf{s}}$ in terms of (7a), (8b), (9b), and

$$\begin{aligned}\sigma_{zz}(r,z)=J_0(\gamma r)\{&(-\lambda k_L^2+2\mu\alpha^2)(Ae^{-\alpha z}+Be^{\alpha z})\\ &+2\mu\beta\gamma^2(-Ce^{-\beta z}+De^{\beta z})\}\end{aligned} \tag{13}$$

yields

$$\bar{\mathbf{s}}_2\equiv\begin{Bmatrix}\bar{u}\\ \bar{\sigma}_{zz}\\ \bar{w}\\ \bar{\tau}_{rz}\end{Bmatrix}_z=\begin{bmatrix}M_1 & 0\\ 0 & M_2\end{bmatrix}\begin{bmatrix}\Gamma & I\\ -\Gamma & I\end{bmatrix}[\mathbf{e}_z]\begin{Bmatrix}A\\ B\\ C\\ D\end{Bmatrix}$$

$$\mathbf{M}_1=\begin{bmatrix}\gamma & \beta\gamma\\ -\lambda k_L^2+2\mu\alpha^2 & 2\mu\beta\gamma^2\end{bmatrix};$$

$$\mathbf{M}_2=\begin{bmatrix}\alpha & \gamma^2\\ 2\mu\alpha\gamma & \mu\gamma(\beta^2+\gamma^2)\end{bmatrix},$$

$$[\mathbf{e}_z]=\begin{bmatrix}e^{-\alpha z} & 0 & 0 & 0\\ 0 & e^{-\beta z} & 0 & 0\\ 0 & 0 & e^{+\alpha z} & 0\\ 0 & 0 & 0 & e^{+\beta z}\end{bmatrix},\quad I=\begin{bmatrix}1 & 0\\ 0 & 1\end{bmatrix},$$

$$\Gamma=\begin{bmatrix}1 & 0\\ 0 & -1\end{bmatrix}, \tag{14}$$

$\{A,B,C,D\}^T$ are the undetermined constants of the homogeneous solutions (6a), (6b). Evaluating (14) at $z=0$ and $z=h$ then eliminating $\{A,B,C,D\}^T$ produces the transfer matrix of a layer:

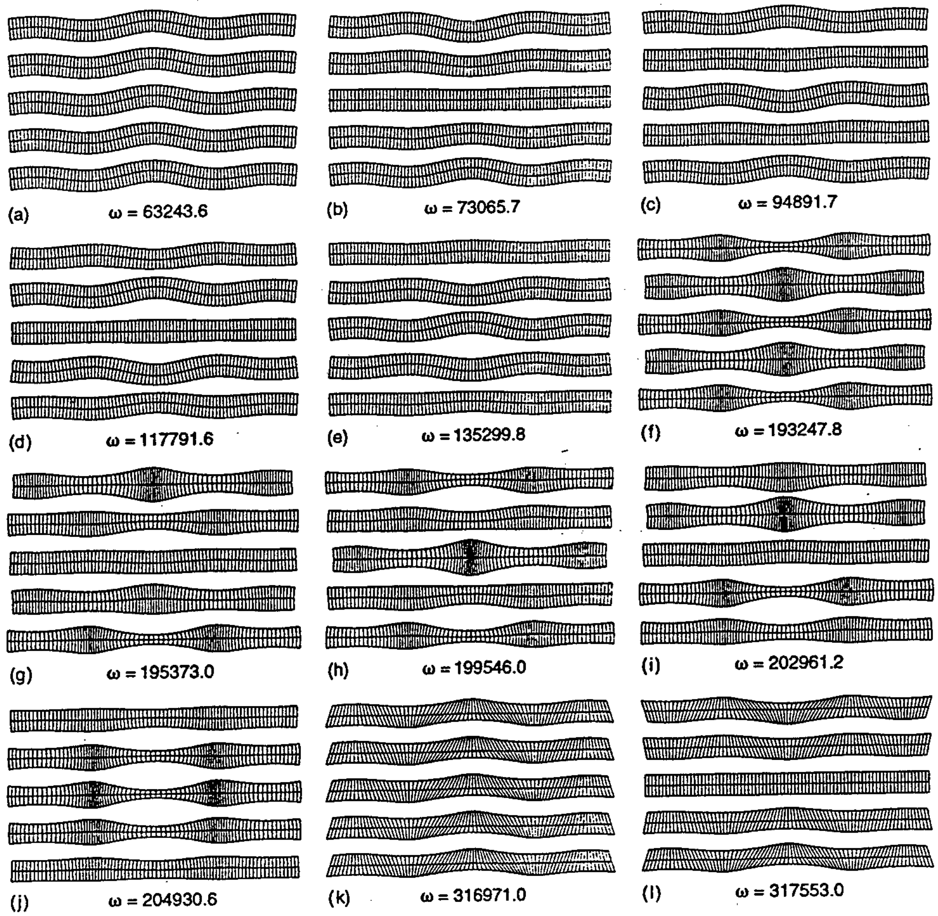

FIG. 6. Eigen modes of 2-D basic stack for radial wave number m_r=2.71719.

$$\bar{\mathbf{s}}_h=\mathbf{T}_h\bar{\mathbf{s}}_0$$

$$\mathbf{T}_h=\frac{1}{2}\begin{bmatrix}\mathbf{M}_1 & 0\\ 0 & \mathbf{M}_2\end{bmatrix}\begin{bmatrix}\Gamma & \mathbf{I}\\ -\Gamma & \mathbf{I}\end{bmatrix}[\mathbf{e}_h]\begin{bmatrix}\Gamma & -\Gamma\\ I & I\end{bmatrix}\times\begin{bmatrix}\mathbf{M}_1^{-1} & 0\\ 0 & \mathbf{M}_2^{-1}\end{bmatrix},$$

$$[\mathbf{e}_h]=[\mathbf{e}_z]_{z=h}. \tag{15}$$

Equation (15) relates state vectors at the two faces $z=0$ and $z=h$ of a layer in the stack. Enforcing continuity of $\bar{\mathbf{s}}$ at interfaces of layers and applying the known traction conditions $\mathfrak{F}$ at top and bottom faces of the stack produces a tridiagonal block matrix $[\mathbf{D}]$ in the ensemble of the $4L$ unknown displacements and tractions $\mathfrak{S}$ at all interfaces of L layers

$$[\mathbf{D}]\mathfrak{S}=\mathfrak{F}$$

$$\mathbf{D}=\begin{bmatrix}\mathbf{I} & 0 & 0 & 0 & & & \\ \mathbf{T}_{h1} & \mathbf{T}_{h2} & \mathbf{I} & 0 & & & \\ \mathbf{T}_{h3} & \mathbf{T}_{h4} & 0 & -\mathbf{I} & 0 & 0 & \\ 0 & 0 & \mathbf{T}_{h1} & \mathbf{T}_{h2} & \mathbf{I} & 0 & \\ & & \mathbf{T}_{h3} & \mathbf{T}_{h4} & 0 & -\mathbf{I} & \cdots\\ & & 0 & 0 & \mathbf{T}_{h1} & \mathbf{T}_{h2} & \cdots\\ & & & & \cdots & \cdots & \cdots\end{bmatrix}, \tag{16}$$

where $\mathbf{T}_{hi}$ are constituent submatrices of $\mathbf{T}_h$ in (15) defined by

$$\mathbf{T}_h=\begin{bmatrix}\mathbf{T}_{h1} & \mathbf{T}_{h2}\\ \mathbf{T}_{h3} & \mathbf{T}_{h4}\end{bmatrix}$$

$$\mathfrak{S}=[\bar{\mathbf{s}}_{h1},\bar{\mathbf{s}}_{h2},\ldots,\bar{\mathbf{s}}_{hn}]^T$$

is the ensemble of state vectors at all interfaces and

$$\mathfrak{F}=\{\mathbf{f}_1,0,0,\ldots,0\}^T$$

is the vector of all boundary tractions where $\mathbf{f}_1$ is the traction applied on the top face of the first layer.

The eigenproblem det $[\mathbf{D}]=0$ produces the modal set $\{\Phi_j,\omega_j\}$ used in the forced response.

Steps in the analysis of the forced response now follow. Assume that the displacement vector $\mathbf{u}$ is the linear superposition of a static solution $\mathbf{u}_s$ times the external time-dependent excitation $f(t)$, and a dynamic solution $\mathbf{u}_d$ satisfying traction-free boundary conditions at the top and bottom faces of the stack.[5] Where $\mathbf{x}=\{r,z\}$ then

$$\mathbf{u}(\mathbf{x},t)=\mathbf{u}_s(\mathbf{x})f(t)+\mathbf{u}_d(\mathbf{x},t). \tag{17}$$

Expand $\mathbf{u}_d$ in terms of eigenfunctions $|j\rangle\equiv\{u,w\}_j(\mathbf{x})$

$$\mathbf{u}_d=\sum_{j=1} a_j(t)|j\rangle, \tag{18}$$

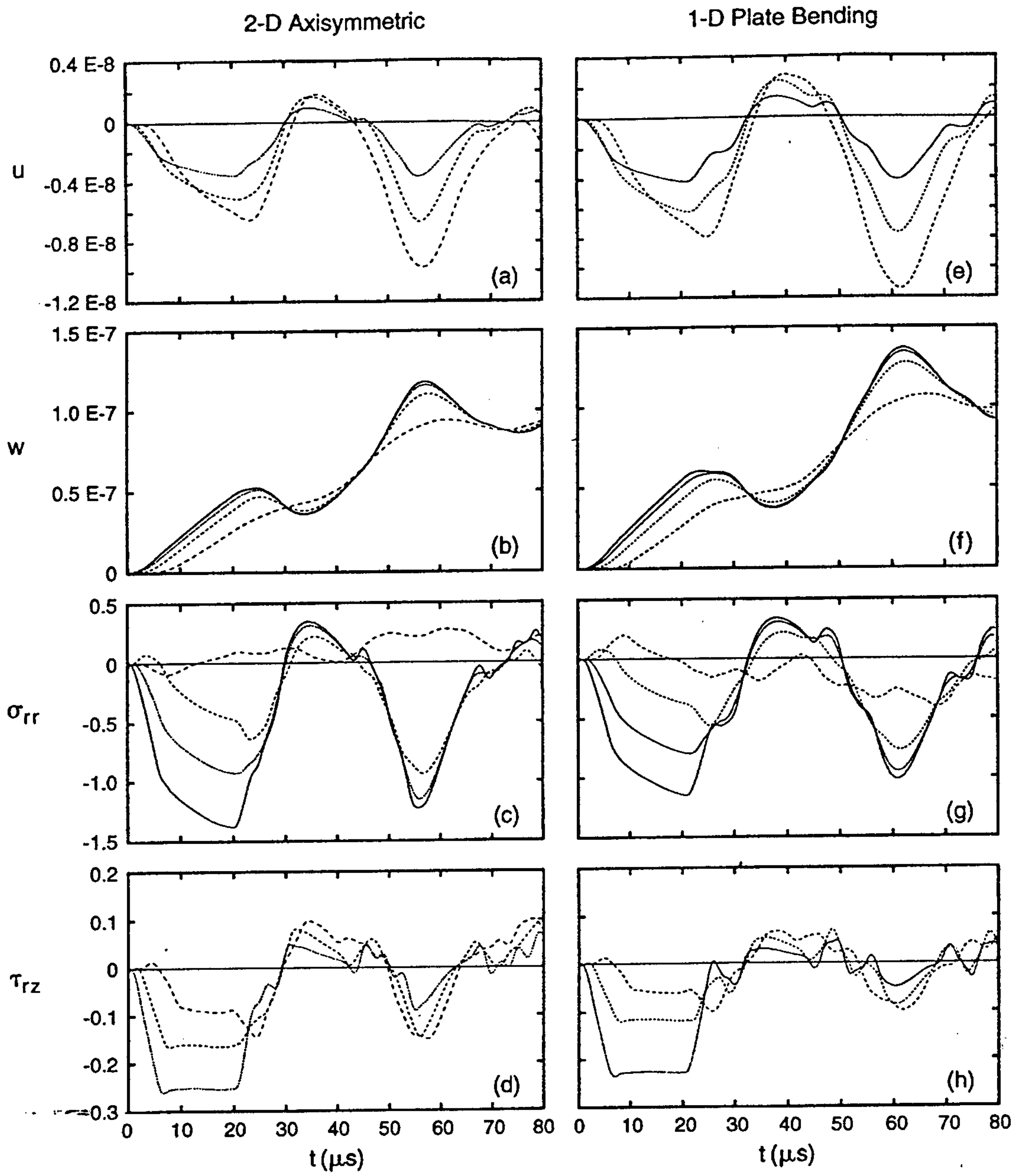

FIG. 7. Lone disk histories: (a)–(d) 2-D Axisymmetric analysis; (e)–(f) plate bending analysis — $r=0$, — $r=r_p$, ------- $r=2r_p$, ---- $r=4r_p$.

where the expansion in (18) includes all truncated sets for all γ's considered.

Substituting (17) and (18) in the unsteady equations of motion (1) assuming zero initial conditions yields

$$\sum_j (\ddot{a}_j+\omega_j^2 a_j)\rho(\mathbf{x})|j\rangle=-\ddot{f}(t)\rho(\mathbf{x})\mathbf{u}_s(\mathbf{x}). \tag{19}$$

Eliminating the spatial dependence by inner products of $|j\rangle$ which means integrating over all layers in the stack gives

$$\begin{aligned}&\sum_j \mathbf{N}_{ij}(\ddot{a}_j+\omega_j^2 a_j)=-\ddot{f}(t)\mathbf{N}_{ai},\\ &\mathbf{N}_{ij}=\langle i|\rho(\mathbf{x})|j\rangle,\\ &\mathbf{N}_{ai}=\langle i|\cdot\rho(\mathbf{x})u_s(\mathbf{x})\rangle.\end{aligned} \tag{20}$$

Since $|j\rangle$ are not orthogonal, $\mathbf{N}=[N_{ij}]$ is not diagonal.

Decoupled equations in the vector of generalized coordinates $\mathbf{a}$ are found by inverting $\mathbf{N}$:

$$\ddot{a}_i+\omega_i^2 a_i=-[\mathbf{N}^{-1}\quad \mathbf{N}_a]_i\ddot{f}(t). \tag{21}$$

A solution to (21) is found in terms of Duhamel's integral:

$$a_i(t)=-\frac{1}{\omega_i}[\mathbf{N}^{-1}\quad \mathbf{N}_a]_i\int_0^t \ddot{f}(\tau)\sin\,\omega_i(t-\tau)d\tau. \tag{22}$$

For the special case of a polygonal $f(t)$ with n_t vertices

$$f(t)=\sum_{k=1}^{n_t}[H(t-t_k)-H(t-t_{k+1})](d_{1k}+d_{2k}t), \tag{23a}$$

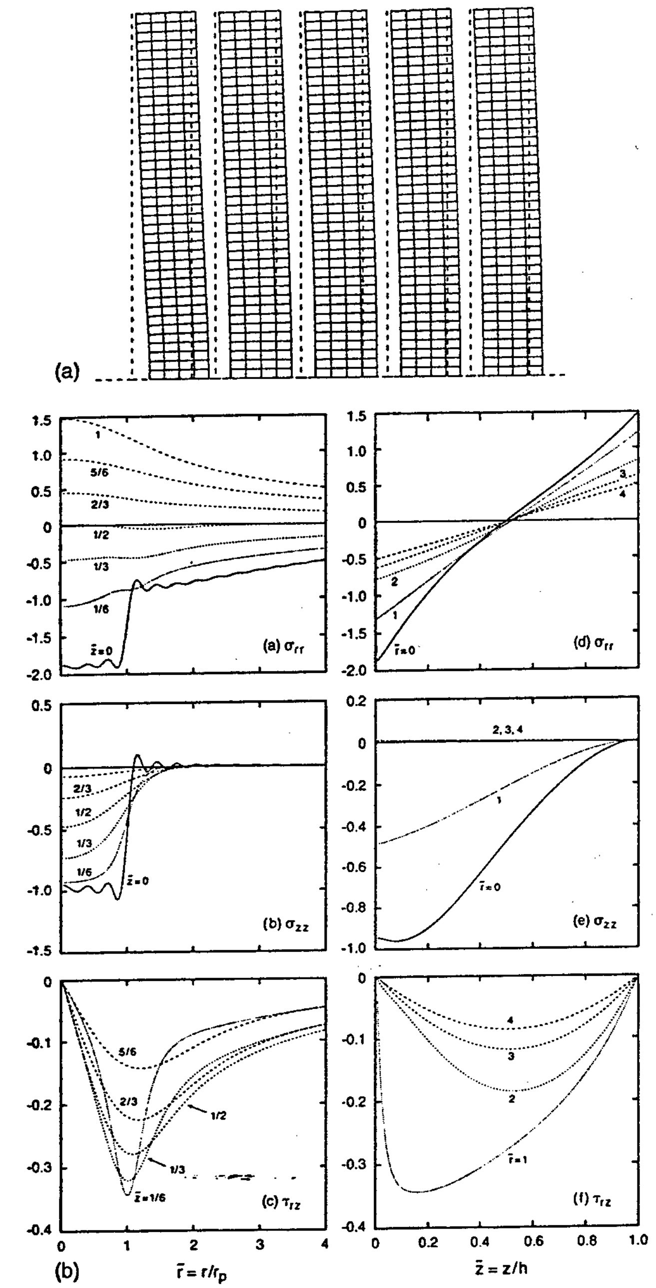

FIG. 8. A. Statically deformed shape of basic stack. B. Static stress distribution in lone disk; (a)–(c) along $\tilde{r}$, (d)–(f) along $\tilde{z}$.

$$\ddot{f}(t)=\sum_{k=1}^{n_t}\left[\delta(t-t_k)-\delta(t-t_{k+1})\right]d_{2k}. \tag{23b}$$

Substituting (23) in (22) yields

$$a_i(t)=-\frac{1}{\omega_i}[\mathbf{N}^{-1}\quad \mathbf{N}_a]_i\sum_{k=1}^{n_t} d_{2k}[\sin \omega_i(t-t_k) \\ -\sin \omega_i(t-t_{k+1})]. \tag{24}$$

Static analysis of the stack is developed in Appendix A. Inner products $\mathbf{N}$ and $\mathbf{N}_a$ are evaluated analytically using MATHEMATICA™.

When radial wave number γ is large compared to k_L or k_T, exponents (α,β) in the axial solutions (6a), (6b) are real and truncation error is inevitable when $e^{2\alpha h}$ or $e^{2\beta h}$ is greater than e^{2M} where it and $(e^{2M}-1)$ cannot be distinguished within machine precision. To treat this error in the evaluation of inner products $\mathbf{N}$ and $\mathbf{N}_a$, a method developed in Ref. 7, termed selective abbreviation is adapted to the present problem. An exposition of how it is applied can be found in Appendix B.

II. RESULTS

The basic stack consists of five hard A and four weak B layers (see Fig. 1). Properties are listed below:

$E_A=45\times 10^6$ lb/in.^{2}; $E_B=20\times 10^3$ lb./in.^{2}

$\rho_A=3\times 10^{-4}$ lb s^2/in.^{4}; $\rho_B=1\times 10^{-4}$ lb. s^2/in.^{4}

$\nu_A=0.25$; $\nu_B=0.48$

$h_A=0.5$ in.; $h_B=0.01$ in.

$a=3$ in.; $r_p=0.25$ in.

For motions along the axis of the stack, the compressional impedance ratio $\tilde{z}_c$ and travel time ratio $\tilde{\tau}_c$ are

$$\tilde{z}_c=\left\{\frac{\rho_A E_A(1-\nu_A)}{(1+\nu_A)(1-2\nu_A)}\frac{(1+\nu_B)(1-2\nu_B)}{\rho_B E_B(1-\nu_B)}\right\}^{1/2}=30.37,$$

$$\tilde{\tau}_c=\frac{h_B}{h_A}\left\{\frac{E_A(1-\nu_A)}{\rho_A(1+\nu_A)(1-2\nu_A)}\frac{\rho_B(1+\nu_B)(1-2\nu_B)}{E_B(1-\nu_B)}\right\}^{1/2} \tag{25}$$

$$=0.20.$$

Figure 4 plots resonant frequency Ω(Hz) against radial wave number $m_r=\gamma a/\pi$, where (γa) are the roots of dispersion relation (10), for the first 14 modes at fixed m_r. Frequency lines form groups with specific dominant motions. Figures 5 and 6 illustrate shapes of some of these modes, showing only the hard A layers and exaggerate the thickness of the spring between the layers for clarity. For $m_r=0.586$, the first two resonances involve flexure of the hard layer with the weak layer acting as an elastic spring [Fig. 5(a) and (b)]. The next four modes involve radial extension [Fig. 5(c)–(f)]. The next three modes [Fig. 5(g),(h),(i)] complete the group of flexural modes. The last four modes [for example Fig. 5(k),(l)] involve shear motions of the hard layer. For this m_r, flexural and extensional modes overlap. For $m_r=2.717$, the groups are well separated as shown in Fig. 6. Here, the first 5 modes [Fig. 6(a)–(e)] involve flexure only. The next five modes [Fig. 6(f)–(j)] include extension through the thickness of the hard layer. The last four modes [for example Fig. 6(k),(l)] include shear of the hard layer.

More generally, among the modes for $0.58\leq m_r\leq 4.7$, there are three frequency groups (see Fig. 4):

(a) The first group, F, consists of L flexural modes of the hard layer with the weak layer acting as a coupling spring. In this way it resembles the $(L-1)$ modes in the first propagation zone PZ1 in a 1-D chain.[2] The difference is that in 2 D, hard layers do not move as rigid masses but instead flex radially. Shear reaction from flexure accounts for the mode added by two dimensionality.

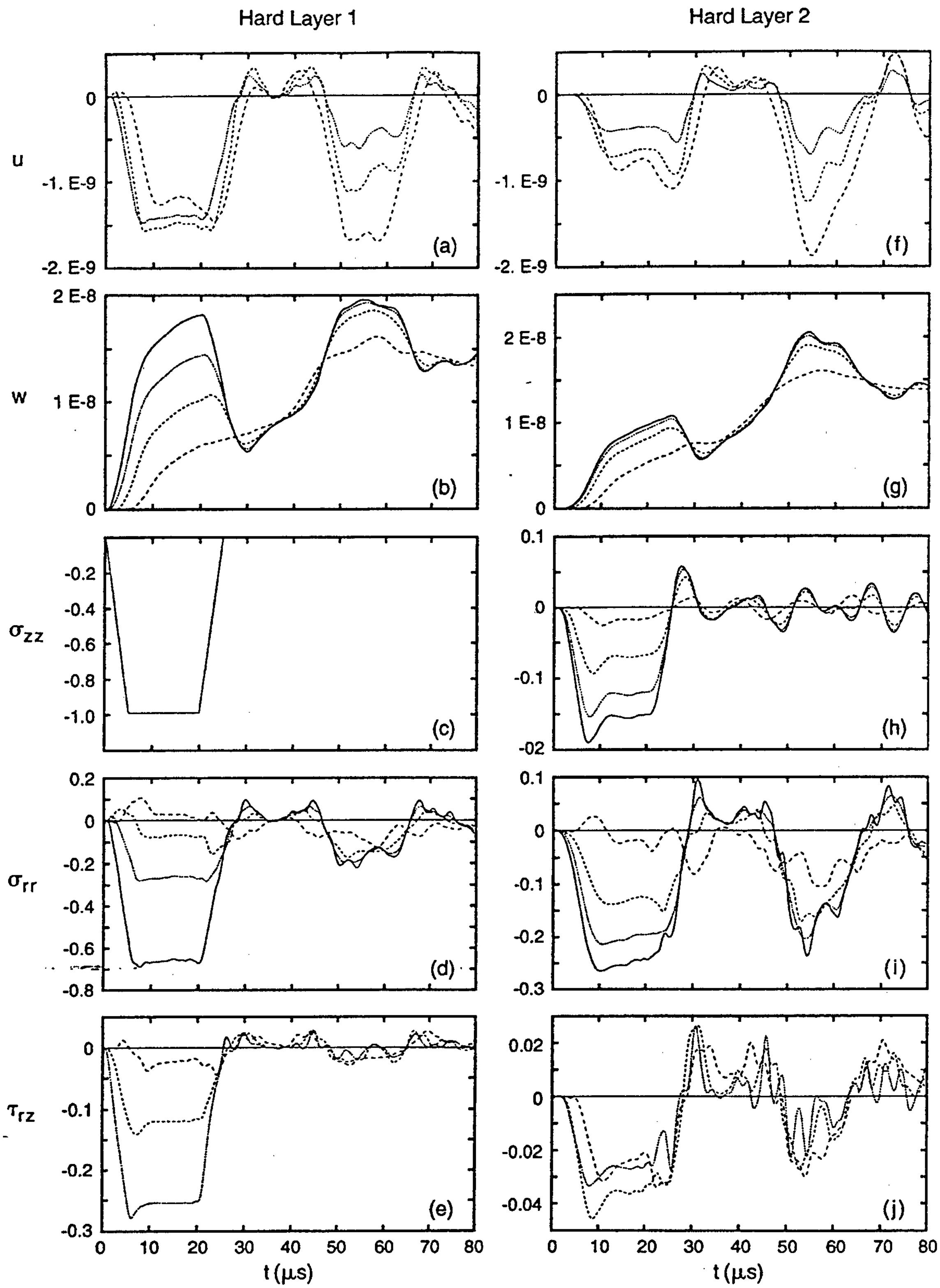

FIG. 9. Histories of hard layers 1 and 2 of basic stack: — $r=0$, ---- $r=r_p$, ------ $r=2r_p$, ----- $r=4r_p$.

(b) The second group, $E1$, consists of L extensional modes of the hard layer. Extension is primarily radial only for the lowest $m_r=0.58$, then changes to axial with one half-wave through the thickness when $m_r>0.58$. In this way, it resembles the L modes of PZ2 in 1D.

(c) The third group, $S1$, consists of $(L-1)$ shear modes of the hard layer and is without a 1-D counterpart. Since shear motions are primarily radial, $S1$ produces negligible generalized accelerations $|(N^{-1}N_a)|$ in response to axial forcing functions.

At $m_r \simeq 4.8$, the third group, $S1$, changes to a fourth

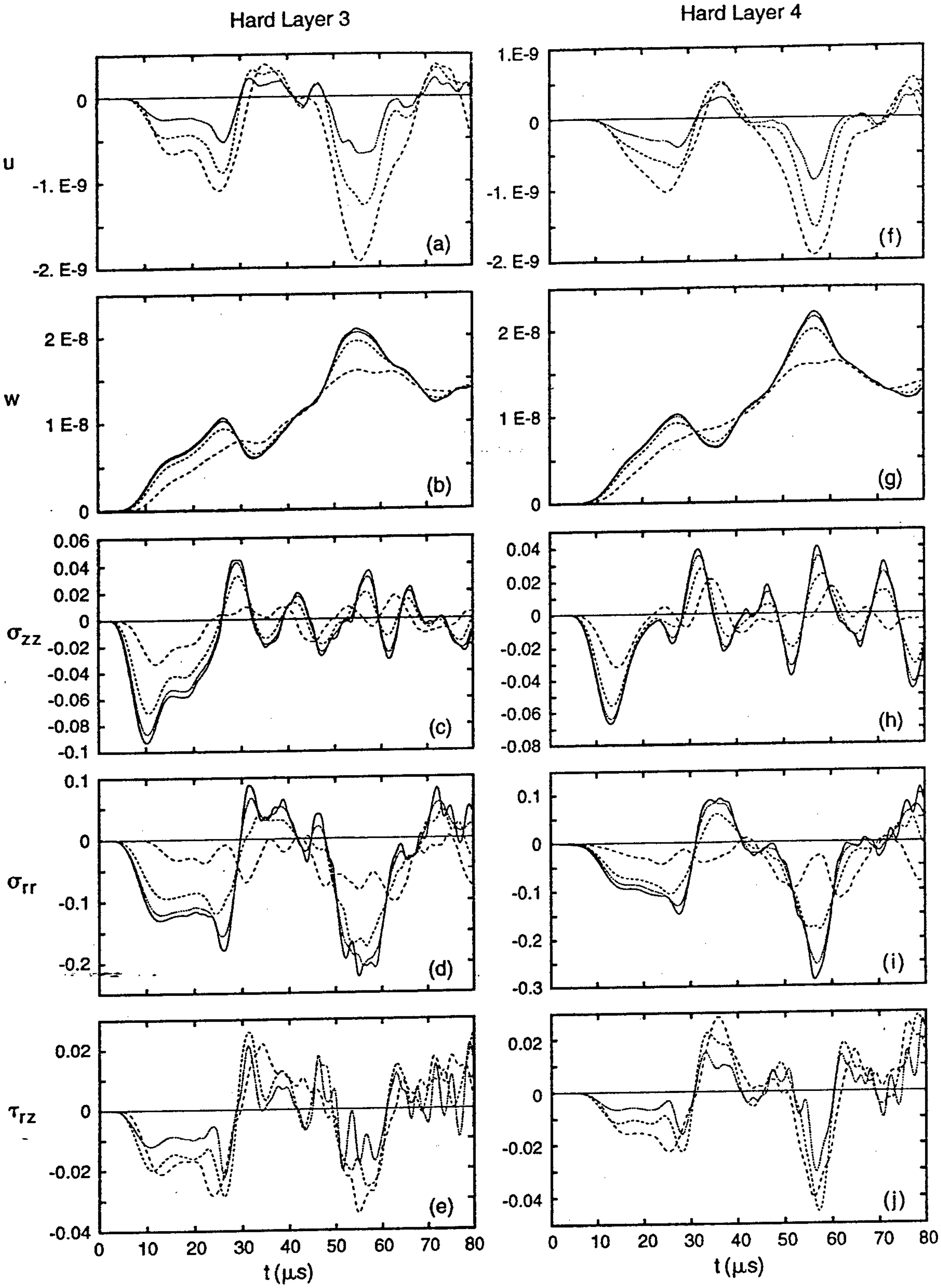

FIG. 10. Histories of hard layers 3 and 4 of basic stack: — $r=0$, ----- $r=r_p$, ------- $r=2r_p$, ---- $r=4r_p$.

group, $BS1$, involving shear motions of the weak layer and includes $(L-1)$ resonances. In the interval $6.7<m_r<8.7$, three smooth transitions occur; each involving $(L-1)$ modes: $F \rightarrow BS1$, $E1 \rightarrow F$, and $S1 \rightarrow E1$. This mode transition, called coalescence, is similar to what results from changing a parameter in other multicoupled dynamical systems.

Note that frequency lines of the F group narrow as they approach the $E1 \rightarrow F$ transition, then widen after the transition. One explanation relies on coupling between τ_{rzB} and σ_{zzB}, and the resonant state of the weak layer at $BS1$. Near this resonance, radial stress σ_{rrB} follows the plain strain approximation:

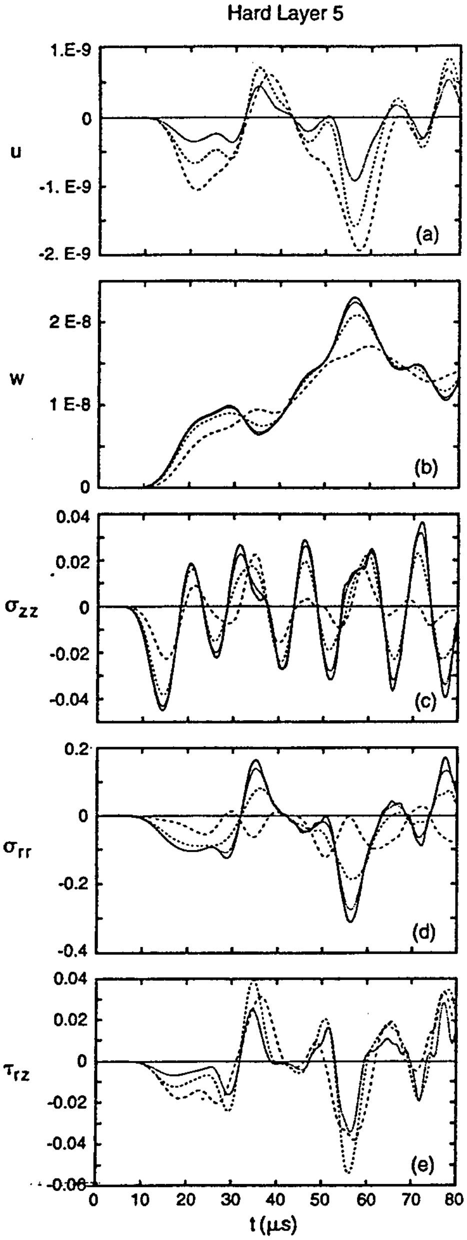

FIG. 11. Histories of hard layer 5 of basic stack: — $r=0$, ----- $r=r_p$, ------- $r=2r_p$, ---- $r=4r_p$.

$$\sigma_{rrB} \simeq \frac{E_B}{(1+\nu_B)(1-2\nu_B)}\left[(1-\nu_B)\frac{\partial u_B}{\partial r}+\nu_B\frac{u_B}{r}\right],$$

$$\sigma_{zzB} \simeq \frac{(\nu_B E_B)}{(1+\nu_B)(1-2\nu_B)}\left[\frac{\partial u_B}{\partial r}+\frac{u_B}{r}\right]=\lambda_B \epsilon_{\nu B},$$

$$\tau_{rzB}=\frac{E_B}{2(1+\nu_B)}\frac{\partial u_B}{\partial z}.$$

Since $\nu_B=0.48$, $\sigma_{rrB} \simeq \sigma_{zzB}$, a hydrostatic state of stress. At $BS1$, u_B is symmetric about $z=h_B/2$, producing a net volumetric strain, ϵ_{VB}, i.e., $\int_0^{h_B}\epsilon_{VB}\,dz \neq 0$. Accordingly, σ_{rrB} and σ_{zzB} are large near $BS1$. Slightly below $BS1$, traction on the faces and stress in the weak layer are in phase reducing the resistance of the weak layer to relative motions at the two faces. This effectively weakens coupling between hard layers and explains narrowing of the frequency lines in Fig. 4. Slightly above $BS1$, traction and stress are out of phase, effectively strengthening coupling between hard layers, which explains widening of the lines. If $\tau_{rzB}=0$ at $z=0$ and $z=h_B$ (slip interfaces), u_B at $BS1$ is antisymmetric about $z=h_B/2$ allowing equivoluminal shear deformation. In this case, $\int_0^{h_B}\epsilon_{VB}\,dz = 0$, invalidating the arguments above.

At higher frequencies, other groups emerge, such as $E2$, $E3$, etc., where axial motions of the hard layer include two or three half-waves through the thickness. The same applies to $S2$, $S3$, etc., and $BS2$, $BS3$, etc. Here also, transition between groups occurs near coalescence. Note that for an axial forcing function, the F and E_n groups dominate response.

The first test is to compare transient response of a lone hard disk to results from 1-D Mindlin plate theory[3] having the same boundary condition: $J_0''(\gamma a) = 0$. The disk is forced by a trapezoidal pressure pulse of unit magnitude, 25 μs in duration and 5-μs rise and fall times acting over a circular area of radius $r_p=0.25$ in. its footprint. In this way, it is identical to the pulse used to compute response in Figs. 1 and 3. Figure 7 compares histories of displacement and stress by the two methods. Plate bending theory's displacements are 15% higher, and its stresses are 15% lower. This implies that the disk is stiffer in 2D than in plate theory. Contrary to the 1-D assumption that radial displacement u varies linearly with axial position z, in 2D, u varies nonlinearly with z and reaches a larger magnitude at the surface $z=\pm h/2$. Specifically in 1-D, $u=\alpha_1(2z/h-1)$, while in 2D, $u=\alpha_1(2z/h-1)+\alpha_3(2z/h-1)^3$, where α_1 and α_3 are positive definite and depend on slope of the cross section. Moreover, the volumetric part of stress raises magnitude of σ_{rr} along the excited face for $r \leqslant r_p$ as explained later for the static problem. Except for a slight difference in phase velocity, histories from both methods agree in shape before and after reflection from the lateral boundary.

A prerequisite to solving the transient response of the stack by static-dynamic decomposition is the solution of the static problem. Figure 8(A) illustrates the statically deformed basic stack. Figure 8B plots static stress distributions of the lone disk by the analysis in Appendix A with 80 radial wave numbers. In Fig. 8B(a), the sharp increase in $|\sigma_{rr}|$ at $r=r_p$ and $z=0$ can be explained as follows. Stress σ_{rr} is the sum of an equivoluminal part $[\sigma_{rr}]_{\text{equiv.}}$ from flexure, antisymmetric about $z=h/2$, and a volumetric part $[\sigma_{rr}]_{\text{vol.}}$ from normal traction σ_{zz0} over the footprint $r<r_p$. The volumetric part is substantial close to σ_{zz0} ($r<r_p$ and $z<h/6$), and diminishes steeply elsewhere [see Fig. 8B(a)]. For $r>3r_p$, the flexural part becomes paramount as evidenced by the antisymmetry of σ_{rr} about $z=h/2$ in Fig. 8B(d). In fact, $[\sigma_{rr}]_{\text{equiv.}}$ follows the plane stress approximation which at $(r,z)=(0,0)$ yields[8]

$$[\sigma_{rr}(0,0)]_{\text{equiv.}}=\frac{3}{2}\left(\frac{r_p}{h}\right)^2\left[1+(1+\nu)\ln\left(\frac{a}{r_p}\right)-\frac{(1-\nu)}{4}\left(\frac{r_p}{a}\right)^2\right]\sigma_{zz0}$$

and $[\sigma_{rr}]_{\text{vol.}}$ at $(r,z)=(0,0)$ follows the uniaxial strain approximation

$$[\sigma_{rr}(0,0)]_{\text{vol.}} = \nu/(1-\nu)\sigma_{zz0}.$$

Clearly, $[\sigma_{rr}]_{\text{vol.}}$ is independent of geometry while $[\sigma_{rr}]_{\text{equiv.}}$ increases with $(r_p/h)^2$ and $\ln(a/r_p)$. For the example in Fig. 8(b), $h=0.5$ in., $r_p=0.25$ in., $a=3$ in. and $\nu=0.25$, yielding $[\sigma_{rr}(0,0)]_{\text{equiv.}}=1.54$ and $[\sigma_{rr}(0,0)]_{\text{vol.}}=1/3$. These values agree with those obtained from Fig. 8B(a), where $[\sigma_{rr}(0,0)]_{\text{equiv.}}=|\sigma_{rr}(0,h)|$ and $[\sigma_{rr}(0,0)]_{\text{vol.}}=|\sigma_{rr}(0,0)| - |\sigma_{rr}(0,h)|$. The above applies also to $\sigma_{\theta\theta}$. At $z=0$, σ_{zz}'s profile along r duplicates that of the external traction $\sigma_{zz0}=H(r)-H(r-r_p)$, where $H(r)$ is the Heviside function [see Fig. 8B(b)]. At $r=r_p$, shear stress $|\tau_{rz}|$ along z achieves a maximum at $z=h/6$ then drops smoothly following a skewed parabolic profile [see Fig. 8B(f)]. For $r>2r_p$, this profile changes to a parabola, symmetric about $z=h/2$ as predicted by 1-D plate flexure theory. In Fig. 8B(c), the symmetry of τ_{rz} is confirmed by the coalescence of the τ_{rz} profile pairs at $\{z=h/3;\ z=2h/3\}$ and at $\{z=h/6;\ z=5h/6\}$ for $r>3r_p$. As with $\{\sigma_{rr},\sigma_{\theta\theta}\}$ the asymmetry of τ_{rz} close to the footprint is caused by the volumetric part of the stress field from the applied traction. Since the static solution is included in the forcing function of the dynamic solution [see Eq. (22)], the volumetric part must be represented in the set of eigenfunctions by including extensional modes along r and z.

Histories of the basic stack forced by the same pulse as that of the lone disk are shown in Figs. 9, 10, and 11. Sensors are located at the top face of each hard layer. For each dependent variable, four histories are superimposed at $r=0,r_p,2r_p,4r_p$. Histories of layer 1 are shown in Fig. 9(a)–(e). To see what effect the stack has, compare its results with those of the lone plate. Note that before arrival of waves reflected from the $r=a$ boundary, marked by a second prolonged drop of u to negative values, u and w [Fig. 9(a),(b)] are smaller [Fig. 7(a),(b)], σ_{rr} [Fig. 9(d)] is approximately half [Fig. 7(c)] and τ_{rz} is almost the same. After the first reflection from the $r=a$ boundary σ_{rr} [Fig. 9(d)] is further reduced [Fig. 7(e)]. Transmission into the second layer, reducing the difference in σ_{zz} between the two faces of the layer that causes flexure, accounts for this reduction.

Figure 9(f)–(j) plot histories of layer 2. σ_{zz} [Fig. 9(h)] is attenuated to 20% of the input pressure σ_0 although transmissibility

$$\mathscr{T}=\frac{2}{\pi}\frac{c_A}{h_A}(\tilde{z}\,\tilde{\tau})^{-1/2}t_f$$

has a value, 4.1, that in 1D would magnify σ_{zz}. This attenuation is caused by spreading of the footprint through radial propagation. The spreading is evident from Fig. 9(j), where the maximum τ_{rz} is reached at $r=2r_p$, which indicates that while propagating through layer 1, the footprint has spread from $r=r_p$ to $r=2r_p$ [compare Fig. 9(e) and (j)]. The spreading continues into the third layer, as seen from Fig. 10(e) and (j) where the maximum τ_{rz} is reached at $r=4r_p$.

Magnitude of σ_{rr} after the first reflection from $r=a$, $|\sigma_{rr}|_2$ rises with axial distance. Figures 9(d), (i), 10(d), (i), and 11(d), reveal a succession of values, 0.2, 0.24, 0.23, 0.28, 0.30, for $|\sigma_{rr}|_2$. Meanwhile, the magnitude at σ_{rr} on first arrival, $|\sigma_{rr}|_1$, falls with axial distance, and in fact is surpassed by $|\sigma_{rr}|_2$ at layer 3. If the isostress for principal tensile stress were traced, the resulting figure would take the form of an hourglass—wider at the top, narrowing at its middle, then opening out again toward the boundary from which the reflected waves come. This "hour-glass" shape of the damaged zone in weakly coupled stacks of brittle ceramics was observed experimentally [see Ref. 1, Fig. 3(b)].

III. CONCLUSION

Wave propagation in a finite 2-D axisymmetric biperiodic stack is studied, adopting transfer matrices and modal analysis. An approximation to the lateral boundary condition $w(a,z)\equiv(\partial u/\partial r)(a,z)=0$ yields separable eigenproblems in r and z and a dispersion relation $J_0''(\gamma a) = 0$. With this approximation, histories of a lone disk computed by Mindlin's plate theory agree closely to those of the traction free disk and those with "exact" simple supports, even after reflection from $r=a$. Important features of 2-D propagation are

(1) The Ω vs m_r plot includes resonance lines belonging to one of four groups

(a) the F group of L resonances includes flexure of the hard layers coupled by quasistatic stiffness of the weak layers,
(b) the $E1$ group of L resonances includes radial and axial motions of the hard layers with the same coupling as in (a),
(c) the $BS1$ group of $(L-1)$ resonances includes shear motions of the weak layers between rigid hard layers,
(d) the $S1$ group of L resonances includes shear motions of the hard layers with the same coupling as in a).

Transition of groups from one type to another occurs near coalesence where $F\rightarrow BS1$, $E1\rightarrow F$, and $S1\rightarrow E1$. Only the F and $E1$ groups have appreciable generalized acceleration and contribute to response.

(2) When forced by a trapezoidal pulse of short duration, the basic stack responds in the following way:

(a) $(\sigma_{zz})_1$ of first arrival attenuates along the stack more than in the equivalent 1-D stack because of radial spreading from flexural waves.
(b) $(\sigma_{rr})_1$ and $(\sigma_{\theta\theta})_1$ are lower than in the single hard layer and attenuate less sharply than $(\sigma_{zz})_1$ along the stack.
(c) After the first reflection from $r=a$, $(\sigma_{rr})_2$ rises along z and exceeds $(\sigma_{rr})_1$ deeper than layer 3 of the basic stack. This feature explains the "hour glass" shape of the damaged zone observed experimentally.

ACKNOWLEDGMENT

The authors appreciate Pat Dougherty for her patience and accuracy in typing the manuscript.

APPENDIX A: ELASTOSTATIC SOLUTION OF THE STACK

Expanding Eq. (1) with $\partial^2 u/\partial t^2=0$ yields the elastostatic equations of equilibrium:

$$\left[(\lambda+2\mu)\nabla_1^2+\mu\frac{\partial^2}{\partial z^2}\right]\mu+(\lambda+\mu)\frac{\partial^2 w}{\partial r\,\partial z}=0, \tag{A1a}$$

$$(\lambda+\mu)\frac{\partial}{\partial z}\left(\frac{\partial}{\partial r}+\frac{1}{r}\right)u+\left[\mu\nabla_0^2+(\lambda+2\mu)\frac{\partial^2}{\partial z^2}\right]w=0,$$

$$\nabla_n^2\equiv\frac{\partial^2}{\partial r^2}+\frac{1}{r}\frac{\partial}{\partial r}-\frac{n^2}{r^2},\quad n=0,1. \tag{A1b}$$

Operating on each equation to eliminate w from (A1a) and u from (A1b) yields the decoupled equations:

$$\mu(\lambda+2\mu)\left(\nabla_1^2+\frac{\partial^2}{\partial z^2}\right)^2 u=0, \tag{A2a}$$

$$\mu(\lambda+2\mu)\left(\nabla_0^2+\frac{\partial^2}{\partial z^2}\right)^2 w=0. \tag{A2b}$$

Consider Yih's primitive solutions of the hyper Bessel equation[6]

$$(\nabla_n^2+\gamma^2)^m f=0, \tag{A3a}$$

$$f_p(r)=\{r^jJ_{n+j}(\gamma r);r^jY_{n+j}(\gamma r)\},\quad j=1,\quad m-1. \tag{A3b}$$

The $[r^jY_{n+j}(\gamma r)]$ must be excluded since it is singular at $r=0$. Applying (A3) to (A2) produces the following primitives

$$u_p(r,z)=\{J_1(\gamma r);rJ_2(\gamma r)\}\{e^{\pm\gamma z};\gamma ze^{\pm\gamma z}\}, \tag{A4a}$$

$$w_p(r,z)=\{J_0(\gamma r);rJ_1(\gamma r)\}\{e^{\pm\gamma z};\gamma ze^{\pm\gamma z}\}. \tag{A4b}$$

The terms $[rJ_n(\gamma r)]$ must be excluded since they fail to satisfy the original second-order equations (A1a,b).

The general homogeneous solution of (A1) is the sum of products of the remaining "r" and "z" primitives with constant coefficients

$$u(r,z)=\sum_{j=1}^{N}J_1(\gamma_jr)[C_{1j}e^{\gamma_jz}+C_{2j}e^{-\gamma_jz}+C_{3j}\gamma_jze^{\gamma_jz}+C_{4j}\gamma_jze^{-\gamma_jz}], \tag{A5a}$$

$$w(r,z)=\sum_{j=1}^{N}J_0(\gamma_jr)[D_{1j}e^{\gamma_jz}+D_{2j}e^{-\gamma_jz}+D_{3j}\gamma_jze^{\gamma_jz}+D_{4j}\gamma_jze^{-\gamma_jz}]. \tag{A5b}$$

Equations relating D_{nj} to C_{nj} are found by substituting (A5) in (A1) and equating coefficients of each term to zero. This yields

$$D_{1j}=-C_{1j}+\hat{\nu}C_{3j},\quad D_{3j}=-C_{3j},$$
$$D_{2j}=C_{2j}+\hat{\nu}C_{4j},\quad D_{4j}=C_{4j}, \tag{A6}$$

where $\hat{\nu}=(\lambda+3\mu)/(\lambda+\mu)=3-4\nu$. Substituting (A6) in (A5b) gives

$$w(r,z)=\sum_{j=1}^{N}J_0(\gamma_jr)[-C_{1j}e^{\gamma_jz}+C_{2j}e^{-\gamma_jz}+(\hat{\nu}-\gamma_jz)\times C_3e^{\gamma_jz}+(\hat{\nu}+\gamma_jz)C_4e^{\gamma_jz}]. \tag{A7}$$

Expressions for stress are

$$\sigma_{zz}=\lambda\left(\frac{\partial u}{\partial r}+\frac{u}{r}+\frac{\partial w}{\partial z}\right)+2\mu\frac{\partial w}{\partial z}$$
$$=\sum_{j=1}^{N}\{-2\mu\gamma_j(C_{1j}e^{\gamma_jz}+C_{2j}e^{-\gamma_jz})+[(\hat{\nu}-1)\times(\lambda+2\mu)-2\mu\gamma_jz]C_{3j}e^{\gamma_jz}-[(\hat{\nu}-1)(\lambda+2\mu)+2\mu\gamma_jz]C_{4j}\}J_0(\gamma_jr), \tag{A8a}$$

$$\tau_{rz}=\mu\left(\frac{\partial u}{\partial z}+\frac{\partial w}{\partial r}\right)$$
$$=\sum_{j=1}^{N}\mu\gamma_jJ_1(\gamma_jr)[2C_{1j}e^{\gamma_jz}-2C_{2j}e^{-\gamma_jz}-(\hat{\nu}-1-2\gamma_jz)C_{3j}e^{\gamma_jz}-(\hat{\nu}-1+2\gamma_jz)C_{4j}e^{-\gamma_jz}]. \tag{A8b}$$

Consistent with the dynamic problem, the approximation to simple supports requires $BC4$

$$\frac{\partial\tau_{rz}}{\partial r}=\frac{\partial u}{\partial r}=0\quad\text{at}\quad r=a\Rightarrow J_0''(\gamma_ja)=0, \tag{A9}$$

which determines the same set $\{\gamma_j\}$ found in the dynamic problem. Define the state vector of stress and displacement in the lth layer as

$$\mathbf{S}_l(r,z)\equiv[\Psi_l;\Phi_l]\mathbf{C}=\{\sigma_{zz},\tau_{rz};u,w\}_l^{\mathrm{T}}, \tag{A10}$$

Φ and Ψ are matrices of the functions in (A5) and (A8) while $\mathbf{C}$ is the vector $\{C_{nj}\}$. Continuity of $\mathbf{S}_l(r,z)$ at the interface of layer "l" and "$l+1$" requires

$$\mathbf{S}_l(r,h)-\mathbf{S}_{l+1}(r,0)=0;\quad 1\leq l\leq L-1, \tag{A11}$$

where z is a local axial coordinate $0\leq z\leq h$ and h is layer thickness. Traction conditions at the free faces take the form:

$$\Psi_1(r,0)\mathbf{C}_1=\{\sigma_0,0\},$$
$$\Psi_L(r,h)\mathbf{C}_L=\{0,0\}. \tag{A12}$$

The r dependence in (A11) and (A12) is eliminated by inner products N_{0ij} and N_{1ij}, where

$$N_{0ij}=\langle J_0(\gamma_ir)|rJ_0(\gamma_jr)\rangle,$$
$$N_{1ij}=\langle J_1(\gamma_ir)|rJ_1(\gamma_jr)\rangle, \tag{A13}$$

applied to $\{\sigma_{zz},w\}$ and $\{\tau_{rz},u\}$, respectively. This determines a system of simultaneous equations in tridiagonal form:

$$\begin{bmatrix}\mathbf{A}_{10} & & & & \\ \mathbf{A}_{1h} & -\mathbf{A}_{20} & & & \\ \mathbf{B}_{1h} & -\mathbf{B}_{20} & & & \\ & \mathbf{A}_{2h} & -\mathbf{A}_{30} & & \\ & & \cdots & & \\ & & & \mathbf{A}_{(L-1)h} & -\mathbf{A}_{L0} \\ & & & \mathbf{B}_{(L-1)h} & -\mathbf{B}_{L0} \\ & & & & \mathbf{A}_{Lh}\end{bmatrix}\begin{Bmatrix}\mathbf{C}_1\\ \mathbf{C}_2\\ \mathbf{C}_3\\ \cdots\\ \cdots\\ \cdots\\ \mathbf{C}_{L-1}\\ \mathbf{C}_L\end{Bmatrix}$$

$$=\begin{Bmatrix}\mathbf{F}_0\\0\\0\\\cdots\\\cdots\\\cdots\\0\\0\end{Bmatrix}, \tag{A14}$$

where

$$\mathbf{F}_0=\{f_{0j}\},\quad f_{0j}=\begin{cases}\sigma_0\langle r|J_0(\gamma_j r)\rangle, & j=1,2N\\ 0, & j=2N+1,4N\end{cases},$$

and $\mathbf{A}_{lz}$, $\mathbf{B}_{lz}$ are $(2N\times 4N)$ matrices constructed by combining all Ψ_l and Φ_l matrices in (A11) and (A12) after applying the appropriate inner products (A13).

APPENDIX B: SELECTIVE ABBREVIATION

Most generally before abbreviation, the expression for one component of N, say N_{12}, is

$$N_{12}=\int_z\int_r U_1(r,z)U_2(r,z)r\,dr\,dz, \tag{B1a}$$

where

$$U_i(r,z)=\bar{U}_i(r)\{a_ie^{\alpha_iz}+b_ie^{\beta_iz}+c_ie^{-\alpha_iz}+d_ie^{-\beta_iz}\}. \tag{B1b}$$

Substituting (B1b) in (B1a) yields

$$\begin{aligned}N_{12}&=\left[\int_r\bar{U}_1(r)\bar{U}_2(r)r\,dr\right]\left[\int_z(\mathbf{A}_1\cdot\mathbf{e}_{1z})(\mathbf{A}_2\cdot\mathbf{e}_{2z})dz\right]\\&=\mathbf{I}_r\mathbf{I}_z,\\ \mathbf{A}_i&=\{a_i,b_i,c_i,d_i\}^{\mathrm{T}},\quad \mathbf{e}_{iz}=\{e^{\alpha_iz},e^{\beta_iz},e^{-a_iz},e^{-\beta_iz}\}^{\mathrm{T}}.\end{aligned} \tag{B1c}$$

The z integral in (B1c) I_z is composed of 16 terms each with the form

$$\mathbf{I}_z^{(mn)}=\int u_{1m}u_{2n}dz,\quad u_{im}=e^{\eta_{im}z}$$

and

$$\eta_i\in\{\alpha_i,\beta_i,-\alpha_i-\beta_i\}. \tag{B2}$$

Similarly, each component N_{ai} is composed of a sum of terms, each containing a z integral with the form

$$I_z^{(mn)}=\int u_{1m}u_{2n}(1+\zeta z)dz,\quad u_{im}=e^{\eta_{im}z}$$

and

$$\eta_i\in\{\alpha_i,\beta_i,-\alpha_i-\beta_i\} \tag{B3}$$

and of which (B2) is just the special case when $\zeta=0$. Define abbreviation as the application of a functional $A_b(f)$

$$\mathbf{A}_b(e^{-|\eta|z})=\begin{cases}e^{-|\eta|z}, & \text{if } z<\epsilon\\ e^{-M}, & \text{if } z\geq\epsilon\end{cases} \tag{B4a}$$

$$\mathbf{A}_b(e^{|\eta|z})=\begin{cases}1, & \text{if } z<h-\epsilon\\ e^{M-|\eta|(h-z)}, & \text{if } z\geq h-\epsilon,\end{cases} \tag{B4b}$$

where ϵ is a boundary layer thickness such that $|\eta|\epsilon=M$. Abbreviating $I_z^{(mn)}$ in (B3) falls under one of the following cases.

Case 1: $\eta_1,\eta_2>0$ and $\eta_1<\eta_2$; u_{1m} and u_{2n} abbreviated. Let $z_{0i}=h-M/\eta_i=h-\epsilon_i$ and $\eta_p=\eta_1+\eta_2$

$$\begin{aligned}I_z^{(m,n)}&=\int_0^{z_{01}}u_{1m}u_{2n}\,dz+\int_{z_{01}}^{z_{02}}u_{1m}u_{2n}\,dz\\&\quad+\int_{z_{02}}^{h}u_{1m}u_{2n}\,dz\\&=I_{1z}^{(mn)}+I_{2z}^{(mn)}+I_{3z}^{(mn)},\\ I_{1z}^{(mn)}&=z_{01}+\zeta z_{01}^2/2,\\ I_{2z}^{(mn)}&=\eta_1^{-1}[(1+\zeta(z_{02}-\eta_1^{-1}))e^{\eta_1(z_{02}-z_{01})}\\&\quad-(1+\zeta(z_{01}-\eta_1^{-1}))],\\ I_{3z}^{(mn)}&=e^{2M}\eta_p^{-1}[1+\zeta(h-\eta_p^{-1})\\&\quad-(1+\zeta(z_{02}-\eta_p^{-1})e^{-(\eta_1+\eta_2)z_{02}})].\end{aligned} \tag{B5}$$

Case 2: $\eta_1<0$, $\eta_2>0$, $\epsilon_1<z_{02}$; u_{1m},u_{2n} abbreviated.

$$\begin{aligned}I_z^{(mn)}&=\int_0^{\epsilon_1}+\int_{\epsilon_1}^{z_{02}}+\int_{z_{02}}^{h},\\ I_{1z}^{(mn)}&=\eta_1^{-1}[(1+\zeta(\epsilon_1-\eta_1^{-1}))e^{-M}-1+\zeta/\eta_1],\\ I_{2z}^{(mn)}&=e^{-M}[z_{02}+\zeta z_{02}^2/2-\epsilon_1-\zeta\epsilon_1^2/2],\\ I_{3z}^{(mn)}&=\eta_2^{-1}[1+\zeta(h-\eta_2^{-1})-(1+\zeta(z_{02}-\eta_2^{-1}))e^{-M}].\end{aligned} \tag{B6}$$

Case 3: $\eta_1<0$, $\eta_2>0$; $z_{02}<\epsilon_1$.

$$\begin{aligned}I_z^{(mn)}&=\int_0^{z_{02}}+\int_{z_{02}}^{\epsilon_1}+\int_{\epsilon_1}^{h},\\ I_{1z}^{(mn)}&=\eta_1^{-1}[(1+\zeta(z_{02}-\eta_1^{-1}))e^{\eta_1z_{02}}-1+\zeta/\eta_1],\\ I_{2z}^{(mn)}&=e^{-M}\eta_p^{-1}[(1+\zeta(\epsilon_1-\eta_p^{-1}))e^{\eta_2(\epsilon_1-z_{02})}\\&\quad-(1+\zeta(z_{02}-\eta_p^{-1}))e^{-\eta_1(\epsilon_1-z_{02})}],\\ I_{3z}^{(mn)}&=\eta_2^{-1}[1+\zeta(h-\eta_2^{-1})\\&\quad-(1+\zeta(\epsilon_1-\eta_2^{-1}))e^{-\eta_2z_{01}}].\end{aligned} \tag{B7}$$

Case 4: $\eta_1,\eta_2<0$ and $|\eta_1|<|\eta_2|$.

$$I_z^{(mn)}=\int_0^{\epsilon_2}+\int_{\epsilon_2}^{\epsilon_1}+\int_{\epsilon_1}^{h},$$

$$I_{1z}^{(mn)}=\eta_p^{-1}[(1+\zeta(\epsilon_2-\eta_p^{-1})e^{-M+\eta_1\epsilon_2}-1+\zeta/\eta_p)],$$

$$I_{2z}^{(mn)}=e^{-2M}\eta_1^{-1}[1+\zeta(\epsilon_1-\eta_1^{-1}) \qquad \text{(B8)}$$

$$-(1+\zeta(\epsilon_2-\eta_1^{-1}))e^{-\eta_1(\epsilon_1-\epsilon_2)}],$$

$$I_{3z}^{(mn)}=e^{-2M}[h+\zeta h^2/2-\epsilon_2-\zeta\epsilon_2^2/2].$$

Case 5: $\eta_1<0$ and u_{1m} unabbreviated.

$$I_z^{(mn)}=\int_0^{\epsilon_2}+\int_{\epsilon_2}^{h}=I_{1z}^{(mn)}+I_{2z}^{(mn)},$$

$$I_{1z}^{(mn)}=\eta_p^{-1}[(1+\zeta(\epsilon_2-\eta_p^{-1})e^{-M+\eta_1\epsilon_2}-1+\zeta/\eta_p)], \qquad \text{(B9)}$$

$$I_{2z}^{(mn)}=e^{-M}\eta_1^{-1}[(1+\zeta(h-\eta_1^{-1}))e^{\eta_1 h}$$

$$-(1+\zeta(\epsilon_2-\eta_1^{-1}))e^{\eta_1\epsilon_2}].$$

Case 6: $\eta_2>0$ and u_{1m} unabbreviated.

$$I_z^{(mn)}=\int_0^{z_{02}}+\int_{z_{02}}^{h}=I_{1z}^{(mn)}+I_{2z}^{(mn)},$$

$$I_{1z}^{(mn)}=\eta_1^{-1}[(1+\zeta(z_{02}-\eta_1^{-1}))e^{\eta_1 z_{02}}-1+\zeta/\eta_1], \quad \text{(B10)}$$

$$I_{2z}^{(mn)}=\eta_p^{-1}[(1+\zeta(h-\eta_p^{-1}))e^{M+\eta_1 h}$$

$$-(1+\zeta(z_{02}-\eta_p^{-1}))e^{\eta_1 z_{02}}].$$

[1] M. El-Raheb, "Transient elastic waves in finite layered media: One-dimensional analysis," J. Acoust. Soc. Am. 94, 172–184 (1993).

[2] M. El-Raheb, "Simplified models of transient uniaxial waves in a layered periodic stack," submitted to Int. J. Solids Struct.

[3] M. El-Raheb, "Flexural waves in a disk soon after impact," J. Acoust. Soc. Am. 94, 172–184 (1994).

[4] J. Miklowitz, *The Theory of Elastic Waves and Wave Guides* (North Holland, Amsterdam, The Netherlands, 1984), 1st ed., pp. 214–221.

[5] M. Abramowitz and I. Stegun, *Handbook of Mathematical Functions*, 10th ed. (National Bureau of Standards, Washington, DC, 1972), Appl. Math Series 55, pp. 409, 411.

[6] Y. C. Fung, *Foundations of Solid Mechanics* (Prentice-Hall, Englewood Cliffs, NJ, 1965), 1st ed., p. 209.

[7] M. El-Raheb and P. Wagner, "Damped response of shells by a constrained visco-elastic layer," Trans. ASME J. Appl. Mech. 53, 902–905 (1986).

[8] R. Szilard, *Theory and Analysis of Plates* (Prentice-Hall, Englewood Cliffs, NJ, 1974), 1st ed., p. 617, case 3.

Reference [2]
Simplified Models of Transient Elastic Waves in Finite Axisymmetric Layered Media

Simplified models of transient elastic waves in finite axisymmetric layered media

Michael El-Raheb
The Dow Chemical Company, Midland, Michigan 48674

(Received 12 December 1997; accepted for publication 14 August 1998)

A simplified model, termed the flexure model, is used to analyze elastic waves in a weakly coupled periodic stack of disks bonded by thin layers of a weak polymer. Comparison with results of a more complete two-dimensional (2-D) axisymmetric model reveals the importance of axial stress and nonlinear distribution of radial displacement across the thickness. Also, in the 2-D model, it is possible to eliminate extensional modes through the thickness and inertia of the bond without compromising accuracy. In the 2-D model and for low radial wave numbers for a defined mode, its phase and group velocities can be approximated by the 1-D mass–spring model. They undergo discontinuities at the boundaries of extensional propagation zones. The flexure model reproduces the 2-D characteristic speeds but with slightly wider propagation zones and faster wavefronts. © *1998 Acoustical Society of America.* [S0001-4966(98)04811-5]

PACS numbers: 43.40.Dx, 43.20.Jr [CBB]

INTRODUCTION

Wave propagation in layered media finds a wide variety of applications. Examples include geological oil exploration, shock isolation and crash management in automotive components, delamination in composites, and ballistic protection by passive stacked armor. Elastic waves in layered media have been studied extensively. Propagation of harmonic waves in one-dimensional (1-D) layered media by monochromatic sources can be found in Refs. 1–5. Extension of the theory to 3-D periodic media is treated in Refs. 6–10. Analysis of simple periodic structures adopting Floquet theory to propagation and attenuation zones is treated in Refs. 11–21. The methods used to analyze this problem ranged from purely numerical, like discretization and geometric optics, to purely analytical, like modal and transform techniques. In contrast with the extensive work reported on harmonic waves, relatively less attention was devoted to transient waves despite their importance in many practical applications. Reference 22 treats transient uniaxial waves in finite ordered and disordered bi-periodic stacks. The method relies on deriving transfer matrices in harmonic space relating state vectors at the interface between layers. Equilibrium of stress and continuity of displacement at each interface produces a system of tri-diagonal block matrices yielding modal characteristics of the stack. Transient response is found from an expansion of these modes. Simplified analytical models of the exact analysis in Ref. 22 are constructed in Ref. 23 yielding insights into the mechanics of uniaxial waves by reducing the parameters to those essential in controlling propagation.

Reference 24 extends the analysis in Ref. 22 to 2-D axisymmetric waves in a finite periodic stack of disks bonded by weak layers. In this work, radial dependence satisfies approximately the condition of "simple supports", i.e., axial displacement and radial derivative of radial displacement vanish at the lateral boundary. This approximation yields a dispersion relation in radial wave number enabling the separation of axial and radial dependencies. Transfer matrices relating displacement and surface traction at the two faces of a disk in the stack are then determined. The solution then proceeds along steps similar to the 1-D analysis. From Ref. 24, important results of analyzing 2-D propagation in a stack of N periodic sets are:

(1) Fixing the radial wave number m_r, there exists an infinite number of system resonant frequencies of the stack $\Omega_j(m_r)$, $j=1,2,3,\ldots$, which appear as an ascending series of points in an Ω vs m_r plot. A line drawn through the lowest Ω_j $(j=1)$ for each m_r forms the first "frequency line." Similarly, a line drawn through the next higher Ω_j $(j=2)$ forms the second frequency line, etc. In a plot of resonant frequency Ω versus radial wave number m_r satisfying the dispersion relation, Ω follows lines belonging to one of four groups:

(a) a flexural group of N lines with dominant flexural motion of the disk;

(b) an extensional group of N lines with dominant radial and axial motions of the disk;

(c) a shear group of $N-1$ lines with dominant shear motion of the bond;

(d) a second shear group of N lines with dominant shear motion of the disk.

Lines of one group may change type to another near coalescence although frequency lines never cross. Groups (c) and (d) above may be neglected without changing the response appreciably.

(2) For the excited disk, radial and circumferential stress $(\sigma_{rr},\sigma_{\theta\theta})$ is the sum of an equivoluminal part from flexure, antisymmetric about the disk's neutral plane, and a volumetric part from axial stress over the footprint of the excitation. The volumetric part is large close to the footprint and diminishes steeply elsewhere.

(3) For other disks in the stack, $(\sigma_{rr},\sigma_{\theta\theta})$ mostly depend on flexure with an anti-symmetric distribution about the disk's neutral plane. Unlike the linear distribution characteristic to plate flexure theory, termed the Kirchhoff assump-

tion, the 2-D distribution is not linear and deviation from linearity rises with disk thickness.

The purpose of this study is to understand the roles of axial stress, the Kirchhoff assumption in the Mindlin plate equations,[25] inertia of the bond producing motions in 1(c) above, and extensional motions of the disk producing motions in 1(b) above. Neglecting these motions yields a simpler and more efficient algorithm with prescribed error bounds, useful in preliminary parametric analysis of wave propagation in periodic stacks. Characteristic of wave propagation in periodic media is the existence of propagation and attenuation zones, PZ's and AZ's. Within each zone, propagation constants, and phase and group velocities control transmission and speeds of wavefront and energy. These will be called propagation quantities. They reveal in a more direct way the effects of various assumptions and approximations than can be seen from frequency spectra and histories of transient response.

A number of simplified models will be constructed, some based on the flexure model which allows only flexure of the disks, and others based on a more complete 2-D axisymmetric analysis. Comparing results from these models reveals the importance of their underlying approximations and the effects which they ignore.

Section I develops the analysis of a periodic stack adopting Mindlin's plate flexure theory. It treats the bond as an elastic spring resisting relative axial and shear motions from flexure of the adhering disks. Section II revises the analysis of the periodic stack adopting the 2-D Navier equations of elasto-dynamics. It differs from Ref. 24 in that displacements rather than potentials are chosen for dependent variables. In contrast to the flexure model which uses a body force, the 2-D model for the external excitation uses the static-dynamic superposition method which reduces substantially the number of eigenfunctions needed for convergence of transient response by modal analysis (see Ref. 26). Section III compares transient histories computed by the various models and explains how differences in response amplitude relate to the approximations in flexure analysis. Section IV compares propagation quantities (μ, c_p, c_g) by the various models and explains how they change with radial wave number where μ is propagation constant and c_p, c_g are phase and group velocities.

I. ANALYSIS BY PLATE FLEXURE THEORY

Assume that the stack is made of disks of radius a, bonded by thin elastic layers modeled as linear springs resisting relative axial motion along z and radial motion along r of the adhering disks. In cylindrical coordinates and axisymmetric motions, Mindlin's plate equations for axial displacement w and cross sectional rotation ψ are

$$\frac{D}{2}\left[(1-\nu)\nabla_1^2\psi+(1+\nu)\frac{\partial\varphi}{\partial r}\right]-\kappa Gh\left(\psi+\frac{\partial w}{\partial r}\right)=\rho\frac{h^3}{12}\frac{\partial^2\psi}{\partial t^2}+\bar{M}_r, \tag{1a}$$

$$kGh(\nabla_0^2 w+\varphi)+q_z=\rho h\frac{\partial^2 w}{\partial t^2}, \tag{1b}$$

$$\varphi=\nabla\cdot\psi=\frac{\partial\psi}{\partial r}+\frac{\psi}{r},$$

$$\nabla_n^2=\frac{\partial^2}{\partial r^2}+\frac{1}{r}\frac{\partial}{\partial r}, \tag{1c}$$

where r is radial coordinate, $D=Eh^3/12(1-\nu^2)$, κ is shear constant, ν is Poisson's ratio, (E,G) are moduli of elasticity and shear, h is thickness, ρ is density, t is time; q_z is transverse loading from external pressure or bond extension, and $\bar{M}_r$ is moment from bond shear. Operating (1a) by $(\partial/\partial r+1/r)$ converts ψ to φ, then eliminating φ from (1b) reduces (1a,b) to a single fourth order equation in w:

$$\left\{\left[\nabla_0^2-\frac{1}{c_0^2}\frac{\partial^2}{\partial t^2}\right]\left[\nabla_0^2-\frac{1}{c_s^2}\frac{\partial^2}{\partial t^2}\right]+\frac{12}{c_s^2h^2}\frac{\partial^2}{\partial t^2}\right\}w$$
$$=\frac{1}{D}\left[1-\frac{Eh^2}{12kG(1-\nu^2)}\nabla_0^2+\frac{h^2}{12c_s^2}\frac{\partial^2}{\partial t^2}\right]q_z+\frac{1}{D}\left(\frac{\partial\bar{M}_r}{\partial r}+\frac{\bar{M}_r}{r}\right),$$

$$c_0^2=\frac{E}{\rho(1-\nu^2)},\quad c_s^2=\frac{\kappa G}{\rho}. \tag{2}$$

Let "i" denote the order of a disk in the stack. For disks bonded by thin elastic layers, q_z applied to disk "i" is proportional to the bond axial stiffness and relative axial displacement of disks "i", "$i+1$," and "$i-1$":

$$q_z=\frac{E_{b\epsilon}}{h_b}(2w_i-w_{i-1}-w_{i+1}),$$
$$E_{b\epsilon}=E_b\frac{(1-\nu_b)}{(1+\nu_b)(1-2\nu_b)}. \tag{3}$$

$E_{b\epsilon}$ is the modulus of the bond in uniaxial strain, (E_b,ν_b) are bond modulus in uniaxial stress and Poisson ratio, and h_b is bond thickness. From Appendix A, $\bar{M}_r$ is proportional to bond shear stiffness and relative radial motion of disks "i", "$i+1$," and "$i-1$":

$$\bar{M}_r=\frac{G_bh^2}{h_b}(2\psi_i+\psi_{i-1}+\psi_{i+1}), \tag{4}$$

where G_b is bond shear modulus. Invoking (4) in (2) yields

$$\frac{\partial\bar{M}_r}{\partial r}+\frac{\bar{M}_r}{r}=\frac{G_bh^2}{h_b}(2\varphi_i+\varphi_{i+1}+\varphi_{i-1}); \tag{5a}$$

eliminating φ_i in (5a) using (1b) yields

$$\frac{\partial\bar{M}_r}{\partial r}+\frac{\bar{M}_r}{r}=-\frac{G_bh^2}{h_b}\left(\nabla_0^2-\frac{1}{c_s^2}\frac{\partial^2}{\partial t^2}\right)\times(2w_i+w_{i-1}+w_{i+1}). \tag{5b}$$

Substituting (3) and (5b) in (2) produces the coupled flexural equation of the ith disk

$$\left\{\left[\nabla_0^2-\frac{1}{c_0^2}\frac{\partial^2}{\partial t^2}\right]\left[\nabla_0^2-\frac{1}{c_s^2}\frac{\partial^2}{\partial t^2}\right]+\frac{12}{c_s^2h^2}\frac{\partial^2}{\partial t^2}\right\}w_i$$
$$=\frac{12E_{b\epsilon}(1-\nu^2)}{Eh_bh^3}\left[1-\frac{Eh^2}{12kG(1-\nu^2)}\nabla_0^2+\frac{h^2}{12c_s^2}\frac{\partial^2}{\partial t^2}\right]$$
$$\times(\hat{\delta}_iw_i-w_{i-1}-w_{i+1})-\frac{3G_b(1-\nu^2)}{Eh_bh}\left[\nabla_0^2-\frac{1}{c_s^2}\frac{\partial^2}{\partial t^2}\right]$$
$$\times(\hat{\delta}_iw_i+w_{i-1}+w_{i+1}),\tag{6}$$
$$\hat{\delta}_i=3-\text{integer}\left(\frac{i+1}{i}+\frac{i}{N}\right).$$

The left-hand side of (6) accounts for flexural stiffness and inertia of the disk. On the right hand side, the first part accounts for axial coupling along z of neighboring disks by the bond, and the second part accounts for shear coupling along r by the bond.

It was shown in Ref. 24 that simple supports at the lateral boundary of the disk can be approximated by $\partial u(a)/\partial r\equiv 0$, which in plate theory reduces to $\partial\psi(a)/\partial r\equiv 0$. This boundary condition allows separation of variables and yields the dispersion relation

$$J_0''(\gamma_r)=0,\quad \gamma_r=k_ra,\tag{7}$$

where k_r is the radial wave number. Assuming harmonic motions in time with frequency ω, a solution to (6) satisfying (7) has the form:

$$w_i(r,t)=w_{0i}J_0(k_rr)e^{i\omega t},$$
$$\psi_i(r,t)=\left(-\gamma_r^2+\frac{\omega^2a^2}{c_s^2}\right)\frac{w_{0i}}{\gamma_ra}J_1(k_rr)e^{i\omega t}.\tag{8}$$

Substituting (8) in (1) for all disks in the stack determines a banded system of simultaneous equations with width 3:

$$\mathbf{A}\mathbf{w}_0=\mathbf{0},$$
$$A_{ii}=(-\gamma_r^2+\gamma_0^2)(-\gamma_r^2+\gamma_s^2)-\gamma_0^2\frac{a^2}{h_1^2}+\hat{\delta}_iB_a+\hat{\delta}_iB_s,$$
$$A_{i,i+1}=A_{i,i-1}=-B_a+B_s,$$
$$B_a=\frac{12E_{b\epsilon}(1-\nu^2)a^4}{Eh_bh_3}\left[1+\gamma_r^2\frac{h_2^2}{a^2}-\gamma_s^2\frac{h_1^2}{a^2}\right],\tag{9}$$
$$B_s=\frac{3G_b(1-\nu^2)a^2}{Eh_bh}(-\gamma_r^2+\gamma_s^2),$$
$$h_1^2=\frac{h^2}{12},\quad h_2^2=\frac{h^2}{6(1-\nu)\kappa},\quad \gamma_0=\frac{\omega a}{c_0},$$
$$\gamma_s=\frac{\omega a}{c_s}.$$

Solution of the implicit eigenproblem (9) yields eigenfrequencies ω_{fm} and eigenfunctions Φ_{fm} of the stack for flexural and shear motions. Since dispersion relation (7) does not satisfy natural boundary conditions, the set $\{\Phi_{fm}\}$ is not orthogonal.

TABLE I. Properties of basic stack.

	E (lb/in.^{2})	ρ (lb s^2/in.^{4})	ν	h (in.)
Disk	4.64×10^7	3.04×10^{-4}	0.24	0.5
Bond	2×10^4	10^{-4}	0.48	0.01

Consider a stack of five disks with radius $a=3$ in. bonded by four weak layers with the properties given in Table I. This will be termed the "basic stack." Let N be the number of disks in the periodic stack. Fixing the number of radial half-waves, $m_r=\gamma_r/\pi$, there exists a group of N low resonant frequency lines corresponding to flexural modes and a group of N high resonant frequency lines corresponding to disk shear modes. In the flexural group, the first mode is anti-symmetric about the stack's plane of bilateral symmetry, i.e., all deformed disks are identical in shape and magnitude [see Fig. 1(a) and (f)]. Its frequency is slightly higher than that of the lone disk because of shear stiffness from the bond. The second mode is symmetric about the plane of bilateral symmetry, i.e., deformed disks on one side of this plane are mirror images to those on the other side [see Fig. 1(b) and (j)]. More complex coupled modes follow with shapes alternating between symmetric and anti-symmetric [see Fig. 1(c), (d), (e), and 1(h), (i), (j)]. For each m_r, the set of N flexural modes resembles the set of $(N-1)$ modes in the first propagation zone PZ1 of a 1-D free stack.[22] In 2-D, N distinct coupled motions are possible. In 1-D, only $(N-1)$ possible motions have nonzero frequency, the Nth being a rigid body translation of the 1-D stack.

At this point it is possible to create another approximate model by neglecting bond inertia in the flexure model above. Comparing the resulting frequency spectra will reveal its effect. Figure 2(a) plots eigenfrequency Ω(Hz) of the flexural group versus m_r for the stack with massless bond and properties in Table I. The gap between Ω lines narrows smoothly with m_r. Figure 2(b) plots Ω of the disk's flexural and shear groups versus m_r including bond inertia. Close to the shear frequency of the bond, the lowest $(N-1)$ lines of the disk shear group change type and follow the bond shear line until coalescence with the flexural group. These lines change type again near coalescence with the flexural group, while $(N-1)$ lines of the flexural group change type to become the bond shear group. This coalescence without crossing of frequency lines manifests uniqueness of the solution imposed by linearity of the problem. The gap between frequency lines of the flexural group widens after coalescence with the shear group because of the drop in bond mobility caused by a change in phase after crossing the bond shear resonance.

Transient response to external excitation is found by modal decomposition of the axial displacement vector $\mathbf{w}$

$$\mathbf{w}(r,z,t)=\sum_{m=1}^{M}a_m(t)\Phi_{fm}(r,z).\tag{10}$$

Substituting (10) in (6), multiplying each side by $\Phi_{fm}(r,z)$, and integrating over the stack's volume yields

$$\mathbf{M}(\ddot{\mathbf{a}}+\omega^2\mathbf{a})=\mathbf{F}f_0(t),\tag{11a}$$

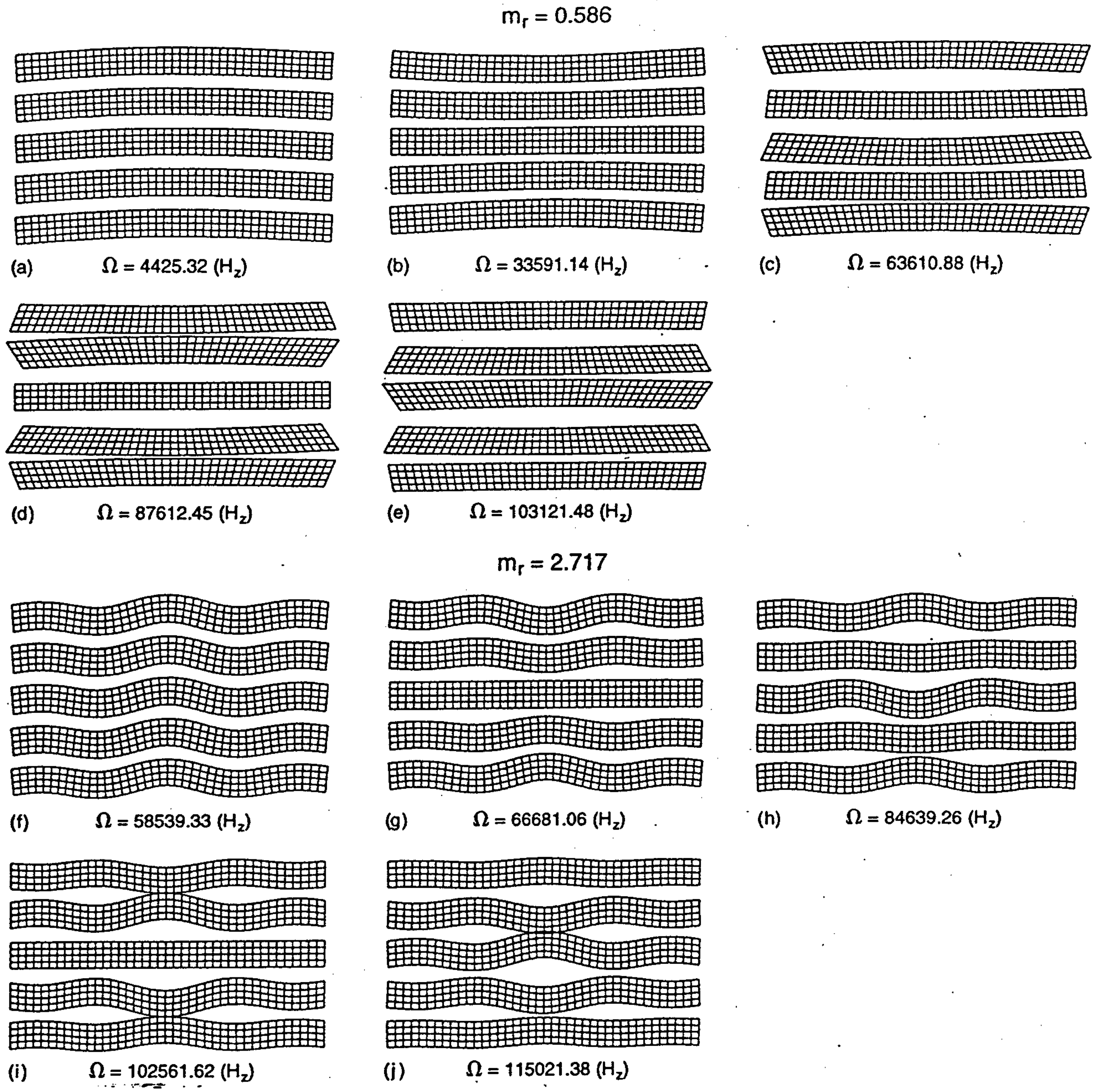

FIG. 1. Eigenmodes of the stack of five periodic sets (flexure model): (a)–(e) $m_r = 0.586$; (f)–(j) $m_r = 2.717$.

where ($\dot{}$) is time derivative, $\mathbf{M}$ is the full matrix of generalized mass, and $\mathbf{F}$ is the vector of generalized force:

$$M_{mn} = \langle m|\rho|n\rangle, \quad F_n = \langle n|p_0\rangle, \tag{11b}$$

where $p(r,t) = p_0(r)\, f_0(t)$ is the external pressure excitation acting on the stack. Inverting $\mathbf{M}$ in (11a) yields uncoupled equations in the generalized coordinates $\mathbf{a}(t)$:

$$\ddot{a}_m(t) + \omega_m^2 a(t) = P_m f_0(t), \quad \mathbf{P} = \mathbf{M}^{-1}\mathbf{F}. \tag{12}$$

A solution to (12) follows in terms of Duhamel's integral:

$$a_m(t) = -\frac{P_m}{\omega_m} \int_0^t f_0(\tau) \sin \omega_m(t-\tau)\, d\tau. \tag{13}$$

II. ANALYSIS BY 2-D AXISYMMETRIC THEORY

For axisymmetric motions of a disk, the Navier equations of elasto-dynamics in cylindrical coordinates are:

$$(\lambda + 2\mu)\nabla_1^2 u + \mu \frac{\partial^2 u}{\partial z^2} + (\lambda + \mu) \frac{\partial^2 w}{\partial r \partial z} = \rho \frac{\partial^2 u}{\partial t^2}, \tag{14}$$

$$(\lambda + \mu) \frac{\partial}{\partial z}\left(\frac{\partial u}{\partial r} + \frac{u}{r}\right) + \mu \nabla_0^2 w + (\lambda + 2\mu) \frac{\partial^2 w}{\partial z^2} = \rho \frac{\partial^2 w}{\partial t^2},$$

$$\nabla_n^2 \equiv \frac{\partial^2}{\partial r^2} + \frac{1}{r}\frac{\partial}{\partial r} - \frac{n^2}{r^2}, \tag{15}$$

where (u,w) are radial and axial displacements, and (λ,μ) are Lame's constants. Assuming harmonic motions in time with frequency ω, separation of variables yields:

$$u(r,z,t) = J_1(k_r r)\bar{u}(z) e^{i\omega t}, \quad w(r,z,t) = J_0(k_r r)\bar{w}(z) e^{i\omega t}. \tag{16}$$

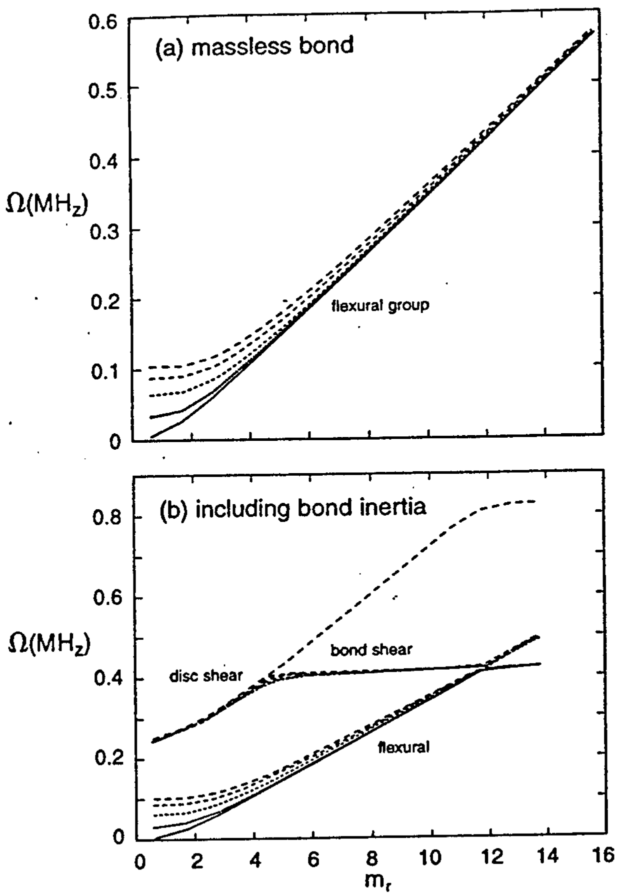

FIG. 2. Spectra of stack resonant frequency Ω vs m_r (flexure model): (a) massless bond; (b) including bond inertia.

The radial function approximates simple supports at $r=a$ [see Eq. (7)]:

$$\frac{\partial u(a,z,t)}{\partial r}=0 \tag{17a}$$

which defines the radial wave number k_r as

$$J_0''(k_r a)=0. \tag{17b}$$

Substituting (16) in (14) and (15) yields

$$\begin{aligned}&\frac{\mu}{\lambda+2\mu}\frac{\partial^2\bar{u}}{\partial z^2}+\left(\frac{\rho\omega^2}{\lambda+2\mu}-k_r^2\right)\bar{u}-\frac{\lambda+\mu}{\lambda+2\mu}k_r\frac{\partial\bar{w}}{\partial z}=0,\\&\frac{\lambda+\mu}{\mu}k_r\frac{\partial\bar{u}}{\partial z}+\frac{\lambda+2\mu}{\mu}\frac{\partial^2\bar{w}}{\partial z^2}+\left(\frac{\rho\omega^2}{\mu}-k_r^2\right)\bar{w}=0.\end{aligned} \tag{18}$$

Equations (18) admit solutions in the form:

$$\bar{u}(z)=Ce^{\alpha z},\quad \bar{w}(z)=De^{\alpha z}, \tag{19}$$

where C,D are constant coefficients. Substituting (19) in (18) produces the axial dispersion relation in α:

$$\begin{bmatrix}a_{11} & a_{12}\\ a_{21} & a_{22}\end{bmatrix}\begin{Bmatrix}C\\ D\end{Bmatrix}=0, \tag{20}$$

$$C=-\left(\frac{a_{12}}{a_{11}}\right)D, \tag{20a}$$

$$a_{11}=\frac{\mu}{\lambda+2\mu}\alpha^2+\left(\frac{\rho\omega^2}{\lambda+2\mu}-k_r^2\right), \tag{20b}$$

$$a_{12}=-\frac{\lambda+\mu}{\lambda+2\mu}k_r\alpha;\quad a_{21}=\frac{\lambda+\mu}{\mu}k_r\alpha,$$

$$a_{22}=\frac{\lambda+2\mu}{\mu}\alpha^2+\left(\frac{\rho\omega^2}{\mu}-k_r^2\right).$$

Equation (20) is quadratic in α^2 yielding four complex values α_j, $j=1,4$. From (19),

$$\begin{aligned}&\bar{u}(z)=\sum_{j=1}^{4}C_je^{\alpha_j z}=-\sum_{j=1}^{4}\left(\frac{a_{12}}{a_{11}}\right)_j D_je^{\alpha_j z},\\&\bar{w}(z)=\sum_{j=1}^{4}D_je^{\alpha_j z}.\end{aligned} \tag{21}$$

The constitutive equations are

$$\bar{\sigma}_{zz}=\lambda k_r\bar{u}+(\lambda+2\mu)\frac{\partial\bar{w}}{\partial z},\quad \bar{\tau}_{rz}=\mu\left(\frac{\partial\bar{u}}{\partial z}-k_r\bar{w}\right). \tag{22}$$

Define the state vector $\mathbf{S}$ as

$$\mathbf{S}=\{\mathbf{f},\mathbf{g}\}^T, \tag{23a}$$

where $\mathbf{f}=\{\bar{\sigma}_{zz},\bar{\tau}_{rz}\}^T$ and $\mathbf{g}=\{\bar{u},\bar{w}\}^T$ are traction and displacement vectors over a face of the disk. Substituting (21) in (22) relates the state vector $\mathbf{S}=\{\bar{\sigma}_{zz},\bar{\tau}_{rz},\bar{u},\bar{w}\}^T$ to coefficients $\mathbf{D}=\{D_j\}^T$:

$$\mathbf{S}(z)=\mathbf{B}(z)\mathbf{D}, \tag{23b}$$

$$\begin{aligned}&B_{1j}(z)=\{\lambda k_rC_j+(\lambda+2\mu)\alpha_jD_j\}e^{\alpha_j z},\\&B_{2j}(z)=(\mu\alpha_jC_j-k_r)e^{\alpha_j z},\\&B_{3j}(z)=C_je^{\alpha_j z},\\&B_{4j}(z)=D_je^{\alpha_j z},\end{aligned} \tag{23c}$$

where in (23c) C_j is related to D_j by (20a). Evaluating (23b) at $z=0$ and $z=h$, then eliminating $\mathbf{D}$, produces the transfer matrix $\mathbf{T}$ relating state vectors on the two faces of a disk:

$$\mathbf{S}(h)=\mathbf{T}\mathbf{S}(0),\quad \mathbf{T}=\mathbf{B}(h)\mathbf{B}^{-1}(0). \tag{24}$$

$\mathbf{T}$ is expressed in terms of four submatrices t_{k1} as

$$\mathbf{T}=\begin{bmatrix}\mathbf{t}_{11} & \mathbf{t}_{12}\\ \mathbf{t}_{21} & \mathbf{t}_{22}\end{bmatrix}. \tag{25}$$

For a bi-periodic stack of N repeated sets, where each set except the last is made of two layers (one disk and one bond) continuity of $\mathbf{S}$ at the interfaces of layers produces the global tri-diagonal block matrix $\mathbf{M}_G$:

$$\mathbf{M}_G\mathbf{S}_G=\mathbf{0}, \tag{26a}$$

where $\mathbf{S}_G$ is the ensemble of the $\mathbf{S}_k$ at all interfaces and the two boundaries of the stack:

$$\mathbf{S}_G=\{\mathbf{S}_1,\mathbf{S}_2,\ldots,\mathbf{S}_{2N-1}\}^T, \tag{26b}$$

$$\mathbf{M}_G=\left[\begin{array}{cccccccccccc}
\mathbf{I} & \mathbf{0} & \mathbf{0} & \mathbf{0} & & & & & & & & \\
\mathbf{t}_{11}^{(1)} & \mathbf{t}_{12}^{(1)} & \mathbf{I} & \mathbf{0} & & & & & & & & \\
\mathbf{t}_{21}^{(1)} & \mathbf{t}_{22}^{(1)} & \mathbf{0} & \mathbf{I} & \mathbf{0} & \mathbf{0} & & & & & & \\
\mathbf{0} & \mathbf{0} & \mathbf{t}_{11}^{(2)} & \mathbf{t}_{12}^{(2)} & \mathbf{I} & \mathbf{0} & & & & & & \\
 & & \mathbf{t}_{21}^{(2)} & \mathbf{t}_{22}^{(2)} & \mathbf{0} & \mathbf{I} & \mathbf{0} & \mathbf{0} & & & & \\
 & & \mathbf{0} & \mathbf{0} & \mathbf{t}_{11}^{(1)} & \mathbf{t}_{12}^{(1)} & \mathbf{I} & \mathbf{0} & & & & \\
 & & & & \mathbf{t}_{21}^{(1)} & \mathbf{t}_{22}^{(1)} & \mathbf{0} & \mathbf{I} & & & & \\
 & & & & & & \cdot & \cdot & \cdot & \cdot & & \\
 & & & & & & \cdot & \cdot & \cdot & \cdot & & \\
 & & & & & & \mathbf{0} & \mathbf{0} & \mathbf{t}_{11}^{(1)} & \mathbf{t}_{12}^{(1)} & \mathbf{I} & \mathbf{0} \\
 & & & & & & & & \mathbf{t}_{21}^{(1)} & \mathbf{t}_{22}^{(1)} & \mathbf{0} & \mathbf{I} \\
 & & & & & & & & \mathbf{0} & \mathbf{0} & \mathbf{I} & \mathbf{0}
\end{array}\right], \tag{26c}$$

where $\mathbf{I}$ is the unit matrix and the superscript (l) in $t_{ij}^{(l)}$ denotes layer number in the bi-periodic set. The first and last rows in (26b) correspond to the free traction conditions at the two faces of the stack. Eigenvalues ω_m and eigenfunctions Φ_{Gm} of the stack are determined by the condition:

$$\det|\mathbf{M}_G|=0. \tag{27}$$

Just as in the case of the flexure model, it is possible to create an approximate 2-D model by neglecting inertia of the bond. In this way, its effect can be evaluated. For the stack with properties in Table I, Fig. 3 plots Ω vs m_r for the first two frequency groups when the bond is massless. The first group includes five lines of flexure dominant motions of the disks and resembles the group in Fig. 2(a), while the second group includes five lines of radial and axial extensional dominant motions of the disks. When $m_r<2$, the two groups are not segregated, i.e., radial modes occur among flexural modes. Including bond inertia introduces additional groups with dominant shear motions of the bond.

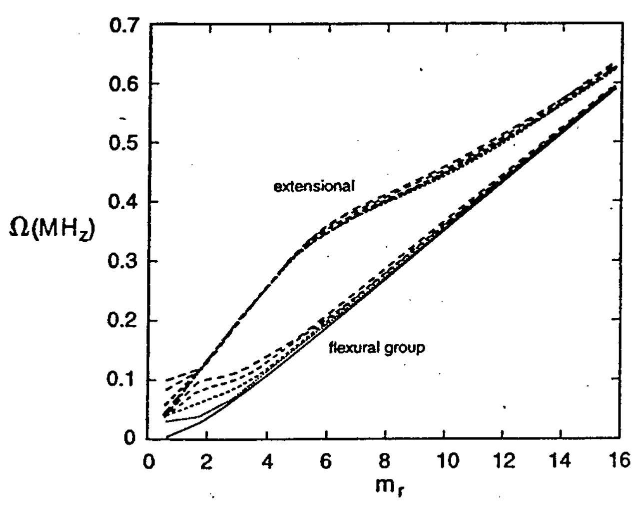

FIG. 3. Spectra of stack resonant frequency Ω vs m_r with massless bond (2-D model).

Transient response proceeds by the static-dynamic superposition method. Displacement $\mathbf{u}$ is expressed as the sum

$$\mathbf{u}=\mathbf{u}_d+f_0(t)\mathbf{u}_s, \tag{28}$$

where $\mathbf{u}_d$ and $\mathbf{u}_s$ are homogeneous dynamic and inhomogeneous static solutions and $f_0(t)$ is time dependence of the excitation. Expand $\mathbf{u}_d$ is eigenfunctions

$$\mathbf{u}_d=\sum_j a_j(t)\Phi_j(\mathbf{x})\equiv\sum_j a_j(t)|j\rangle, \tag{29}$$

where $\{\Phi_j(\mathbf{x}),\omega_j\}$ is the modal set of nonorthogonal eigenfunctions and eigenvalues. Substituting (28) and (29) in the equations of motion

$$\mathscr{D}(\mathbf{u})+\rho\frac{\partial^2\mathbf{u}}{\partial t^2}=\mathbf{0} \tag{30}$$

yields

$$\sum_j(\ddot{a}_j+\omega_j^2 a_j)\rho|j\rangle=-\ddot{f}(t)\rho\mathbf{u}_s(\mathbf{x}). \tag{31}$$

Performing inner products on both sides of (31) yields

$$N_{kj}(\ddot{a}_j+\omega_j^2 a_j)=-N_{ak}\ddot{f}(t), \tag{32a}$$

$$N_{kj}=\langle k|\rho|j\rangle, \tag{32b}$$

$$N_{ak}=\langle k|\cdot\rho\mathbf{u}_s(\mathbf{x})\rangle. \tag{32c}$$

Expressions for N_{ak} and N_{kj} are derived in Appendix B.

III. RESULTS OF TRANSIENT ANALYSIS

The basic bi-periodic stack with the five sets and properties listed in Table I is chosen for comparing results from the various models. A trapezoidal forcing pulse of unit intensity is assumed with 5-μs rise and fall times and 25-μs duration acting over a concentric circle with radius $r_p=0.25$ in. On the top face of each disk, displacement and normal stress histories are computed at four radial stations:

$r=0, r_p, 2r_p$, and $4r_p$. In contrast, shear stress is computed along the neutral plane ($z=h/2$) of each disk and at the same four radial stations. Plots of histories of displacements (u,w), and stress $(\sigma_{zz}, \sigma_{rr}, \sigma_{rz})$ are presented for each disk in columnar form. The column at left results from a flexure model, while the column at right results from a 2-D model. In both models, bond inertia is neglected and 16 radial wave numbers are considered in the radial expansion. In the flexure model, only the flexural group shown in Fig. 2(a) is included. In the 2-D model, the flexural and first extensional groups shown in Fig. 3 are included.

Figure 4 compares histories on the first disk subjected to the forcing pulse. Flexure analysis underestimates displacements and stresses by 15%. For $r \leqslant r_p$, σ_{rr} and u are lower by 50% and 30% respectively, while the difference drops to 15% for $r > r_p$. In 2-D analysis, σ_{rr} and $\sigma_{\theta\theta}$ are made of two parts: an equivoluminal part from flexure anti-symmetric about the disk's neutral plane and a volumetric part from axial stress. The latter is large under the footprint and diminishes rapidly remote from it. It is this part in 2-D which accounts for the larger σ_{rr} and u when $r \leqslant r_p$. For $r > r_p$, the difference in the two models is caused by the Kirchhoff assumption in plate theory.

Figure 5 compares histories on the second disk. In contrast to the first disk, flexure analysis overestimates displacements by 15% and stresses by 25%. This can be explained as follows. In the first disk, the volumetric part in 2-D from axial stress raises strain energy. Since total instantaneous strain energy of the stack is conserved, strain energy of succeeding disks along the stack must be reduced. Also, the shape of the τ_{rz} histories from the two analyses differ substantially before reflexion from the lateral boundary [compare Fig. 5(e_1) to (e_2)] yet the relative magnitudes are still within 25%.

Figure 6 compares histories on the third disk. As with the second disk, flexure analysis overestimates all variables by 15%. The difference in τ_{rz} histories grows even more although magnitude drops, diminishing its importance in response. The drop in τ_{rz} is caused by radial dispersion of the pulse as it propagates across the stack.

The same observations apply to histories on the fourth disk (not shown), where the difference between the two analyses drops to 10%. However, this trend is broken for the fifth disk where the difference in magnitude depends on the variable (see Fig. 7). After 60 μs, σ_{rr} traveling at the shear speed reaches the axis of the stack after reflecting from the lateral boundary. After dropping to a minimum on the second disk, σ_{rr} rises again and peaks on the last disk.

Figure 8 illustrates instantaneous snapshots of the deformed stack at intervals of 5 μs for the duration of 60 μs. At $t=5$ μs [Fig. 8(a)], the pulse applied to the lower disk produces local deformation confined by the wave front. At $t=10$ μs [Fig. 8(b)], the pulse spreads radially along the first disk, and propagates axially reaching the second disk. At $t=20$ μs [Fig. 8(d)], the pulse reaches the back of the stack. Note that disk curvature diminishes along the stack, producing lower flexural stress, consistent with the inverted conoid of fracture observed experimentally. At $t=25$ μs [Fig. 8(e)], the forcing pulse elapses, reducing local deformation of the forced disk over the footprint. At $t=30$ μs [Fig. 8(f)], flexural waves in the first two disks reach the lateral boundary. At $t=50$ μs [Fig. 8(j)], dispersion has caused all disks to move in unison with almost equal amplitude and shape, which is not clearly described by specific waves propagating with defined wave fronts. At $t=60$ μs [Fig. 8(l)], reflections from the lateral boundary reach the axis raising amplitude and flexural stress of the last disk, as confirmed in Fig. 7(d_2) by the negative peak of σ_{rr} at 60 μs. This is the second highest intensity of σ_{rr} next to that on the excited face of the first disk. This tensile stress on the bottom face of the stack causes "spallation."

IV. RESULTS OF PROPAGATION QUANTITIES

This section derives propagation quantities (μ, c_p, c_g) of the bi-periodic stack adopting flexure and 2-D models. Since radial wave number γ_r is prescribed by a dispersion relation that satisfies approximate simple supports at the lateral boundaries [see Eq. (7)] propagation quantities are computed for specific values of γ_r. In this way, propagation relates to frequency groups in Figs. 2 and 3.

In the flexural model, Floquet theory requires that

$$w_i = e^{\mu} w_{i-1}, \quad w_{i+1} = e^{\mu} w_i, \tag{33}$$

where w_i, w_{i-1}, and w_{i+1} are axial displacement of disks i, $i-1$, and $i+1$, respectively, and μ is propagation constant. Substituting (33) in the ith row of Eq. (9) yields

$$A_{ii} + A_{i,i+1}(e^{\mu} + e^{-\mu}) = 0. \tag{34a}$$

Solving the quadratic in (34a) for e^{μ} gives

$$e^{\mu} = (-A_{ii} \pm \sqrt{A_{ii}^2 - 4A_{i,i+1}})/(2A_{i,i+1}) \equiv \lambda_{1,2},$$

$$\Rightarrow \mu = \log(\lambda). \tag{34b}$$

Since μ is related to axial wave number k_z by

$$k_z = \mu / h_s, \tag{35a}$$

where h_s is set thickness $(h_s = h + h_b)$, then phase and group velocities c_p and c_g follow:

$$c_p = \frac{\omega h_s}{\mu}, \quad c_g = h_s \frac{\partial \omega}{\partial \mu}. \tag{35b}$$

In the 2-D model, the transfer matrix $\mathbf{T}$ in Eq. (25) relates state vectors at two faces of a layer:

$$\mathbf{S}_{i+1} = \mathbf{T}\mathbf{S}_i,$$

$$\mathbf{S}_{i+2} = \mathbf{T}_b \mathbf{S}_{i+1}, \tag{36a}$$

where $\mathbf{T}$ and $\mathbf{T}_b$ correspond to disk and bond in the bi-periodic set. $\mathbf{T}_s$ of a set then follows from (36a)

$$\mathbf{T}_s = \mathbf{T}_b \mathbf{T}. \tag{36b}$$

Floquet theory requires that

$$\mathbf{S}_{i+2} = e^{\mu} \mathbf{I} \mathbf{S}_i = \mathbf{T}_s \mathbf{S}_i, \tag{37a}$$

$$\Rightarrow |\mathbf{T}_s - \mathbf{I} e^{\mu}| = \mathbf{0}. \tag{37b}$$

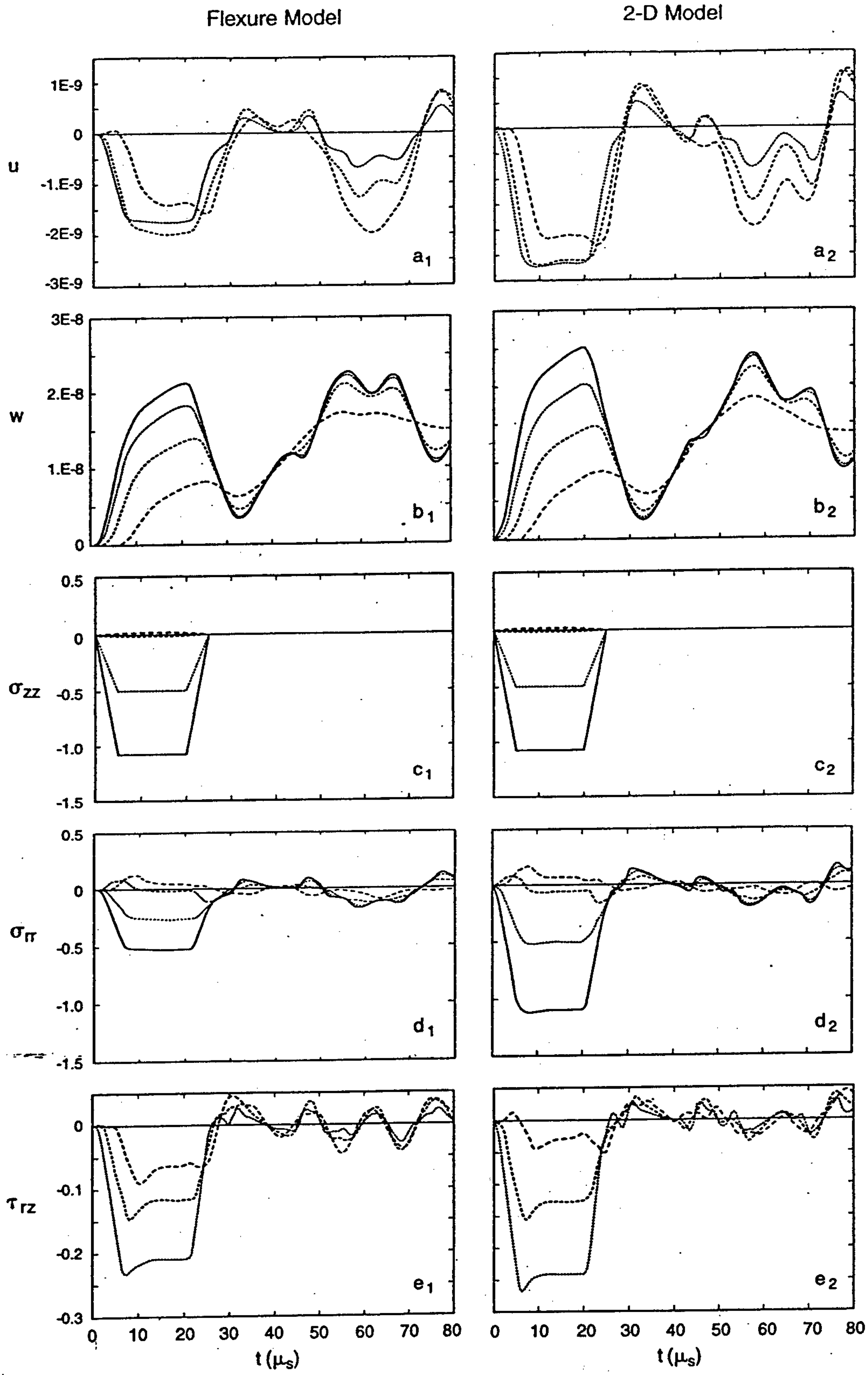

FIG. 4. Comparison of histories from the two models for disk 1: ——— $r=0$; · · · · $r=r_p$; ------- $r=2r_p$; – – – – – – – $r=4r_p$.

Propagation constants are related to the eigenvalues of $\mathbf{T}_s$ yielding (c_p, c_g) by applying (35b).

Results from the 2-D model are presented first, while those of the flexure model are presented later because it is more approximate and the disappearance of any features can be readily observed. For direct comparison with the 1-D results in Ref. 23, $\mu=(\mu_R, \mu_I)$ is normalized by π, and c_p and c_g are normalized by c_0 where

$$c_0 = h_s\left[\frac{E_{b\epsilon}}{\rho h h_b(1+\bar{\tau}/\bar{z})(1+1/(\bar{z}\bar{\tau}))}\right]^{1/2},$$

$$\bar{z}=\rho c/\rho_b c_{b\epsilon}, \quad \bar{\tau}=h_b c/h c_{b\epsilon}, \quad c_{b\epsilon}=\sqrt{E_{b\epsilon}/\rho_b}. \tag{38a}$$

$(\bar{z},\bar{\tau})$ are impedance and travel time ratios in the bi-periodic

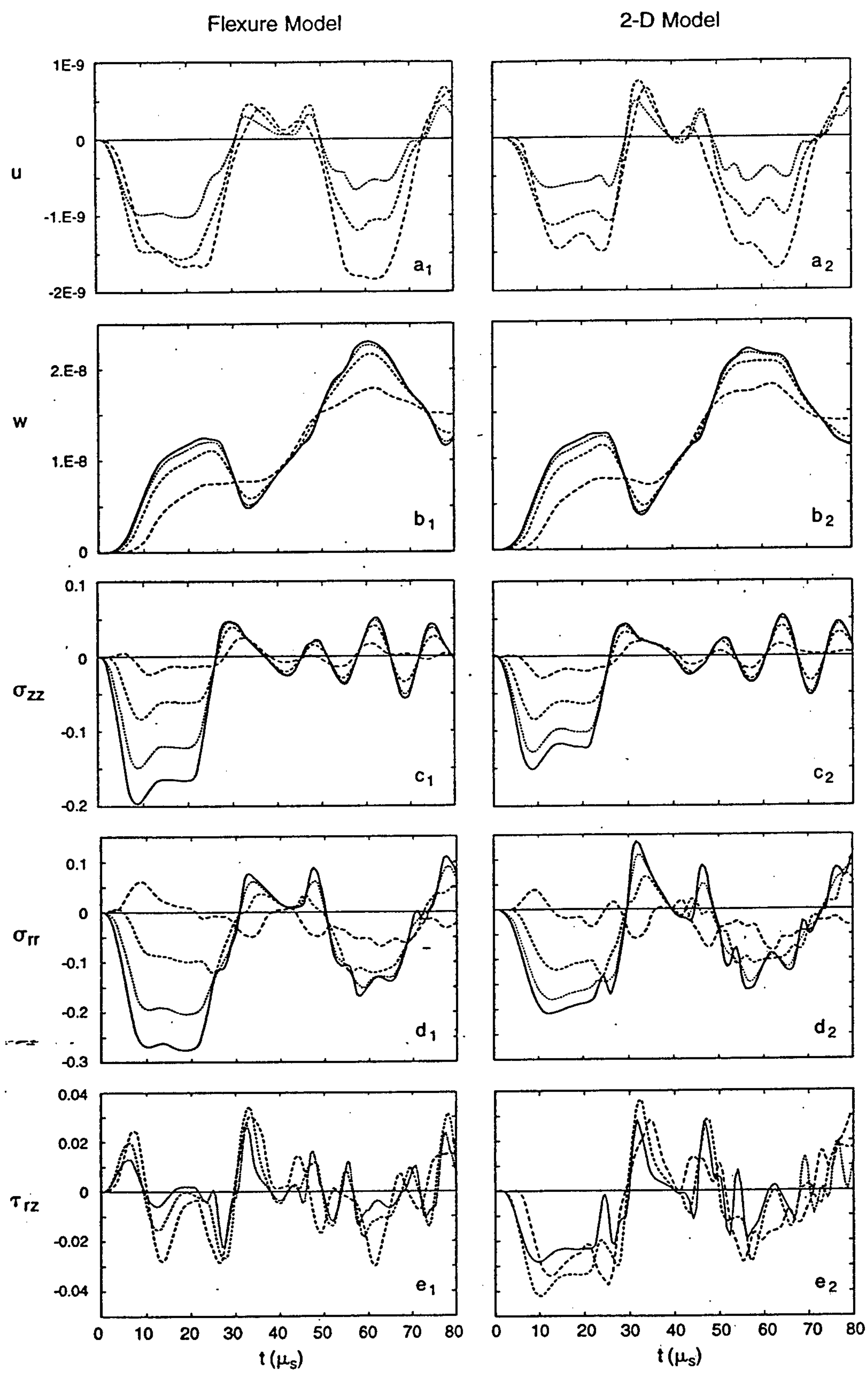

FIG. 5. Comparison of histories from the two models for disk 2: ——— $r=0$; · · · · $r=r_p$; --------- $r=2r_p$; – – – – – – – $r=4r_p$.

set. For some number of radial half-waves $m_r=\gamma_r/\pi$, propagation quantities $(\mu_R/\pi,\mu_I/\pi,c_p/c_0,c_g/c_0)$ are plotted against normalized frequency $\omega h_s/c_0$, where (μ_R,μ_I) are real and imaginary parts of μ. Note that

$$\omega_e=c_0/h_s \tag{38b}$$

is the resonant frequency of the set when the disk acts as arigid mass and the bond as an elastic spring (see Ref. 23 and Appendix A). To reproduce 1-D results in Ref. 23, propagation quantities are computed for $m_r=0$, as shown in Fig. 9. The solid lines in c_p/c_0 and c_g/c_0 agree closely with those of 1-D shown in Fig. 5(a) of Ref. 23.

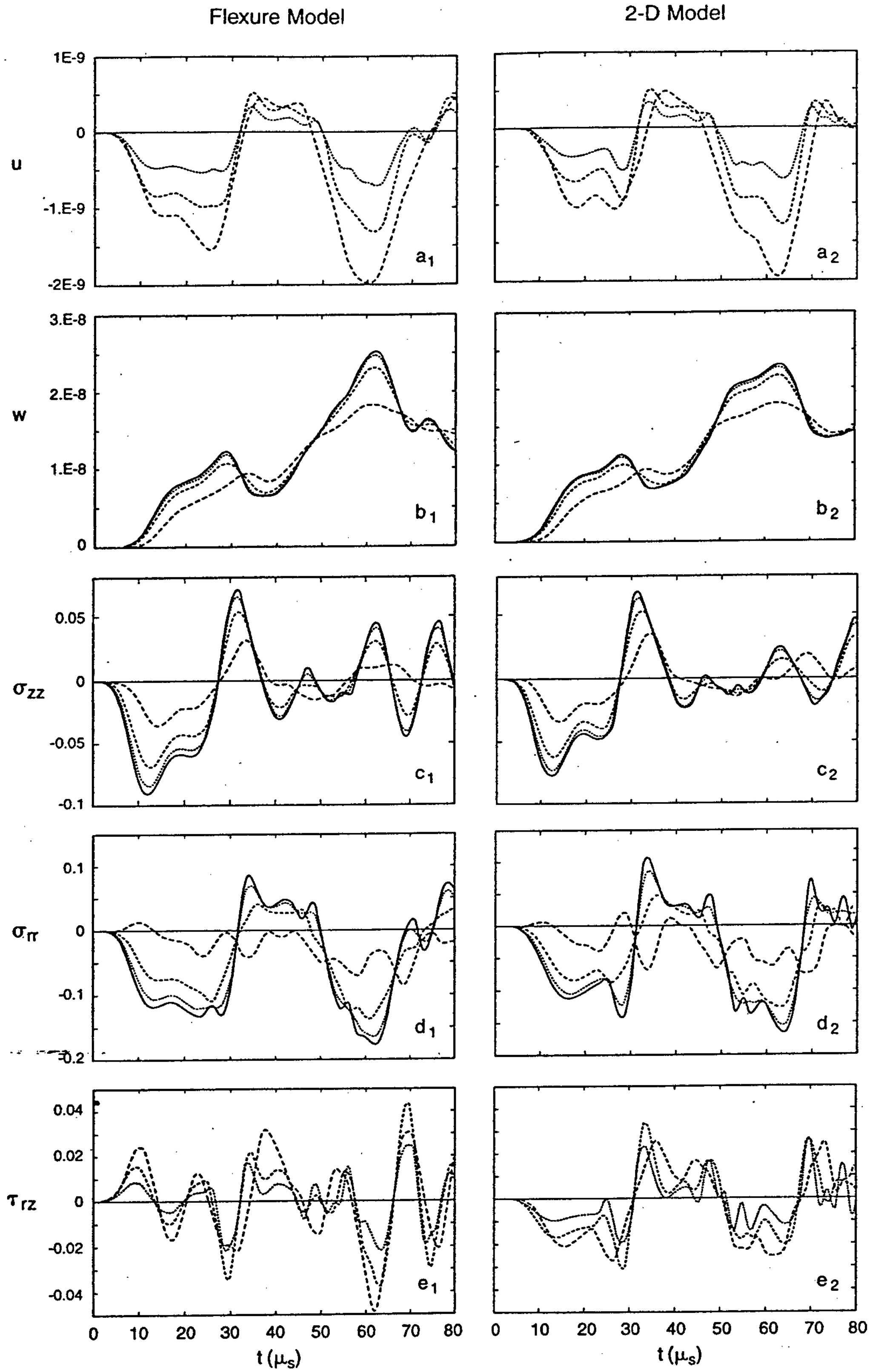

FIG. 6. Comparison of histories from the two models for disk 3: ——— $r=0$; · · · · $r=r_p$; --------- $r=2r_p$; ——— $r=4r_p$.

For the first radial mode with $\frac{1}{4}$ wave along r, $m_r=0.59$, propagation quantities of the flexural group shown as solid lines in Fig. 10 are not segregated from those of the first extensional group shown as dashed lines, as also noted in Fig. 3. Lines of (c_p, c_g) undergo discontinuities marking the start of PZ2 and the end of PZ1. Ignoring the singular behavior of c_p and the sharp drop of c_g at the boundaries of PZ1 and PZ2, their average lines follow approximately the same shape and magnitude as the $m_r=0$ lines in Fig. 9. The fact that the propagation quantities for the low m_r are similar to those for $m_r=0$ supports a valuable simplification. The $m_r=0$ case is the same as a 1-D model of periodic masses

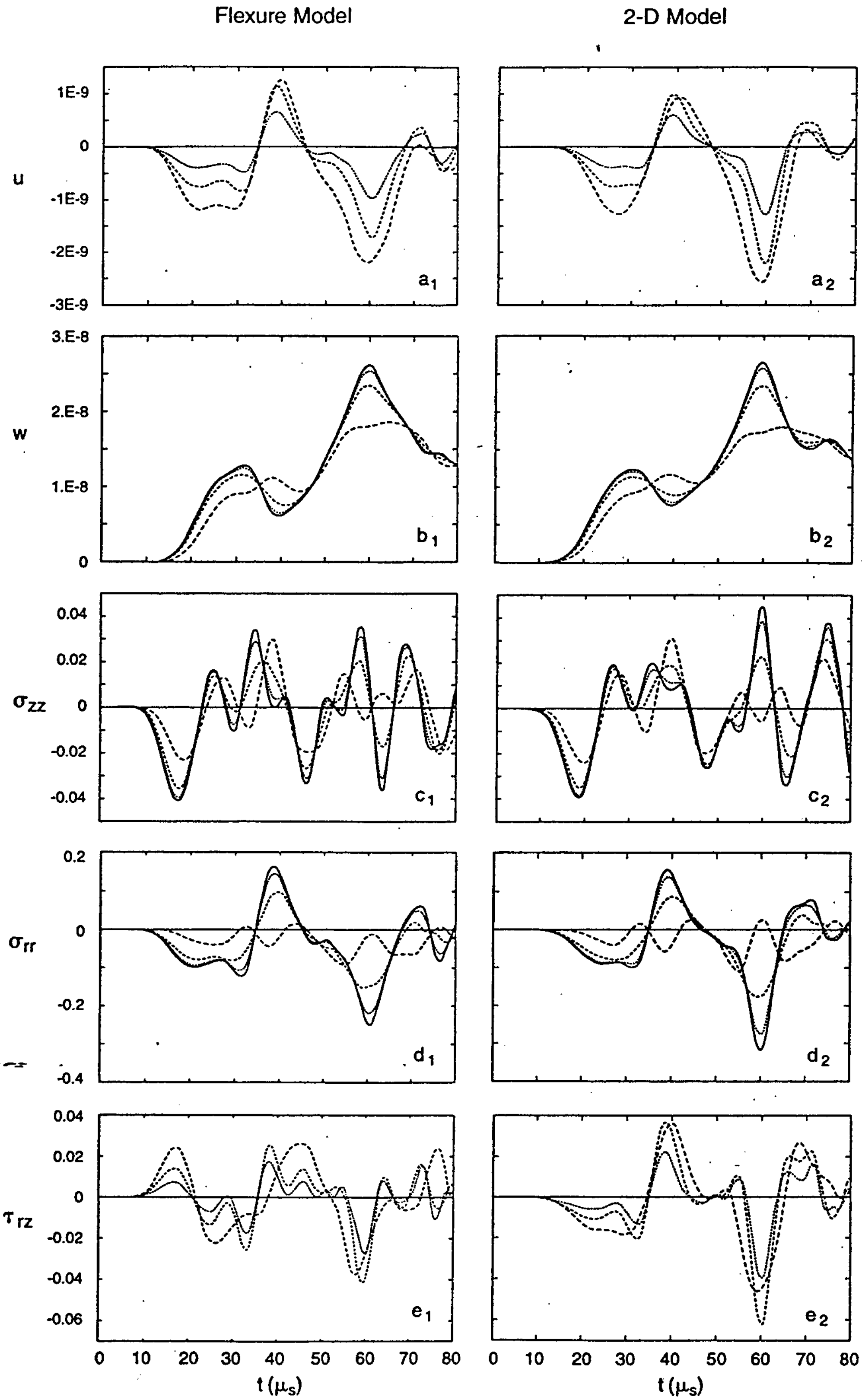

FIG. 7. Comparison of histories from the two models for disk 5: ——— $r=0$; · · · · $r=r_p$; -------- $r=2r_p$; ------- $r=4r_p$.

and springs described in Ref. 23 where propagation quantities are extensively characterized. This implies that all conclusions drawn from the 1-D model can be carried over to a good approximation to both flexure and 2-D models.

As m_r increases, PZ1 becomes narrow, reproducing the width of the flexural frequency group in Fig. 3 (see Figs. 11 and 12 for $m_r=1.7$ and 2.72). In fact, fixing m_r, all stack resonant frequencies within a group (see Fig. 3) fall within the boundaries of PZ's.

Propagation quantities drawn from the flexure model re-

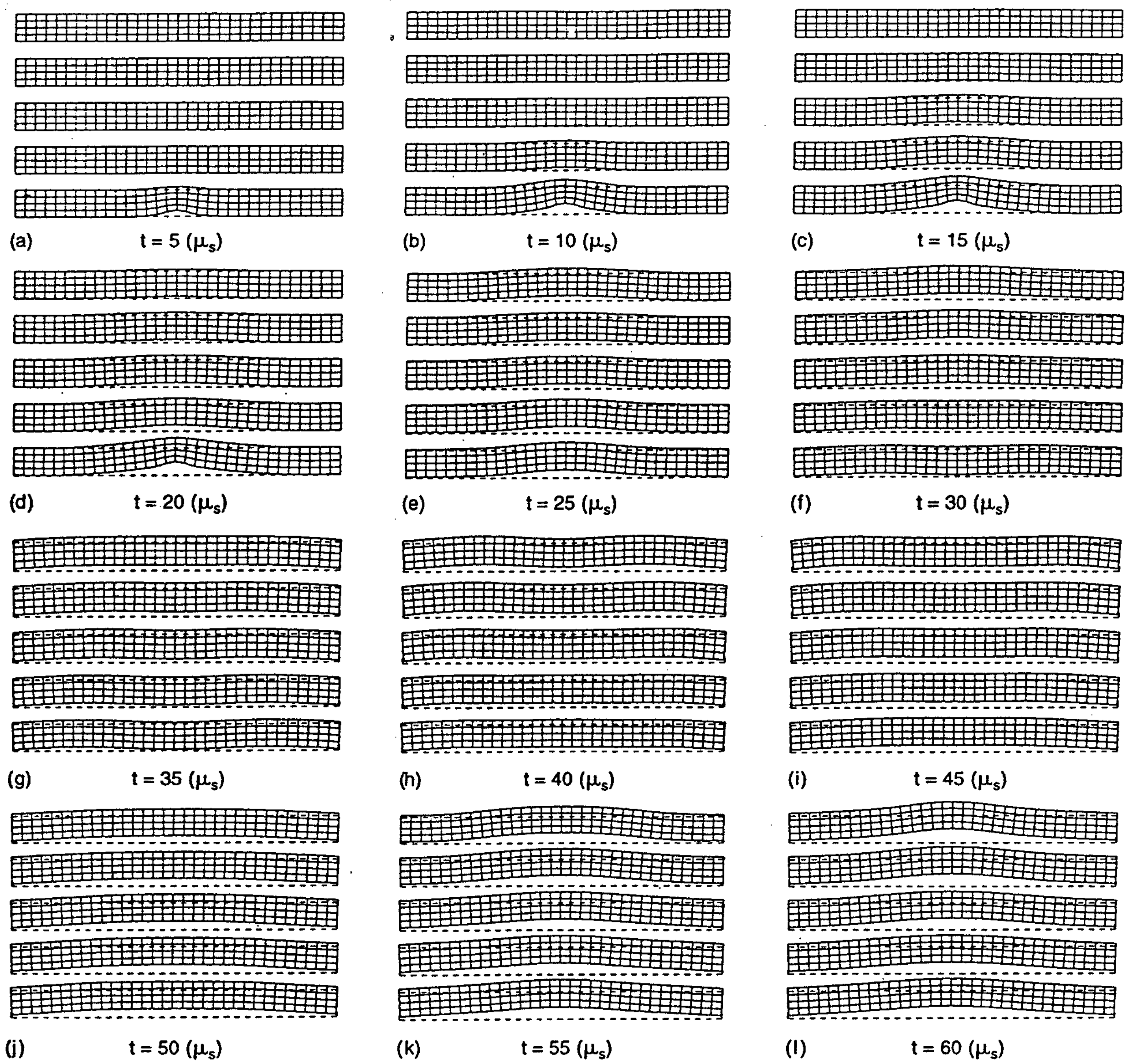

FIG. 8. Snap shots of the deformed stack.

semble those drawn from the 2-D model in the following way. For the lowest m_r where flexure and extensional groups are not segregated, lines of propagation quantities (Fig. 13) follow the trend of the 2-D's (Fig. 10) except that they are continuous across boundaries of PZ2. For the higher m_r, when flexure and extensional groups are segregated, the lines resemble those of the 2-D's flexural group. Also, flexure analysis over-estimates (c_p, c_g) and width of PZ's by at least 5%. In turn, wavefronts predicted by the flexure model move faster than those predicted by the 2-D model, yielding shorter arrival times of waves along the stack. This is seen by comparing arrival times, which can be measured as the times when a dependent variable's history first departs from the undisturbed state, in corresponding columns of Figs. 6 and 7. The plane stress and Kirchhoff assumptions behind the flexure model are the causes of this discrepancy.

V. CONCLUSION

Results from treating wave propagation in a finite periodic stack according to the different models developed above are compared in order to reveal the effects of their differing assumptions. Histories of a stack forced by a trapezoidal pulse were used. Important features from comparison of the two primary models are:

(1) On the forced disk, the flexure model underestimates all variables by 15% remote from the footprint and by as much as 50% in the vicinity of the footprint. This difference is caused by the volumetric part of the stress from axial compression.
(2) On succeeding disks, the flexure model overestimates all variables by as much as 25%, while the difference diminishes along the stack. This difference is caused by the Kirchhoff assumption behind the flexure model.

The effects on response of the approximations in the 2-D models are:

(3) Neglecting inertia of the bond suppresses frequencies of the bond shear group leaving response histories unchanged.
(4) Omitting the extensional frequency groups in the modal

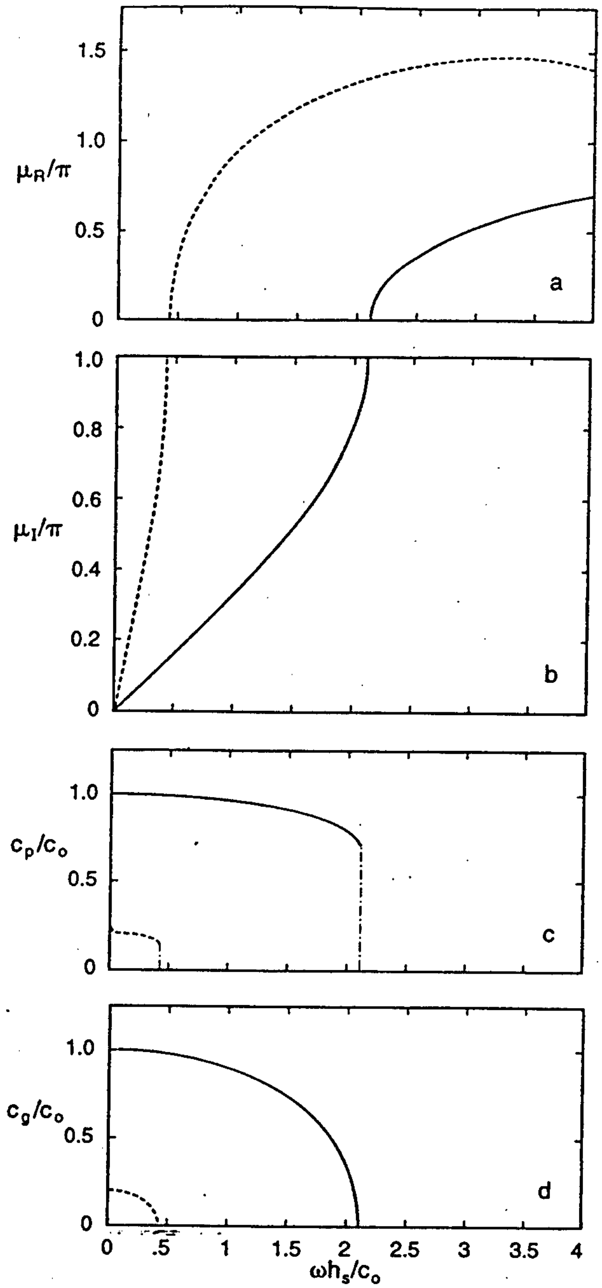

FIG. 9. Propagation quantities for $m_r=0$ (2-D model).

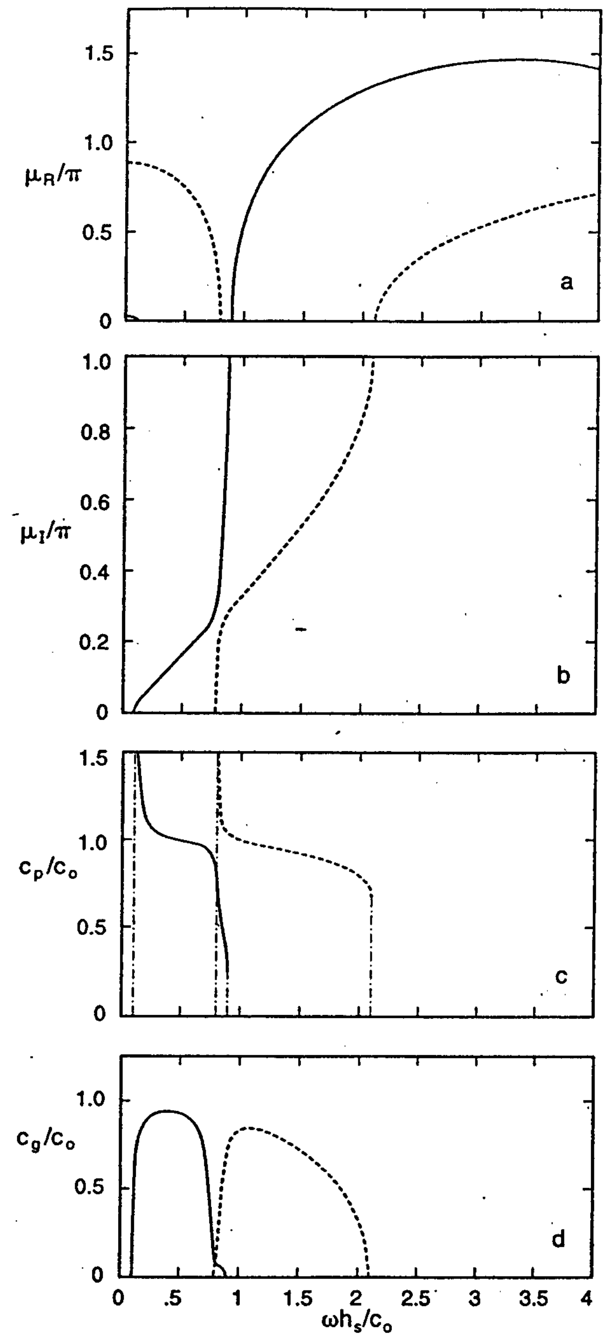

FIG. 10. Propagation quantities for $m_r=0.59$ (2-D model).

expansion does not alter response histories.

The reason behind conclusion (4) is that extensional motions are already included in the analysis by the static part of the solution in $\mathbf{u}_s f_0(t)$ in (28). This fact emphasizes the importance of using static-dynamic superposition which produces an accurate solution with the smallest set of eigenfunctions. Indeed, the body force method was unsuccessful in modeling the forcing function. Trading computational efficiency for degree of approximation, the plate flexure model may be used with caution for initial screening of parameters in the design of shock isolation devices involving stacks. The 2-D model is preferred when accurate prediction of wave propagation is essential.

Some further conclusions are drawn from consideration of propagation quantities:

(5) To a good approximation, all the conclusions drawn from the 1-D model of periodic masses and springs can be carried over to the flexure and 2-D models (see Ref. 23).
(6) Waves with higher m_r are more dispersed and every transient model becomes dominated eventually by waves with low m_r.
(7) Predictions with the flexure model are close to those of 2-D when limited to the flexure groups.

APPENDIX A: RADIAL MOMENT FROM BOND SHEAR

Flexure of the disks induces shear of the bond. Inertia of the bond introduces shear resonances that raise or lower mobility of the bond depending on their proximity to flexural

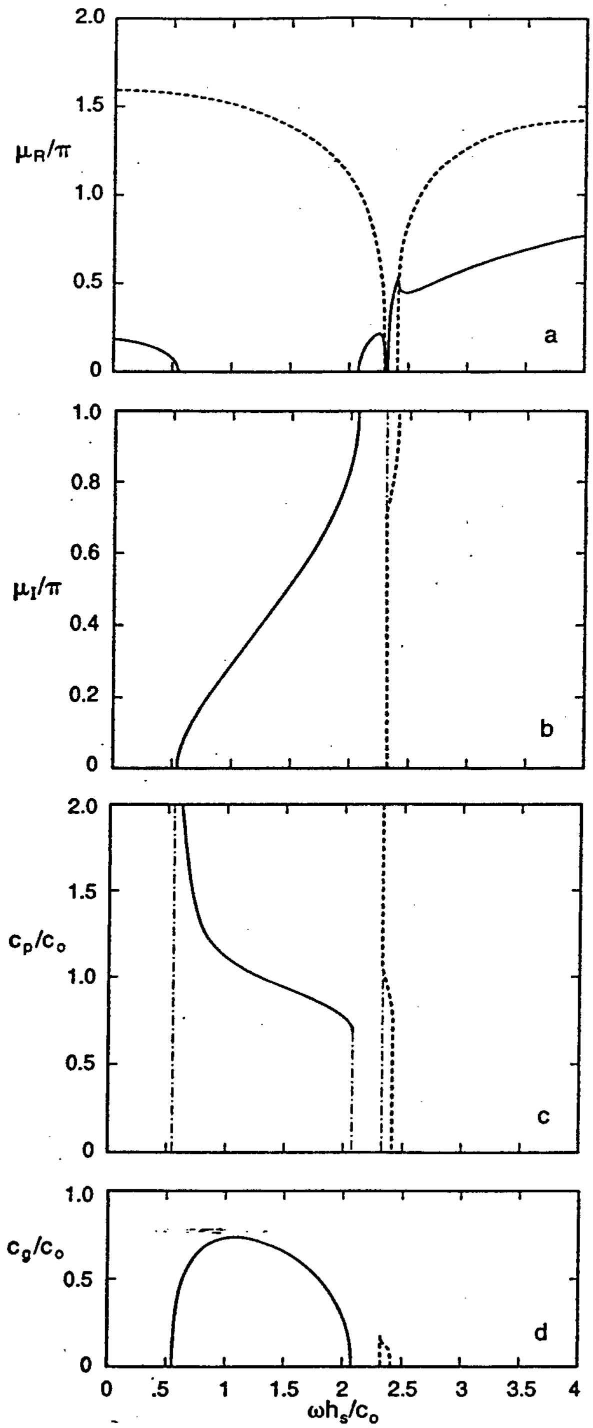

FIG. 11. Propagation quantities for $\gamma_r = 1.70$ (2-D model).

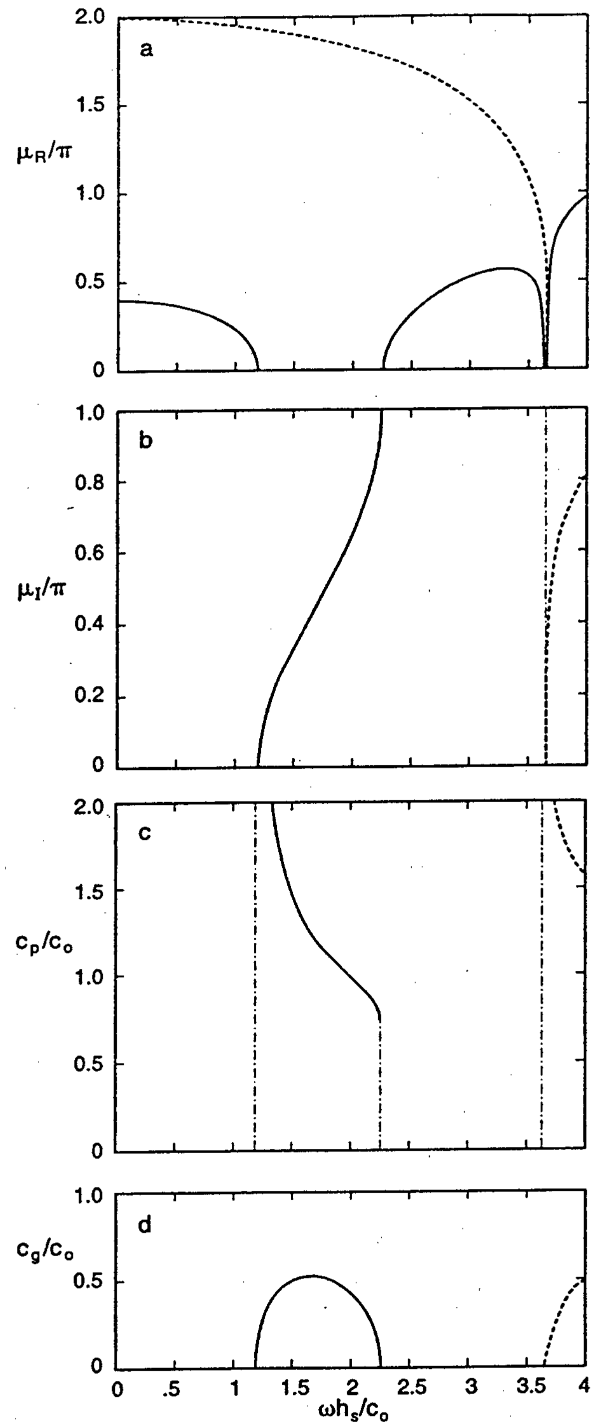

FIG. 12. Propagation quantities for $m_r = 2.72$ (2-D model).

resonances. The effects of bond shear and inertia are considered invoking motions with vanishing axial displacement in the 2-D axisymmetric equations of elasto-dynamics:

$$\alpha^2 \nabla_1^2 u + \frac{\partial^2 u}{\partial z^2} = \frac{1}{c_{s_b}^2} \frac{\partial^2 u}{\partial t^2}; \quad c_{s_b}^2 = \frac{G_b}{\rho_b},$$

$$\nabla_1^2 \equiv \frac{\partial^2}{\partial r^2} + \frac{1}{r}\frac{\partial}{\partial r} - \frac{1}{r^2}, \tag{A1}$$

where u is radial displacement, and (G_b, ρ_b) are shear modulus and density of the bond. For unixial strain $\alpha^2 = 2(1-\nu_b)/(1-2\nu_b)$. For approximate simple supports and harmonic motions in time

$$u(r,z,t) = J_1(k_r r) u_0(z) e^{i\omega t}, \tag{A2}$$

where $J_0''(k_r a) = 0$ [see Eq. (7)]. Substituting (A2) in (A1) produces an equation in $u_0(z)$

$$\frac{d^2 u_0}{dz^2} + k_z^2 u_0 = 0, \quad k_z = \sqrt{\left(\frac{\omega}{c_{s_b}}\right)^2 - (k_r \alpha)^2}. \tag{A3}$$

To find the shear stresses on disk "i" from bonds "1" and "2" connecting it to disks "$i-1$" and "$i+1$," respec-

Erratum: "Simplified models of transient elastic waves in finite axisymmetric layered media" [J. Acoust. Soc. Am. 104, 3369–3384 (1998)]

Michael El-Raheb
The Dow Chemical Company, Midland, Michigan 48674

(Received 4 February 1999; accepted for publication 18 February 1999)

[S0001-4966(99)04305-2]

PACS numbers: 43.20.Jr, 43.40.Dx [CBB]

The definition of ∇_n^2 in Eq. (1c) should be

$$\nabla_n^2=\frac{\partial^2}{\partial r^2}+\frac{1}{r}\frac{\partial}{\partial r}-\frac{n^2}{r^2}. \tag{1c}$$

The factor $G_b h^2/h_b$ in Eqs. (4), (5a), and (5b) should be $G_b h^2/4h_b$. In Appendix A, Eq. (A8) should be

$$\tau_K(z)=-\frac{h}{2}k_zG_b\left[\Psi_{i+k-2}\sin k_z z+(\Psi_{i+k-1}+\Psi_{i+k-2}\cos k_z h_b)\frac{\cos k_z z}{\sin k_z h_b}\right], \tag{A8}$$

while Eq. (A9) should read

$$\bar{M}_r=-(\tau_1(h_b)+\tau_2(0))\frac{h}{2}=\left(\frac{h}{2}\right)^2\frac{1}{h_b}\frac{k_z h_b}{\sin k_z h_b}G_b[2\Psi_i\cos k_z h_b+\Psi_{i+1}+\Psi_{i-1}], \tag{A9}$$

which changes Eq. (A10) to

$$\bar{M}_r=\left(\frac{h}{2}\right)^2 G_b[2\Psi_i+\Psi_{i+1}+\Psi_{i-1}]/h_b. \tag{A10}$$

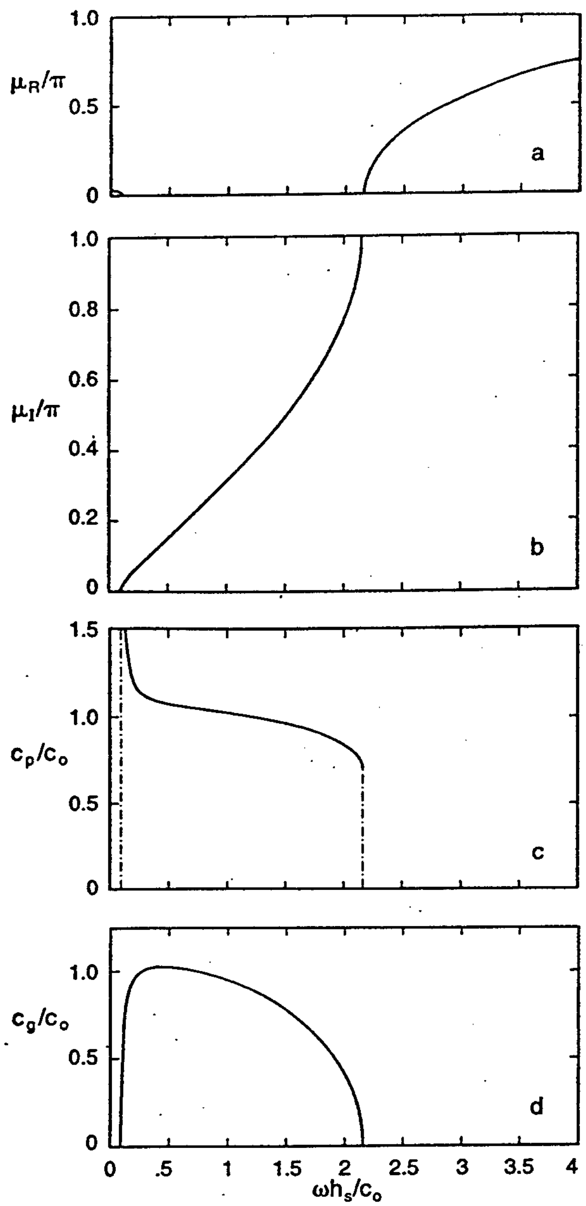

FIG. 13. Propagation quantities for $m_r=0.59$ (flexure model).

tively, solve bond equation (A3) and apply continuity of axial displacement at the interfaces of disks "i," "$i+1$," and "$i-1$." For bond "1" connecting disks "$i-1$" to "i":

$$u_{01}(0)=\frac{h}{2}\,\psi_{i-1},\quad u_{01}(h_b)=-\frac{h}{2}\,\psi_i, \tag{A4}$$

where h_b and h are bond and disk thicknesses, and ψ is rotation angle of the disk cross section. Also for bond "2" connecting disks "i" to "$i+1$":

$$u_{02}(0)=\frac{h}{2}\,\psi_i,\quad u_{02}(h_b)=-\frac{h}{2}\,\psi_{i+1}. \tag{A5}$$

The two solutions of (A3) with boundary conditions (A4) and (A5) yield $u_{ok}(z)$ in the form:
(a) bond "1": connecting "$i-1$" to "i":

$$u_{01}(z)=\frac{h}{2}\,\psi_{i-1}\cos k_2 z-\frac{h}{2}\,(\psi_i+\psi_{i-1}\cos k_z h_b)\,\frac{\sin k_z z}{\sin k_z h_b}; \tag{A6a}$$

(b) bond "2": connecting "i" to "$i+1$":

$$u_{02}(z)=\frac{h}{2}\,\psi_i\cos k_z z-\frac{h}{2}\,(\psi_{i+1}+\psi_i\cos k_z h_b)\,\frac{\sin k_z z}{\sin k_z h_b}. \tag{A6b}$$

Shear stress of the kth bond follows from the relation

$$\tau_k(z)=\frac{\partial u_{0k}}{\partial z}\,G_b;\quad k=1,2. \tag{A7}$$

Substituting (A6a,b) in (A7) produces

$$\tau_k(z)=-\frac{h}{2}\,k_z G_b\left[\psi_{i+k-2}\cos k_z z+(\psi_{i+k-1}+\psi_{i+k-2}\cos k_z h_b)\,\frac{\sin k_z z}{\sin k_z h_b}\right]. \tag{A8}$$

Shear stresses $\tau_1(h_b)$ and $\tau_2(0)$ acting on top and bottom faces of disk "i" from bonds "1" and "2" produce a radial moment $\bar{M}_r$ on disk "i":

$$\bar{M}_r=-(\tau_1(h_b)+\tau_2(0))\,\frac{h}{2},$$
$$=\left(\frac{h}{2}\right)^2\frac{k_z h_b}{\sin k_z h_b}\,G_b[2\psi_i\cos k_z h_b+\psi_{i+1}+\psi_{i-1}]. \tag{A9}$$

In the limit as $(k_z h_b)\rightarrow 0$, the quasi-static moment is recovered

$$\bar{M}_r=\left(\frac{h}{2}\right)^2 G_b[2\psi_i+\psi_{i+1}+\psi_{i-1}]. \tag{A10}$$

In (A9) as $(k_z h_b)\rightarrow\pi$, the fundamental shear resonance of the bond is crossed. As this resonance is approached from below, the bond mobility rises, reducing coupling between disks which narrows the gap between resonances. As shear resonance is crossed, bond mobility falls abruptly because of a change in phase, raising coupling between disks which widens the gap between resonances.

APPENDIX B: INNER PRODUCTS IN 2-D AXYSYMMETRIC ANALYSIS

Consider the nth eigenfunction and lth layer in the stack

$$N_{aln}=\langle u_s|\rho|u_{dn}\rangle_l+\langle w_s|\rho|w_{dn}\rangle_l. \tag{B1}$$

From Ref. 24

$$u_s(r,z)=\sum_{m=1}^{\infty}\left\{\sum_{j=1}^{2}C_{smj}e^{\beta_{mj}z}+\sum_{J=3}^{4}C_{smj}|\beta_{mj}|ze^{\beta_{mj}z}\right\}J_1(k_{rm}r),$$

$$w_s(r,z)=\sum_{m=1}^{\infty}\left\{\sum_{j=1}^{2} D_{smj}e^{\beta_{mj}z}\right.$$

$$\left.+\sum_{j=3}^{4} D_{smj}|\beta_{mj}|ze^{\beta_{mj}z}\right\}J_0(k_{rm}r),$$

$$\beta_{mj}=(-1)^{j+1}k_{rm}. \tag{B2}$$

Also from (21a,b)

$$u_{dn}(r,z)=\sum_{i=1}^{4} C_{dni}e^{\alpha_{ni}z}J_1(k_{rn}r),$$

$$w_{dn}(r,z)=\sum_{i=1}^{4} D_{dni}e^{\alpha_{ni}z}J_0(k_{rn}r). \tag{B3}$$

Substituting (B2) and (B3) in (B1) and performing the inner product yields

$$N_{an}^{(l)}=\rho_l\sum_{m=1}^{\infty}\sum_{i=1}^{4}\left\{\sum_{j=1}^{2} C_{dni}C_{smj}\frac{e^{\delta_{mnij}z}}{\delta_{mnij}}\Big|_0^{h_l}\right.$$

$$\left.+\sum_{j=3}^{4} C_{dni}C_{smj}\frac{e^{\delta_{mnij}z}}{\delta_{mnij}^2}(\delta_{mnij}z-1)\Big|_0^{h_l}\right\}\bar{N}_{1mn}$$

$$+\rho_l\sum_{m=1}^{\infty}\sum_{i=1}^{4}\left\{\sum_{j=1}^{2} D_{dni}D_{smj}\frac{e^{\delta_{mnij}z}}{\delta_{mnij}}\Big|_0^{h_l}\right.$$

$$\left.+\sum_{j=3}^{4} D_{dni}D_{smj}\frac{e^{\delta_{mnij}z}}{\delta_{mnij}^2}(\delta_{mnij}z=1)\Big|_0^{h_l}\right\}\bar{N}_{omn},$$

$$\delta_{mnij}=\beta_{mj}+\alpha_{ni}, \tag{B4}$$

$$\bar{N}_{jmn}=\frac{1}{\alpha^2}\int_0^{\alpha} J_j(k_{rm}r)J_j(k_{rn}r)r\,dr, \quad j=1,2.$$

Expressions for $N_{mn}=\langle m|\rho|n\rangle$ follow

$$N_{mn}^{(l)}=\rho_l\sum_{i=1}^{4}\sum_{j=1}^{4} C_{dmi}C_{dnj}\frac{e^{\delta_{mnij}z}}{\delta_{mnij}}\Big|_0^{h_l}\bar{N}_{1mn}$$

$$+\rho_l\sum_{i=1}^{4}\sum_{j=1}^{4} D_{dmi}D_{dnj}\frac{e^{\delta_{mnij}z}}{\delta_{mnij}}\Big|_0\bar{N}_{omn},$$

$$\delta_{mnij}=\alpha_{mi}+\alpha_{nj}. \tag{B5}$$

In (B4) and (B5), h_l is thickness of the lth layer. To find N_{an} and N_{mn} for the stack, sum over all layers

$$N_{an}=\sum_{l=1}^{N} N_{an}^{(l)}, \quad N_{mn}=\sum_{l=1}^{N} N_{mn}^{(l)}. \tag{B6}$$

[1] W. Thomson, "Transmission of elastic waves through a stratified medium," J. Appl. Phys. 21, 89–93 (1950).

[2] N. A. Haskel, "The dispersion of surfaced waves in multi-layered media," Bull. Seismol. Soc. Am. 43, 17–34 (1953).

[3] S. M. Rytov, "Acoustical properties of a thinly laminated medium," Sov. Phys. Acoust. 2, 68–70 (1956).

[4] D. L. Anderson, "Elastic wave propagation in layered anisotropic media," J. Geophys. Res. 66, 2953–2963 (1961).

[5] R. A. Tenenbaum and M. Zindeluk, "An exact solution for the one-dimensional elastic wave equation in layered media," J. Acoust. Soc. Am. 92, 3364–3370 (1992).

[6] C. T. Sun, J. D. Achenbach, and G. Herrmann, "Time harmonic waves in a stratified medium, propagating in the direction of the layering," J. Appl. Mech. 35, 408–411 (1968).

[7] T. J. Delph, G. Herrmann, and R. K. Kaul, "Harmonic wave propagation in a periodically layered infinite elastic body: Antiplane strain," J. Appl. Mech. 45, 343–349 (1978).

[8] T. J. Delph, G. Herrmann, and R. K. Kaul, "Harmonic wave propagation in a periodically layered infinite elastic body: Plane strain, analytical results," J. Appl. Mech. 46, 113–119 (1979).

[9] T. J. Delph, G. Herrmann, and R. K. Kaul, "Harmonic wave propagation in a periodically layered infinite elastic body: Plane strain, numerical results," J. Appl. Mech. 47, 531–537 (1980).

[10] G. Herrmann and M. Hemami, "Plane-strain surface waves in a laminated composite," J. Appl. Mech. 49, 747–753 (1982).

[11] D. J. Mead, "Vibration response and wave propagation in periodic structures," Journal of Engineering in Industry 93, 783–792 (1971).

[12] D. J. Mead, "Wave propagation and natural modes in periodic systems, I: Mono-coupled systems," J. Sound Vib. 40, 1–18 (1975).

[13] D. J. Mead and A. S. Bansal, "Free wave propagation and response to convected loadings," J. Sound Vib. 61, 481–515 (1978).

[14] D. J. Mead and S. M. Lee, "Receptance methods and the dynamics of disordered one-dimensional lattices," J. Sound Vib. 92, 427–445 (1984).

[15] D. J. Mead, "A new method of analyzing wave propagation in periodic structures: Applications to periodic Timoshenko beams and stiffened plates," J. Sound Vib. 104, 9–27 (1986).

[16] R. C. Engels and L. Meirovitch, "Response of periodic structures by modal analysis," J. Sound Vib. 56, 481–493 (1978).

[17] Sen G. Gupta, "Vibration of periodic structures," Shock & Vibration Digest 12(3), 17–29 (1980).

[18] T. J. McDaniel and M. J. Carroll, "Dynamics of biperiodic structures," J. Sound Vib. 81, 311–335 (1982).

[19] M. G. Faulkner and D. P. Hong, "Free vibrations of a mono-coupled periodic systems," J. Sound Vib. 99, 29–42 (1985).

[20] A. J. Keane and W. G. Price, "On the vibrations of mono-coupled periodic and near-periodic structures," J. Sound Vib. 128, 423–450 (1989).

[21] M. Rousseau, "Floquet wave properties in a periodically layered medium," J. Acoust. Soc. Am. 86, 2369–2376 (1989).

[22] M. El-Raheb, "Transient elastic waves in finite layered media: One-dimensional analysis," J. Acoust. Soc. Am. 94, 172–184 (1993).

[23] M. El-Raheb, "Simplified analytical models for transient uniaxial waves in a layered periodic stack," Int. J. Solids Struct. 34(23), 2969–2990 (1997).

[24] M. El-Raheb and P. Wagner, "Transient elastic waves in finite layered media: Two dimensional axisymmetric analysis," J. Acoust. Soc. Am. 99, 3513–3527 (1996).

[25] R. D. Mindlin, "Influence of rotary inertia and shear deformation on flexural motions of isotropic elastic plates," Trans. ASME, J. Appl. Mech. 73, 31–38 (1951).

[26] M. El-Raheb, "The static-dynamic superposition method applied to uniaxial waves in a bi-periodic stack," J. Acoust. Soc. Am. 101, 610–612 (1997).

Reference [3]
Simplified Analytical Models for Transient Uniaxial Waves in a Layered Periodic Stack

Pergamon

Int. J. Solids Structures Vol. 34, No. 23, pp. 2969–2990, 1997

0020–7683/97 $17.00 + .00

PII: S0020–7683(96)00220–X

SIMPLIFIED ANALYTICAL MODELS FOR TRANSIENT UNIAXIAL WAVES IN A LAYERED PERIODIC STACK

MICHAEL EL-RAHEB
Dow Chemical Company, Central Research, Building 1776, Midland, MI 48674, U.S.A.

(*Received* 25 *January* 1996; *in revised form* 10 *October* 1996)

Abstract—A physical understanding is gained of some results acquired in the analysis of transient propagation of uniaxial elastic waves in weakly coupled periodic stacks using simple analytical models. Three simplified models are examined: a mass–spring chain, a single mass spring attached to a delayed moving base, and high frequencies of an elastic mass reacted upon by a spring. Closed-form expressions and asymptotic behavior are obtained for attenuation of maximum stress, characteristic velocities, internal stress distribution and transmission or suppression of high-frequency oscillations. The results provide insights in the design of impact resistant structural systems using layered periodic stacks. © 1997 Elsevier Science Ltd.

1. INTRODUCTION

The study of transient uniaxial waves in layered media is useful in composites, geophysics, ocean acoustics and oil exploration. A large body of work was produced that treated the harmonic propagation of waves in layered media excited by monochromatic sources. Thompson (1950), Haskel (1953), Rytov (1956), Anderson (1961) and Tennenbaum (1992) discussed time harmonic propagation in 1-D layered media. Sun (1968), Delph (1978, 1979, 1980), and Herrmann (1982) extended the time periodic waves to 3-D periodic media. Mead (1971, 1975, 1978, 1984, 1986), Engels (1978), Gupta (1980), McDaniel (1982), Faulkner (1985), Keane (1989) and Rousseau (1989) considered simple periodic structures and applied Floquet theory to propagation and attenuation zones. Robinson (1972), Lee (1973), Chao (1975), Golebiewska (1980), Shah (1982), Kundu (1985), Mal (1988), and Braga (1990) discussed waves in composites. The methods used to analyze this problem ranged from purely numerical, like discretization and geometric optics, to purely analytical, like modal and transform techniques. In contrast with the extensive work reported on harmonic waves, little attention was devoted to transient waves despite their importance in many practical applications. El-Raheb (1993) treated transient uniaxial waves in finite ordered and disordered bi-periodic stacks. The method relied on deriving transfer matrices in harmonic space relating state vectors at the interface between layers. Equilibrium of stress and continuity of displacement at each interface produced a system of tri-diagonal block matrices yielding the modal characteristics of the stack. Transient response was found from an expansion in these modes. Clearly, the complexity of the analytical solution in El-Raheb (1993) limits its usefulness in developing insights into the character of uniaxial propagation. In this reference, results on transient uniaxial waves were obtained for a stack of alternating hard and weak layers excited by a trapezoidal pulse of short duration (see Fig. 1(a)).

The purpose of this study is to gain physical understanding of these results by a series of less general but simpler consistent analytical models, from which concise formulae describing propagation can be obtained. These models include: (A) the lumped mass–spring model; (B) the oscillator with delayed moving boundary model; and (C), the high frequency transmission model. A complete account of each model is found in the Appendices.

Since the first propagation zone (PZ1) of the weakly coupled periodic stack is paramount in propagation, the first simplified Model (A) termed "lumped mass–spring chain"

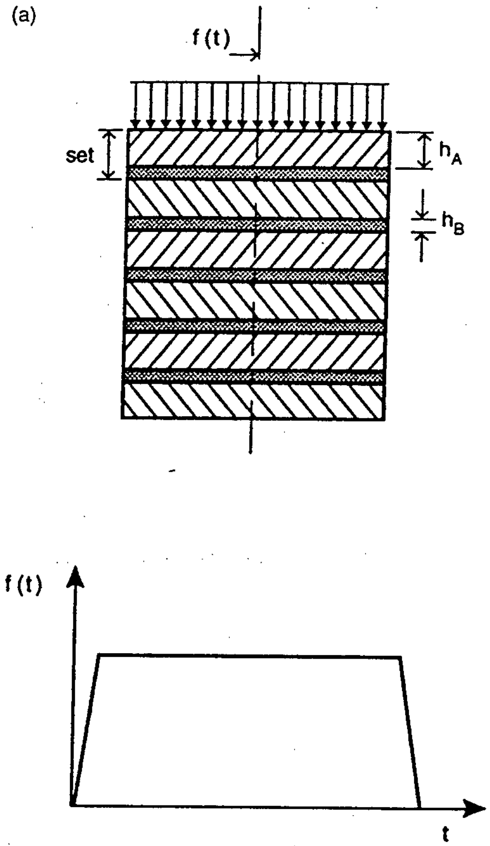

Fig. 1. (a) Geometry of periodic stack and trapezoidal forcing pulse. (b) Histories of u (microns) and σ at interface of sets along the basic stack with $m_s = 20$, $\mathscr{I} = 1.034$, trapezoidal pulse with $t_f = 20$ μs. (*Continued opposite.*)

reduces the continuum to a finite number of identical masses connected by weak springs where each hard layer acts as rigid mass and each weak layer acts as a massless spring. Results from this model re-confirm the importance of PZ1 on transient response and yield simple expressions for phase and group velocities c_p and c_g in PZ1 in terms of properties of hard and weak layers. Furthermore, an integral of the dynamic equations of motion of each set yields a conservation law relating maximum stress of first arrival to width of the trapezoidal forcing pulse and period of the primary stress wave prior to reflections. Indeed, this is identical to the scaling law derived in El-Raheb (1993) relating peak stress of first arrival to frequency interval of PZ1 and width of the trapezoidal forcing pulse. Model (A) also explains distribution of peak stress of first arrival within a hard layer and location of its minimum along the layer.

The almost exact match of response histories from Model (A) and the modal solution in El-Raheb (1993) suggests one more level of simplification and Model (B) termed "the delayed moving boundary", which confines itself to a single mass and a single spring of Model (A) but with the spring connected to a base duplicating a delayed motion of the mass (see Fig. 10(a)). The hypothesis behind this model is that the wave front moves along the stack at the transient phase velocity in PZ1. This means that a pulse produced on top of a set arrives at the interface between one set and the adjacent set after a time delay equaling the thickness of the periodic set divided by transient phase velocity. Since the phase velocity derived in Model (A) is frequency dependent and the resonant frequency of a mass–spring set is the dominant frequency in the dispersed pulse, phase velocity is then evaluated at that frequency, which equals half the frequency interval in PZ1. Results of this model agree closely with results of Model (A). In this way, propagation in a weakly coupled periodic stack is reduced to its simplest constituents, namely frequency of the set and phase

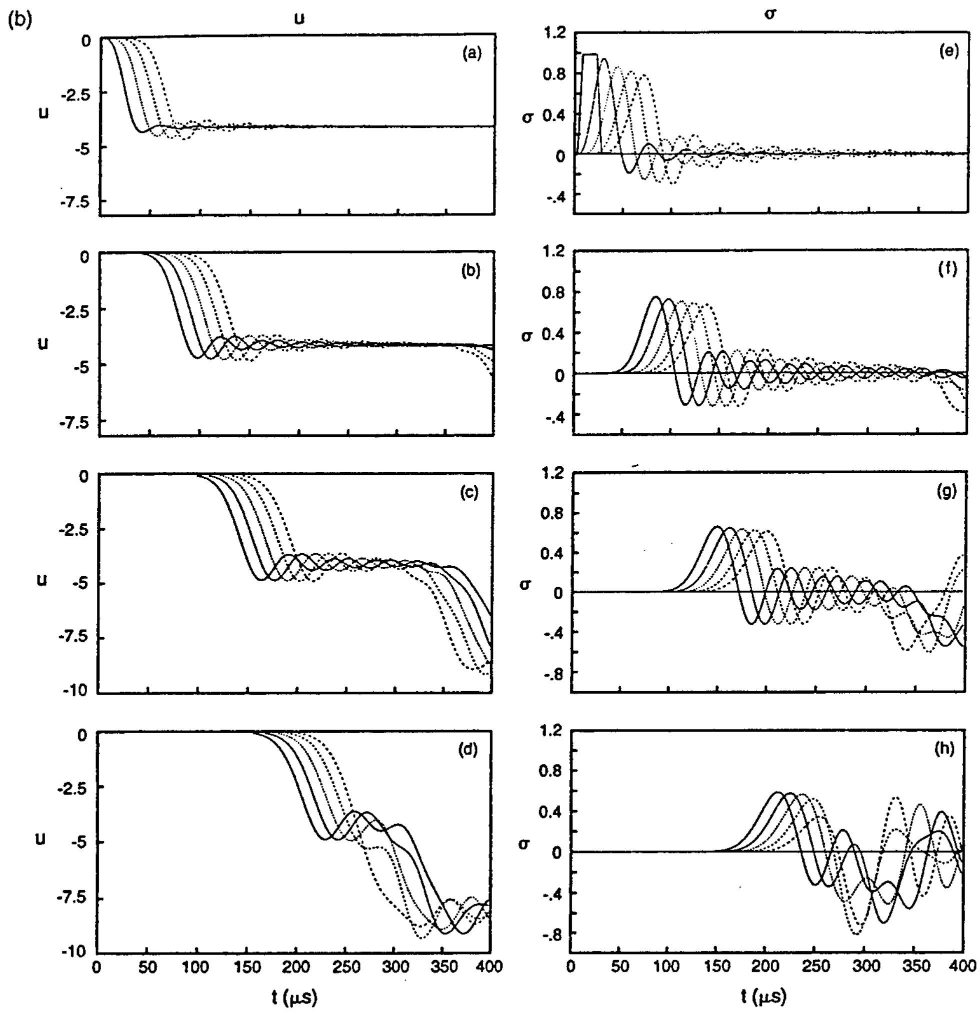

Fig. 1—*Continued.*

velocity evaluated at that frequency. This Model also shows that rate of attenuation of peak stress of first arrival along the stack is proportional to arrival time to the power $-1/3$.

As explained in El-Raheb (1993), the second propagation zone PZ2 modulates response by high frequency from elastic resonances of the hard layer. The third Model (C), termed "transmission of elastic frequencies of the hard layer", relies on analysis of a single set including elasticity of the hard layer. It identifies the two parameters controlling high frequency transmission as rise time of the forcing pulse and dynamic stiffness of the periodic set. Furthermore, a simplified expression for stress response shows that if the period of elastic resonance of the hard layer equals rise time of the forcing pulse, high frequency is suppressed.

Section 2 reviews results of El-Raheb (1993) and summarizes important features of transient uniaxial propagation in a finite periodic stack. Section 3 derives Model A of the finite lumped mass–spring chain. Section 4 derives Model B. Section 5 derives Model C.

2. REVIEW OF RESULTS IN EL-RAHEB (1993)

The following lists results in El-Raheb (1993), each accompanied by a brief explanation or extension obtained by the present analysis:

1. In weakly coupled bi-periodic uniaxial stacks (see Fig. 1(a)), frequency response is divided into propagation zones PZ and attenuation zones AZ similar to pass and stop

bands in a filter. It was observed that the first propagation zone PZ1 is paramount. In fact, motions in PZ1 are those of a finite rigid mass–spring chain.

2. At a fixed point along the stack, peak stress response prior to reflections from an external boundary is termed peak stress of first arrival, σ^1_{mx}. In El-Raheb (1993), a non-dimensional parameter, transmissibility $\mathcal{J}$, was derived that scales and controls σ^1_{mx}. Wave transmissibility is defined as $\mathcal{J} = \Delta\omega_{PZ1}t_f/\pi$ where $\Delta\omega_{PZ1}$ is the frequency interval of PZ1 and t_f is the time interval of the equivalent rectangular forcing function that conserves impulse. In a stack of bi-periodic sets made of two materials A and B, $\Delta\omega_{PZ1} \simeq 2c_A/[h_A(\tilde{z}\tilde{\tau})^{1/2}]$ where $c_{A,B}$ is the speed of sound, $\rho_{A,B}$ is density, $h_{A,B}$ is thickness in layers A and B, $\tilde{z} = (\rho_A c_A)/(\rho_B c_B)$ is ratio of acoustic impedances, and $\tilde{\tau} = (h_B c_A)/(h_A c_B)$ is ratio of travel times. When $\mathcal{J} < 1$, σ^1_{mx} is attenuated, while when $\mathcal{J} > 1$, σ^1_{mx} is initially magnified, reaching a maximum and then attenuating along the stack. These results, as well as a relation between σ^1_{mx} and $\mathcal{J}$ are obtained by the mass–spring chain description in a conservation form.
3. In the hard layer, σ^1_{mx} is larger at the interfaces than within. A caustic generated by the envelope of the instantaneous linear stress distributions is obtained based on the mass–spring chain description that shows a minimum of σ^1_{mx} occuring at $0.6h_A$.
4. An expression was obtained for maximum phase velocity c_0 in the limit when frequency ω is zero. This expression is extended using the mass–spring chain description to a Taylor's series expansion of both phase velocity c_p and group velocity c_g in terms only of even powers of the frequency parameter $(\omega h_s/c_0)$ where $h_s = h_A + h_B$ is the thickness of a periodic set. The ratios c_p/c_0 and c_g/c_0 are insensitive to $\mathcal{J}$.
5. When σ^1_{mx} attenuates along the stack, it does so monotonically. The asymptotic behavior of σ^1_{mx} in terms of arrival time of the wave front t_p is obtained by the delayed moving base model.
6. High frequency oscillations H.F. are enhanced or suppressed depending on stack configuration. By treating the hard layer as an elastic body reacted by the spring of the weak layer, an expression for H.F. response is derived in terms of the fundamental elastic resonant frequency of the hard layer and rise time of the forcing pulse. Also derived is an expression for dynamic stiffness which controls H.F. amplitude.

In the sections to follow, the observations listed above will be tested, explained or expanded upon following the same order as the introduction. Unless otherwise indicated, the same test case will be used in examining the simplified models as in El-Raheb (1993). By generating and displaying again the results of El-Raheb (1993) as well as results of the simplified models, it is assured that they faithfully reproduce the observation to be explained.

From El-Raheb (1993), the properties of the basic stack (see Fig. 1(a)) with 20 biperiodic sets ($m_s = 20$) are:

$$h_A = 1.245\,\text{cm}; \quad h_B = 0.025\,\text{cm}$$

$$E_A = 320\,\text{GPa}; \quad E_B = 69\,\text{MPa}$$

$$\rho_A = 3.25\,\text{g/cm}^3; \quad \rho_B = 1.07\,\text{g/cm}^3.$$

The trapezoidal forcing function is of unit intensity, with 5 μs rise and fall times, and a 15 μs plateau (see Fig. 1(a)). The highest propagation zone in the modal expansion includes the second elastic resonance of the hard layer. For the basic stack this translates to a frequency of 800 kHz.

3. LUMPED MASS–SPRING CHAIN

In Fig. 1(b) there appears histories of displacement u and stress σ at the interfaces between layers in the stack. Each box groups histories at five consecutive interfaces. At each interface, u rises smoothly reaching a plateau after the forcing function elapses. The plateau is disrupted by the reflected wave from the farthest set, $n = 20$. The behavior of succeeding sets is shifted in time by an interval $t_d^{(n)} = nh_s/c_p$ where n is set number. These states of motion are typical of transient waves of rigid masses coupled by weak springs, showing that the response is largely determined by PZ1 (see Appendix A). The results from the method in El-Raheb (1993) and Model A are indistinguishable in this figure, which confirms the adequacy of restricting the continuum model to PZ1. The effects of dispersion, namely attenuation in σ^1_{mx} and growth in trailing oscillations are clear from Fig. 1(b), graphs (e)–(h). As the wave front moves further into the stack, $\partial\sigma/\partial t$ decreases, the pulse becomes wider, and σ^1_{mx} attenuates to conserve linear momentum.

In Appendix A, the mass–spring chain description is developed. With the hypothesis that prior to reflection from an external boundary, displacement histories at interfaces of a layer tend to quiescence, the following form of conservation of momentum is derived:

$$\int_0^{t_L} \sigma_1 \, dt = I_p$$

$$\int_0^{t_L} \sigma_i \, dt = \int_0^{t_L} \sigma_{i-1} \, dt = I_p \tag{A14}$$

where σ_i is stress in the ith spring, t_L is time for quiescence and I_p is impulse. Furthermore, approximating the shape of the dispersed stress wave at the first interface by

$$\sigma_1(t) \simeq \frac{1}{2}\sigma^1_{mx}\left[1-\cos\left(2\pi\frac{t}{T}\right)\right], \quad t \leqslant T \tag{1}$$

where T is the period of the primary wave, and substituting (1) in (A14) with $t_L = T$ yields

$$\sigma^1_{mx}\frac{T}{2} = \sigma_0 t_f = I_p$$

$$\Rightarrow \tilde{\sigma}^1_{mx} \equiv \sigma^1_{mx}/\sigma_0 = 2t_f/T \tag{2}$$

where t_f is the width of the equivalent rectangular forcing pulse delivering I_p. The period T of the primary stress wave depends on the relative magnitude of $2t_f$ and π/ω_e where ω_e is the resonant frequency of the mass–spring set:

$$T \cong \max\,[2t_f, \pi/\omega_e] \tag{3}$$

when $2t_f \leqslant \pi/\omega_e$, $\tilde{\sigma}^1_{mx} \simeq 2\omega_e t_f/\pi = \mathscr{I}$. When $t_f > \pi/\omega_e$, $\tilde{\sigma}^1_{mx} \cong 1$. Therefore, if $\mathscr{I} < 1$, $\tilde{\sigma}^1_{mx} < 1$, and only if $\mathscr{I} > 1$ can $\tilde{\sigma}^1_{mx}$ exceed unity, which was the conclusion also reached in El-Raheb (1993).

In Fig. 2 there appears histories of σ for the basic stack along the first three hard layers. Histories at six equidistant stations in each layer including the interfaces are grouped. Figure 2(a) shows how σ evolves along the first layer from the trapezoidal shape at the excited face, to the dispersed shape at the interface with the weak layer. In each of the following hard layers (see Fig. 2(b), (c)) histories at the different stations in a layer cross at the point where σ^1_{mx} is minimum. This fact, not obvious before the results were obtained and plotted, requires explanation. Consider the distribution of modal stress in a hard layer given by the transfer matrix in eqn (2) of El-Raheb (1993):

$$u_x = \cos(k_A x)u_L + (1/k_A E_A)\sin(k_A x)\sigma_L \tag{4a}$$

$$\sigma_x = -k_A E_A \sin(k_A x)u_L + \cos(k_A x)\sigma_L \tag{4b}$$

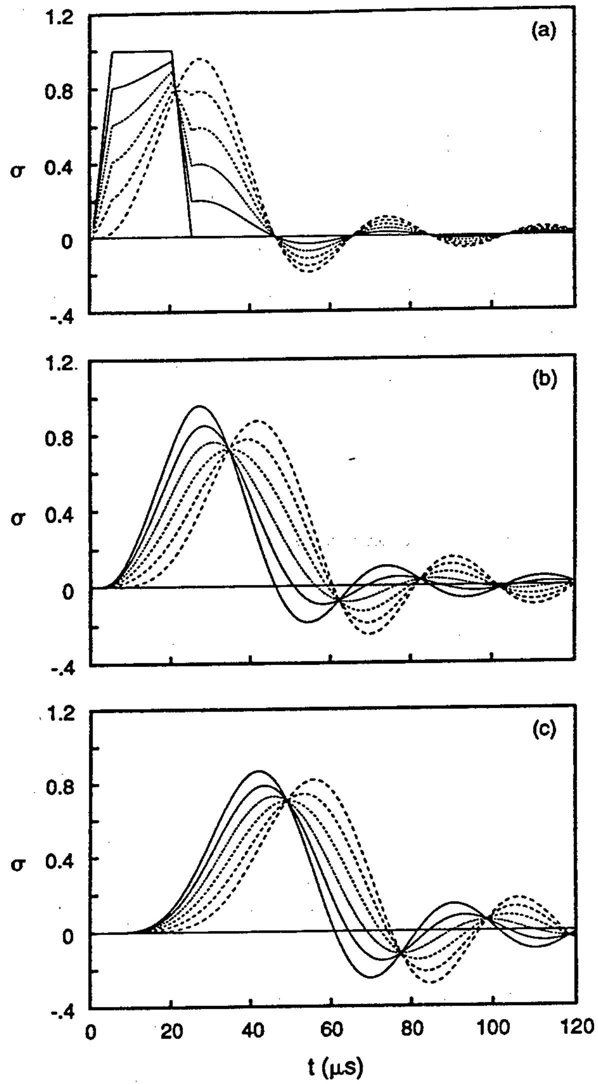

Fig. 2. Histories of σ within each of the first 3 sets of the basic stack with $m_s = 20$, $\mathscr{I} = 1.034$, $t_f = 20$ μs.

where subscripts L and x denote quantities at the left boundary and at station x along the layer, and $k_A = \omega/c_A$. For modes in PZ1:

$$k_A x \leqslant \frac{\Delta\omega_{\mathrm{PZ1}} x}{c_A} \simeq \frac{2x}{h_A}(\bar{z}\bar{\tau})^{-1/2} < 0(1). \tag{5}$$

Expanding $\sin(k_A x)$ and $\cos(k_A x)$ in (4b) for small $(k_A x)$ yields

$$\sigma_x \cong -\omega^2 \rho_A u_L x + \sigma_L. \tag{6}$$

Equation (6) shows that in PZ1, modal stress is linear with x. Since transient stress is the superposition of modal stresses, it too is linear with x.

Figure 3(a)–(d) traces the time evolution of σ within one particular hard layer. Each line corresponds to a σ distribution at some fixed time t. The caustic generated by the envelope of these lines coincides with σ^1_{mx}. The results are shown for four different stacks within the range of $0.478 \leqslant \mathscr{I} \leqslant 1.551$. It is clear in every case that σ^1_{mx} is minimum at $x/h_A = 0.6$. From Fig. 4 showing caustics in the three hard layers following the first for

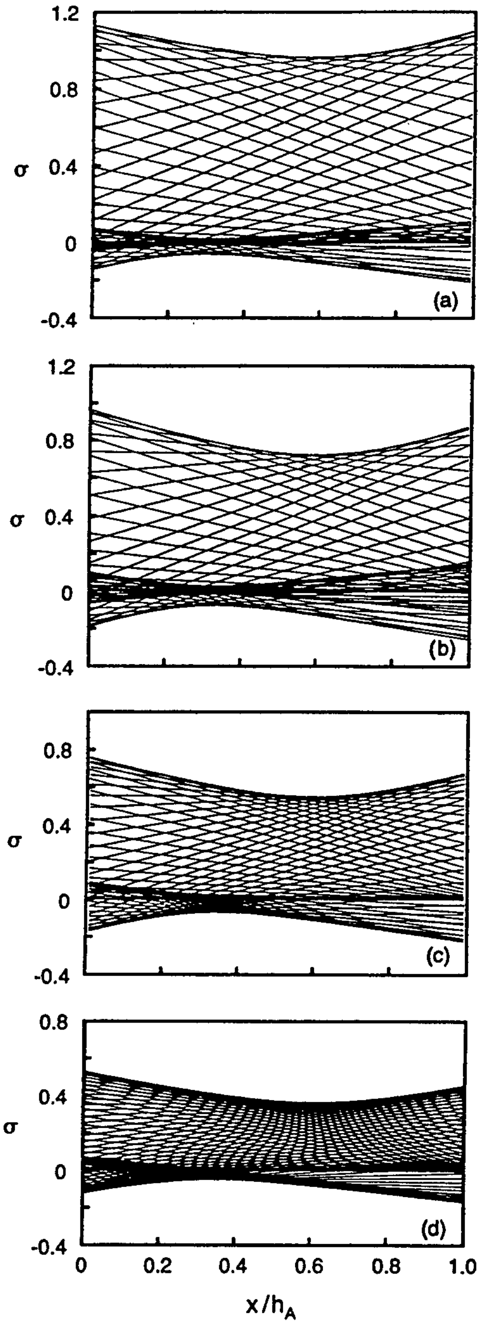

Fig. 3. Distribution of a σ along 2nd hard layer with t as parameter and formation of caustic (a) $\mathscr{I} = 1.551$, (b) $\mathscr{I} = 1.034$, (c) $\mathscr{I} = 0.738$, (d) $\mathscr{I} = 0.478$.

each of the four values of $\mathscr{I}$, it becomes clear that this is true also independent of $\tilde{z}$, $\tilde{\tau}$ and t_f.

The parametric equation of the caustic may be determined from (6) using

$$\sigma(x,t) = (\sigma_R(t) - \sigma_L(t))\frac{x}{h_A} + \sigma_L(t) \tag{7}$$

where subscripts L and R denote quantities at left and right of a layer. If $x_c(t)$ is the local

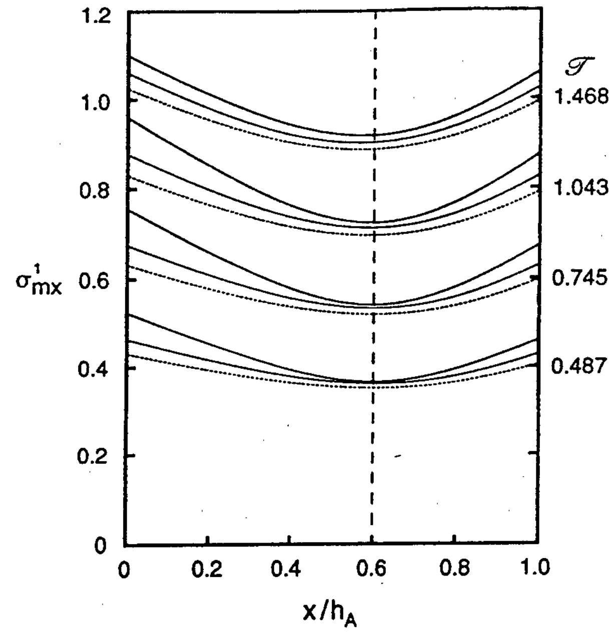

Fig. 4. Distribution of peak stress of first arrival σ^1_{mx} within sets 2 —, 3 ···, 4 --- for different $\mathscr{T}$ values.

axial coordinate at a point on the caustic, holding x fixed, then finding the extrema of the function in (7) yields $(x_c, \sigma_c(x_c))$:

$$\frac{x_c}{h_A} = -\frac{\dot{\sigma}_L}{(\dot{\sigma}_R - \dot{\sigma}_L)} \tag{8}$$

where $(\dot{\ })$ is time derivative. Substituting (8) in (7) gives σ_c at x_c:

$$\sigma_c = -\frac{(\sigma_R - \sigma_L)}{(\dot{\sigma}_R - \dot{\sigma}_L)}\dot{\sigma}_L + \sigma_L = \sigma^1_{mx}(t). \tag{9}$$

Then σ_c is an extremum at the x_c where

$$\frac{\partial \sigma_c}{\partial x_c} = 0 \Rightarrow \frac{\dot{\sigma}}{\dot{x}_c} \equiv \frac{\sigma_R - \sigma_L}{h_A} = 0. \tag{10}$$

Clearly, the minimum occurs at some $t = t_{mn}$ when $\sigma_R(t_{mn}) = \sigma_L(t_{mn})$

$$\sigma_{cmn} = \sigma_L(t_{mn}) = \sigma_R(t_{mn})$$

$$\frac{x_{cmn}}{h_A} = -\left.\frac{\dot{\sigma}_L}{(\dot{\sigma}_R - \dot{\sigma}_L)}\right|_{t=t_{mn}}. \tag{11a}$$

This implies that σ^1_{mx} achieves a minimum within a hard layer when stress is uniform throughout that layer, and confirms that all stress histories cross at t_{mn}. That $x_{cmn}/h_A = 0.6$ implies that instantaneously at $t = t_{mn}$, the σ line rotates about x_{cmn} yielding

$$\dot{\sigma}_R(t_{mn}) = -\tfrac{2}{3}\dot{\sigma}_L(t_{mn}). \tag{11b}$$

From eqn (20) in El-Raheb (1993), the exact expression for propagation constant μ is:

$$\cos\mu = -\frac{1+\tilde{z}^2}{2\tilde{z}}\sin\gamma\sin(\gamma\tilde{\tau})+\cos\gamma\cos(\gamma\tilde{\tau}) \equiv \Gamma \tag{12}$$

where $\gamma = \omega h_A/c_A$. By definition

$$c_p = \frac{\omega}{k} = \frac{\omega h_s}{\mu} = \frac{\omega h_s}{\cos^{-1}(\Gamma)} \tag{13}$$

$$c_g = \frac{\partial\omega}{\partial k} = \frac{h_s c_A}{h_A}\sin\mu\left\{\frac{1+\tilde{z}^2}{2\tilde{z}}[\cos\gamma\sin(\gamma\tilde{\tau})+\tilde{\tau}\sin\gamma\cos(\gamma\tilde{\tau})] + \sin\gamma\cos(\gamma\tilde{\tau})+\tilde{\tau}\cos\gamma\sin(\gamma\tilde{\tau})\right\}^{-1}. \tag{14}$$

In PZ1, $\gamma \leqslant 2(\tilde{z}\tilde{\tau})^{-1/2} < 0(1)$. Expanding (12) for small γ then substituting in (13) and (14) yields

$$c_p \simeq c_0[1-v_2\gamma_p^2 - v_4\gamma_p^4 + 0(\gamma_p^6)] \tag{15a}$$

$$c_g \simeq c_0[1-3v_2\gamma_p^2 - 3v_4\gamma_p^4 + 0(\gamma_p^6)] \tag{15b}$$

where

$$\gamma_p = \frac{\omega h_s}{c_0} = \frac{\omega}{\omega_e} = \frac{2\omega}{\Delta\omega_{\mathrm{PZ1}}} = 2\tilde{\omega}, \quad c_0 = c_A\frac{h_s}{h_A}\left[\tilde{\tau}\frac{1+\tilde{z}^2}{\tilde{z}}+1+\tilde{\tau}^2\right]^{-1/2}$$

$$v_2 = [-2(1+\tilde{\tau}^2)+\tilde{\tau}\tilde{z}]/(24\tilde{\tau}\tilde{z})$$

$$v_4 = [17(\tilde{\tau}\tilde{z})^2 - 20(\tilde{\tau}\tilde{z}+3)(1+\tilde{\tau}^2) - 120\tilde{\tau}^2]/5760(\tilde{\tau}\tilde{z})^2.$$

For $\tilde{\tau} = 0(1)$ and large $(\tilde{\tau}\tilde{z})$: $v_2 \simeq 1/24$, $v_4 \simeq 17/5760$. These values duplicate results in Balanis (1975). From (15a, b) it follows that:

$$c_p > c_g$$

$$c_p - c_g \simeq 2v_2 c_0 \gamma_p^2 + 0(\gamma_p^4).$$

This difference between c_p and c_g is responsible for spreading of the pulse since the wave front moves at c_p and σ_{mx}^1 moves at c_g.

The asymptotic expansions (15a, b) motivate using exact expressions for c_p and c_g in plots of (c_p/c_0) and (c_g/c_0) against γ_p, as shown in Fig. (5a), where the range $0 \leqslant \gamma_p \leqslant 2$ is the width of PZ1. Figure 5(b) plots the same quantities against (h_s/λ) where $\lambda = 2\pi/k$ is wave length. The curves in Fig. 5 are indistinguishable for different $\tilde{\tau}$ and $\tilde{z}$ in the range $0.4 \leqslant \mathscr{I} \leqslant 1.5$.

4. OSCILLATOR WITH DELAYED MOVING BOUNDARY

The simplest adequate model will describe how σ_{mx}^1 varies along the stack. It is built in two steps: first, deriving expressions for stress at the first interface; second, determining how σ_{mx}^1 attenuates in following layers. Recall how the displacement history in Fig. 1(b), graph (a) led to the lumped Model A. Motion of the first layer can be approximated by that of single mass–spring oscillator with mass driven by the external force and spring

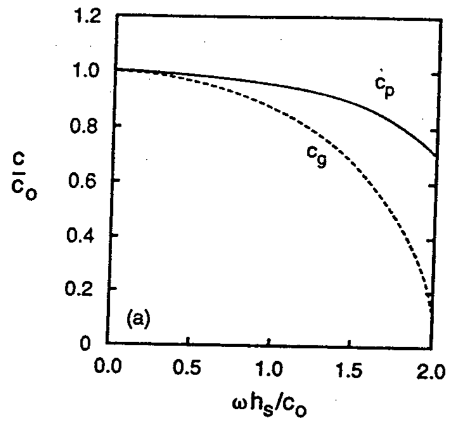

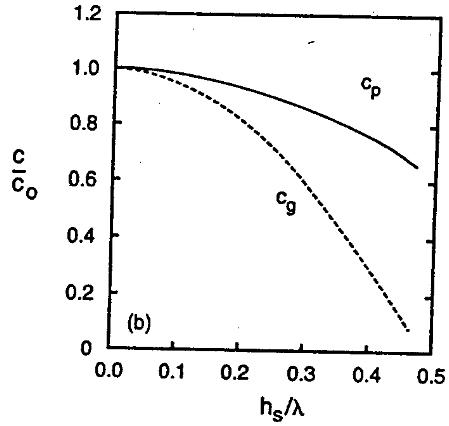

Fig. 5. Phase velocity c_p (—), and group velocity c_g (---), in the first propagation zone.

connected to a moving base. The base displacement is the same as the mass but with a time delay $t_d = c_p(\omega_e)/h_s$ where $c_p(\omega_e)$ is phase velocity evaluated at the frequency of the lumped model, $\omega_e = \frac{1}{2}\Delta\omega_{PZ1}$. Closed-form expressions for u and σ of this new simpler Model B of the oscillator with moving base are derived in Appendix B. The response of succeeding masses can be found by repeating the steps above except that stress in the preceding spring acts as a forcing function and dispersion causes $c_p(\omega_e)$ to rise smoothly to $c_p(0) = c_0$. Figure 6 compares histories of u and σ as predicted by El-Raheb (1993) and Model B. Also in Appendix B is derived an asymptotic value of 1/3 for the attenuation α where $\sigma^1_{mx} \propto t_p^{-\alpha}$, and that $c_p(\omega_e) \leqslant c_p \leqslant c_0$ and $c_g(\omega_e) \leqslant c_g \leqslant c_0$.

Figure 7(a)–(c) shows how σ^1_{mx}, c_σ/c_0 and attenuation index α vary along a 46-set stack for three values of $\mathscr{I}$, where c_σ is the transient group velocity of σ^1_{mx} using the mass–spring description. From Fig. 7(a, b) and for $m = 2$, $c_\sigma/c_0 \simeq 0.85$ which coincides with c_g/c_0 at $\omega = \omega_e$ (i.e., $\omega_e h_s/c_0 = 1$) in Fig. 5(a) and also from eqns (A8) and (A9) yielding $c_g/c_0 = \sqrt{3}/2 = 0.866$. This implies that $c_\sigma \cong c_g(\omega_e)$ where the force acts and c_σ approaches c_0 smoothly as the stress wave disperses. When $\mathscr{I} \leqslant 1$, $\sigma^1_{mx} < 1$ everywhere and α increases with m in the interval $0.21 < \alpha < 0.32$. Note that the asymptotic value of α determined numerically is indeed 1/3. α falls as $\mathscr{I}$ increases, apparent from Fig. 7(c) for $\mathscr{I} = 1.631$ where $0.15 < \alpha < 0.28$.

5. TRANSMISSION OF ELASTIC FREQUENCIES OF THE HARD LAYER

Appendix C derives relations for u and σ in the first hard layer including its high frequency (H.F.) elastic resonances according to Model C. These high frequencies correspond to elastic motions of the hard layer in PZ2. From (C12), H.F. amplitude is proportional to $(\omega_1 t_1)^{-1}$ where ω_1 is fundamental resonance of the hard layer and t_1 is the

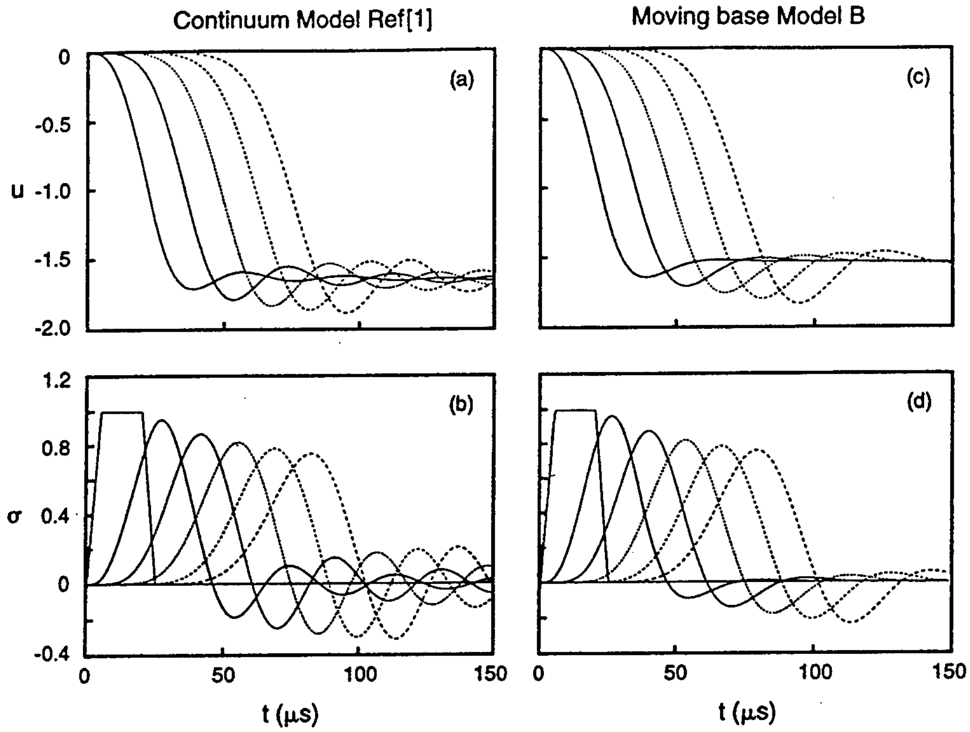

Fig. 6. Histories of u (micro in.) and σ at interface of sets for basic stack with $\mathscr{I} = 1.034$, $t_f = 20$ μs: (a), (b) Continuum Model Ref. [1]; (c), (d) Moving base Model B.

rise time of the trapezoidal pulse. H.F. vanishes if $\omega_1 t_1 = 2j\pi \Rightarrow t_{1s} = j/\Omega_1$. For illustration, return to the case treated in Fig. 2, termed stack I, where $\Omega_1 = 398.2$ kHz and $t_{1s} = j/\Omega_1 = (j)$ 2.5 μs. Clearly, these histories exhibit no H.F. because $t_1 = 5$ μs $= (2) \times 2.5$ μs $= t_{1s}$. Figures 8 and 9 were computed by the method of El-Raheb (1993). In Fig. 8(a)–(f) there appears σ histories in the first two hard layers for $t_1 = 4$ μs, 5 μs and 6 μs. Pulse width has been adjusted to keep t_f at 20 μs. Results for $t_1 = 4$ μs and 6 μs exhibit H.F. The effects are larger for $t_1 = 4$ μs (compare Fig. 8(a) to 8(c)). Figure 8(b), (f) show that H. F. in the second hard layer diminishes. These histories are repeated in Fig. 9(a)–(f) for stack II with $(h_A, h_B) = (0.45, 0.05)$ and unchanged material properties for $t_1 = 3$ μs, 4.6 μs, and 6 μs. For stack II; $\Omega_1 = 433.6$ kHz and $t_{1s} = j/\Omega_1 = (j)$ 2.3 μs. Thus, by the choice $t_1 = 4.6$ μs, the response in Fig. 9(c), (d) becomes free of H.F. Results for $t_1 = 3$ μs and 6 μs exhibit H.F. and the effect is larger for $t_1 = 3$ μs (compare Fig. 9(a) to 9(e)).

Dynamic stiffness of the weak layer determines the nature of transmission of H.F. in hard layers below the first. Except for PZ1, propagation zones belong to one of two types. The first type includes clusters of m_s frequencies centered at a resonance of the unconstrained hard layer $\Omega_{Aj} = jc_A/2h_A$. The second type includes clusters of $(m_s - 1)$ frequencies centered at a resonance of the unconstrained weak layer $\Omega_{Bj} = jc_B/2h_B$. To derive the dynamic spring stiffness k_{Bd} of the weak layer as an extension to Model C by including its inertia, using eqns 4(a), (b), evaluate σ_x, u_x at $x = h_B$, set $u_L = 0$ because the weak layer is assumed fixed to a stationary base as in Model C, and eliminate σ_L:

$$\sigma_x = k_{Bd} u_x$$

$$k_{Bd} = \frac{E_B}{h_B} \gamma_B \cot \gamma_B$$

$$\gamma_B = \frac{2\pi\Omega h_B}{c_B} = \frac{\pi\Omega}{\Omega_{B1}} \tag{16}$$

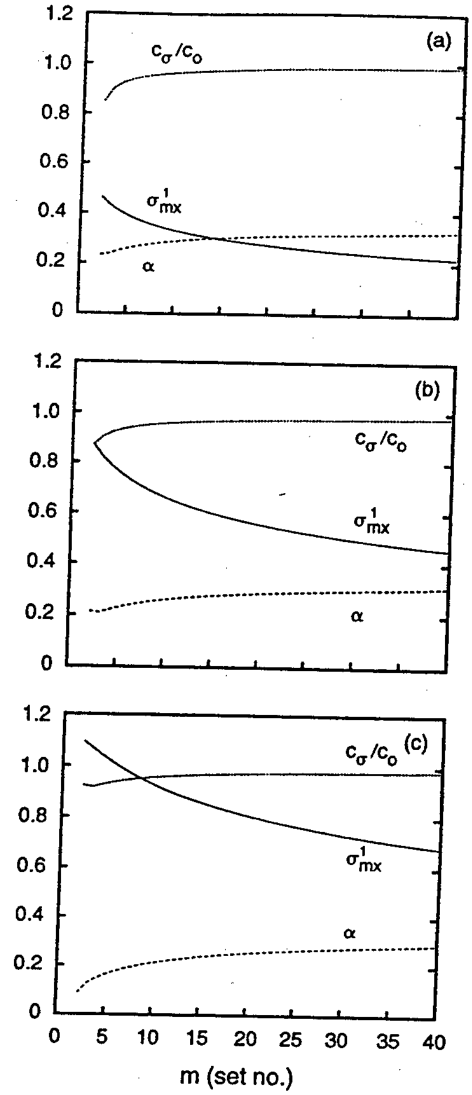

Fig. 7. Variation of σ^1_{mx}, c_σ/c_0 and α along stack with $m_s = 48$, (a) $\mathscr{I} = 0.484$, (b) $\mathscr{I} = 1.040$, (c) $\mathscr{I} = 1.631$.

where Ω is circular frequency of excitation. In PZ1

$$\Omega \ll \Omega_{B1} \Rightarrow \gamma_B \ll 1 \Rightarrow \gamma_B \cot \gamma_B \simeq 1$$
$$\Rightarrow k_{Bd} \simeq E_B/h_B$$

recovering the purely spring stiffness in Model C. In a PZ centered at Ω_{A1}

$$k_{Bd} = \frac{E_B}{h_B}\left(\pi \frac{\Omega_{A1}}{\Omega_{B1}}\right)\cot\left(\pi \frac{\Omega_{A1}}{\Omega_{B1}}\right).$$

As k_{Bd} increases, so does transmission, while amplitude of H.F. diminishes. As k_{Bd} decreases, so does transmission, while amplitude of H.F. intensifies and becomes confined to the first layer. For stack I, $\Omega_{A1} = 398.2$ kHz and $\Omega_{B1} = 500$ kHz producing a $(k_{Bd})_{\text{I}} = 336.3\ E_B$. For stack II, $\Omega_{A1} = 433.6$ kHz and $\Omega_{B1} = 100$ kHz producing a $(k_{Bd})_{\text{II}} = 154.3\ E_B$. Comparing amplitude of H.F. in Fig. 8(a), (b) and Fig. 9(a), (b) shows that stack II is almost twice stack I, consistent with the ratio $(k_{Bd})_{\text{I}}/(k_{Bd})_{\text{II}} \cong 2.2$.

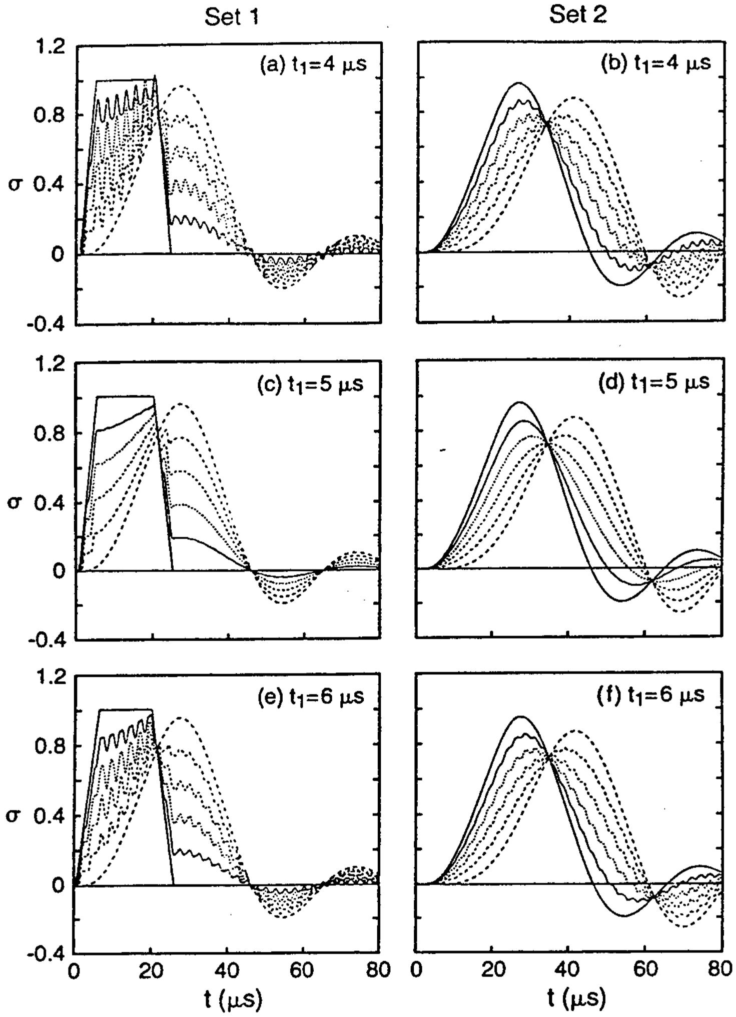

Fig. 8. Histories of σ in the first two sets of stack I with $(h_A, h_B) = (0.49, 0.01)$, $t_f = 20\ \mu s$, $\mathscr{I} = 1.034$: (a), (b) $t_1 = 4\ \mu s$; (c), (d) $t_1 = 5\ \mu s$; (e), (f) $t_1 = 6\ \mu s$.

6. CONCLUSION

Some insights into uniaxial transient waves in weakly coupled periodic stacks are captured by examining a series of simplified analytical models suitably modified to include periodicity and coupling. These models provide accurate description and insights into the mechanics of propagation and interpretation of experimental results. They also provide concise formulas helpful in the design of impact resistant structures by judicious attenuation along the stack of the forcing pulse. Noteworthy results are:

(1) A lumped mass–spring model, Model A, demonstrates that PZ1 dominates response and reduces the governing equations to conservation form. It also establishes transmissibility $\mathscr{I}$ as a scaling parameter.

(2) Model B, a single mass–spring oscillator with delayed moving base, captures the main features of propagation using the dynamic properties of a single set and phase velocity evaluated as its natural frequency, and provides simple expressions for stress at the first interface.

(3) Within a hard layer, peak stress of first arrival σ^1_{mx} achieves a minimum at 0.6 h_A. The phenomenon can be viewed as instantaneous stress lines intersecting to form a caustic surface.

(4) Asymptotic expansions for phase and group velocities c_p and c_g are derived in terms of even powers of frequency parameters $(\omega h_s/c_0)$. The expansions demonstrate that $c_p > c_g$ for all ω in PZ1 and that $(\Delta\omega_{PZ1}h_s)/c_0 \cong 2$. Simpler expressions for c_p and c_g

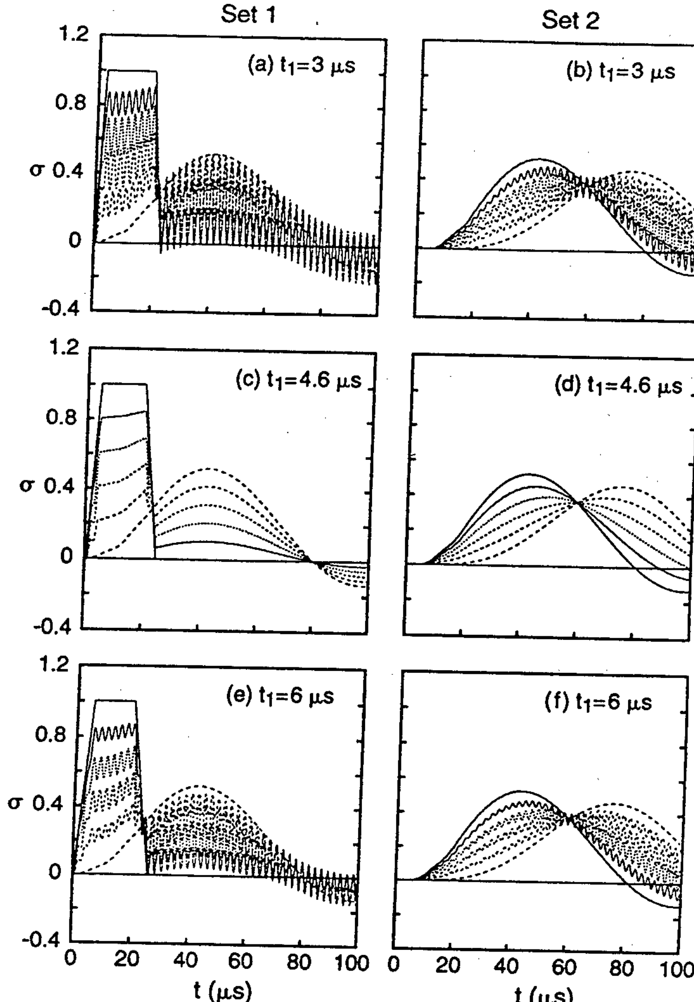

Fig. 9. Histories of σ in the first two sets of stack II with $(h_A, h_B) = (0.45, 0.05)$, $t_f = 20\ \mu s$, $\mathscr{I} = 0.478$: (a), (b) $t_1 = 3\ \mu s$; (c), (d) $t_1 = 4.6\ \mu s$; (e), (f) $t_1 = 6\ \mu s$.

produced by Model A demonstrate that $c_p(\omega_e) \leqslant c_p \leqslant c_0$ and $c_g(\omega_e) \leqslant c_g \leqslant c_0$ where ω_e is frequency of the periodic set.

(5) The attenuation index α, defined by $\sigma^1_{mx} \propto t_p^{-\alpha}$, rises smoothly and slowly along the stack with an asymptote at $\alpha = 1/3$, where t_p is the arrival time of σ^1_{mx}.

(6) Transmission of H.F. into the succeeding hard layers depends on dynamic stiffness of the weak layer k_{Bd} and rise time t_1. Transmission is suppressed for the special cases when $\omega_1 t_1 = 2\pi j$, where ω_1 is elastic axial resonant frequency of the hard layer.

Acknowledgement—The author appreciates Pat Dougherty for her patience and accuracy in typing the manuscript.

REFERENCES

Anderson, D. L. (1961) Elastic wave propagation in layered anisotropic media. *Journal of Geophysical Research* **66**, 2953–2963.

Balanis, G. (1975) Analysis of the dispersion of low frequency uniaxial waves in heterogeneous periodic elastic media. *Journal of Mathematical Physics* **16**, 1383–1387.

Braga, A. M. B. (1990) Wave propagation in anisotropic layered composites. Ph.D. dissertation, Stanford University, Palo Alto, California.

Chao, T. and Lee, P. C. Y. (1975) Discrete-continuum theory for periodically layered composite materials. *Journal of the Acoustical Society of America* **57**, 78–88.

Delph, T. J., Herrmann, G. and Kaul, R. K. (1978) Harmonic wave propagation in a periodically layered infinite elastic body: antiplane strain. *Journal of Applied Mechanics* **45**, 343–349.

Delph, T. J., Herrmann, G. and Kaul, R. K. (1979) Harmonic wave propagation in a periodically layered infinite elastic body: plane strain, analytical results. *Journal of Applied Mechanics* **46**, 113–119.

Delph, T. J., Herrmann, G. and Kaul, R. K. (1980) Harmonic wave propagation in a periodically layered infinite elastic body: plane strain, numerical results. *Journal of Applied Mechanics* **47**, 531–537.

El-Raheb, M. (1993) Transient elastic waves in finite layered media: One-dimensional analysis. *Journal of the Acoustical Society of America* **94**, 172–184.

Engels, R. C. and Meirovitch, L. (1978) Response of periodic structures by modal analysis. *Journal of Sound and Vibration* **56**, 481–493.

Faulkner, M. G. and Hong, D. P. (1985) Free vibrations of a mon-coupled periodic systems. *Journal of Sound and Vibration* **99**, 29–42.

Golebiewska, A. A. (1980) On dispersion of periodically layered composites in plane strain. *Journal of Applied Mechanics* **47**, 206–207.

Gradshteyn, I. and Ryzhik, I. (1970) *Table of Integrals, Series and Products*. Academic Press, New York.

Gupta, Sen G. (1980) Vibration of periodic structures. *The Shock and Vibration Digest* **12**(3), 17–29.

Haskel, N. A. (1953) The dispersion of surfaced waves in multi-layered media. *Bulletin of the Seismic Society of America* **43**, 17–34.

Herrmann, G. and Hemami, M. (1982) Plane-strain surface waves in a laminated composite. *Journal of Applied Mechanics* **49**, 747–753.

Keane, A. J. and Price, W. G. (1989) On the vibrations of mono-coupled periodic and near-periodic structures. *Journal of Sound and Vibration* **128**, 423–450.

Kundu, T. and Mal, A. K. (1985) Elastic waves in a multilayered solid due to a dislocation source. *Wave Motion* **7**, 459–471.

Lee, E. H. and Yang, W. H. (1973) On waves in composite materials with periodic structure. *SIAM Journal of Applied Mathematics* **25**, 492–488.

Mal, A. K. (1988) Wave propagation in layered composite laminates under periodic surface loads. *Wave Motion* **10**, 257–266.

McDaniel, T. J. and Carroll, M. J. (1982) Dynamics of biperiodic structures. *Journal of Sound and Vibration* **81**, 311–335.

Mead, D. J. (1971) Vibration response and wave propagation in periodic structures. *Journal of Engineering for Industry* **93**, 783–792.

Mead, D. J. (1975) Wave propagation and natural modes in periodic systems, I: mono-coupled systems. *Journal of Sound and Vibration* **40**, 1–18.

Mead, D. J. (1975) Wave propagation and natural modes in periodic systems, II: multi-coupled systems with and without damping. *Journal of Sound and Vibration* **40**, 19–39.

Mead, D. J. (1986) A new method of analyzing wave propagation in periodic structures: applications to periodic Timoshenko beams and stiffened plates. *Journal of Sound and Vibration* **104**, 9–27.

Mead, D. J. and Bansal, A. S. (1978) Free wave propagation and response to convected loadings. *Journal of Sound and Vibration* **61**, 481–515.

Mead, D. J. and Lee, S. M. (1984) Receptance methods and the dynamics of disordered one-dimensional lattices. *Journal of Sound and Vibration* **92**, 427–445.

Robinson, C. W. (1972) Shear waves in layered composites. *Report SCL-RR*-720351, Sandia National Laboratories, Albuquerque, U.S.A.

Rousseau, M. (1989) Floquet wave properties in a periodically layered medium. *Journal of the Acoustical Society of America* **86**, 2369–2376.

Rytov, S. M. (1956) Acoustical properties of a thinly laminated medium. *Soviet Physics-Acoustics* **2**, 68–70.

Shah, A. H. and Datta, S. K. (1982) Harmonic waves in a periodically laminated medium. *International Journal of Solids and Structures* **18**, 301–317.

Sun, C. T., Achenbach, J. D. and Herrmann, G. (1968) Time harmonic waves in a stratified medium, propagating in the direction of the layering. *Journal of Applied Mechanics* **35**, 408–411.

Tenenbaum, R. A. and Zindeluk, M. (1992) An exact solution for the one-dimensional elastic wave equation in layered media. *Journal of the Acoustical Society of America* **92**, 3364–3370.

Thomson, W. (1950) Transmission of elastic waves through a stratified medium. *Journal of Applied Physics* **21**, 89–93.

Wang, Y. Y. and Lee, K. H. (1973) Propagation of a disturbance in a chain of interacting harmonic oscillators. *American Journal of Physics* **41**, 51–54.

Whitham, G. B. (1973) *Linear and Nonlinear Waves*. Wiley, New York.

APPENDIX A: MODEL A: FINITE MASS–SPRING CHAIN

As an approximation to the continuum bi-periodic system including m_s hard layers of material A, bonded by $(m_s - 1)$ weak layers of material B, consider the following lumped mass–spring system consisting of m_s masses "m_e" connected by $(m_s - 1)$ springs with stiffness "k_e".

$$
\begin{aligned}
m_e &= \rho_A h_A + \rho_B h_B \\
k_e &= (h_A/E_A + h_B/E_B)^{-1}.
\end{aligned}
\tag{A1}
$$

In terms of axial displacement u_i of each mass i, the equations of motion are

$$
\begin{aligned}
&\ddot{u}_1 + \omega_e^2(u_1 - u_2) = F(t)/m_e \\
&\ddot{u}_i + \omega_e^2(2u_i - u_{i-1} - u_{i+1}) = 0; \quad 2 \leqslant i \leqslant (m_s - 1)
\end{aligned}
$$

$$\ddot{u}_{m_s} + \omega_e^2 (u_{m_s} - u_{m_s - 1}) = 0 \tag{A2}$$

where $(\dot{})$ is the time derivative and ω_e is the frequency of the set

$$\omega_e = (k_e/m_e)^{1/2} = \left[\frac{E_B}{\rho_A h_A h_B (1+\bar{z}^{-1})[1+(\bar{z}\bar{\tau})^{-1}]}\right]^{1/2} = \frac{1}{2}\Delta\omega_{PZ1} \tag{A3}$$

where $\Delta\omega_{PZ1}$ is the frequency width of PZ1. The eigenstates are determined by solving

$$\det[\mathbf{K} - \omega^2 \mathbf{I}] = 0$$

$$\mathbf{K} = \omega_e^2 \begin{bmatrix} 1 & -1 & 0 & 0 & \dots & 0 & 0 \\ -1 & 2 & -1 & 0 & \dots & 0 & 0 \\ 0 & -1 & 2 & -1 & \dots & 0 & 0 \\ \vdots & \vdots & \vdots & \vdots & \vdots & \vdots & \vdots \\ 0 & 0 & 0 & 0 & \dots & -1 & 1 \end{bmatrix} \tag{A4}$$

where $\mathbf{I}$ is the unit matrix. By expanding in eigenfunctions

$$\mathbf{u} = \sum_j a_j(t)\Phi_j \tag{A5}$$

in (A2) and by orthogonality of Φ_j a solution for $a_j(t)$ in terms of Duhamel's integral results:

$$a_j(t) = \frac{1}{\omega_j N_j}\int_0^t \Phi_{j1}^T F(\tau)\sin\omega_j(t-\tau)\,\mathrm{d}\tau$$

$$N_j = m_e \Phi_j^T \mathbf{I} \Phi_j \tag{A6}$$

where Φ_{j1} is the first component of the eigenvector Φ_j.

If the system (A2) were infinite in extent, a Floquet solution periodic in time and space would take the form:

$$u_{i+1} = e^{\mu} u_i. \tag{A7}$$

Substituting (A7) in (A2) with $\ddot{u}_i$ replaced by $-\omega^2 u_i$ yields

$$-\omega^2 + 2\omega_e^2(1-\cos\mu) = 0 \Rightarrow \frac{\mu}{2} = \sin^{-1}\left(\frac{\omega}{2\omega_e}\right). \tag{A8}$$

The propagation constraint μ is related to wave number k by $\mu = kh_s$. Expressions for phase and group velocities c_p and c_g have the form:

$$c_p = \frac{\omega}{k} = c_0 \frac{\sin\left(\frac{\mu}{2}\right)}{\frac{\mu}{2}}$$

$$c_g = \frac{\partial\omega}{\partial k} = c_0 \cos\left(\frac{\mu}{2}\right)$$

$$c_0 = \omega_e h_s. \tag{A9}$$

As $\mu \to 0$, c_p and c_g approach c_0. When $\omega = \omega_e$, $\mu/2 = \pi/6$ and by (A9) $c_p = (3/\pi)c_0$ and $c_g = \sqrt{3}/2c_0$. Also, when $\omega = 2\omega_e \simeq \Delta\omega_{PZ1}$, $c_p = 2/\pi c_0$ and $c_g = 0$. In (A9), c_p is velocity of the wave front and c_g is velocity of peak stress σ^1_{mx}. Expressing c_p and c_g in terms of $\bar{\omega} = \omega/(2\omega_e)$ yields:

$$c_p/c_0 = \bar{\omega}/\sin^{-1}(\bar{\omega})$$

$$c_g/c_0 = \cos[\sin^{-1}(\bar{\omega})] = (1-\bar{\omega}^2)^{1/2}. \tag{A10}$$

Both c_p and c_g peak at $\bar{\omega} = 0$ and decrease uniformly with $\bar{\omega}$.

Stress in the ith spring σ_i is given by

$$\sigma_i = k_e(u_i - u_{i-1}). \tag{A11}$$

Substituting (A11) in (A2) yields the relations

$$m_e\ddot{u}_1+\sigma_1 = F(t)$$

$$m_e\ddot{u}_i+\sigma_i = \sigma_{i-1}\,; \quad 2 \leqslant i \leqslant m_s. \tag{A12}$$

Integrating (A12) gives

$$m_e\dot{u}_1|_0^{t_L}+\int_0^{t_L}\sigma_1\,\mathrm{d}t = \int_0^{t_L}F(t)\,\mathrm{d}t \equiv I_p$$

$$m_e\dot{u}_i|_0^{t_L}+\int_0^{t_L}\sigma_i\,\mathrm{d}t = \int_0^{t_L}\sigma_{i-1}\,\mathrm{d}t \tag{A13}$$

where I_p is the external impulse. Figure (1a) reveals that after the passage of the wave front, a motionless plateau develops in u prior to reflections from the boundary. If t_L is sufficiently large to lie in the motionless plateau, the first term becomes negligible and (A13) expresses conservation of momentum:

$$\int_0^{t_L}\sigma_1\,\mathrm{d}t = \mathbf{I}_p$$

$$\int_0^{t_L}\sigma_i\,\mathrm{d}t = \int_0^{t_L}\sigma_{i-1}\,\mathrm{d}t = \mathbf{I}_p. \tag{A14}$$

For a rectangular forcing pulse of unit intensity applied to a semi-infinite periodic chain, an analytical expression for transient stress response can be derived by inverting the Fourier transform integral. Transforming the dynamic eqns (A2) yields

$$-4\bar{\omega}^2\bar{u}_0+(\bar{u}_0-\bar{u}_1) = \frac{\bar{\sigma}_0}{m_e\omega_e^2}; \quad n = 0 \tag{A15a}$$

$$-4\bar{\omega}^2\bar{u}_n+(2\bar{u}_n-\bar{u}_{n-1}-\bar{u}_{n+1}) = 0; \quad n \geqslant 1 \quad \bar{u}_n(\omega) = \frac{1}{\sqrt{2\pi}}\int_{-\infty}^{\infty}u_n(t)\,e^{i\omega t}\,\mathrm{d}t \tag{A15b}$$

where $\sigma_0 = 1$ is magnitude of the forcing pulse and $\bar{\sigma}_0$ is its transform. Periodicity requires that

$$\bar{u}_n = e^{\mu}\bar{u}_{n-1} \tag{A16}$$

where μ is propagation constant. Substituting (A16) in (A15b) yields the dispersion relation

$$e^{\mu} = 1-2\bar{\omega}^2+2\bar{\omega}(\bar{\omega}^2-1)^{1/2}. \tag{A17}$$

Substituting (A16) in (A15a) and eliminating e^{μ} using (A17) gives the transformed impedance at the excited end

$$\bar{u}_0 = \frac{\bar{\sigma}_0}{m_e\omega_e^2}\frac{1}{2[\bar{\omega}^2+\bar{\omega}(\bar{\omega}^2-1)^{1/2}]}. \tag{A18}$$

Expressing $\bar{u}_n$ in terms of $\bar{u}_0$ by repeated use of (A16) gives

$$\bar{u}_n = [1-2\bar{\omega}^2+2\bar{\omega}(\bar{\omega}^2-1)^{1/2}]^n\bar{u}_0. \tag{A19}$$

The inverse Fourier transform of (A19) is:

$$u_n(t) = \frac{1}{\sqrt{2\pi}}\int_{-\infty}^{\infty}[1-2\bar{\omega}^2+2\bar{\omega}(\bar{\omega}^2-1)^{1/2}]^n\bar{u}_0(\omega)\,e^{-i\omega t}\,\mathrm{d}\omega. \tag{A20}$$

Following Wang and Lee (1973) which specializes in outgoing waves, the integral in (A20) simplifies to:

$$u_n(t) = \delta_{n0}u_0(t)+2n\int_0^t\frac{J_{2n}[2\omega_e(t-t')]}{(t-t')}u_0(t')\,\mathrm{d}t' \tag{A21}$$

where J is the Bessel function of the first kind. Equation (A21) applies also to normalized stress in the form:

$$\sigma_n(t) = \delta_{n0}+2n\int_0^t\frac{J_{2n}[2\omega_e(t-t')]}{(t-t')}\,\mathrm{d}t'. \tag{A22}$$

Equation (A22) is the convolution integral of stress transmissibility at the nth interface. Re-writing the integral in (A22) as

$$\int_0^t \frac{J_{2n}[\beta(t-t')]}{t-t'}\,dt' = -\int_0^t \frac{J_{2n}(\beta\tau)}{\tau^{2n-1}}\tau^{2n-2}\,d\tau; \quad \beta = 2\omega_e$$

then integrating by parts noting that (see Gradshteyn and Ryzhik, 1970)

$$\int^t \frac{J_m(\beta\tau)}{\tau^{m-1}}\,d\tau = -\frac{J_{m-1}(\beta t)}{\beta t^{m-1}}$$

yields an exact expression for stress transmissibility when $t \leqslant t_f$, where t_f is the time interval of the forcing pulse

$$\sigma_n(t) = 1 - \sum_{k=0}^{n-1} \frac{2^{n-k} n!}{k!} \frac{J_{n+k}(\beta t)}{(\beta t)^{n-k}}; \quad t \leqslant t_f. \tag{A23}$$

For $t > t_f$, changing the upper limit of (A21) to t_f noting that

$$\int_0^t F(t-t')\,dt' = \int_{t_f}^{\hat{t}} F(\tau)\,d\tau; \quad \hat{t} = t - t_f$$

then following the procedure that led to (A23) yields

$$\sigma_n(t) = \sum_{k=0}^{n-1} \frac{2^{n-k} n!}{k!} \left[\frac{J_{n+k}(\beta\hat{t})}{(\beta\hat{t})^{n-k}} - \frac{J_{n+k}(\beta t)}{(\beta t)^{n-k}} \right]; \quad t > t_f. \tag{A24}$$

In PZ1, $\sigma_n(t)$ along the nth layer varies linearly (see eqns (6) and (7))

$$\sigma_{n,n+1}(\xi, t) = (1-\xi)\sigma_n(t) + \xi\sigma_{n+1}(t) \tag{A25}$$

where $\xi = x/h_A$ is the normalized local axial coordinate along the hard layer of the nth periodic set. Equation (A24) shows that for large t, $\sigma_n(t)$ is periodic with frequency $\beta = 2\omega_e \simeq \Delta\omega_{PZ1}$. Displacement follows from eqn (16b) of Wang and Lee (1973):

$$u_0(t) = \frac{1}{m_e\omega_0}\int_{-\infty}^t \int_0^{t-t'} \frac{J_1(\beta t'')}{t''}\,dt''$$

$$= \frac{1}{m_e\omega_0}\int_{-\infty}^t \left\{ J_1[\beta(t-t')] + 2\sum_{k=1}^{\infty} J_{2k+1}[\beta(t-t')] \right\} dt'. \tag{A26}$$

Displacement at other junctions then follows from

$$u_n(t) = u_{n-1}(t) - \sigma_n(t)/k_e. \tag{A27}$$

APPENDIX B: MODEL B: OSCILLATOR WITH DELAYED MOVING BASE

Figure 10(a) illustrates the oscillator with moving base. The mass m_e with displacement $u(t)$ is driven by $F(t)$ against a spring with stiffness k_e attached to a moving base with displacement $u(t-t_d)$. It is assumed that $u(t) = 0$ when $t < 0$. The moving base model assumes

$$u_2(t) = u_1(t - t_{d1})$$
$$u_{i+1}(t) = u_i(t - t_{di}), \quad i > 1$$
$$t_{d1} = c_p(\omega_e)/h_s = \frac{3}{\pi}c_0/h_s; \quad t_{di} = c_0. \tag{B1}$$

Substituting (B1) in (A2) produces

$$\ddot{u}_1(t) + \omega_e^2[u_1(t) - u_1(t-t_d)] = F(t)/m_e$$
$$\ddot{u}_1(t) + \omega_e^2[u_1(t) - u_1(t-t_d)] = \sigma_{i-1}(t)/m_e$$
$$\sigma_{i-1}(t) = k_e[u_{i-1}(t) - u_{i-1}(t-t_d)] \tag{B2}$$

where $F(t) = \sigma_0[H(t) - H(t-t_f)]$ and ω_e, m_e, c_p are frequency, mass and phase velocity of Model A.

A solution to eqn (B2) proceeds by segmenting time into intervals of width t_d. In the first interval $0 \leqslant t \leqslant t_d$, $u(t-t_d) = 0$ and $u_1(t)$ is easily found. In each succeeding interval, $u(t-t_d)$ is the u determined in the prior interval,

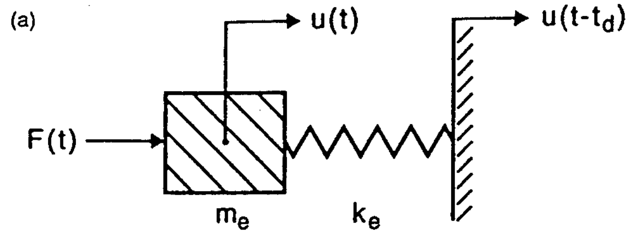

Fig. 10(a). Oscillator with moving base.

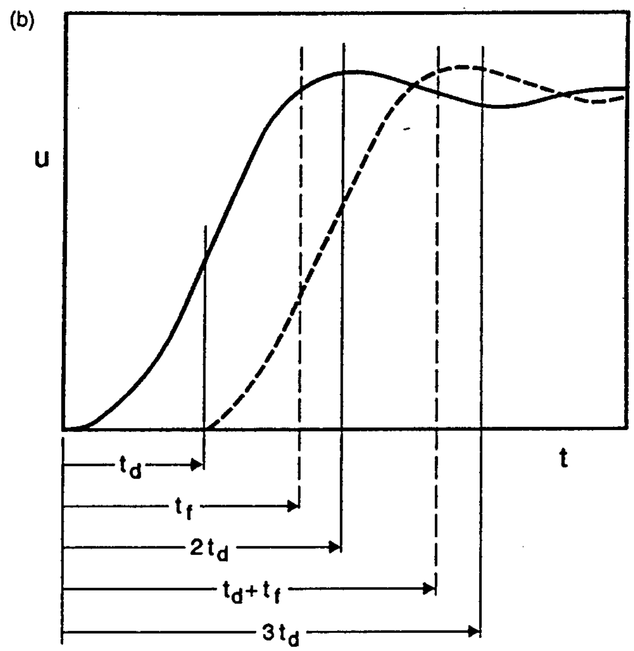

Fig. 10(b). Time segments in moving base model.

making the forcing function known. This simple recursion becomes slightly more complex during the Jth interval $Jt_d \leqslant t_f \leqslant (J+1)t_d$. This and all subsequent intervals are further segmented into two subintervals:

$$Jt_d \leqslant t \leqslant t_f; \quad t_f \leqslant t \leqslant (J+1)t_d$$
$$(J+1)t_d \leqslant t \leqslant t_d+t_f; \quad t_d+t_f \leqslant t \leqslant (J+2)t_d \tag{B3}$$

as shown schematically in Fig. 10(b).

Three special cases arise when t_f lies in the first, second or third t_d interval. Now specializing to the first layer a new notation is used; subscripts refer to mass number, as in (B1) and (B2), but to time interval and sub-interval numbers. When $t \leqslant Jt_d$, a single subscript is used denoting interval number. When $t > Jt_d$, a double subscript is used; the first denotes interval number while the second denotes sub-interval number. For the case when $0 \leqslant t_f \leqslant t_d$, the process yields

$(1)_1 \;\; 0 \leqslant t \leqslant t_f$

$$u_{11}(t) = \frac{1}{\omega_e}\int_0^t \frac{\sigma_0}{m_e}\sin\omega_e(t-\tau)\,\mathrm{d}\tau = \frac{\sigma_0}{k_e}(1-\cos\omega_e t)$$

$$\sigma_{11}(t) = k_e u_{11}(t) \tag{B4a}$$

$(1)_2 \;\; t_f \leqslant t \leqslant t_d$

$$u_{12}(t) = u_{11}(t_f)\cos\omega_e(t-t_f) + \frac{\dot{u}_{11}(t_f)}{\omega_e}\sin\omega_e(t-t_f)$$

$$= \frac{\sigma_0}{k_e}[-\cos\omega_e t + \cos\omega_e(t-t_f)]$$

$$\sigma_{12}(t) = k_e u_{12}(t) \tag{B4b}$$

(2), $t_d \leqslant t \leqslant t_d + t_f$

$$u_{21}(t) = u_{12}(t_d)\cos\omega_e(t-t_d) + \frac{\dot{u}_{12}(t_d)}{\omega_e}\sin\omega_e(t-t_d) + \omega_e\int_{t_d}^{t} u_{11}(\tau - t_d)\sin\omega_e(t-\tau)\,d\tau$$

$$u_{21}(t) = \frac{\sigma_0}{k_e}\left[1-\cos\omega_e t - \cos\omega_e(t-t_d) + \cos\omega_e(t-t_f) - \frac{\omega_e}{2}(t-t_d)\sin\omega_e(t-t_d)\right]$$

$$\sigma_{21}(t) = k_e[u_{21}(t) - u_{11}(t-t_d)]$$

$$= \sigma_0\left[-\cos\omega_e t + \cos\omega_e(t-t_f) - \frac{\omega_e}{2}(t-t_d)\sin\omega_e(t-t_d)\right]. \tag{B4c}$$

A similar process applies to the cases when $t_d \leqslant t_f \leqslant 2t_d$ and $2t_d \leqslant t_f \leqslant 3t_d$, etc.

The second step in building Model B develops an expression for the attenuating of σ^1_{mx} in layers below the first. In Whitham (1973), wave amplitude $A(x, t_p)$ is related to arrival time t_p asymptotically in a uniaxial dispersive medium. $A(x, t)$ is expressed as a Fourier integral.

$$A(x,t) = \int_{-\infty}^{\infty} F(\kappa)\exp[i\kappa x - iW(\kappa)t]\,d\kappa \tag{B5}$$

where $F(\kappa)$ is an arbitrary function satisfying initial and boundary conditions, and $\omega = W(k)$ is the dispersion relation. To find the asymptotic expression for large x and t provided (x/t) is held fixed, re-write (B5) as

$$A(x,t) = \int_{-\infty}^{\infty} F(\kappa)\,e^{-i\chi t}\,d\kappa$$

$$\chi(\kappa) = W(\kappa) - \kappa\frac{x}{t};\quad \frac{x}{t}\text{ fixed.} \tag{B6}$$

By the method of steepest descent, the main contribution to the integral in (B6) is from the neighborhood of stationary point $\kappa = k$ such that

$$\chi'(k) = W'(k) - \frac{x}{t} = 0. \tag{B7}$$

If $\chi''(k) \neq 0$, it will be assumed that $F(\kappa)$, $\chi(\kappa)$ can be expanded in Taylor series near $\kappa = k$

$$F(\kappa) \simeq F(k)$$

$$\chi(\kappa) \simeq \chi(k) + \tfrac{1}{2}(\kappa-k)^2\chi''(k). \tag{B8a}$$

Substituting (B8A) in (B6) and invoking the error integral yields

$$A(x,t_p) \simeq \sum_{\text{S.P.}} F(k)\left[\frac{2\pi}{t_p|W''(k)|}\right]^{1/2}\exp\left[ikx - iW(k)t_p - \frac{i\pi}{2}\operatorname{sgn} W''(k)\right] \tag{B8b}$$

where the sum is over all stationary points k. If $\chi''(k) = 0$ and $\chi'''(k) \neq 0$, then the expansion for $\chi(\kappa)$ becomes

$$\chi(\kappa) \simeq \chi(k) + \tfrac{1}{6}(\kappa-k)^3\chi'''(k) \tag{B9a}$$

producing the asymptotic amplitude

$$A(x,t_p) \simeq \left(\frac{1}{3}\right)!\,2^{1/3}3^{5/6}\sum_{\text{s.p.}}\frac{F(k)}{[t_p|W'''(k)|]^{1/3}}\exp[ikx - iW(k)t_p]. \tag{B9b}$$

For the present case, $W(k)$ is given implicitly by eqn (12). Specializing in waves in PZ1, reduces (12) to (A8), which when inverted yields the form

$$W(k) = \frac{2}{h_s}c_0\sin\left(\frac{1}{2}kh_s\right) \tag{B10a}$$

with derivatives

$$W'(k) = c_0\cos(\tfrac{1}{2}kh_s) \tag{B10b}$$

$$W''(k) = -\tfrac{1}{2}c_0h_s\sin(\tfrac{1}{2}kh_s) \tag{B10c}$$

$$W'''(k) = -\tfrac{1}{4}c_0h_s^2\cos(\tfrac{1}{2}kh_s). \tag{B10d}$$

From (B10b), $k_n = 4n\pi/h_s$ is a stationary point because

$$W'(k_n)-\frac{x}{t}\equiv W'(0)-c_0=0.$$

Since $W''(k_n)=0$ and $W'''(k_n)\neq 0$, the asymptotic behavior emerges from (B9b)

$$\sigma^1_{mx}(x,t_p)\propto t_p^{-1/3}. \tag{B11}$$

More generally, at any point in the stack σ^1_{mx}, can be expected to obey

$$\sigma^1_{mx}\propto t_p^{-\alpha} \tag{B12}$$

where the attenuation index α is determined numerically.

APPENDIX C: MODEL C: TRANSMISSION OF ELASTIC FREQUENCIES OF THE HARD LAYER

If we consider that the first hard layer is acted upon its left by the trapezoidal pulse $F_L(t)$ and on its right by the reaction of the soft layer $F_R(t)$:

$$F_L(t)=\frac{t}{t_1}\sigma_0[H(t)-H(t_1)]+\sigma_0[H(t-t_1)-H(t-t_2)]+\sigma_0\left[-\frac{(t-t_2)}{(t_3-t_2)}+1\right][H(t-t_2)-H(t-t_3)] \tag{C1}$$

$$F_R(t)\simeq\frac{\eta\sigma_0}{2}\left(1-\cos\frac{2\pi t}{T}\right) \tag{C2}$$

where $\eta<1$. Equation (C2) is the same as (1) with σ^1_{mx} replaced by $\eta\sigma_0$. From the definition of t_f

$$t_f=\tfrac{1}{2}(t_1+t_2+t_3)-t_1 \tag{C3}$$

and from (A17) for $2t_f<\pi/\omega_e$

$$T=\pi/\omega_e=\pi h_s/c_0. \tag{C4}$$

If $u(x,t)$ is expressed as the superposition of static and dynamic solutions to each of $F_L(t)$ and $F_R(t)$

$$u(x,t)=u_{dL}(x,t)+u_{sL}(x)F_L(t)+u_{dR}(x,t)+u_{sR}(x)F_R(t) \tag{C5}$$

where subscripts s and d denote static and dynamic solutions. If $u_{dL}(x,t)$ is expanded in eigenfunctions of the traction-free layer

$$u_{dL}(x,t)=\sum_i a_{iL}(t)\varphi_i(x)$$

$$\ddot a_{iL}+\omega_i^2 a_{iL}=-\frac{1}{N_i}\left[\rho_A\langle u_{sL}\,|\,\varphi_i\rangle\ddot F+\frac{1}{h_A}\langle\varphi_i\,|\,1\rangle F\right]$$

$$N_i=\rho_A\langle\varphi_i\,|\,\varphi_i\rangle \tag{C6}$$

and similarly for $u_{dR}(x,t)$. For the fundamental mode of the hard layer

$$\varphi_1(x)=\cos(\pi x/h_A),\quad \omega_1=\pi c_A/h_A \tag{C7}$$

the static solutions are

$$u_{sL}(x)=\frac{h_A}{E_A}\left(\xi-\frac{1}{2}\xi^2-\frac{1}{3}\right)$$

$$u_{sR}(x)=\frac{h_A}{E_A}\left(\frac{1}{2}\xi^2-\frac{1}{6}\right);\quad \xi=\frac{x}{h_A}. \tag{C8}$$

Using (C7) and (C8) in (C6) yields

$$N_a\equiv\langle\varphi_1\,|\,1\rangle=0;\quad N_1=\tfrac{1}{2}\rho_A h_A$$

$$N_{sL}\equiv\langle u_{sL}\,|\,\varphi_1\rangle=h_A/\pi^2$$

$$N_{sR}\equiv\langle u_{sR}\,|\,\varphi_1\rangle=h_A/\pi^2. \tag{C9}$$

Solving and summing contributions from $a_{1L}(t)$ and $a_{1R}(t)$ yields:

(A) $0 \leqslant t \leqslant t_1$

$$u_d(x,t) = -\sigma_0 \frac{h_A}{E_A}\frac{2}{\pi^2}\frac{\sin\omega_1 t}{\omega_1 t_1}\cos\pi\xi$$

$$-\sigma_0\frac{h_A}{E_A}\eta\frac{4}{T^2}\frac{\left(\cos\frac{2\pi t}{T}-\cos\omega_1 t\right)}{(\omega_1^2-4\pi^2/T^2)}\cos\pi\xi$$

$$u_s(x)F(t) = \sigma_0\frac{h_A}{E_A}\left[\frac{t}{t_1}\left(\xi-\frac{1}{2}\xi^2-\frac{1}{3}\right)+\frac{\eta}{2}\left(1-\cos\frac{2\pi t}{T}\right)\left(\frac{1}{2}\xi^2-\frac{1}{6}\right)\right]$$

$$\sigma_d(x,t) = \sigma_0\left\{\frac{2}{\pi}\frac{\sin\omega_1 t}{\omega_1 t_1}+\eta\frac{4\pi}{T^2}\frac{\left(\cos\frac{2\pi t}{T}-\cos\omega_1 t\right)}{(\bar{\omega}_1^2-4\pi^2/T^2)}\right\}\sin\pi\xi$$

$$\sigma_s(x)F(t) = \sigma_0\left\{\frac{t}{t_1}(1-\xi)+\frac{\eta}{2}\left(1-\cos\frac{2\pi t}{T}\right)\xi\right\}. \tag{C10}$$

If $2\omega_e < \omega_1$

$$\sigma_{dL} \leqslant \frac{2}{\pi}\frac{\sigma_0}{\omega_1 t_1}, \quad \sigma_{dR} \leqslant \frac{2}{\pi}\eta\sigma_0\left(\frac{2\omega_e}{\omega_1}\right)^2 \Rightarrow \sigma_{dR} < \eta\omega_1 t_1\left(\frac{2\omega_e}{\omega_1}\right)^2\sigma_{dL} \tag{C11}$$

from which $\sigma_{dR}(t)$ may be neglected.

(B) $t_1 \leqslant t \leqslant t_2$

$$u_d(x,t) \simeq -\sigma_0\frac{2}{\pi^2}\frac{h_A}{E_A}\frac{1}{\omega_1 t_1}[\sin\omega_1 t-\sin\omega_1(t-t_1)]\cos\pi\xi$$

$$u_s(x)F(t) = \sigma_0\frac{h_A}{E_A}\left[\left(\xi-\frac{1}{2}\xi^2-\frac{1}{3}\right)+\frac{\eta}{2}\left(1-\cos\frac{2\pi t}{T}\right)\left(\frac{1}{2}\xi^2-\frac{1}{6}\right)\right]$$

$$\sigma_d(x,t) \simeq \sigma_0\frac{2}{\pi}\frac{1}{\omega_1\omega_1}[\sin\omega_1 t-\sin\omega_1(t-t_1)]\sin\pi\xi$$

$$\sigma_s(x)F(t) = \sigma_0\left[1-\xi+\frac{\eta}{2}\left(1-\cos\frac{2\pi t}{T}\right)\xi\right]. \tag{C12}$$

To first order, σ_d vanishes if

$$[\sin\omega_1 t-\sin\omega_1(t-t_1)] = 0. \tag{C13}$$

(C13) is satisfied for all t if

$$\omega_1 t_1 = 2j\pi \Rightarrow t_1 = \frac{2j\pi}{\omega_1} \equiv \frac{j}{\Omega_1}. \tag{C14}$$

Since $\omega_i = i\omega_1$, elastic waves of the hard layer are not transmitted when the product of fundamental frequency ω_1 and rise time t_1 is a multiple of 2π.

Reference [4]
Transient Waves in a Periodic Stack: Experiments and Comparison with Analysis

Transient waves in a periodic stack: Experiments and comparison with analysis

Michael El-Raheb
The Dow Chemical Company, Midland, Michigan 48674

Reinhard Tham
Ernst Mach Institut fur Kurzzeitdynamik, Freiburg, Germany

(Received 15 December 1995; revised 22 August 1996; accepted 25 September 1996)

Transient waves were initiated by allowing a thick PMMA disk to strike a periodic stack of ceramic layers bonded by thin weak silicone rubber layers. Pressure at interfaces of ceramic and bond layers was measured by carbon gauges along the centerline of the stack. Comparison of experimental histories with those from a 1-D analysis [J. Acoust. Soc. Am. **94**, 172–184 (1993)] and a 2-D axisymmetric analysis [J. Acoust. Soc. Am. **99**, 3513–3527 (1996)] reveals that waves propagate two-dimensionally and that flexure of the ceramic layers controls attenuation and shape of compressive wave of first arrival. Viscoelasticity of the bond material sharply reduces tensile stresses. © *1997 Acoustical Society of America.* [S0001-4966(97)01702-5]

PACS numbers: 43.40.At [PJR]

INTRODUCTION

Shock hardening of structures is receiving more interest due to increasing applications. One recent application is the protection of sensitive devices on board of space probes whose mission is to land on planets at velocities sufficient to penetrate the soil and perform subterranial measurements of soil properties. One method of shock attenuation is by crushing material of collapsible structures, transforming kinetic energy to plastic work irreversibly. This method is limited to velocities not exceeding 100 m/s as volume of crushable material rises with speed nonlinearly to reach impractical limits of space and weight. Weakly coupled periodic chains exhibit dispersive properties when subjected to impulse of short duration. When combined to the concept of collapsible structures, periodic chains add an advantage by raising the limiting speed. In weakly coupled chains, attenuation of a transient pulse along the chain can be tailored to specific requirements of force or acceleration by judicious choice of geometry and material properties.

Studies on wave propagation in periodic media are mostly limited to the frequency domain (see Refs. 1–10). Reference 11 treated transient waves in 1-D weakly coupled biperiodic stacks, concluding that the first propagation zone or pass band is paramount. In this zone, hard layers act as rigid masses and weak layers act as springs. Reference 12 extended the analysis to 2-D axisymmetric stacks including flexure of the hard layers and demonstrated that flexural phase velocity is essential in spreading the pulse radially.

In this paper we describe results of an experiment designed to verify the analysis in Refs. 11 and 12 and define the limitation of 1-D theory. In Sec. I we analyze the experimental stress histories. In Sec. II we compare experimental stress histories to 1-D and 2-D numerical results. We identify regimes of propagation, explain the difference between experimental and theoretical histories, and conclude with the limitation of 1-D and 2-D linear analyses.

I. EXPERIMENT

Transient stress waves were initiated in a weakly coupled periodic stack of square aluminum nitride (AlN) ceramic tiles 10.16 cm in side, bonded by a thin weak silicone rubber, ME625.[13] Tile and bond thicknesses were 1.27 and 0.03 cm. Piezo resistive carbon gauges 0.008 cm thick of the type C300-50-EKRTE from Dynasen Inc. were inserted at the bottom face of the first four tiles along the center line of a stack with ten tiles [see Fig. 1(a)]. Each gauge served as the active resistor of a Wheatstone quarter-bridge circuit. Just before the passage of the wave, the bridge was supplied by a 45-V pulse with a 300-μs duration. The initially balanced bridge was unbalanced by the change in resistance of the gauge from applied pressure. The output voltage was recorded by a 200-MHz transient recorder. Given the specific gauge calibration and nonlinearity of the bridge, pressure histories are valid up to 300 μs from impact. The high electric current in the system produced an inevitable temperature drift of the gauges yielding a fictitious pressure rise of the order of 1.75 MPa per 100 μs.

The stack was placed in a metal casing facing the muzzle of a 6-cm-diam compressed air gun at the Ernst Mach Institute, Freiburg, Germany. The stack was struck in its center by a PMMA disk 5.75 cm in diameter and 2 cm thick, launched by a compressed air accelerator. Velocity of the disk at impact ranged from 14–58 m/s. Velocities were kept low to avoid damaging the struck ceramic tile. A laser beam in the axis of the launch tube reflecting from the top surface of the first ceramic tile allowed the alignment of stack and disk axes. This procedure resulted in a tilt smaller than 2 mrad. The assembled experimental setup of the stack is shown in Fig. 1(b).

A typical digitized output of normal stress history σ_{zz} sensed by the carbon gauges in a stack of ten ($10.16\times10.16\times1.27$ cm) ceramic tiles is shown in Fig. 2. The broken horizontal line labeled $p_{1\mathrm{D}}$ defines the computed 1-D pres-

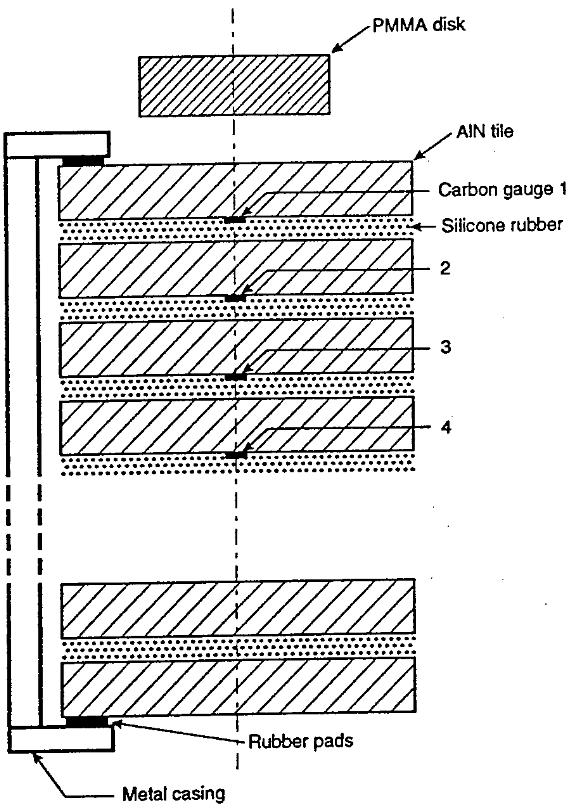

(a)

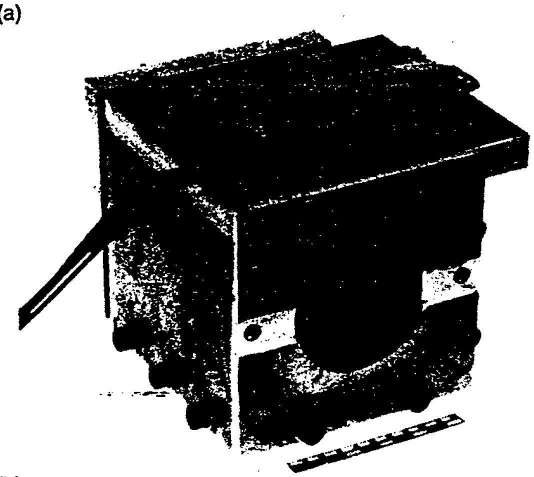
(b)

FIG. 1. (a) Schematic of experimental setup. (b) Assembled test configuration.

sure exerted by the PMMA disk upon the ceramic tile according to

$$p_{1D}=\rho_e c_e V_0, \quad \frac{1}{\rho_e c_e}=\frac{1}{\rho_c c_c}+\frac{1}{\rho_d c_d}, \tag{1}$$

where $\rho_c c_c$ and $\rho_d c_d$ are longitudinal acoustic impedances of ceramic and disk materials, ρ and c are corresponding density and longitudinal speed of sound, $\rho_e c_e$ is the equivalent impedance for determining p_{1D} in a uniaxial strain condition, and V_0 is velocity of PMMA disk at impact in m/s. For PMMA striking AlN, substituting material properties from Table I in Eq. (1) yields $p_{1D} \simeq 3.044 V_0$ MPa. Note that on the second tile the pulse is magnified, i.e., $(\sigma_{zz})_{max} > p_{1D}$. On all following tiles, $(\sigma_{zz})_{max}$ attenuates typical of weakly coupled stacks.[11,12]

At each tile, $(\sigma_{zz})_1$ of first arrival includes a double peak where the second peak is always weaker than the first. A second and third peak occur after $(\sigma_{zz})_1$. The second peak, weaker than the third and delayed by 20 μs after the first, is due to flexural reflection at the perimeter of the disk. The third peak is due to tensile reflection from the bottom tile. Those identifications are from considering flexural phase velocity in AlN (c_{pf}=2.3 km/s), axial phase velocity along the stack (c_{pz}=3.7 km/s), and geometry of disk and tile. The double peak in $(\sigma_{zz})_1$ is caused by axial oscillations of the tile. One final observation of the histories in Fig. 2 is that tensile stresses are very small, which may be caused by viscoelastic effects of the bond material.

II. ANALYSIS

The 1-D and 2-D axisymmetric analyses developed in Refs. 11 and 12 rely on a modal expansion solution of the coupled linear elastodynamic equations of the periodic stack. Both methods are adopted to reproduce the experimental stress histories at interfaces of layers. The effect of viscoelasticity of the bond material is then evaluated by including the standard linear viscoelastic solid in the 1-D simulation.

A. 1-D and 2-D axisymmetric analyses

Applying the 1-D analysis developed in Ref. 11 and 2-D axisymmetric analysis developed in Ref. 12 and comparing their results with the experiments yields further understanding of transient propagation in a periodic stack.

To gain an accurate pressure σ_{zz0} produced by the disk at impact, a finite volume algorithm developed in Ref. 14 was used. It assumes that PMMA and AlN materials are linear elastic for the range of velocities in the experiment. Figure 3 shows the time evolution of deformation of disk and struck tile in the first 16 μs after impact. Note the bulge along the perimeter of the disk from Poisson's effect, propagating toward the free face followed by the lifting of the edge which sets up a shear wave propagating back toward the axis. This lifting diminishes average stress at the interface as Fig. 4. shows by the attenuation of σ_{zz0} with time. Unlike the rectangular pressure profile used to compute p_{1D}, decaying oscillations about a downward sloping line ending 14 μs after impact is the 2-D normalized pressure pulse in Fig. 4. It was used to force both 1-D and 2-D analyses to follow.

The material properties of ceramic and bond are listed in

TABLE I. Properties of AlN ceramic and polymer bond materials.

	AlN ceramic	Polymer bond
Modulus E (MPa)	310×10^3	69
Mass density ρ (kg/m^3)	3200	1070
Poisson ratio ν	0.25	0.49
Longitudinal speed c_L (km/s)	9.8	1.05[a]
Flexural phase velocity c_{pf} (km/s)	2.3[b]	not relevant

[a]Uniaxial strain.
[b]For a 1.27-cm-thick plate.

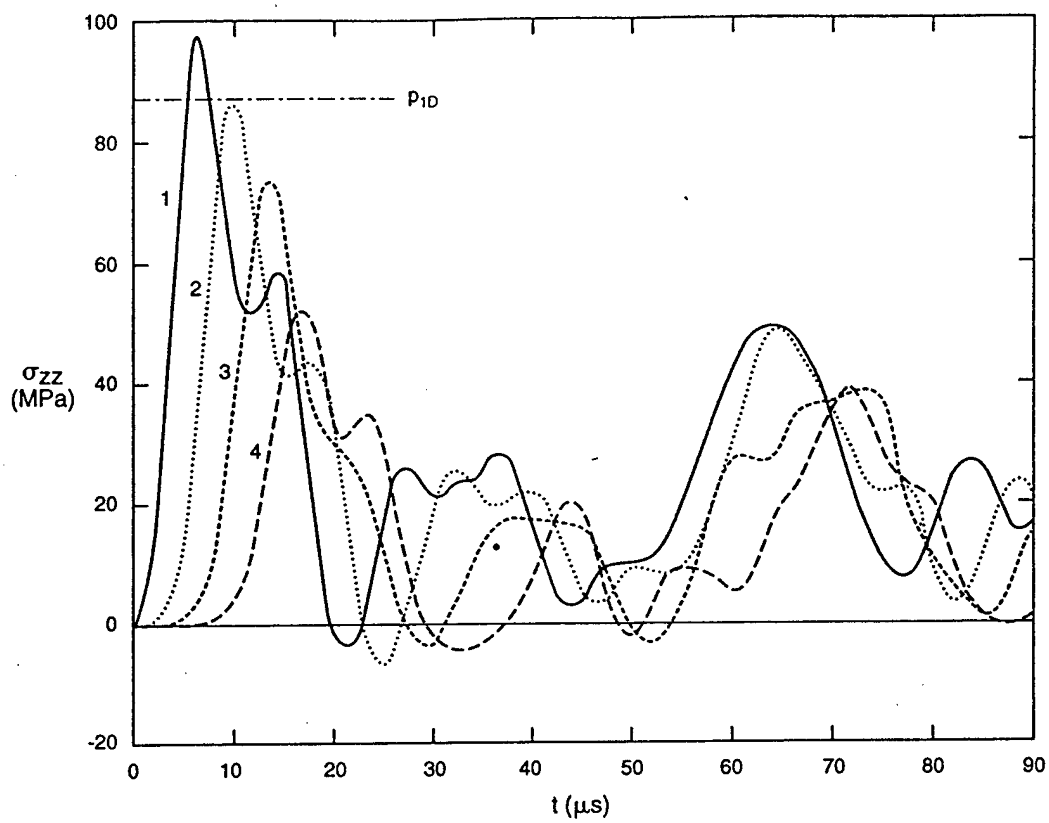

FIG. 2. Experimental histories at bottom of first to fourth tile $V_0 = 28.8$ m/s, $P_{1D} = 87.55$ MPa.

Table I. In one dimension, the equivalent bond modulus in uniaxial strain is

$$E_{be}=\frac{(1-\nu_b)E_b}{(1+\nu_b)(1-2\nu_b)}. \tag{2}$$

Histories of normalized axial stress $\tilde{\sigma}_{zz}$ resulting from the 1-D simulation[11] with constant planform area are shown in Fig. 5. Note that, among other differences, $(\tilde{\sigma}_{zz})_{\max}$ is not attenuated along the stack. As the pressure pulse propagates through the layers, in the real stack flexural waves radially extend the footprint of pressure. Viewed in this way, the effective area of layers increases along a 1-D stack. Indeed, a 1-D simulation of a stack with sets varying in planform area along the direction of propagation produced the histories in Fig. 6(a) and (b) for two different planform area distributions. In Fig. 6(a), the distribution of tile area A_i along the stack follows an extension in radius of the nth ceramic layer r_n according to

$$\begin{aligned} r_n &= r_d+(n-1)c_{pf}\Delta t_s, \\ \Delta t_s &= c_{pz}/h_s, \end{aligned} \tag{3}$$

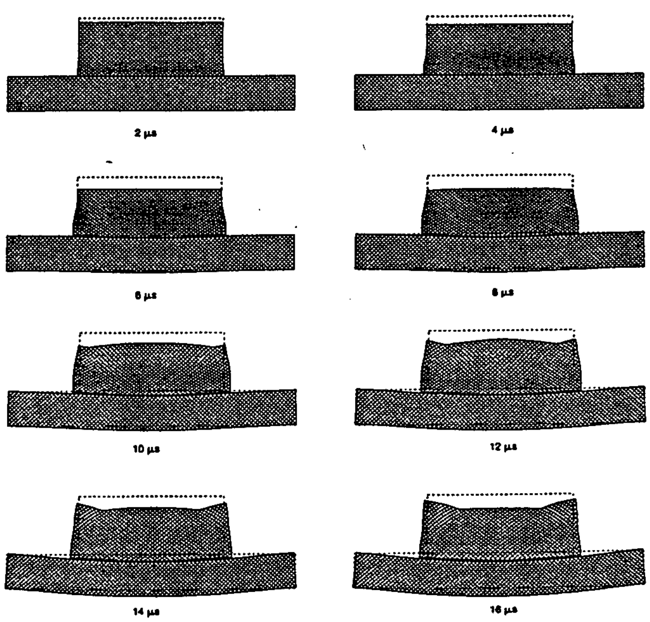

FIG. 3. Evolution of deformation pattern of PMMA disk striking AlN tile.

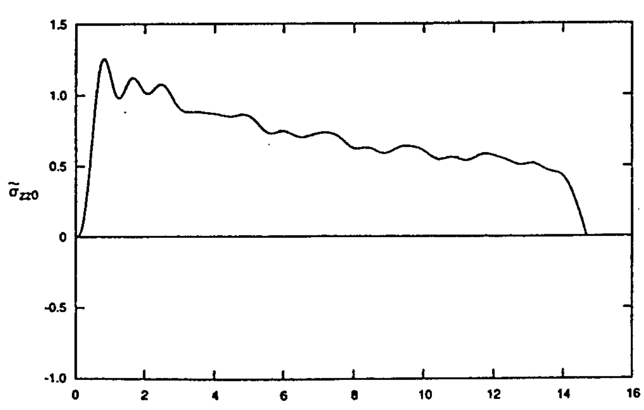

FIG. 4. History of normalized average pressure on struck tile.

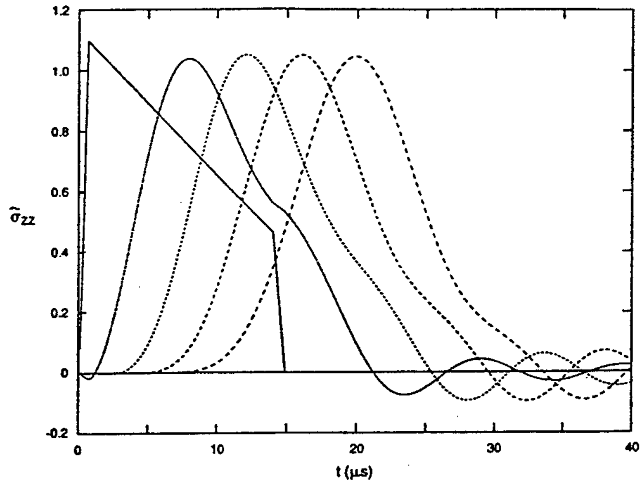

FIG. 5. Normalized $\tilde{\sigma}_{zz}$ histories from 1-D analysis with constant plan form area.

where r_d is radius of disk, $h_s=(h_c+h_b)$ is thickness of a periodic set, c_{pf} is flexural phase velocity in the ceramic tile, and c_{pz} is axial phase velocity along the stack measured experimentally. Note that in Fig. 6(a) $(\tilde{\sigma}_{zz})_{1\,\max}$ attenuates along the stack and is lower than the corresponding experi-

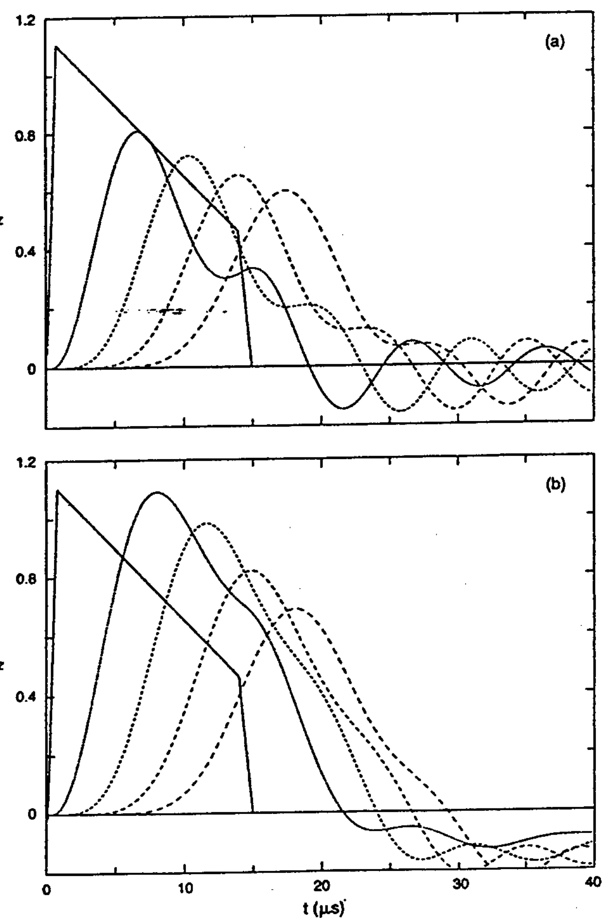

FIG. 6. Histories of $\tilde{\sigma}_{zz}$ in 1-D stack with 2 different plan form area distributions. (a) $A_i/A1 \rightarrow 1.0$, 1.5, 1.9, 2.2, 2.5, 2.8, 3.1, 3.4, 3.7, 4.0; (b) $A_i/A1 \rightarrow 1.0$, 1.0, 1.3, 1.8, 2.4, 3.0, 3.6, 4.0, 4.0, 4.0.

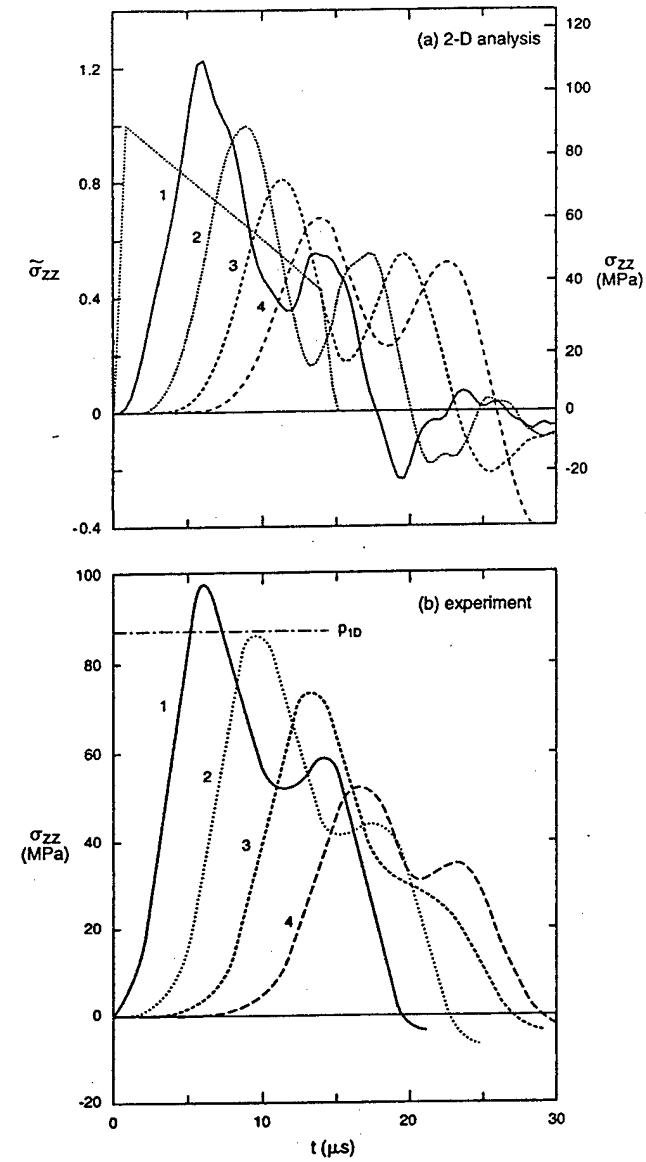

FIG. 7. Comparison of peaks of first arrival $(\sigma_{zz})_1$ from 2-D analysis and experiment.

mental values. An explanation is that in one dimension, tiles move as rigid bodies while, in two dimensions, tiles flex radially as they move axially. The radial deformation reduces contact area at the interface of consecutive tiles which in turn reduces effective planform area A_i. Considering this reduction, a second distribution of A_i produces the histories in Fig. 6(b) where now a better match with experiment of $(\tilde{\sigma}_{zz})_{1\,\max}$ is achieved.

In Fig. 6(a), $(\tilde{\sigma}_{zz})_{1\,\max}$ of all layers includes a double peak similar to that in the experiment. Clearly, this feature cannot be attributed to flexure but is caused from axial oscillations of the ceramic layers at the natural frequency of the set $\omega_{set}=(E_{b\varepsilon}/(\rho_c h_c h_b))^{1/2}$. When the set period $T_{set}=2\pi/\omega_{set}$ is shorter than $2\Delta t_f$, where Δt_f is time interval of the forcing pulse, more than one peak will appear in $(\tilde{\sigma}_{zz})_1$. However, if $T_{set}>2\Delta t_f$, only one peak will appear. In the present stack, $T_{set}=20$ μs while $2\Delta t_f=28$ μs, which explains the double peak.

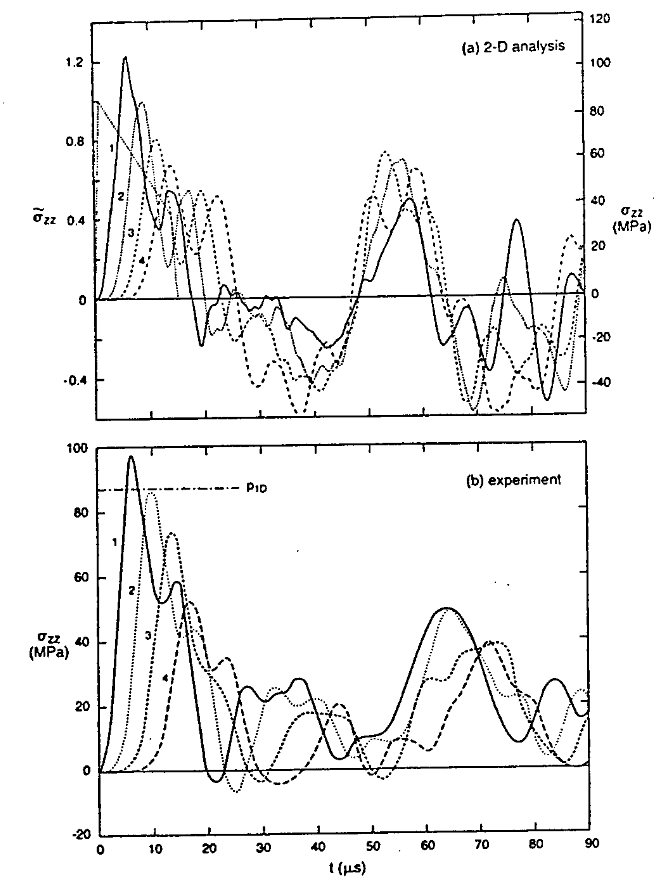

FIG. 8. Comparison of σ_{zz} histories including reflections, from 2-D analysis and experiment.

The preceding 1-D analysis demonstrates that radial propagation from flexure is indispensible for describing wave propagation even in such extreme cases as when the impactor's diameter is half that of the struck tile.

A 2-D simulation[12] based on the geometric and material properties in Table I yielded the histories of $(\tilde{\sigma}_{zz})_1$ shown in Fig. 7(a). Note the following:

(a) Peak stress of first arrival $(\sigma_{zz})_{1\,\max}$ at tile 2 is greater than $(\sigma_{zz0})_{\max}$ with a magnification matching that in Fig. 7(b) of the experiment.
(b) At the following tiles, $(\sigma_{zz})_{1\,\max}$ also matches those in Fig. 7(b).
(c) Histories of $(\sigma_{zz})_1$ at all tiles include the double peak featured in Fig. 7(b).
(d) In Fig. 8(a) the second peak is negative and shifted from the first by 20 μs. It is caused by reflection from the tile's outer boundary. As will be shown below, this second peak in the experiment [see Fig. 8(b)] is positive due to viscoelastic strain of the bond material.
(e) The third peak at 53 μs [see Fig. 8(a)] is caused by reflection from the bottom of the stack, while in Fig. 8(b) that third peak occurs at 63 μs. The deficit of 10 μs is caused by the difference in the number of tiles used in experiment and analysis. The experiment included ten tiles while the 2-D analysis included eight tiles to reduce computational effort. In the experiment, the first pulse has to travel over four additional sets

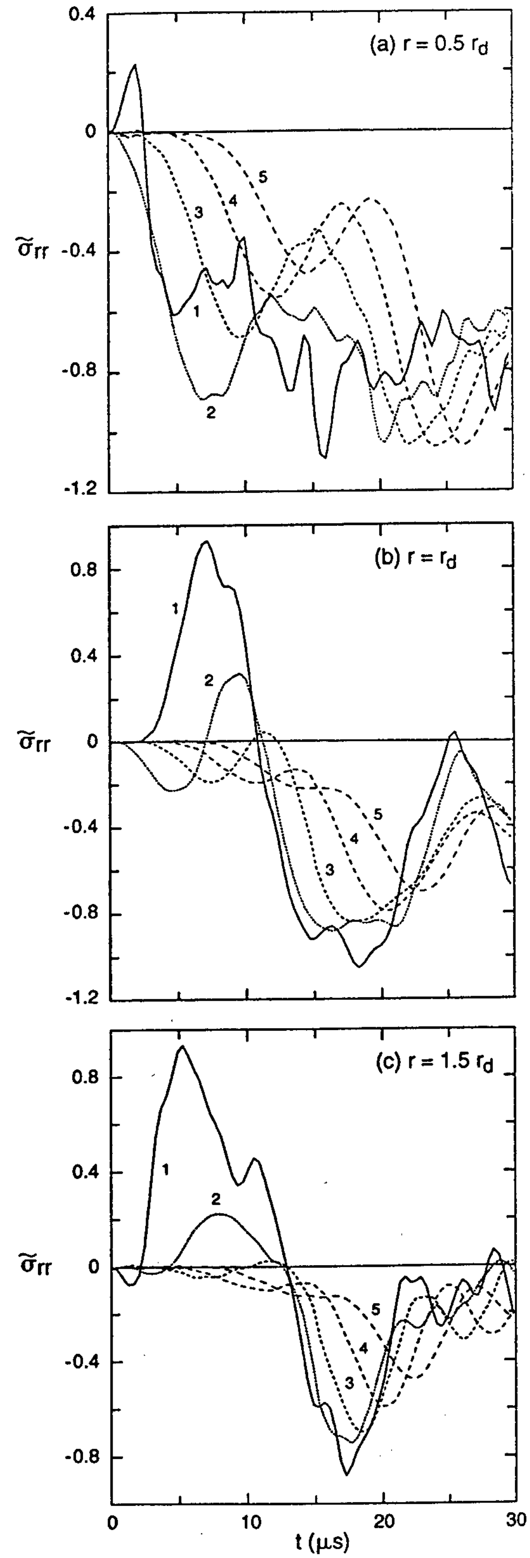

FIG. 9. Normalized radial stress histories $\tilde{\sigma}_{rr}$ on top of first five tiles at radial stations $r=0.5,\ r_d,\ 1.5r_d$.

than in analysis before the reflected pulse reaches the top surface of the stack. Since travel time over a set $\Delta t_s \approx 3$ μs, arrival time in the experiment should be longer by approximately 12 μs, which is indeed the case.
(f) Contrary to 1-D where reflection from the bottom of

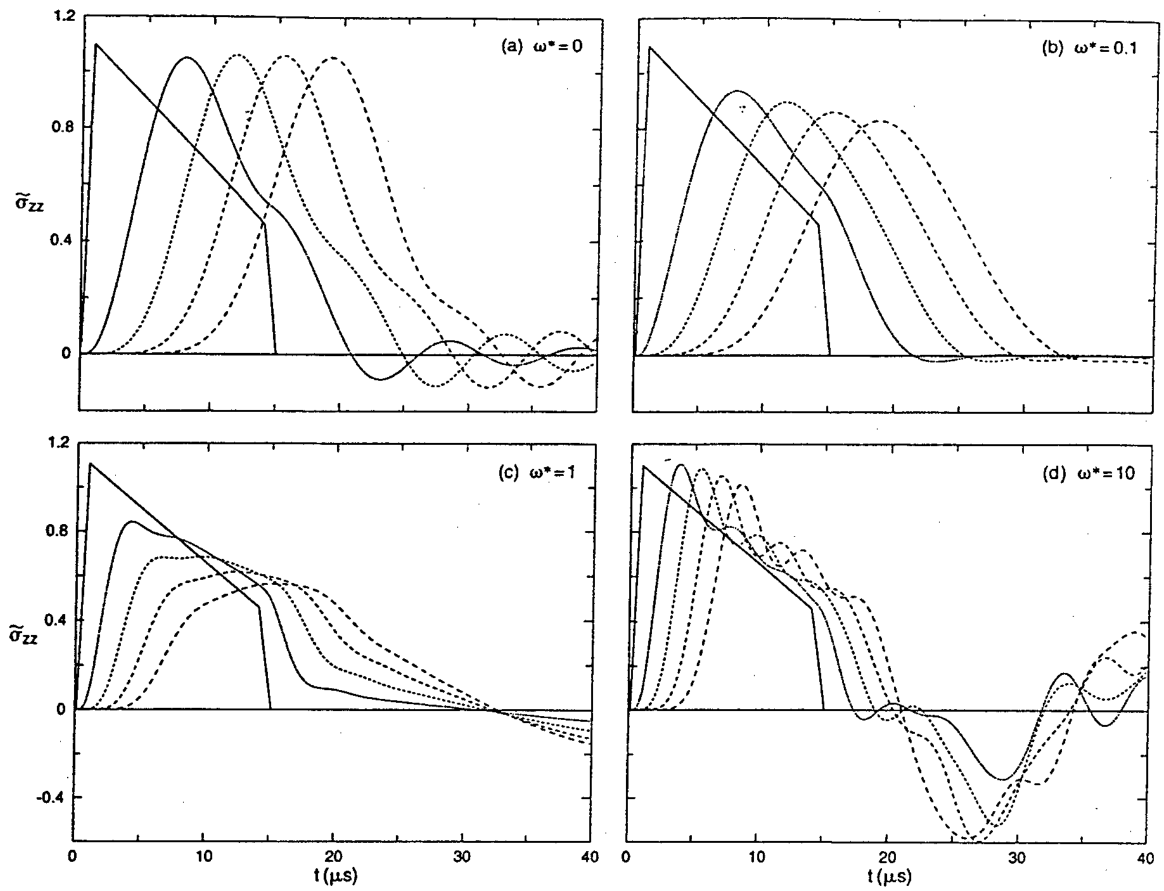

FIG. 10. Histories of $\tilde{\sigma}_{zz}$ in 1-D stack with constant plan from area bonded by viscoelastic layers ($\omega^* = \omega_{set}\sqrt{\tau_\sigma \tau_\epsilon}$).

the stack causes tensile stress at the interfacial bond, experiment and 2-D theory reveal that this reflected wave is compressive as shown in Fig. 8(a) and (b). Applied pressure from impact flexes the struck tile as illustrated in Fig. 3. Succeeding tiles also flex but at a time delayed from finite phase velocity along the stack's axis. When the wave reflects from the bottom of the stack, curvature of the bottom tile is reduced. This reduction in curvature then propagates backward toward the top tile at delayed times. The time delay produces a mismatch in curvature between adjacent tiles which in turn compresses the bond.

One discrepancy between histories in Fig. 7(a) and those in Fig. 7(b) is axial phase velocity c_{pz} computed by

$$c_{pz} \simeq \frac{(h_c + h_b)}{\Delta t_\sigma}, \tag{4}$$

where $(h_c + h_b)$ is total thickness of a periodic set and Δt_σ is time interval between peaks at two consecutive tiles. From Fig. 7(b)

$$(c_{pz})_{\text{exp}} \simeq \frac{1.3\times 10^{-5}}{3.5\times 10^{-6}} = 3.7 \text{ km/s},$$

and from Fig. 7(a)

$$(c_{pz})_{\text{anal}} \simeq \frac{1.3\times 10^{-5}}{2.6\times 10^{-6}} = 5.0 \text{ km/s}.$$

The source of this discrepancy is the following. The speed of sound in the bond c_b used in the analysis was determined from the experimental phase velocity computed from (4) and the 1-D scaling low:[11]

$$c_{pz} \simeq c_b \left(\frac{\rho_b h_c}{\rho_c h_b} \right)^{1/2}, \tag{5}$$

where (ρ_b, h_b) is bond density and thickness, and (ρ_c, h_c) is ceramic density and thickness. Relation (5) assumes that a ceramic tile acts as an unconstrained rigid mass and the bond acts as a linear spring.[15] In two dimension, only that circular portion of the tile bounded by the flexural wave front moves. The portion outside the wavefront adds its own resistance. Therefore, a value of c_{pz} in two dimensions may be realized by a $c_b < (c_b)_{1D}$ because the total spring reaction includes a contribution from material outside the wavefront. Using $(c_b)_{1D}$ in the 2-D analysis, then, results in a too-stiff bond, so $(c_{pz})_{\text{anal}} > (c_{pz})_{\text{exp}}$.

Another discrepancy is the negative stresses among the analytical histories. As will be demonstrated in the analysis to follow, the reduced tensile stress is caused by viscoelastic strain of the bond material, an effect not included in the 1-D and 2-D simulations.[11,12]

Figure 9(a)–(c) plots histories of $\tilde{\sigma}_{rr}$ from 2-D analysis on top of the first five tiles in the stack at three radial stations $r = 0.5r_d$, r_d, and $1.5r_d$. Note that on the first tile $\tilde{\sigma}_{rr}$ develops a tensile precurser whose peak increases radially reaching a magnitude close to $|\tilde{\sigma}_{zz0}|_{\max}$ at the perimeter of the disk $r=r_d$. For an impact velocity $v_0=58$ m/s, $|\sigma_{zz0}|_{\max}\approx 1.15 p_{1D}\approx 203$ MPa, which is above tensile strength of AlN, explaining the formation of circumferential cracks illustrated in Fig. 1(b).

B. Effect of viscoelasticity of bond material

To demonstrate the effect of bond viscoelasticity in one dimension, the elastic bond material is replaced by a linear viscoelastic solid with constitutive law[16]

$$\sigma+\tau_\varepsilon\dot{\sigma}=E_{R\varepsilon}(\varepsilon+\tau_\sigma\dot{\varepsilon}), \tag{6}$$

where $(\tau_\sigma,\tau_\varepsilon)$ are time constants of creep and relaxation and $E_{R\varepsilon}$ is rubbery modulus in uniaxial strain when $\dot{\varepsilon}=0$. In the limit when $\dot{\varepsilon}$ and $\dot{\sigma}\rightarrow\infty$, the material becomes glassy and from (6)

$$\sigma=E_{R\varepsilon}\frac{\tau_\sigma}{\tau_\varepsilon}\dot{\varepsilon}=E_{G\varepsilon}\dot{\varepsilon};\quad \Rightarrow E_{G\varepsilon}=\frac{\tau_\sigma}{\tau_\varepsilon}E_{R\varepsilon}. \tag{7}$$

Treating the tiles as rigid masses, the governing equations are modified to include viscoelasticity of the bond:

$$\begin{aligned}
&m_1\ddot{u}_1=\sigma_0-\sigma_1,\\
&m_i\ddot{u}_i=\sigma_{i-1}-\sigma_i,\\
&m_n\ddot{u}_n=\sigma_{n-1},\\
&\sigma_i+\dot{\sigma}_i\tau_\varepsilon=E_{R\varepsilon}(\varepsilon_i+\dot{\varepsilon}_i\tau_\sigma),\\
&\varepsilon_i=(u_i-u_{i+1})/h_b,\\
&m_i=\rho_c h_c,\quad \tau_\sigma=\tau_\varepsilon E_{G\varepsilon}/E_{R\varepsilon},
\end{aligned} \tag{8}$$

where u_i is axial displacement of the ith mass m_i, σ_i is axial stress between layers i and $i+1$, and σ_0 is the external stress acting on m_1. Assume the following bond properties:

$$E_{R\varepsilon}=1.211\ \text{GPa},\quad E_{G\varepsilon}=6.9\ \text{GPa},\quad \omega^*=0.1,1,10, \tag{9}$$

where $\omega^*=\omega_{\text{set}}\sqrt{\tau_\sigma\tau_\varepsilon}$ and ω_{set} is resonant frequency of the periodic set with rubbery modulus $E_{R\varepsilon}$ (Ref. 15) and $\omega_{\text{set}}=(E_{R\varepsilon}/(\rho_c h_c h_b))^{1/2}$. Figure 10(a)–(c) plots 1-D histories of $(\tilde{\sigma}_{zz})_1$ for the stack with material properties from Table I but with the viscoelastic bond in (9) for three values of ω^*. Clearly the viscoelastic effect is to reduce tensile stress. Note that maximum damping occurs when $\omega^*=1$ (see Ref. 16).

III. CONCLUSION

Nondestructive experiments were performed on periodic stacks of AlN tiles bonded by a thin weak silicone rubber. Pressure measured by carbon gauges on the bottom surface of ceramic tiles was higher than applied pressure on the first tile, and attenuated on all tiles to follow. The close match of experimental histories to 2-D analysis confirmed how flexure controls the evolution of the pulse by spreading it radially. Flexure also modifies the nature of the reflected wave from the bottom of the stack, changing it from tensile to compressive. The absence of normal tensile stress in the experimental histories may be caused by viscoelastic effects of the bond material.

[1] W. Thomson, "Transmission of Elastic Waves Through a Stratified Medium," J. Appl. Phys. **21**, 89–93 (1950).

[2] N. A. Haskel, "The Dispersion of Surfaced Waves in Multi-Layered Media," Bull. Seismic Soc. Am. **43**, 17–34 (1953).

[3] D. L. Anderson, "Elastic Wave Propagation in Layered Anisotropic Media," J. Geophys. Res. **66**, 2953–2963 (1961).

[4] C. T. Sun, J. D. Achenbach, and G. Herrmann, "Time Harmonic Waves in a Stratified Medium, Propagating in the Direction of the Layering," J. Appl. Mech. **35**, 408–411 (1968).

[5] E. H. Lee and W. H. Yang, "On Waves in Composite Materials with Periodic Structure," SIAM (Soc. Ind. Appl. Math.) J. Appl. Math. **25**, 492–488 (1973).

[6] T. J. Delph, C. Herrmann, and R. K. Kaul, "Harmonic Wave Propagation in a Periodically Layered Infinite Elastic Body: Antiplane Strain," J. Appl. Mech. **45**, 343–349 (1978).

[7] R. C. Engels and L. Meirovitch, "Response of Periodic Structures by Modal Analysis," J. Sound Vib. **56**, 481–493 (1978).

[8] A. A. Golebiewska, "On Dispersion of Periodically Layered Composites in Plane Strain," J. Appl. Mech. **47**, 206–207 (1980).

[9] A. H. Shah and S. K. Datta, "Harmonic Waves in a Periodically Laminated Medium," Int. J. Solids Struct. **18**, 301–317 (1982).

[10] A. K. Mal, "Wave Propagation in Layered Composite Laminates Under Periodic Surface Loads," Wave Motion **10**, 257–266 (1988).

[11] M. El-Raheb, "Transient Elastic Waves in Finite Layered Media: One Dimensional Analysis," J. Acoust. Soc. Am. **94**, 172–184 (1993).

[12] M. El-Raheb and P. Wagner, "Transient elastic waves in finite layered media: Two-dimensional axisymmetric analysis," J. Acoust. Soc. Am. **99**, 3513–3527 (1996).

[13] R. Tham, "Transient Elastic Waves in Finite Layered Media, Experimental Results," EMI Report E (6/95).

[14] M. El-Raheb and P. Wagner, "Wave propagation in a plate after imact by a projectile," J. Acoust. Soc. Am. **82**, 498–505 (1987).

[15] M. El-Raheb, "Simplified Analytical Models of Uniaxial Waves in a Periodic Stack," to appear in Int. J. Solids Struct.

[16] Y. C. Fung, *Foundations of Solid Mechanics* (Prentice–Hall, Englewood Cliffs, NJ, 1965), 1st ed.

Reference [5]
Transient Flexural Waves in a Disk and Square Plate from Off-Center Impact

Transient flexural waves in a disk and square plate from off-center impact

Michael El-Raheb

The Dow Chemical Co., Midland, MI 48674

Paul Wagner

1020 Crestview Drive, Pasadena, CA 91107

ABSTRACT

Flexural waves in a disk and square plate produced by off-center impact are analyzed. The effects on maximum transient stress σ_{max} of boundary shape, edge constraint, thickness, side of square plate or diameter of disk, and eccentricity of center of impact are studied. While prior analytical work has been confined to disks for simplicity, ballistic experiments were performed using square plates for practical reasons. The two geometries agree better for central impact or edges that are simply supported or clamped. Analytical results show some intensification as center of impact approaches the edge, but this is insufficient to explain the measured rise in residual projectile kinetic energy after penetrating a ceramic tile. This reveals the inadequacy of the crack initiation mechanism as the primary model of defeating the projectile by ceramic tiles.

INTRODUCTION

Ceramic materials such as silicon carbide and aluminum nitride AlN are presently used to harden structures against impact by high velocity projectiles. Replacing metal with these materials yields lower weight because of increased compressive strength in spite of reduced toughness. Compressive strength is paramount in breaking brittle projectiles and eroding soft projectiles, and dispersing momentum in the early stages of penetration. Ballistic experiments on AlN tiles struck by tungsten allow cylindrical projectiles revealed that residual kinetic energy of the projectile, measured by depth of penetration "DOP" into an adjacent aluminum block, increases monotonically with the distance between center of impact and tile center called eccentricity r_e. This effect is caused by at least two mechanisms:

1) As r_e approaches the tile's edge, maximum transient stress σ_{max} initiating micro-cracks in the brittle material, may intensify from constructive interference between waves radiating from the area of impact and earlier waves reflected from the edge. This is similar to the intensification of σ_{max} from central impact when tile size is reduced, also called "tile size effect".
2) Even after crack initiation, resistance continues because the comminuted material persists due to inertia and reaction of nearby unbroken material, confining the residual projectile. This effect is also called "self confinement".

Clearly, both mechanisms affect penetration although they act at different time intervals, the first acts early before cracking starts, while the other acts later after cracking. A possible conclusion of this work is the relative importance of each mechanism.

In the last two decades, general purpose finite element, finite difference and finite volume computer programs were developed for predicting penetration of projectiles in elasto-plastic metals. Because of the large strains and strain rates involved during these events, non-linear constitutive laws, energy balance, and shock discontinuities had to be addressed. These computer programs are successful in accurately predicting penetration depth and crater geometry in metals. This success relies on the fact that metals subjected to these intense transient loads behave almost like viscous fluids, which explains the widely used term ""hydro code". However, when applied to penetration in brittle materials, hydro-codes are less successful especially in the later stage of the event when cracks form, breaking the material into small pieces with size depending on their vicinity to center of impact.

Since ceramic materials remain linear elastic before crack initiation, they can be analyzed using small amplitude linear flexural waves. Previous work treated transient waves from central impact in 1-D layered media [1,2], plates [3], thick disks [4], 2-D axisymmetric layered media [5], and stacks of layered plates adopting flexure theory [6]. The objective of this work is to study how σ_{max} changes with eccentricity while varying the following parameters

(a) boundary shape, either disk or square plate

(b) edge constraint, either simply supported or free

(c) thickness and lateral dimension

Relating how σ_{max} varies with these parameters to experimental DOP reveals the relative importance of each mechanism on penetration.

Section I treats flexural waves in a disk based on Mindlin's plate equations [7] for an asymmetric forcing pulse. Transient response uses an exact modal solution satisfying simply supported or free edges.

Section IIA treats flexural waves in a square plate. Unlike the disk where circumferential and radial dependence separate yielding eigenfunctions which satisfy all natural boundary conditions exactly, the square plate does not allow separation of variables along the two axes x and y. Instead, a Galerkin solution is adopted. Trial functions of a 1-D strip along x are determined that satisfy edge conditions at $x = (0, \ell)$ where ℓ is side length. Since the plate is square, and constraints along the four edges are the same, trial functions along y are identical to those along x. Minimizing the error committed in the differential equations of motion by enforcing their orthogonality with the trial functions produces an eigenvalue problem. For simply supported and clamped edges, trial functions also satisfy the plate's edge constraints exactly. However, for free edges, the zero moment constraints are not satisfied identically yielding a stiffer constraint and a higher fundamental resonance than the free plate's.

Section IIB remedies the method in Section IIA when applied to a plate with free edges by augmenting the Lagrangian by certain unsatisfied constraints. The spatially dependent multipliers of these constraints are expanded in terms of the trial functions in Section IIA. Orthogonalizing the augmented equations and constraint equations by the trial functions determines sufficient equations in the generalized coordinates and undetermined multipliers.

Section III compares stress histories of disk and square plate with simply supported edges for different eccentricities r_e. This is followed by histories of the disk with free edges. A stress factor "α_σ" is defined as the ratio of σ_{max} for some r_e to σ_{max} for central impact. Plots of α_σ against r_e reveal regions of stress magnification $(\alpha_\sigma > 1)$, and regions of stress reduction $(\alpha_\sigma < 1)$, depending on plate thickness, lateral dimension and edge constraint. The variation does not follow a simple trend since it depends on the interference between waves radiating from the area of impact and incoherent reflexions from the edges.

I. DISK

Mindlin's plate equations [7] may be written in vector form as

$$\frac{D}{2}\left[(1 - \nu)\nabla^2\Psi + (1 + \nu)\nabla\Phi\right] - \kappa Gh(\Psi + \nabla w) = \frac{\rho h^3}{12}\frac{\partial^2\Psi}{\partial t^2} \tag{1}$$

$$\kappa Gh\left(\nabla^2 w + \Phi\right) + p = \rho h\frac{\partial^2 w}{\partial t^2}$$

$$\Phi = \nabla \cdot \Psi \quad , \quad D = \frac{Eh^3}{12\left(1 - \nu^2\right)} \tag{2}$$

where Ψ is the vector of rotations, w is transverse displacement, (ρ, ν) are density and Poisson ratio, (E,G) are Young's and shear moduli, κ is shear constant, h is thickness, t is time, p is applied pressure, ∇^2 is the Laplacian and ∇ is the gradient operator. Taking the divergence of (1)

$$D\nabla^2\Phi - \kappa Gh\left(\Phi + \nabla^2 w\right) = \frac{\rho h^3}{12}\frac{\partial^2\Phi}{\partial t^2} \tag{3}$$

Eliminating Φ from (2) and (3)

$$\left[\left(\nabla^2 - \frac{1}{c_\varepsilon^{\,2}}\frac{\partial^2}{\partial t^2}\right)\left(\nabla^2 - \frac{1}{c_s^{\,2}}\frac{\partial^2}{\partial t^2}\right) + \frac{1}{c_\varepsilon^{\,2}h^2}\frac{\partial^2}{\partial t^2}\right]w = \left[\frac{1}{D} - \frac{1}{\kappa Gh}\left(\nabla^2 - \frac{1}{c_s^{\,2}}\frac{\partial^2}{\partial t^2}\right)\right]p$$

$$c_\varepsilon^{\,2} = \frac{E}{\rho\left(1 - \nu^2\right)}, \quad c_s^{\,2} = \frac{\kappa G}{\rho} \tag{4}$$

Eliminating $\nabla^2 w$ from (2) and (3) yields

$$\left[D\nabla^2 - \frac{\rho h^3}{12}\frac{\partial^2}{\partial t^2}\right]\Phi = \rho h\frac{\partial^2 w}{\partial t^2} - p \tag{5}$$

Taking the curl of (1)

$$\left[\frac{D}{2}(1-\nu)\nabla^2 - \kappa G h - \frac{\rho h^3}{12}\frac{\partial^2}{\partial t^2}\right](\nabla \times \Psi) = 0 \tag{6}$$

from which it can be inferred that $(\nabla \times \Psi)$ is not a function of w while Ψ may actually be,

$$\Psi = \nabla[g(w)] + \nabla \times \Gamma \tag{7}$$

where Γ is a vector potential for Ψ independent of w. Substituting (7) in (5) using the definition of Φ yields

$$\left[D\nabla^2 - \frac{\rho h^3}{12}\frac{\partial^2}{\partial t^2}\right]\nabla^2 g = \rho h \frac{\partial^2 w}{\partial t^2} \tag{8}$$

Substituting (7) in (6) using the identity

$$\nabla \times \nabla \times A = \nabla(\nabla \cdot A) - \nabla^2 A \tag{9}$$

produces

$$\left[\frac{D}{2}(1-\nu)\nabla^2 - \kappa G h - \rho\frac{h^3}{12}\frac{\partial^2}{\partial t^2}\right]\nabla^2 \Gamma = 0 \tag{10}$$

Defining $\tau = \nabla^2 \Gamma$, reduces (10) to:

$$\left[\nabla^2 - \frac{12\kappa}{h^2} - \frac{2}{(1-\nu)c_\varepsilon^2}\frac{\partial^2}{\partial t^2}\right]\tau = 0 \tag{11}$$

For a solid disk and periodic motions in time with frequency ω, the homogeneous solution of (4) takes the form

$$w(r, \theta, t) = w(r)\cos n\theta \; e^{i\omega t} \tag{12a}$$

$$w(r) = C_1 J_n(\lambda_1 r) + C_2 J_n(\lambda_2 r) \tag{12b}$$

$$\lambda^4 - 2\beta_1 \lambda^2 + \beta_2 = 0$$

$$\beta_1 = \frac{1}{2}\frac{c_\varepsilon^2 + c_s^2}{c_\varepsilon^2 c_s^2}\omega^2 \quad , \quad \beta_2 = \frac{\omega^2}{c_\varepsilon^2}\left(\frac{\omega^2}{c_s^2} - \frac{12}{h^2}\right) \tag{12c}$$

where (r, θ) are radial and circumferential coordinates, n is circumferential wave number, $i = \sqrt{-1}$ and J_n is the Bessel function. Since g is a function of w, and from (8) linear with w, it can be expressed like (12a,b) as

$$g_j(r) = C_g J_n(\lambda_j r) \quad , \qquad \nabla^2 g_j = -\lambda_j^2 g_j \; ; \qquad j = 1,2 \tag{13}$$

Substituting (13) in (8) yields

$$-\left[-\lambda_j^2 + \frac{\omega^2}{c_\varepsilon^2}\right] \lambda_j^2 C_{gj} = -\frac{12\omega^2}{h^2 c_\varepsilon^2} C_j \tag{14}$$

then using (4), equation (14) simplifies to

$$C_{gj} = \frac{1}{\lambda_j^2}\left(-\lambda_j^2 - \frac{\omega^2}{c_s^2}\right) C_j \tag{15}$$

Taking the gradient of (14)

$$\nabla g_j = \left(\frac{\partial}{\partial r} , -\frac{n}{r}\right) C_{gj} \; J_n(\lambda_j r) \tag{16}$$

Furthermore, since τ and Ψ are orthogonal and Ψ is in the plane of the disk then $\tau = (0, 0, \tau_z)$ and

$$\tau_z = C_\tau J_n(\lambda_\tau r) \tag{17}$$

Substituting (17) in (11) produces the dispersion relation

$$\lambda_\tau^2 = \frac{2\omega^2}{(1 - \nu) c_\varepsilon^2} - \frac{12\kappa}{h^2} \tag{18}$$

Equation (18) exhibits a cut-off above

$$\omega_\tau = \sqrt{6k(1 - \nu)} \frac{c_\varepsilon}{h} = \frac{\sqrt{12} c_s}{h} \tag{19}$$

which is the same as that in (12c). Finally, using λ_τ in (18) and since Γ

and τ are parallel then $\Gamma = (0,0,\Gamma_z)$, and

$$\Gamma_z = C_\Gamma J_n(\lambda_\tau r) \tag{20}$$

Taking the curl of (20)

$$\nabla \times \Gamma = \left(\frac{n}{r}, -\frac{\partial}{\partial r}\right) C_\Gamma J_n(\lambda_\tau r) \tag{21}$$

Substituting (16) and (21) in (7) determines the solutions

$$\psi_r(r,\theta,t) = \cos n\theta\ e^{i\omega t}\left\{\sum_{j=1}^{2} C_{gj}\lambda_j J_n'(\lambda_j r) + \frac{n}{r} C_\Gamma J_n(\lambda_\tau r)\right\} \tag{22a}$$

$$\psi_\theta(r,\theta,t) = \sin n\theta\ e^{i\omega t}\left\{\sum_{j=1}^{2} -\frac{n}{r} C_{gj} J_n(\lambda_j r) - \lambda_\tau C_\Gamma J_n'(\lambda_\tau r)\right\} \tag{22b}$$

$$w(r,\theta,t) = \cos n\theta\ e^{i\omega t}\sum_{i=1}^{2} C_j J_n(\lambda_j r) \tag{22c}$$

where C_{gi} is related to C_i by (15).

Moments and shear resultants are expressed in terms of (ψ_r, ψ_0, w) as

$$M_{rr} = D\left[\frac{\partial \psi_r}{\partial r} + \nu\left(\frac{\psi_r}{r} + \frac{1}{r}\frac{\partial \psi_\theta}{\partial \theta}\right)\right] \tag{23a}$$

$$M_{\theta\theta} = D\left[\nu\frac{\partial \psi_r}{\partial r} + \frac{\psi_r}{r} + \frac{1}{r}\frac{\partial \psi_\theta}{\partial \theta}\right] \tag{23b}$$

$$M_{r\theta} = \frac{D(1-\nu)}{2}\left[\frac{1}{r}\frac{\partial \psi_r}{\partial \theta} + \frac{\partial \psi_\theta}{\partial r} - \frac{\psi_\theta}{r}\right] \tag{23c}$$

$$Q_r = \kappa G h\left(\frac{\partial w}{\partial r} + \psi_r\right) \tag{23d}$$

$$Q_\theta = \kappa G h\left(\frac{1}{r}\frac{\partial w}{\partial \theta} + \psi_\theta\right) \tag{23e}$$

For a solid disk with radius r_d, normal stresses on the disk surface are related to moment resultants by

$$\sigma_{rr} = \frac{6M_{rr}}{h^2}, \qquad \sigma_{\theta\theta} = \frac{6M_{\theta\theta}}{h^2}, \qquad \sigma_{r\theta} = \frac{6M_{r\theta}}{h^2} \tag{24a}$$

and shear stresses along the neutral plane are related to shear resultants by

$$\tau_{rz} = Q_r / h, \qquad \tau_{\theta z} = Q_\theta / h \tag{24b}$$

For a free edge

$$M_{rr}(r_d) \equiv M_{r\theta}(r_d) \equiv Q_r(r_d) = 0 \tag{25a}$$

and for a simply supported edge

$$M_{rr}(r_d) \equiv \psi_\theta(r_d) \equiv w(r_d) = 0 \tag{25b}$$

Substituting (22) in (23) then in either (25a) or (25b) produces the implicit eigenvalue problem

$$B(a)\,\mathbf{c} = \mathbf{0} \tag{26a}$$

where $\mathbf{B}$ is a 3x3 matrix of the fundamental solutions in (Ψ_r, Ψ_θ, w) and their first derivatives, and

$$\mathbf{c} = \left\{c_{g_1}, c_{g_2}, c_\Gamma\right\}^T \tag{26b}$$

Expanding $\{\Psi_r, \Psi_\theta, w\}$ in terms of the eigenset $\{\omega_{nj}\,;\ \eta_{rnj}, \eta_{\theta nj}, \varphi_{nj}\}$

$$\psi_r(r,\theta,t) = \sum_{n=0}^{N} \sum_{j=1}^{M} a_{nj}\, \eta_{rnj}(r) \cos n\theta \tag{27a}$$

$$\psi_\theta(r,\theta,t) = \sum_{n=0}^{N} \sum_{j=1}^{M} a_{nj}\, \eta_{\theta nj}(r) \sin n\theta \tag{27b}$$

$$w(r,\theta,t) = \sum_{n=0}^{N} \sum_{j=1}^{M} a_{nj}\, \varphi_{nj}(r) \cos n\theta \tag{27c}$$

where (M,N) is the number of radial and circumferential modes in the expansion. Substituting in (1) and (2) and enforcing the orthogonality of the eigenfunctions yields a set of uncoupled differential equations in the generalized coordinates a_{nj}

$$\ddot{a}_{nj} + \omega^2{}_{nj}\, a_{nj} = -\frac{\pi(1+\delta_{n0})}{N_{nj}} p_{nj} f(t) \tag{28}$$

$$N_{nj} = \rho h \langle \varphi_{nj} | \varphi_{nj} \rangle + \frac{\rho h^3}{12}\left[\langle \eta_{rnj} | \eta_{rnj} \rangle + \langle \eta_{\theta nj} | \eta_{\theta nj} \rangle\right]$$

where δ_{n0} is the Knonecker delta, and f(t) is time dependence of the forcing pulse. For a circular footprint of radius r_p and eccentricity r_e (see Fig. 1)

$$p_{nj} = 2p_o \int_0^{\theta_e}\int_{r_1}^{r_2} \varphi_{nj}(r) \cos n\theta \; r dr \; d\theta$$

$$\theta_e = \sin^{-1}(r_p / r_e)$$

$$r_{1,2} = \frac{1}{2}\left[r_e \cos\theta \pm \sqrt{(r_e\cos\theta)^2 - 4\left(r_e{}^2 - r_p{}^2\right)}\right] \tag{29}$$

The solution of (28) can be expressed as a Duhamel integral

$$a_{nj}(t) = -\frac{\pi(1+\delta_{n0})}{\omega_{nj} N_{nj}} p_{nj} \int_0^t f(\tau) \sin \omega_{nj}(t-\tau) d\tau \tag{30}$$

IIA. SQUARE PLATE WITH RESTRAINED EDGES

In Cartesian coordinates, Mindlin's equations are given by (1) and (2) with

$$\Psi = \{\psi_x, \psi_y\}^T \quad , \quad \Phi = \frac{\partial \psi_x}{\partial x} + \frac{\partial \psi_y}{\partial y} \tag{31}$$

where (x,y) is a rectangular coordinate system with origin at the lower left corner of the square. Since solutions along x and y are not separable, a Galerkin approximation is adopted. Trial functions (φ_x, η_x) are defined on strips along x satisfying the edge constraints at $x = (0, \ell)$ and the 1-D Mindlin's equations

$$D \frac{\partial^2 \eta_x}{\partial x^2} - \kappa G h \left(\eta_x + \frac{\partial \varphi_x}{\partial x} \right) = -\frac{\rho h^3}{12} \omega^2 \eta_x \tag{32a}$$

$$\kappa G h \left(\frac{\partial^2 \varphi_x}{\partial x^2} + \frac{\partial \eta_x}{\partial x} \right) = -\rho h \omega^2 \varphi_x \tag{32b}$$

For the square plate, trial functions (φ_y, η_y) along y are identical to (φ_x, η_x) since edge constraints are the same on all four edges. Expand $\{\Psi_x, \Psi_y, w\}$ in terms of these trial functions:

$$\psi_x(x, y, t) = \sum_{i=1}^{N} \sum_{j=1}^{N} a_{ij}(t) \ \eta_{xi}(x) \ \varphi_{yi}(y) \tag{33a}$$

$$\psi_y(x, y, t) = \sum_{i=1}^{N} \sum_{j=1}^{N} a_{ij}(t) \ \varphi_{xi}(x) \ \eta_{yi}(y) \tag{33b}$$

$$w(x, y, t) = \sum_{i=1}^{N} \sum_{j=1}^{N} a_{ij}(t) \ \varphi_{xi}(x) \ \varphi_{yi}(y) \tag{33c}$$

where N is the number of trial functions in the expansion. Substituting (33) into equations (1) and (2) gives

$$\mathcal{D}_1 \equiv \sum_i \sum_j \left\{ \frac{D}{2} \left[2\eta''_{xi} \varphi_{yi} + (1 - \nu) \eta_{xi} \varphi''_{yi} + (1 + \nu) \varphi'_{xi} \eta'_{yi} \right] a_{ij} \right.$$
$$\left. - \kappa G h \left(\eta_{xi} \varphi_{yi} + \varphi'_{xi} \varphi_{yi} \right) a_{ij} - \frac{\rho h^3}{12} \eta_{xi} \varphi_{yi} \ddot{a}_{yi} \right\} = 0 \tag{34a}$$

$$\mathfrak{D}_2 \equiv \sum_i \sum_j \left\{ \frac{D}{2}\left[(1-\nu)\varphi''_{xi}\eta_{yj} + 2\varphi_{xi}\eta''_{yj} + (1+\nu)\eta'_{xi}\varphi'_{yi}\right] a_{ij} \right.$$

$$\left. - \kappa G h\left(\varphi_{xi}\eta_{yi} + \varphi_{xi}\varphi'_{yi}\right) a_{ij} - \frac{\rho h^3}{12}\varphi_{xi}\eta_{yi}\ddot{a}_{ij} \right\} = 0 \tag{34b}$$

$$\mathfrak{D}_3 \equiv \sum_i \sum_j \left\{ \kappa G h\left(\varphi''_{xi}\varphi_{yi} + \varphi_{xi}\varphi''_{yi} + \eta'_{xi}\varphi_{yi} + \varphi_{xi}\eta'_{yi}\right) a_{ij} - \rho h\,\varphi_{xi}\varphi_{yi}\ddot{a}_{ij} \right\} = -p \tag{34c}$$

Where $(\,)'$ is derivative w.r.t. the argument. Multiply $\mathfrak{D}_1$ in (34a) by $(\eta_{xm}\varphi_{yn})$, $\mathfrak{D}_2$ in (34b) by $(\varphi_{xm}\eta_{yn})$ and $\mathfrak{D}_3$ in (34c) by $(\varphi_{xm}\eta_{yn})$, integrate over the square's surface, then add the three integrated equations to produce

$$A_1\ddot{\mathbf{a}} + A_2\mathbf{a} = \boldsymbol{F}\, f(t)$$

$$\boldsymbol{F} = \left\{ 2\int_0^{\theta_e}\int_{r_1}^{r_2} \varphi_{xm}(r\cos\theta)\,\varphi_{yn}(r\sin\theta)\, r\,dr\,d\theta \right\}^T \tag{35}$$

where the integral is over a circular footprint with eccentricity r_e as defined in (29), and f(t) is the time dependence of the forcing pulse. Pre-multiplying (35) by A_1^{-1}

$$\ddot{\mathbf{a}} + \overline{A}\mathbf{a} = \overline{\boldsymbol{F}}\,\mathbf{f(t)}$$
$$\overline{A} = A_1^{-1}A_2 \quad , \quad \overline{\boldsymbol{F}} = A_1^{-1}\boldsymbol{F} \tag{36}$$

To diagonalize $\overline{\mathbf{A}}$, apply the transformation

$$\mathbf{a} = \mathbf{V}\mathbf{a}^* \Leftrightarrow \mathbf{a}^* = \mathbf{V}^{-1}\mathbf{a} \tag{37}$$

$$\Rightarrow \ddot{\mathbf{a}}^* + \mathbf{V}^{-1}\overline{A}\,\mathbf{V}\,\mathbf{a}^* = \mathbf{V}^{-1}\overline{\boldsymbol{F}}\, f(t) \tag{38}$$

and impose the condition

$$\mathbf{V}^{-1}\,\overline{A}\,\mathbf{V} = \omega^2$$

This requires that **V** be the eigen-vectors of $\overline{A}$, <u>i.e.</u>

$$\left\lfloor \overline{A} - \omega^2 \right\rfloor \mathbf{V} = \mathbf{0}$$

and ω the diagonal matrix of the corresponding eigen-values.

Equations (36) then decouple in the generalized coordinate vector $\mathbf{a}^*$

$$\ddot{\mathbf{a}}^* + \omega^2 \mathbf{a}^* = \mathbf{V}^{-1}\, \overline{\mathbf{F}}\, f(t) \tag{41}$$

with solution of each component in the form of equation (30). Moment and shear resultants and corresponding stresses are the Cartesian counterpart to (23) and (24):

$$M_{xx} = D\left(\frac{\partial \psi_x}{\partial x} + \nu \frac{\partial \psi_y}{\partial y}\right) \quad \Rightarrow \sigma_{xx} = 6M_{xx} / h^2 \tag{42a}$$

$$M_{yy} = D\left(\frac{\partial \psi_y}{\partial y} + \nu \frac{\partial \psi_x}{\partial x}\right) \quad \Rightarrow \sigma_{yy} = 6\, M_{yy} / h^2 \tag{42b}$$

$$M_{xy} = \frac{D(1-\nu)}{2}\left(\frac{\partial \psi_x}{\partial y} + \frac{\partial \psi_y}{\partial x}\right) \quad \Rightarrow \sigma_{xy} = 6M_{xy} / h^2 \tag{42c}$$

$$Q_x = \kappa G h\left(\frac{\partial w}{\partial x} + \psi_x\right) \quad \Rightarrow \tau_{xz} = Q_x / h \tag{42d}$$

$$Q_y = \kappa G h\left(\frac{\partial w}{\partial y} + \psi_y\right) \quad \Rightarrow \tau_{yz} = Q_y / h \tag{42e}$$

They are expressed in terms of modal quantities by (33) noting that $\mathbf{a}$ is related to $\mathbf{a}^*$ by (37). For simply supported and clamped edges, expressions (33) satisfy the edge constraints identically. However, for free edges

$$M_{xx}(x_c, y) \equiv M_{yy}(x, y_c) = 0 \tag{43a}$$

$$M_{xy}(x_c, y) \equiv M_{xy}(x, y_c) = 0 \tag{43b}$$

$$Q_x(x_c, y) \equiv Q_y(x, y_c) = 0 \tag{43c}$$

where $x_c = (0, \ell)$ and $y_c = (0, \ell)$. Only (43c) is satisfied identically by these trial functions. For example

$$\begin{aligned} M_{xx}(0, y) &= D\sum_i \sum_j \left(\eta'_{xi}(0)\, \varphi_{yi}(y) + \nu \varphi_{xi}(0)\, \eta'_{yi}(y)\right) a_{ij} \\ &= D\sum_i \sum_j \nu \varphi_{xi}(0)\, \eta'_{yi}(y)\; a_{ij} \end{aligned} \tag{44}$$

which will not in general vanish. This error is equivalent to a spring loaded edge resisting rotation which stiffens the plate and raises its resonances.

IIB. SQUARE PLATE WITH FREE EDGES

An alternative approach that satisfies (43a,b) in the average uses Lagrange undetermined multipliers. Let each of the 8 edge constraint in (43a,b) not identically satisfied by the trial functions be expressed by an equation in the form

$$\Omega\left(w, \psi_x, \psi_y, \frac{\partial\psi_x}{\partial x}, \frac{\partial\psi_y}{\partial y}, \frac{\partial\psi_x}{\partial y}, \frac{\partial\psi_y}{\partial x}\right) = 0 \tag{45}$$

There the modified Lagrangian "L" which accounts for these unmet constraints can be written as

$$L = T - W + \sum_{k=1}^{8} \lambda_k \; \Omega_k \tag{46}$$

$$T = \int_y\int_x \left[\frac{\rho h^3}{24}\left(\dot\psi_x^2 + \dot\psi_y^2\right) + \frac{\rho h}{2}\dot w^2\right] dxdy$$

$$W = \int_y\int_x \left\{\frac{D}{4}(1+\nu)\left(\psi_{x,x} + \psi_{y,y}\right)^2 + \frac{\kappa G h}{2}\left[\left(\psi_x + w_x\right)^2 + \left(\psi_y + w_y\right)^2\right]\right.$$

$$\left. + \frac{D(1-\nu)}{4}\left[\left(\psi_{x,x} - \psi_{y,y}\right)^2 + \left(\psi_{x,y} + \psi_{y,x}\right)^2\right]\right\} dxdy$$

where $(\;)_{,x}$ is partial derivative and (T,W) are kinetic and strain energy, and $\lambda_k(x,y)$ are the Lagrange undetermined multipliers. For each unknown $u \in \{\psi_x, \psi_y, w\}$ Lagrange-Euler equation states that

$$\frac{d}{dx}\left(\frac{\partial W}{\partial(\partial u/\partial x)}\right) + \frac{d}{dy}\left(\frac{\partial W}{\partial(\partial u/\partial y)}\right) - \frac{\partial W}{\partial u} - \frac{d}{dt}\frac{\partial T}{\partial \dot u}$$

$$+ \sum_{k=1}^{8}\left\{\lambda_k\frac{\partial\Omega_k}{\partial u} - \frac{d}{dx}\left[\lambda_k\frac{\partial\Omega_k}{\partial(\partial u/\partial x)}\right] - \frac{d}{dy}\left[\lambda_k\frac{\partial\Omega_k}{\partial(\partial u/\partial y)}\right]\right\} = 0 \tag{47}$$

After substituting T and W from (46) into the first part of (47) and integrating by parts yields the differential operators $\mathcal{D}_i, i = 1,3$ in (34).

The second part accounts for the unsatisfied constraints. Applying (47) when $\Omega_1 = M_{yy}$, $\Omega_2 = M_{xx}$ and $\Omega_3 = M_{xy}$ in (42) yields

$$\mathfrak{D}_1(w, \psi_x, \psi_y) - D\left[\nu \frac{\partial \lambda_{1,2}}{\partial_x} + \frac{1-\nu}{2} \frac{\partial \lambda_{3,4}}{\partial y}\right] \tag{48a}$$

$$\mathfrak{D}_2(w, \psi_x, \psi_y) - D\left[\nu \frac{\partial \lambda_{5,6}}{\partial y} + \frac{1-\nu}{2} \frac{\partial \lambda_{7,8}}{\partial x}\right] \tag{48b}$$

$$\mathfrak{D}_3(w, \psi_x, \psi_y) = -p(x, y)\ f(t) \tag{48c}$$

On edges parallel to the x axis,

$$\lambda(x, y) = \lambda(x)\ \delta(y - y_c) \quad ; \qquad y_c = (0, \ell) \tag{49a}$$

while on edges parallel to the y axis,

$$\lambda(x, y) = \lambda(y)\ \delta(x - x_c) \quad ; \qquad x_c = (0, \ell) \tag{49b}$$

where in (49) δ is the Dirac delta function. Expanding $\lambda(x)$ and $\lambda(y)$ in the trial functions

$$\lambda(x) = \sum_{k=1}^{N_c} \left(\lambda_k^{(1)} \varphi_{xk}(x) + \lambda_k^{(2)} \eta_{xk}(x)\right) \tag{50a}$$

$$\lambda(y) = \sum_{k=1}^{N_c} \left(\lambda_k^{(1)} \varphi_{yk}(y) + \lambda_k^{(2)} \eta_{xk}(y)\right) \tag{50b}$$

where $N_c \le N$. Substituting (49) and (50) into (48) yields

$$\begin{aligned}\mathfrak{D}_1 = D\sum_{k=1}^{N_c} \sum_{c=1}^{2} \Big\{ &\nu\left(\lambda_{ck}^{(1)} \varphi'_{xk} + \lambda_{ck}^{(2)} \eta'_{xk}\right)\delta(y - y_c) \\ &+ \frac{1-\nu}{2}\left(\lambda_{ck}^{(3)} \varphi'_{yk} + \lambda_{ck}^{(4)} \eta'_{yk}\right) \delta(x - x_c)\Big\}\end{aligned} \tag{51a}$$

$$\begin{aligned}\mathfrak{D}_2 = D\sum_{k=1}^{N_c} \sum_{c=1}^{2} \Big\{ &\nu\left(\lambda_{c}^{(5)} \varphi'_{yk} + \lambda_{ck}^{(6)} \eta'_{y}\right)\delta(x - x_c) \\ &+ \frac{1-\nu}{2}\left(\lambda_{ck}^{(7)} \varphi'_{xk} + \lambda_{ck}^{(8)} \eta'_{xk}\right) \delta(y - y_c)\Big\}\end{aligned} \tag{51b}$$

$$\mathfrak{D}_3 = -p_0(x, y)\ f(t) \tag{51c}$$

Since geometry and edge constraints are symmetric about axes with origin at the square's center, trial functions may be segregated into symmetric and anti-symmetric sets. It follows that

$$\int_0^{\ell} \varphi_{xi}\ \varphi'_{xj}\ dx \equiv \int_0^{\ell} \eta_{xi}\ \eta'_{xj}\ dx = 0 \tag{52a}$$

$$\int_0^{\ell} \varphi_{yi}\varphi'_{yj}\ dy \equiv \int_0^{\ell} \eta_{yi}\eta'_{yj}\ dx = 0 \tag{52b}$$

Multiplying (51a) by $\left(\eta_{xm}\varphi_{yn}\right)$, (51b) by $\left(\varphi_{xm}\eta_{yn}\right)$ and (51c) by $\left(\varphi_{xm}\varphi_{yn}\right)$ then integrating over the square's surface allowing for (52) reduces (51) to

$$\overline{\mathfrak{D}}_1 = D\left\{\sum_{c=1}^{2}\left[\nu\varphi_{yn}(y_c)\sum_{k=1}^{N_c}\gamma_{mk}\lambda_{ck} + \frac{1-\nu}{2}\eta_{xm}(x_c)\sum_{k=1}^{N_c}\beta_{nk}\lambda_{(c+2)k}\right]\right\} \tag{53a}$$

$$\overline{\mathfrak{D}}_2 = D\left\{\sum_{c=1}^{2}\left[\nu\varphi_{xm}(x_c)\sum_{k=1}^{N_c}\gamma_{nk}\lambda_{(c+4)k} + \frac{1-\nu}{2}\eta_{yn}(y_c)\sum_{k=1}^{N_c}\beta_{mk}\lambda_{(c+6)k}\right]\right\} \tag{53b}$$

$$\overline{\mathfrak{D}}_3 = -f(t)\int_0^{\ell}\int_0^{\ell} p_0(x, y)\ \varphi_{xm}(x)\ \varphi_{yn}(y)\ dxdy \tag{53c}$$

$$\gamma_{ij} = \int_0^{\ell} \eta_{xi}\varphi'_{xj}dx = \int_0^{\ell} \eta_{yi}\ \varphi'_{yi}\ dy \tag{53d}$$

$$\beta_{ij} = \int_0^{\ell} \varphi_{xi}\eta'_{xj}dx = \int_0^{\ell} \varphi_{yi}\ \eta'_{yi}\ dy \tag{53e}$$

In (53), $\overline{\mathfrak{D}}_k$ are the $\mathfrak{D}_k$ after the same operations. Adding (53a,b,c) produces

$$A_1\ddot{\mathbf{a}} + A_2\mathbf{a} + B\lambda = \mathbf{F}\, f(t) \tag{54}$$

where $\mathbf{A}_1$ and $\mathbf{A}_2$ are $N^2 \times N^2$ matrices, $\mathbf{B}$ is $N^2 \times 8N_c$ with $8N_c$ additional unknowns λ_{ck}, c = 1, 8. The remaining $8N_c$ equations are found in the constraints themselves.

For $M_{xx}(x_c, y) = 0$, substituting (33) in (42a), multiplying by $\varphi_{yk}(y)$ and integrating along edges $x = x_c$ yields two equations for each $k = 1, N_c$:

$$\sum_i \sum_j \left\{\eta'_{xi}(x_c)\alpha_{jk} + \nu\varphi_{xi}(x_c)\beta_{kj}\right\} a_{ij} = 0 \quad ; \quad x_c = (0, \ell)$$

$$\alpha_{jk} = \int_0^\ell \varphi_{yi}\varphi_{yk}\,dy \quad , \quad \overline{\alpha}_{jk} = \int_0^\ell \eta_{xj}\eta_{xk}\,dx \tag{55a}$$

For $M_{yy}(x, y_c) = 0$, $M_{xy}(x_c, y) = 0$ and $M_{xy}(x, y_c) = 0$, a similar procedure yields the remaining $6N_c$ equations:

$$\sum_i \sum_j \left\{\eta'_{yj}(y_c)\alpha_{ki} + \nu\varphi_{yi}(y_c)\beta_{ki}\right\} a_{ij} = 0 \quad ; \quad y_c = (0, \ell) \tag{55b}$$

$$\sum_i \sum_j \left\{\varphi'_{xi}(x_c)\overline{\alpha}_{kj} + \eta_{xi}(x_c)\gamma_{kj}\right\} a_{ij} = 0 \quad ; \quad x_c = (0, \ell) \tag{55c}$$

$$\sum_i \sum_j \left\{\eta_{yi}(y_c)\gamma_{\ell i} + \varphi'_{yj}(y_c)\overline{\alpha}_{\ell i}\right\} a_{ij} = 0 \quad ; \quad y_c = (0, \ell) \tag{55d}$$

The four sets in (55) when assembled in matrix form become

$$\mathbf{C}\mathbf{a} = \mathbf{0} \tag{56}$$

where $\mathbf{C}$ is an $8N_c \times N^2$ matrix.

Since the trial functions are segregated into odd and even functions and each set can be solved separately, then constraints on side x=0 automatically carry over to its opposite at $x = \ell$ and only one constraint is used. This also applies to constraints on sides $y = 0, \ell$. This reduces the number of λ's to $4N_c$. It also reduces the size of **C** to $4N_c \times N^2$.

Equations (54) and (56) when combined are sufficient to solve for the N^2 generalized coordinates **a** and the $4N_c$ Lagrange multipliers λ. The constraint equations may be used to eliminate an equal number of a_{ij}. Partition (54) and the vector of unknowns in the following way

$$\mathbf{a} = \begin{Bmatrix} \mathbf{a}_k \\ \mathbf{a}_e \end{Bmatrix} \ , \ \mathbf{B} = \begin{Bmatrix} \mathbf{B}_k \\ \mathbf{B}_e \end{Bmatrix} \ , \ \mathbf{F} = \begin{Bmatrix} \mathbf{F}_k \\ \mathbf{F}_e \end{Bmatrix} \tag{57a}$$

$$\mathbf{A}_{1,2} = \begin{Bmatrix} \mathbf{A}_{kk} & \mathbf{A}_{ke} \\ \mathbf{A}_{ek} & \mathbf{A}_{ee} \end{Bmatrix}_{1,2} \ , \ \mathbf{C} = \left[\mathbf{C}_k \mathbf{C}_e\right] \tag{57b}$$

Then

$$\mathbf{A}_{kk1}\ddot{\mathbf{a}}_k + \mathbf{A}_{ke1}\ddot{\mathbf{a}}_e + \mathbf{A}_{kk2}\mathbf{a}_k + \mathbf{A}_{ke2}\mathbf{a}_e + \mathbf{B}_k\lambda = \mathbf{F}_k f(t) \tag{58a}$$

$$\mathbf{A}_{ek1}\ddot{\mathbf{a}}_k + \mathbf{A}_{ee1}\ddot{\mathbf{a}}_e + \mathbf{A}_{ek2}\mathbf{a}_k + \mathbf{A}_{ee2}\mathbf{a}_e + \mathbf{B}_e\lambda = \mathbf{F}_e f(t) \tag{58b}$$

$$\mathbf{C}_k\mathbf{a}_k + \mathbf{C}_e\mathbf{a}_e = 0 \tag{58c}$$

where the lengths of $\mathbf{a}_e$ and $\mathbf{F}_e$ are the same as λ. Solving for λ in (58b)

$$\lambda = \mathrm{B}_e^{-1}\left[\mathbf{F}_e f(t) - \left(\mathbf{A}_{ek1}\ddot{\mathbf{a}}_k + \mathbf{A}_{ee1}\ddot{\mathbf{a}}_e + \mathbf{A}_{ek2}\mathbf{a}_k + \mathbf{A}_{ee2}\mathbf{a}_e\right)\right] \tag{59}$$

then substituting back into (58a) yields

$$\overline{\mathbf{A}}_{kk1}\ddot{\mathbf{a}}_k + \overline{\mathbf{A}}_{ke1}\ddot{\mathbf{a}}_e + \overline{\mathbf{A}}_{kk2}\mathbf{a}_k + \overline{\mathbf{A}}_{ke2}\mathbf{a}_e = \mathbf{F}_c f(t) \tag{60}$$

$$\overline{\mathbf{A}}_{kki} = \mathbf{A}_{kki} - \mathbf{B}_k\mathbf{B}_e^{-1}\mathbf{A}_{eki} \ , \ i = 1,2$$

$$\overline{\mathbf{A}}_{kei} = \mathbf{A}_{kei} - \mathbf{B}_k\mathbf{B}_e^{-1}\mathbf{A}_{eei} \ , \ i = 1,2$$

$$\mathbf{F}_c = \mathbf{F}_k - \mathbf{B}_k\mathbf{B}_e^{-1}\mathbf{F}_e$$

Eliminating $\ddot{\mathbf{a}}_e$ and $\mathbf{a}_e$ from (58c)

$$\mathbf{a}_e = -\mathbf{C}_e^{-1}\mathbf{C}_k\mathbf{a}_k \tag{61}$$

then substituting (60) yields the condensed equations

$$
\begin{aligned}
&\mathbf{A}_{c1}\ddot{\mathbf{a}}_k + \mathbf{A}_{c2}\mathbf{a}_k = \mathbf{F}_c\, f(t) \\
&\mathbf{A}_{ci} = \overline{\mathbf{A}}_{kki} - \overline{\mathbf{A}}_{kei}\,\mathbf{C}_e^{-1}\mathbf{C}_k \qquad ; \qquad i = 1,2
\end{aligned}
\tag{62}
$$

Equations (62) are analogous to the unconstrained equations (35) derived in Section IIA. The total solution can then be reconstructed by $\{\mathbf{a}_k, \mathbf{a}_e\}$ from (61) and (62). The steps adopted in diagonalizing $\mathbf{A}_{c1}^{-1}\,\mathbf{A}_{c2}$ are identical to those used in equations (35) through (41) of Section IIA.

RESULTS

Results are divided into two parts. The first part compares disk and plate stress histories $(\sigma_{rr}, \sigma_{\theta\theta}, t_{rz})$ where plate side length equals disk diameter. The edges are simply supported. The purpose is to investigate in detail how response is affected by shape of boundary at different eccentricities of center of impact. Further comparisons are made with free edges to determine the effect of edge constraint. The second part studies the sensitivity of maximum transient stress σ_{max} to eccentricity at various lateral dimensions, thicknesses, pulse widths, and edge constraints. In all cases, the time dependence f(t) of the forcing pulse is trapezoidal with 5μs rise and fall times, and either 40μs or 15μs plateau of unit magnitude, yielding a total pulse width of 50μs and 25μs respectively. The 50μs is typical of a pressure pulse produced by a 50 caliber rifle projectile at 3000 ft/sec. The forcing pressure is uniform over a circular footprint with radius $r_p = 0.25"$ and eccentricity r_e. Stress histories are computed at four radial positions or "sensors" as shown in Fig. 1. Sensors 1 and 4 are symmetric about center of impact and should yield identical histories prior to reflexions from the edge. Sensor 2 is on the footprint perimeter and measures maximum shear stress τ_{rz} along the neutral plane. Sensor 3 is at the center of impact and measures maximum normal stresses σ_{rr} and $\sigma_{\theta\theta}$ on the plate's surface. Sensor 5 replaces sensor 4 only when footprint touches the edge. Disks and square plates are made of AlN with properties

$$E = 40\times10^6\,\text{lb}/\text{in}^2 \quad , \quad \rho = 3.04\times10^{-4}\,\text{lb sec}^2/\text{in}^4 \quad , \quad \nu = 0.25$$

Both disk and plate have the same thickness and lateral dimensions, i.e. $h = 0.5"$ and $\ell = 2r_d = 6"$.

Fig. 2a,b plot resonant frequency Ω in Hz against circumferential wave number n with radial wave number m as parameter for disks with simply supported and free edges. Shear modes are omitted since they do not contribute to response. For n>2, Ω varies almost linearly with n, and as expected, for fixed (m,n) Ω for simply supported edges is higher than Ω for free edges since the former yields a stiffer boundary for $n \geq 2$. For free edges Ω lines undergo a reversal in slope between n=1 and n=2 as shown in Fig. 2b.

Fig. 3,4 and 5 compare disk and plate stress histories for r_e = 0",1" and 2.5" respectively, for simply supported edges. For r_e=0 (see Fig. 3a→3f), disk and plate reach the same maxima for all stress components. For the disk, reflexions from the edge produce strong fluctuations in response because, in radiating from the center of impact, each wave front is reflected from the edge at the same time producing a condition of the reflected waves called coherance (see Fig. 3a,b,c). For r_e=1" (see Fig. 4a→4f) maxima of both geometries are again the same. Histories at sensors 1 and 4 coincide in the first 15 μs from impact prior to reflexions from the edge. For r_e=2.5" (see Fig. 5a→5f), the only change is that histories at sensors 1 and 4 never coincide because sensor 4 is at the edge. Stress histories resemble the trapezoidal shape of the forcing pulse because it is more important than the reflected waves in determining the shape of the response.

Figures 6,7,8 and 9 plot histories of the disk with free edges for r_e=0", 1", 2.5" and 2.75". Here, maximum stress is higher than that for simply supported edges. For r_e=2.5" (see Fig. 8a,b,c), σ_{rr} is negative at sensor 1, and becomes positive at sensors 2 and 3. As center of impact approaches the free edge, it bends a sector of the disk like a cantilever producing negative flexural stress σ_{rr} at sensors remote from the edge (see Fig. 8a). This is called the cantilever effect. For r_e=2.75" (see Fig. 9a,b,c), both sensors 1 and 2 record negative σ_{rr} as the cantilever sector of the disk is more flexible because its cord is shorter. This is also evidenced by the larger peak magnitude of σ_{rr} (compare Fig. 8a and 9a). Although σ_{rr} diminishes with r_e, $\sigma_{\theta\theta}$ rises with r_e.

To study how the various parameters affect peak stress response σ_{max}, let the stress factor α_σ be defined as:

$$\alpha_\sigma(r_e) = \sigma_{max}(r_e) / \sigma_{max}(0)$$

An $\alpha_\sigma > 1$ means a magnification from the situation of central impact, and an $\alpha_\sigma < 1$ means a reduction. The feducial $\sigma_{max}(0)$ for a disk with simply supported edges is plotted against h with r_d as parameter in Fig. 10. For fixed r_d, the σ_{max} line appears inversely proportional to h^2. This is consistent with the approximation derived in Ref. [3] for σ_{max} based on the approximate model of an expanding cone of influence:

$$\sigma_{zz}(0,t) = \sigma_{\theta\theta}(0,t) \approx \frac{3(1+\nu)}{2} p_0 \frac{r_p^2}{h^2}\left[\ell n\left(\frac{r_p}{\tilde{\ell}}\right) - \frac{1}{4}\left(\frac{r_p}{\tilde{\ell}}\right)^2\right]$$

$$\tilde{\ell} = 1.25\left(\frac{\pi c_\varepsilon}{2\sqrt{3}} ht\right)^{1/2} + 1.25\, r_p$$

where c_ε is defined in (4) and p_0 in (29).

Figure 10 also shows that increasing r_d reduces σ_{max} for a fixed h because reflected waves contribute less to total stress. In fact, depending on pulse width of Δt_ε there is a threshold r_d above which σ_{max} does not change [3]. Figure 11a plots α_σ against r_e/r_p with h as parameter for a disk with simply supported edges, r_d=3″, and 0.25" ≤ h ≤ 1". For h=0.4″ and 0.5″, α_σ rises above unity, and well above the other h's. As r_e approaches the edge, α_σ diminishes smoothly for all h. Fig. 11b plots α_σ for h=0.5″ and two Δt_f's. The shapes of the two curves are similar while the maximum α_σ's occur at different r_e's. Fig. 12 plots α_σ for r_d=2″. There, α_σ is always below unity. The plots of α_σ in Fig. 13a,b are for a disk with free edges. α_σ reaches a minimum near r_e/r_p=8, then rises smoothly with r_e for all h. This rise is consistent with the cantilever effect. In general, the shape of α_σ does not follow trends predictable by simplified models since it depends on the interference between waves radiating from the footprint and incoherent reflexions from the edges. The interference is a function of disk geometry, eccentricity and pulse width.

REFERENCES

[1] M. El-Raheb, "Transient elastic waves in layered media: One-dimensional analysis", J. Acoust. Soc. Am. **94**, 172-184 (1993).

[2] M. El-Raheb, "Simplified models for transient uniaxial waves in a layered periodic stack", Int. J. Solids Struct. **34** (23), 2969-2990, (1997).

[3] M. El-Raheb, "Flexural waves in a disk soon after impact", J Acoust. Soc. Am. **96**, 221-234 (1994).

[4] M. El-Raheb and P. Wagner, "Transient waves in a thick disk", J Acoust. Soc. Am. **95**, 3287-3299 (1994).

[5] M. El-Raheb and P. Wagner, "Transient elastic waves in finite layered media Two dimensional axisymmetric analysis", J. Acoust. Soc. Am. **99**, 3513-3527 (1996).

[6] M. El-Raheb, "Simplified models of transient elastic waves in finite axisymmetric layered media", J. Acoust. Soc. Am., **104**, 3200-3221 (1998).

[7] R. D. Mindlin, "Influence of rotary inertia and shear deformation on flexural motions of isotropic elastic disks", Trans. ASME J. Appl. Mech. **73**, 31-38 (1951).

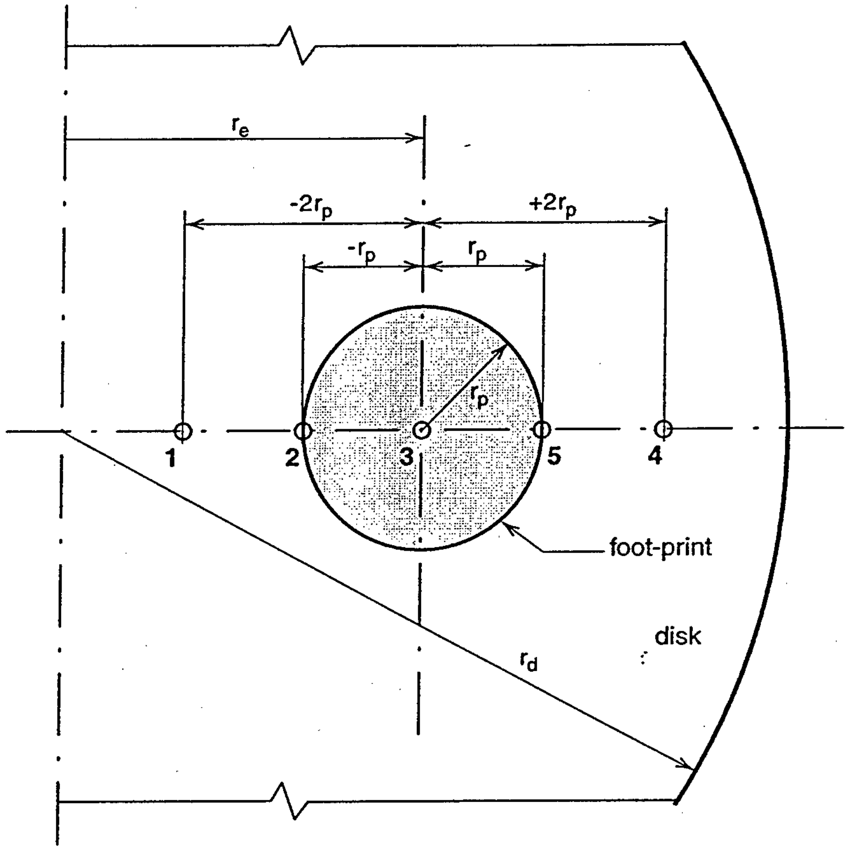

Figure 1. Convention for sensor positions of eccentric foot-print

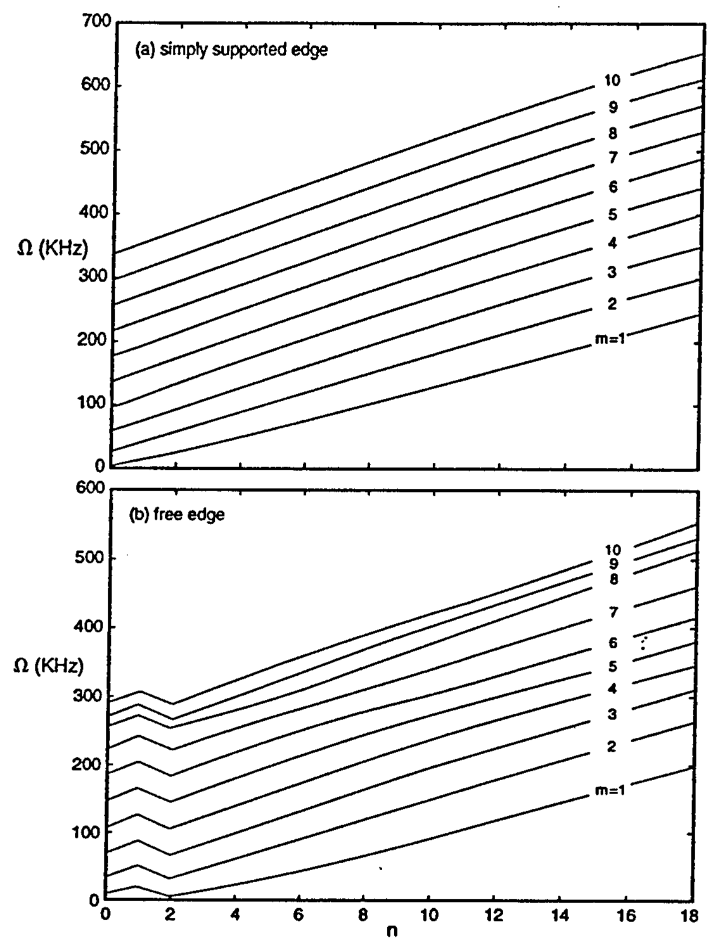

Figure 2. Resonant frequency lines of disk as a function of "n" with "m" as parameter; $r_d = 3"$, $h = 0.5"$

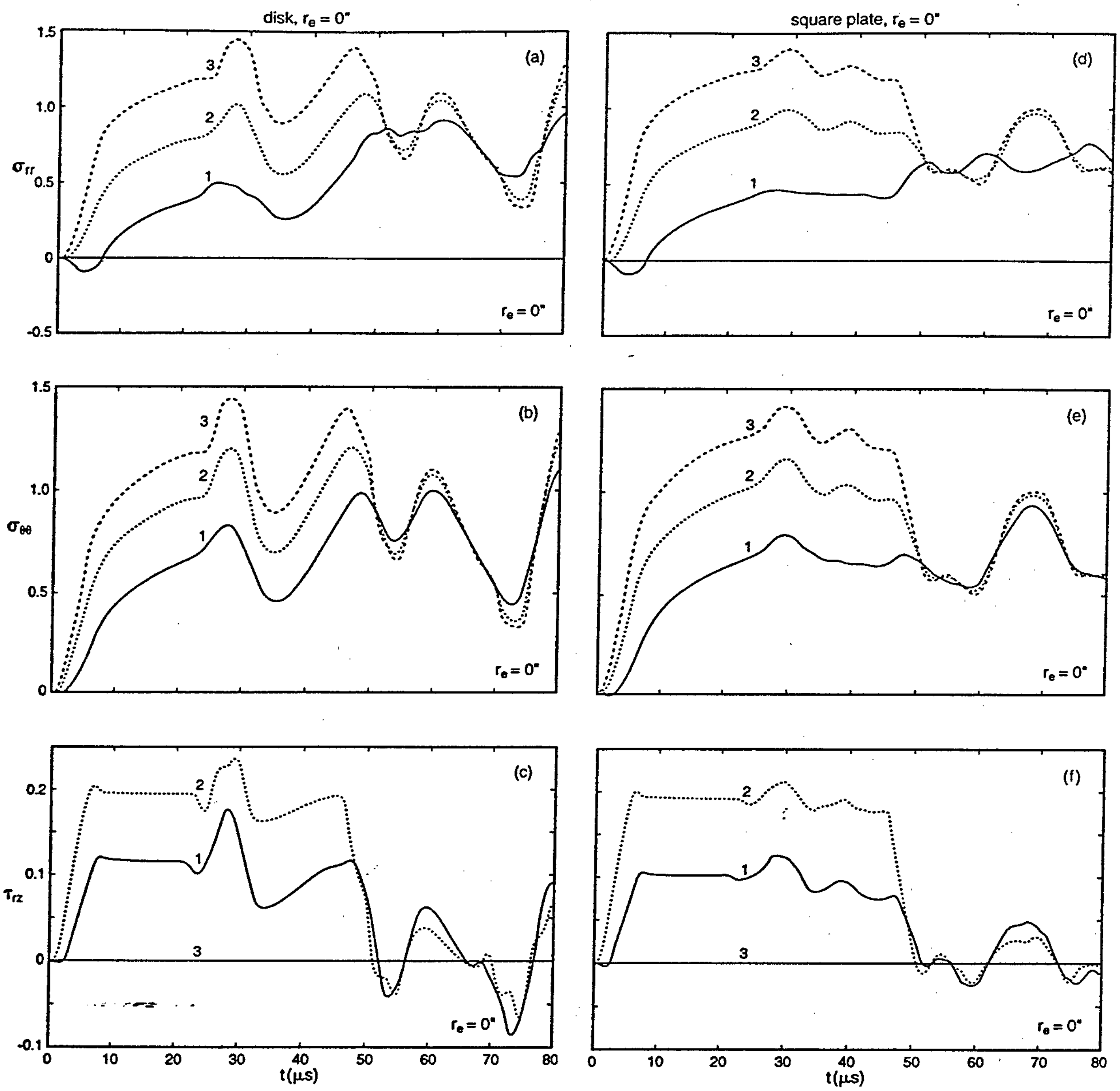

Figure 3: Stress histories of disk and square plate with "simply supported edge";
$r_d = 3"$, $h = 0.5"$, $r_p = 0.25"$, $r_e = 0"$, $\Delta t_f = 50\mu s$
(a), (b), (c) → disk; (d), (e), (f) → square plate

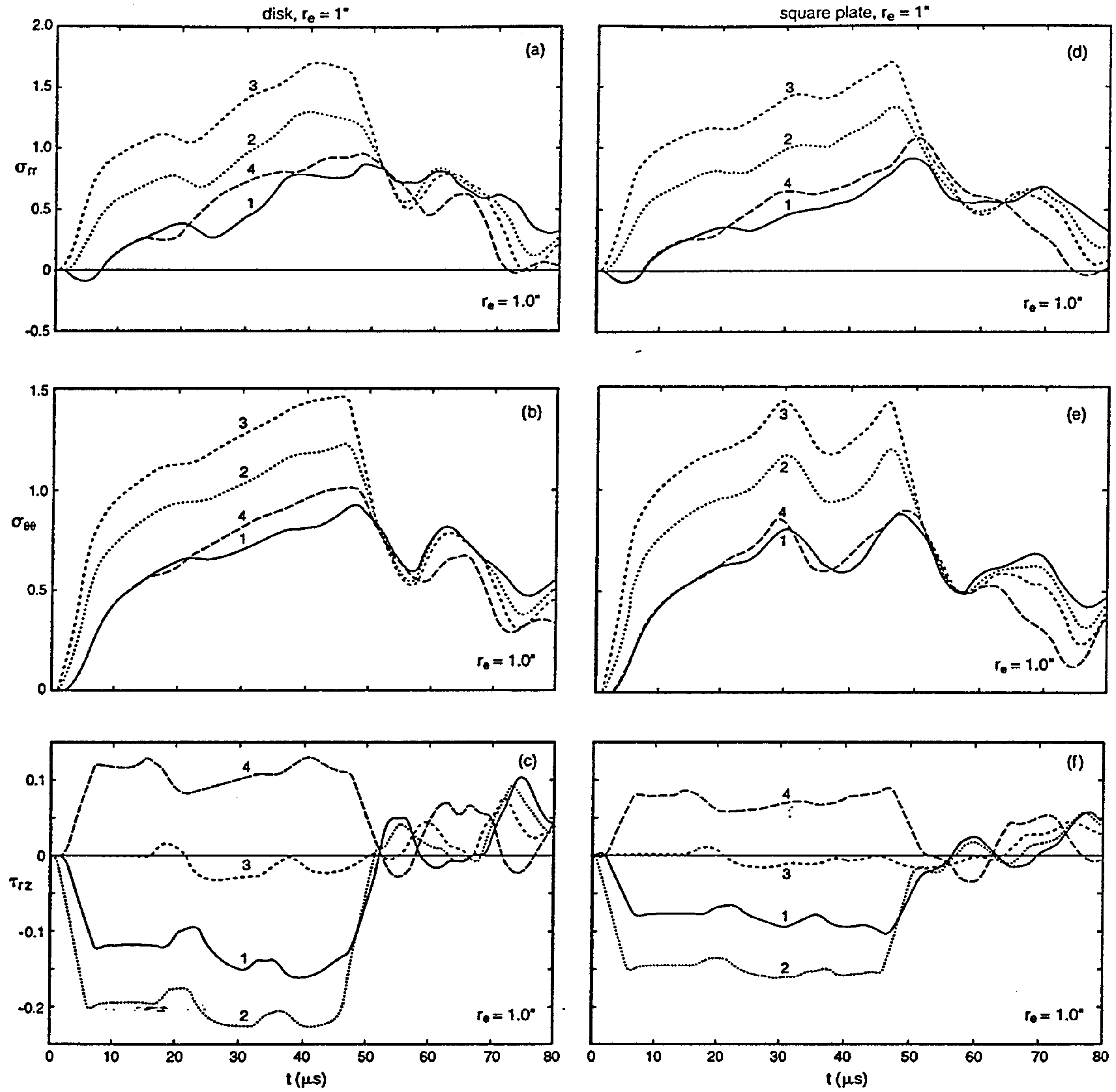

Figure 4: Stress histories of disk and square plate with "simply supported edge";
$r_d = 3"$, $h = 0.5"$, $r_p = 0.25"$, $r_e = 1.0"$, $\Delta t_f = 50\mu s$
(a), (b), (c) $\rightarrow$ disk; (d), (e), (f) $\rightarrow$ square plate

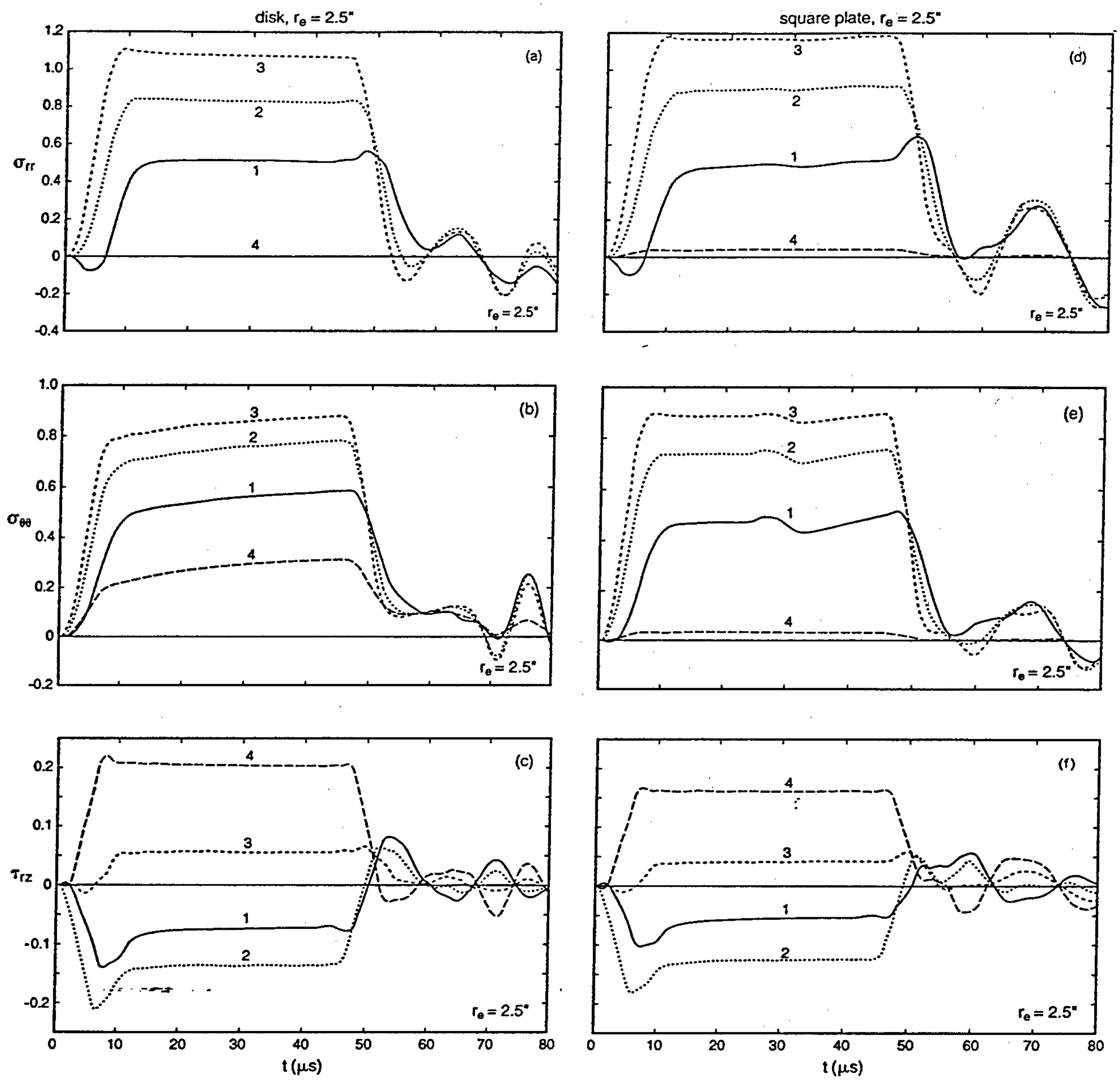

Figure 5: Stress histories of disk and square plate with "simply supported edge";
$r_d = 3"$, $h = 0.5"$, $r_p = 0.25"$, $r_e = 2.5"$, $\Delta t_f = 50\mu s$
(a), (b), (c) → disk; (d), (e), (f) → square plate

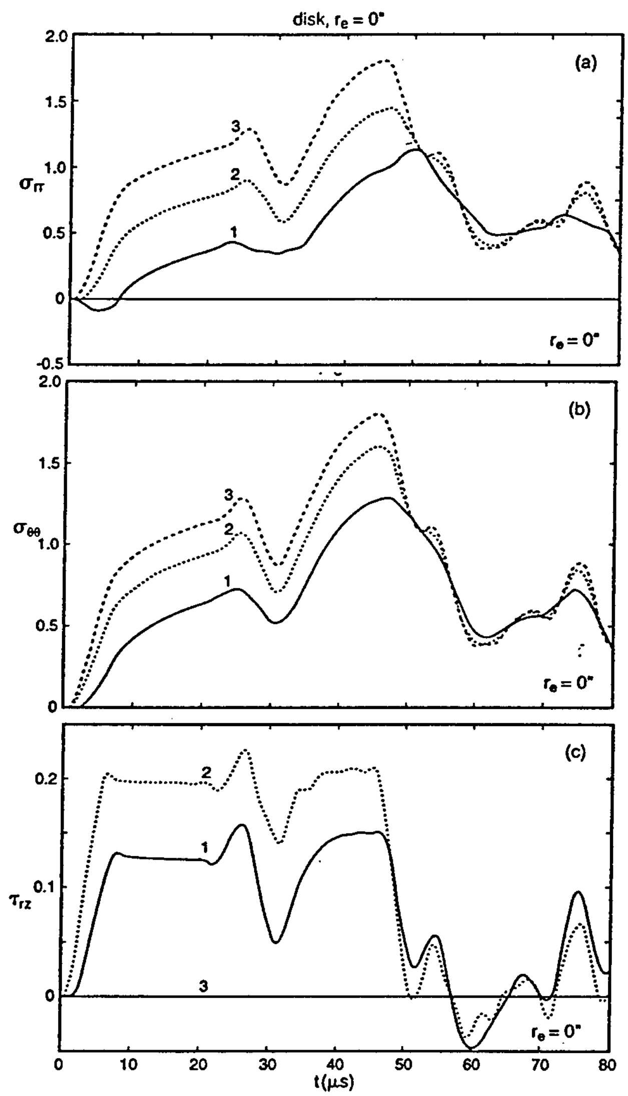

Figure 6: Stress histories of disk with "free edge";
$r_d = 3"$, $h = 0.5"$, $r_p = 0.25"$, $r_e = 0"$, $\Delta t_f = 50\mu s$

8441 GWLJ 12/22/98

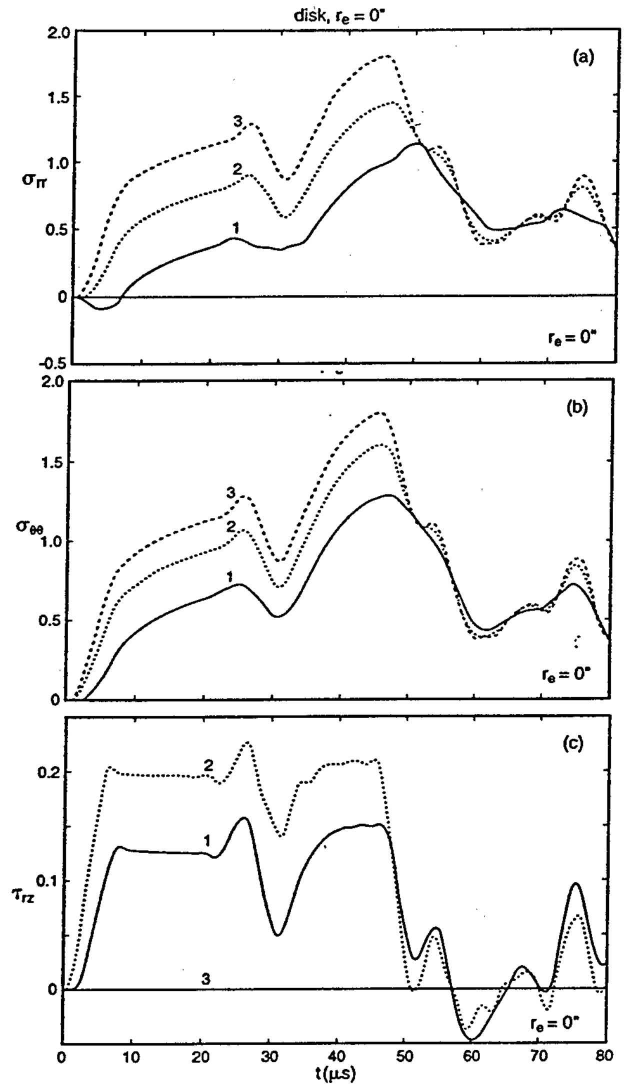

Figure 6: Stress histories of disk with "free edge";
$r_d = 3"$, $h = 0.5"$, $r_p = 0.25"$, $r_e = 0"$, $\Delta t_f = 50\mu s$

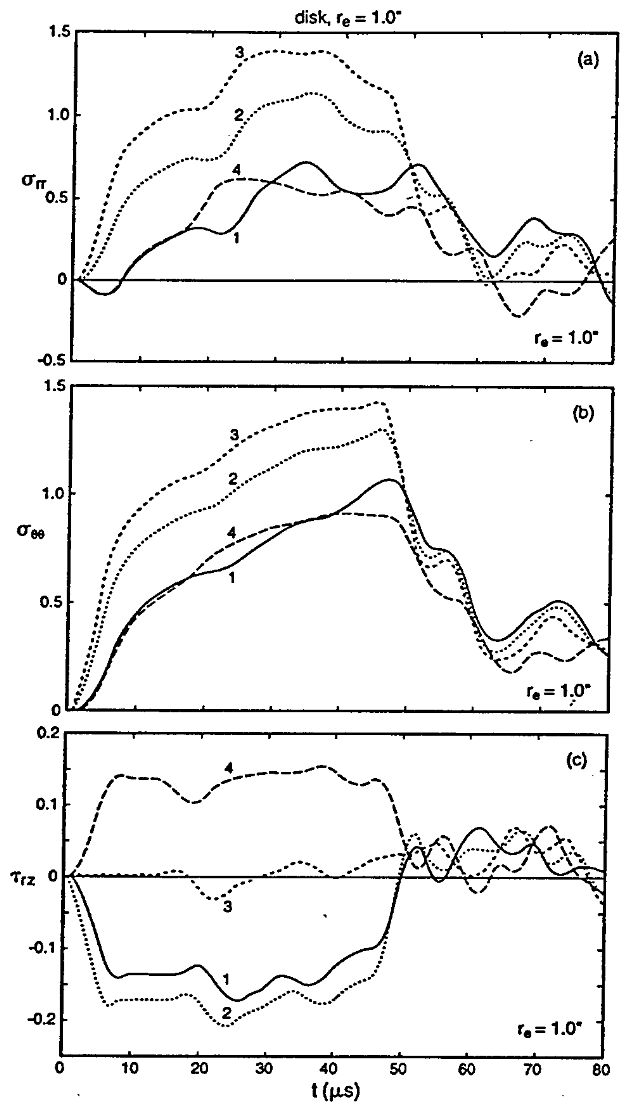

Figure 7: Stress histories of disk with "free edge";
$r_d = 3"$, $h = 0.5"$, $r_p = 0.25"$, $r_e = 1.0"$, $\Delta t_f = 50\mu s$

8441 GWLJ 12/8/98

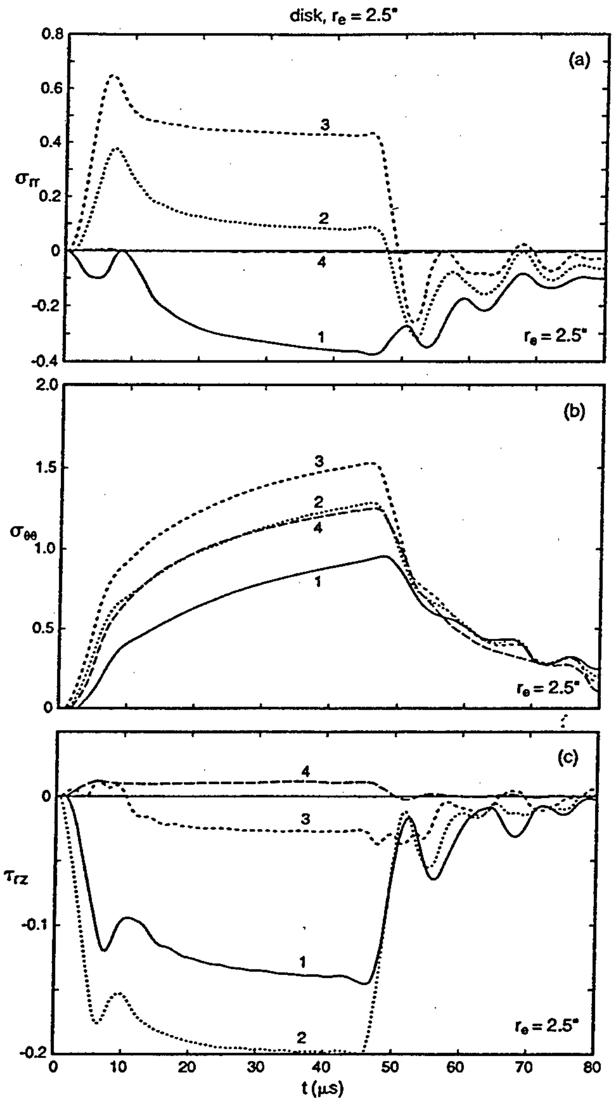

Figure 8: Stress histories of disk with "free edge";
$r_d = 3"$, $h = 0.5"$, $r_p = 0.25"$, $r_e = 2.5"$, $\Delta t_f = 50\mu s$

8441 GWLJ 12/8/98

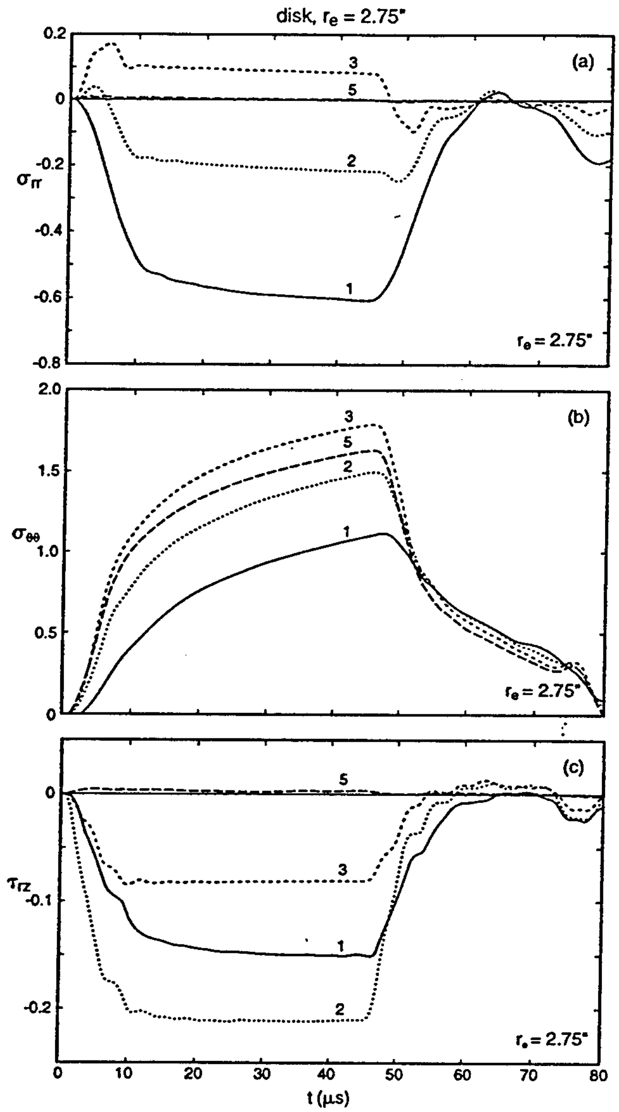

Figure 9: Stress histories of disk with "free edge";
$r_d = 3"$, $h = 0.5"$, $r_p = 0.25"$, $r_e = 2.75"$, $\Delta t_f = 50\mu s$

8441 GWLJ 12/9/98

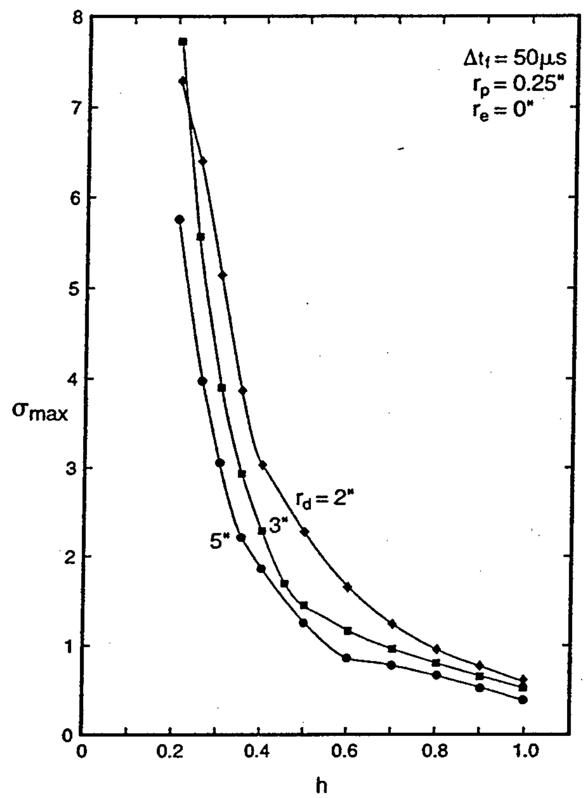

Figure 10: Varitation of σ_{max} with "h" for central impact, and "simply supported edge"

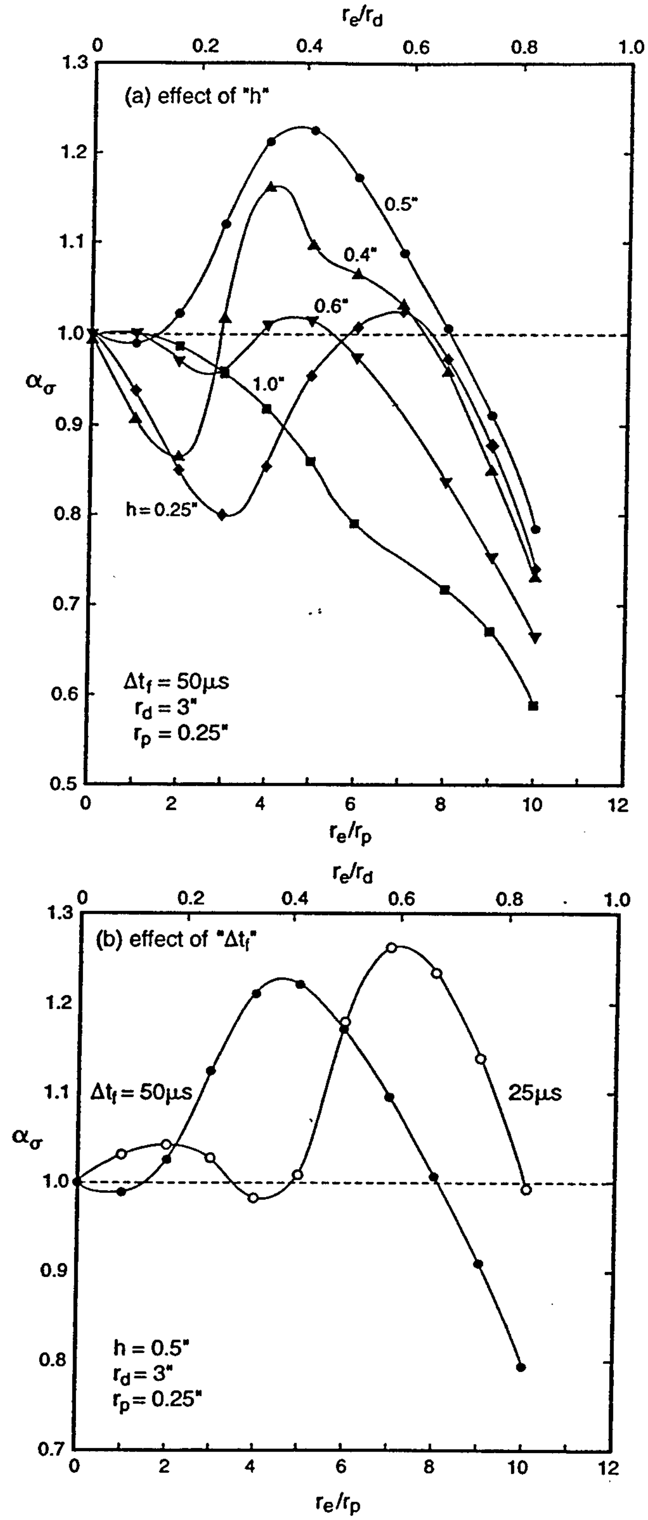

Figure 11: Varitation of "α_σ" with "r_e" for "simply supported edge"; $r_d = 3"$

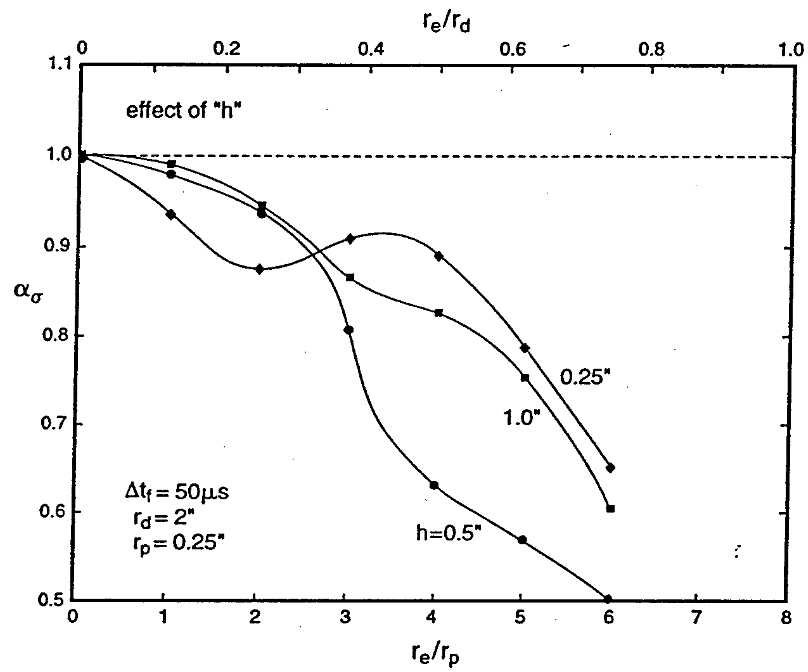

Figure 12: Varitation of "α_σ" with "r_e" for "simply supported edge"; $r_d = 2"$

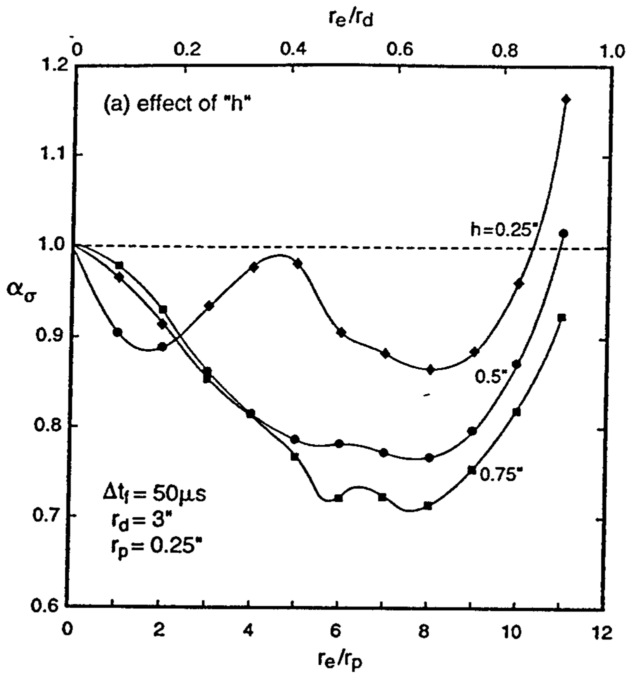

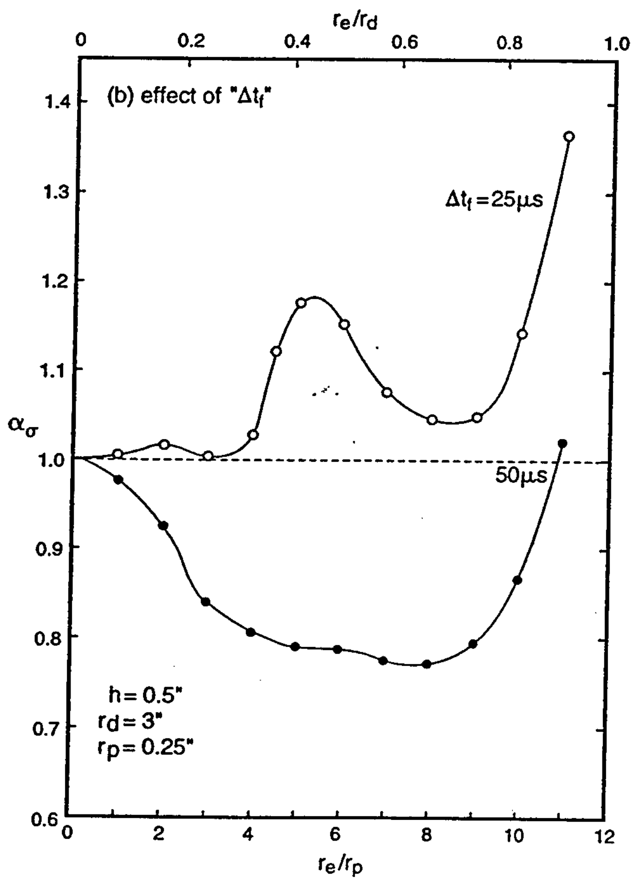

Figure 13: Varitation of "α_σ" with "r_e" and "free edge"; $r_d = 3"$

Reference [6]
Protection Efficiency of Layered AIN Ceramic Targets Bonded with PMMA

Fraunhofer Institut
Kurzzeitdynamik
Ernst-Mach-Institut

Protection Efficiency of Layered AlN Ceramic Targets Bonded with PMMA

Terminal Ballistic Experiments

Project No. 06-275 760, Subcontract Agreement No. R097-4

Report E 11/96

Prepared by
K. Weber
V. Hohler
A. J. Stilp

30. January 1997

Freiburg, Germany

Prepared by:

K. Weber

Staff Scientist - Terminal Ballistics I Group

Management:

Dr. V. Hohler

Head of Terminal Ballistics I Group

Concurred:

Dr. A.J. Stilp

Deputy Director of Ernst-Mach-Institut
Head of Impact Physics Department

Prof. Dr. K. Thoma

Director of Ernst-Mach-Institut

Kurzfassung

Zur Untersuchung der Schutzwirkung von Keramiklaminaten wurden Versuche mit Stabpenetratoren aus Wolframsinterlegierung (D = 11 mm, L/D = 6, $m_P \approx 110$ g) bei einer Auftreffgeschwindigkeit von $v_P \approx 2100$ m/s durchgeführt. Die Keramiklaminate bestanden aus 6.35 mm, 12.7 mm, 19.05 mm, 25.4 mm und 38.1 mm dicken AlN - Kacheln mit den lateralen Abmessungen von 100 x 100 mm und 150 x 150 mm. Zur Reduzierung der Druck-/ Dehnrateneffekte wurden zwischen den einzelnen Keramikplatten PMMA-Zwischenschichten eingelegt und mit einem Zweikomponenten-Epoxydharzkleber verbunden. Die Dicke der PMMA-Einlagen wurde zwischen 0 mm, 0.5 mm und 1 mm variiert. Zur Beurteilung der Schutzwirkung wurden zwei Bewertungsmethoden angewendet: 1) die „Depth-of-penetration-Methode (DOP)" zur Bestimmung der Resteindringtiefe im Panzerstahlbacking und 2) die zeitaufgelöste Methode zur Beobachtung des Eindringvorgangs des Projektils ins Keramiklaminat. Aus den Meßergebnissen ist ersichtlich, daß mit zunehmender PMMA-Schichtdicke die Schutzwirkung des Keramiklaminats abnimmt. Die kinetische Energie des gewählten Stabpenetrators ($m_P \approx 110$ g, $v_P \approx 2100$ m/s) erwies sich für die zu untersuchenden Targets als zu hoch; alle Laminate wurden vollkommen zerlegt, sodaß nach dem Versuch keine Beurteilung des Schadensbildes möglich war.

Abstract

Terminal ballistic experiments were carried out with tungsten sinter alloy rods (D = 11 mm, L/D = 6, $m_P \approx 110$ g) against ceramic layer systems. The 100 x 100 mm and 150 x 150 mm targets consisted of 0.25", 0.5", 0.75", 1" and 1.5" AlN ceramic layers with 0 mm, 0.5 mm and 1 mm PMMA intermediate layers bonded with a 0.1 mm to 0.23 mm thick two-component epoxy resin adhesive. The tests have been performed at an impact velocity v_P around 2100 m/s. Two evaluation methods have been applied: 1) the depth-of-penetration method (DOP) for estimation of the protection efficiency of the ceramic by means of the residual penetration depth in the RHA backing plate and 2) the time-resolved method for observation of the penetration process into the ceramic layers. It has been found that for increasing PMMA layer thickness the ballistic performance of the ceramic target decreases. The kinetic energy of the rod penetrator with a mass and impact velocity of 110 g and 2100 m/s, respectively, was much too high for the target under investigation. Therefore, all ceramic tiles were totally destroyed; an examination of target damage and crater formation could not be done after the test.

Content

1 Introduction

During the last decades the use of ceramics in modern armor became of increasing interest because of its high protection efficiency at relatively low areal density. The ballistic performance of ceramics depends on the type of the ceramic (compression strength, material density), the geometry (lateral dimensions, thickness), the layer sectioning, the confinement as well as the material properties of the projectile and the impact velocity.

The layer sectioning was the main topic of the research program carried out in cooperation between the DOW Chemical Company and the Ernst-Mach-Institut. In former experiments it has been found that the damage in a monolithic ceramic block is much stronger than in a layered target. Therefore, there was a strong economic and technical motivation to investigate ceramic layer concepts. The DOW Chemical Company developed 1-D and 2-D axisymmetric analytical models to describe the stress wave propagation dependent on impact velocity, lateral target dimensions, tile thickness, type and thickness of the intermediate layers for aluminum nitride (AlN) tiles. Each model is limited by simplifications from assumptions necessary to make the problem numerically tractable. Further progress could only be achieved by finding new effects and parameters from experiments. These tests were carried out at the Ernst-Mach-Institut. The shock wave propagation in layered targets was investigated by planar impact experiments, published in References [1] to [3].

This report summarizes the results of first terminal ballistic tests of AlN ceramic tiles with PMMA intermediate layers bonded with an epoxy resin adhesive.

2 Experimental procedure and test parameters

For acceleration of the heavy tungsten sinter alloy (WS-alloy) projectile the EMI range 1 two-stage light gas gun with pump/launch tube diameters of 65/31 mm was used. The rod projectile (Fig. 1) was embedded into a four-finger sabot with a pusher both made of Polycarbonat (trade name „Makrolon") and a 4 mm thick titanium disc. In Fig. 2 the in-flight seperation of sabot, pusher and titanium disc by aerodynamic forces is shown.

2.1 Test set-ups

The tungsten sinter alloy projectile had a mass of $m_P \approx 110$ g (Table 1) and a diameter of D = 11 mm (L/D = 6). The head of the projectile had a blunt shape. The experiments have been performed at an impact velocity v_P around 2100 m/s against AlN layer targets with PMMA intermediate layers of the thicknesses 0 mm, 0.5 mm and 1 mm. They were bonded with an epoxy resin adhesive 0.10 mm to 0.23 mm thick.

Two test set-ups were applied: 1) the depth-of-penetration method (DOP) and 2) the time-resolved observation method. They are depicted in Figs. 3 and 4. For both test methods there was no lateral confinement. Only a RHA backing (HV20 = 412) was arranged behind the ceramic layer stack.

In the case of the DOP method (Fig. 3) the lateral tile dimensions were 150 x 150 mm. The total target thickness of the ceramic tiles was about 3" ≈ constant, consisting of 0.25" (12 layers), 0.5" (6 layers), 0.75" (4 layers), 1" (3 layers) and 1.5" (2 layers).

For observation of the penetration process of the projectile into the ceramic layers the time-resolved observation method has been applied for the 0.25" and the 1.5" tiles with 0 mm and 1 mm PMMA layers in between the tiles. The use of the 600 kV flash X-ray tube made it necessary to reduce the lateral tile dimensions from 150 x 150 mm to 100 x 100 mm. For this test set-up the target was surrounded (not confined!) by a rectangular tube of an inner cross section area of 190 x 190 mm with an observation window of 140 x 50 mm at both sides. The 40 mm thick polystyrene foam sheet between target (ceramic tiles + steel backing) and base plate support minimized disturbances from the target chamber. For determination of the yaw angles α_1 and α_2 two 180 kV flash X-rays were arranged vertically and horizontally prior to the target.

2.2 AlN ceramic tiles

The 0.25", 0.5", 0.75", 1" and 1.5" AlN ceramic tiles with 100 x 100 mm and 150 x 150 mm lateral dimensions have been delivered by the DOW Chemical Company, Midland, MI, USA (product name XUS 35532.00). The tiles consist of 95-100% aluminum nitride, 0-5% aluminum oxide and 0-5% yttrium oxide. Its material density is $\rho = 3.26$ g/cm^3 (boiling point 2150°C). Other material properties are unknown.

2.3 Bonding materials

In the planar impact tests the influence of tile thickness, thickness of the intermediate film, and the lateral stack geometry on the first pulse propagation into the stack, the phase velocity and the shock wave attenuation has been investigated. Different coupling media have been used: Latex, single-component silicone rubber (SR 118Q) and two-component silicone rubber (ME 625). The planar impact tests have been carried out at an impact velocity between 10 m/s and 60 m/s. The two-component silicone rubber delivered the most reliable results of the pressure profiles, phase velocity and shock wave attenuation (good coupling, complete vulcanization). PMMA intermediate layers reduced the strain rate effects to a minimal level. In contrast to the two-component silicone rubber PMMA was not strain rate dependent over a large range.The weak strain rate effects were due to the epoxy bonding. The compounds A and B of the epoxy resin adhesive are available commercially in the USA as WELDON-10 A&B, manufactured by IPS corporation, Gardena, California. The two part compound A&B were thoroughly mixed in the ratio of 100 parts by weight monomer (A) and 13 parts by weight catalyst (B). The bond was cured at room temperature for 48 hours.

3 Experimental results and discussion

3.1 Depth-of-penetration (DOP) method

Table 1 summarizes the experimental results of the depth-of-penetration (exps. 8399 through 8414) and the time-resolved observation methods (exps. 8415 through 8418). For both procedures the residual depth of penetration p_R has been determined in the 2 x 50 mm RHA backing supported by 2 x 50 mm mild steel plates to evaluate the protection efficiency of the ceramic layer system. p_R is given in Table 1 as well as in the histogram of Fig. 11. For the 0.25", 0.75" and 1.5" tile thicknesses tests are carried out with an intermediate layer of 0 mm, 0.5 mm and 1mm PMMA sheet. For experiments 8402, 8409 and 8413 the p_R values may be additionally influenced by the relatively great yaw angle of $\alpha_1 = 3°$ to $4°$ (definition in Fig. 5). For all three tile thicknesses the highest p_R was found for the 1 mm PMMA, i.e., the best terminal ballistic performance has the ceramic layer system without PMMA layers. This behavior of the ceramic layer system is not yet understood: in the planar impact tests it has been found that the PMMA intermediate layer is not pressure/strain rate sensitive in the velocity range 12.3 m/s to 45.2 m/s. It is assumed that PMMA changes its behavior at higher impact velocities. Additional tests would be necessary to give evidence for this supposition. An other explanation could be the delamination between AlN tiles and PMMA layers observed in the planar impact tests.

A reduction of the lateral tile dimensions from 150 x 150 mm to 100 x 100 mm decreased the ballistic performance.

3.2 Time-resolved observation method (Ref. [4])

The flash X-ray photographs in Figs. 7 through 10 show the penetration process of the WS-alloy rod into the AlN ceramic layers. The targets consisted of 2 x 1.5" (Figs. 7 and 8) and 12 x 0.25" tiles (Figs. 9 and 10) with no PMMA (Figs. 7 and 9) and 1 mm PMMA (Figs. 8 and 10) intermediate layers, respectively. The yaw angles were controlled by 180 kV flash X-ray photographs prior and at the moment of impact. The interaction between penetrator and ceramic tiles has been observed by means of a 600 kV flash X-ray tube at some selected times. Fig. 7 represents the penetration process short time after impact (because of a malfunction of the time measurement system the time could not be measured) into the 1.5" AlN tiles with no PMMA. The crater formed in the target was relatively narrow compared to the crater formed in the target with 1 mm PMMA (Fig. 8). In this case the rod has already passed the PMMA intermediate layer visible by the strong lateral spread of the eroded rod material. The same behavior could be observed for the 0.25" layers. For the 1.5" tiles the crater shape shows a strong discontinuity at the PMMA intermediate layer. However, for the 0.25" layers the crater contour is much smoother than for the thicker tiles.

The qualitative results of the X-ray evaluation are given in Table 2. The notations used in Table 2 are explained in Fig. 6. Because of the poor number of experiments carried out no remarkable influences of layer partitioning and PMMA intermediate layers on momentary rod length l, head velocity u and tail velocity v have been found. Additional tests would be necessary.

4 Conclusions and continuation of the program

By means of the terminal ballistic tests for the 0.25", 0.75" and 1.5" AlN ceramic tiles with 0 mm, 0.5 mm and 1 mm PMMA intermediate layers it was shown that the protection efficiency of the ceramic layer system slightly decreased with increasing PMMA thickness. Furthermore, it was found that the kinetic energy of the used projectile (WS-alloy, $\rho = 17.45$ g/cm^3, D = 11 mm, L/D = 6, $m_p \approx 110$ g) was distinctly too high to investigate this type of target. From these test results it was decided to continue the experiments with a projectile of lower mass ($m_p \approx 65$ g) at a lower impact velocity of $v_p \approx$ 1500 m/s. For all tests AlN targets of 2.5" total thickness, consisting of 0.25", 0.5", 0.75", 1" and 1.5" tiles of 100 x 100 mm and 150 x 150 mm lateral dimensions are planned to be used. The ceramic layer system will be laterally confined by 20 mm mild steel. Additionally, mild steel cover and RHA backing plates are mounted. The tiles will be bonded by a 0.3 mm thick two-component silicone rubber film (most reliable planer impact results) without any PMMA layers in between the tiles.

References

1. R. Tham Transient elastic waves in finite layered elastic media - experimental investigation of the wave propagation. *EMI report E6/95.*

2. M. El-Raheb and R. Tham. Experiments on transient waves in a periodic stack. *Structures under Shock and Impact IV, Computational Mechanics, Southampton, 1996, pp. 543-551.*

3. R. Tham Transient elastic waves in finite layered elastic media bonded with PMMA - experimental investigation of the wave propagation. *EMI report E2/96.*

4. V. Hohler and A.J. Stilp (1984). Visualization of the penetration process of rods into glass and armor steel targets by means of flash X-ray photographs. Proc. 35th ARA Meeting, Meppen, Germany.

Projectile: Rod (Material: W5H) ;, D = 11 mm, L / D = 6, , m_p = 109.45g, ρ = 17.55 g/cm³, R_m = 1550±9 MPa, A_5 = 8.2±1.9 %
RHA-Catcher: Vickers hardness number HV20 = 412

Exp. No.	v_p [m/s]	α_1 / α_2 [deg]	Lateral target dimensions [mm]	No. of tiles	AlN total tile thickness [mm]	AlN average tile thickness [mm]	PMMA total sheet thickness [mm]	PMMA average sheet thickness [mm]	Adhesive total layer thickness [mm]	Adhesive av. layer thickn. [mm]	RHA thickness [mm]	Total target thickness [mm]	p_R [mm]
8401	2130	+1.5/---	150x150	12	76.33	6.36	11.85	0.99	4.88	0.20	50.06	143.12	27.9
8402	2132	+3.5/-1.0	150x150	12	76.25	6.35	5.88	0.49	4.07	0.17	49.73	135.93	25.4
8403	2133	+1.5/-0.5	150x150	12	76.21	6.35	0	0	1.95	0.16	50.05	128.21	23.5
8413	2129	+4.0/-1.0	150x150	6	76.64	12.77	5.81	0.97	2.75	0.23	50.24	135.44	20.1
8412	2134	+2.0/-0.5	150x150	6	76.81	12.80	0	0	0.84	0.14	50.33	127.98	19.8
8405	2120	+2.0/-0.5	150x150	4	77.23	19.31	3.9	0.98	0.76	0.10	49.87	131.76	22.2
8406	2128	+0.5/-0.5	150x150	4	76.39	19.10	1.93	0.48	1.66	0.21	50.06	130.04	21.6
8407	2120	0/-0.5	150x150	4	76.47	19.12	0	0	0.83	0.21	50.22	127.52	19.2
8411	2131	+2.0/-0.5	150x150	3	76.29	25.43	2.96	0.99	1.28	0.21	50.07	130.60	23.8
8408	2129	+2.0/-0.5	150x150	2	76.24	38.12	1.94	0.97	0.89	0.22	50.17	129.24	26.7
8409	2124	+3.0/-0.5	150x150	2	76.19	38.10	0.99	0.50	0.92	0.23	50.19	128.29	20.6
8410	2118	+2.5/-1.0	150x150	2	76.13	38.07	0	0	0.38	0.19	50.16	126.67	16.0
8399	1975	+1.5/---	150x150	---	---	---	---	---	---	---	3x50	---	89.8
8400	1996	+2.5/-0.5	150x150	---	---	---	---	---	---	---	3x50	---	91.4
8414	2120	-0.5/-0.5	150x150	---	---	---	---	---	---	---	3x50	---	90.4
8418	2108	+1.0/0	100x100	12	75.78	6.32	11.68	0.97	3.90	0.16	50.15	141.51	31.1
8417	2123	+1.0/-0.5	100x100	12	76.23	6.35	0	0	1.57	0.13	49.92	127.72	28.6
8416	2119	+1.0/-0.5	100x100	2	76.22	38.11	2.0	1.0	0.78	0.20	50.12	129.12	25.7
8415	2116	+0.5/-0.5	100x100	2	76.40	38.20	0	0	0.28	0.14	50.00	126.68	26.4

Table 1 Results of the depth-of-penetration (DOP) measurements

Exp. no.	v_p [m/s]	t [µs]	s_K [mm]	s_H [mm]	l [mm]	u [m/s]	v [m/s]	u / v_p	v / v_p	Tiles no.	Tiles thickn. [mm]	PMMA thickn. [mm]
8415	2116	---	27.0	43.4	49.6	---	---	---	---	2	38.2	0
8416	2119	47.2	56.7	92.7	30.0	1201	2025	0.567	0.956	2	38.1	1.0
8417	2123	47.3	58.5	93.2	31.3	1237	2027	0.583	0.955	12	6.35	0
8418	2108	40.1	55.1	81.0	40.1	1374	2039	0.651	0.967	12	6.32	0.97

Table 2 Results of the time-resolved observation measurements

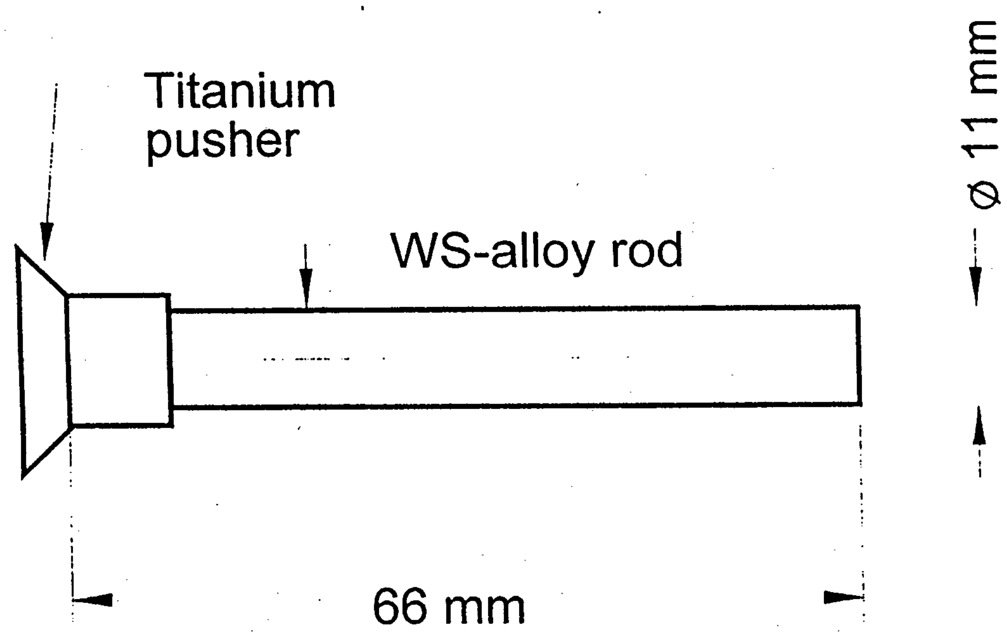

Fig. 1 Rod penetrator geometry

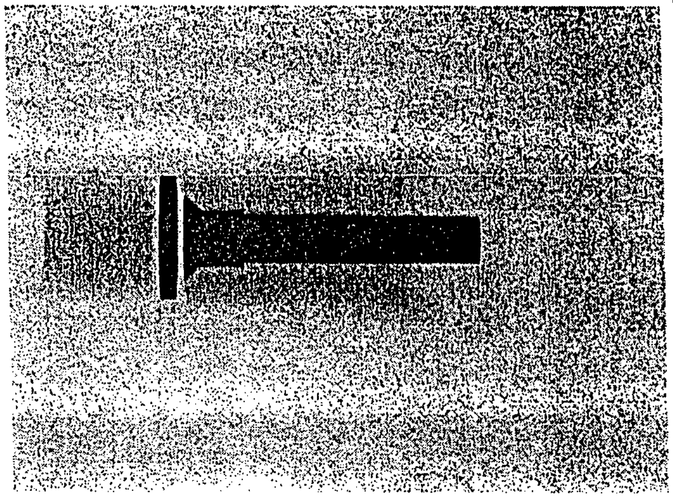

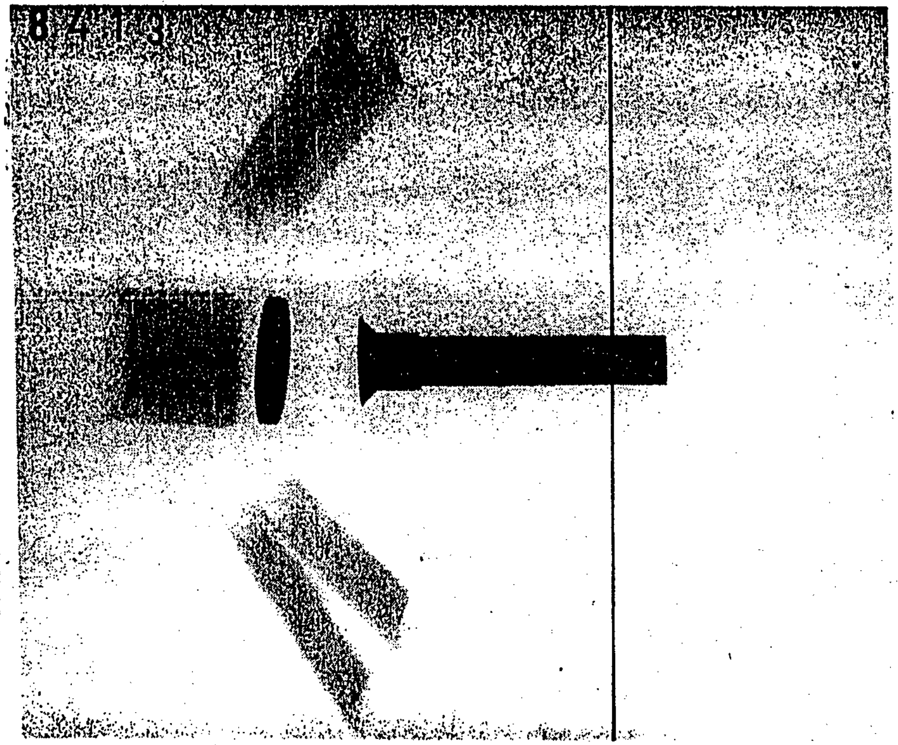

Fig. 2 In-flight separation of sabot, pusher and titanium disc from the projectile by aerodynamic forces.

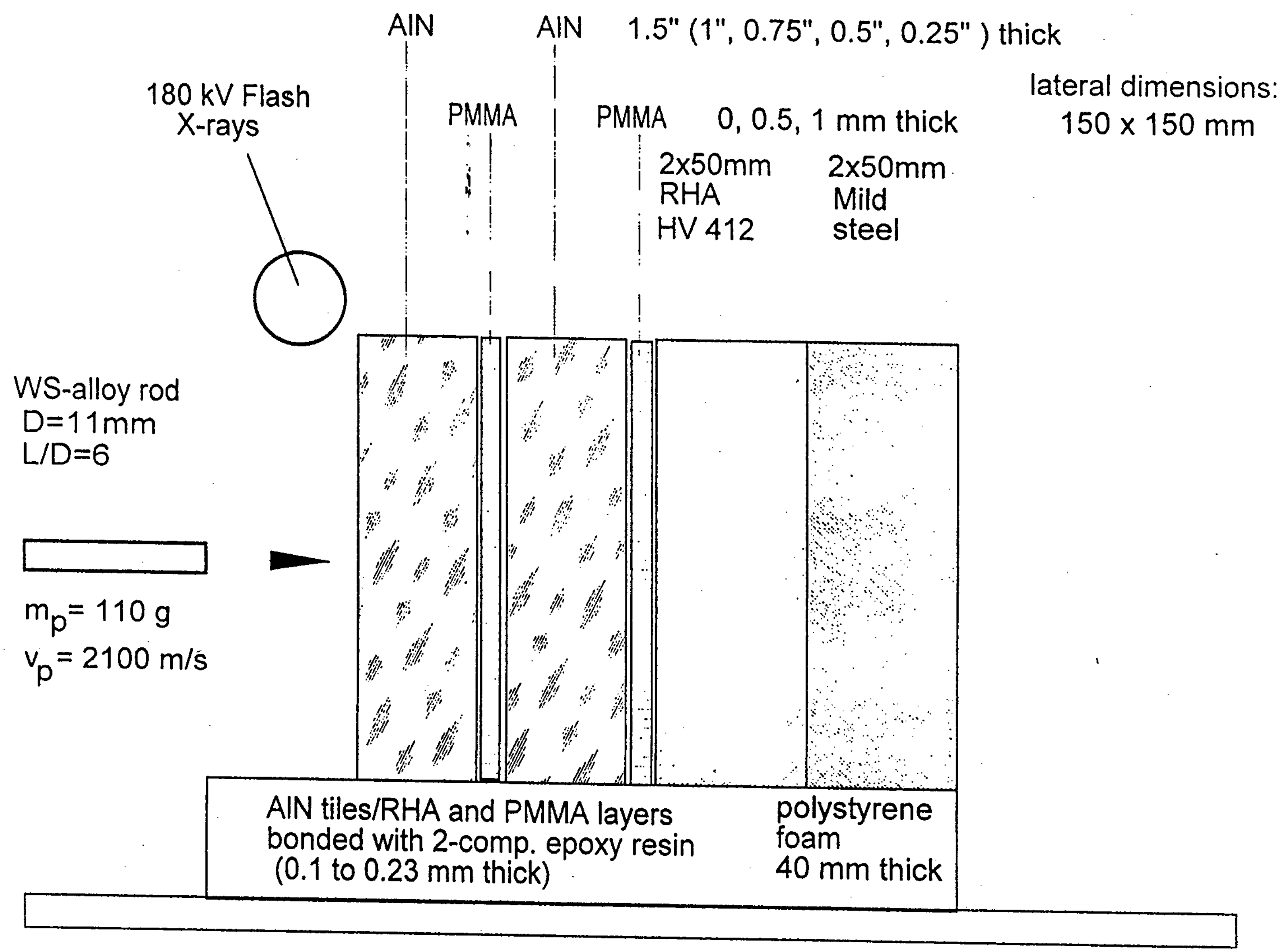

Fig. 3 Test set-up of the depth-of-penetration test method

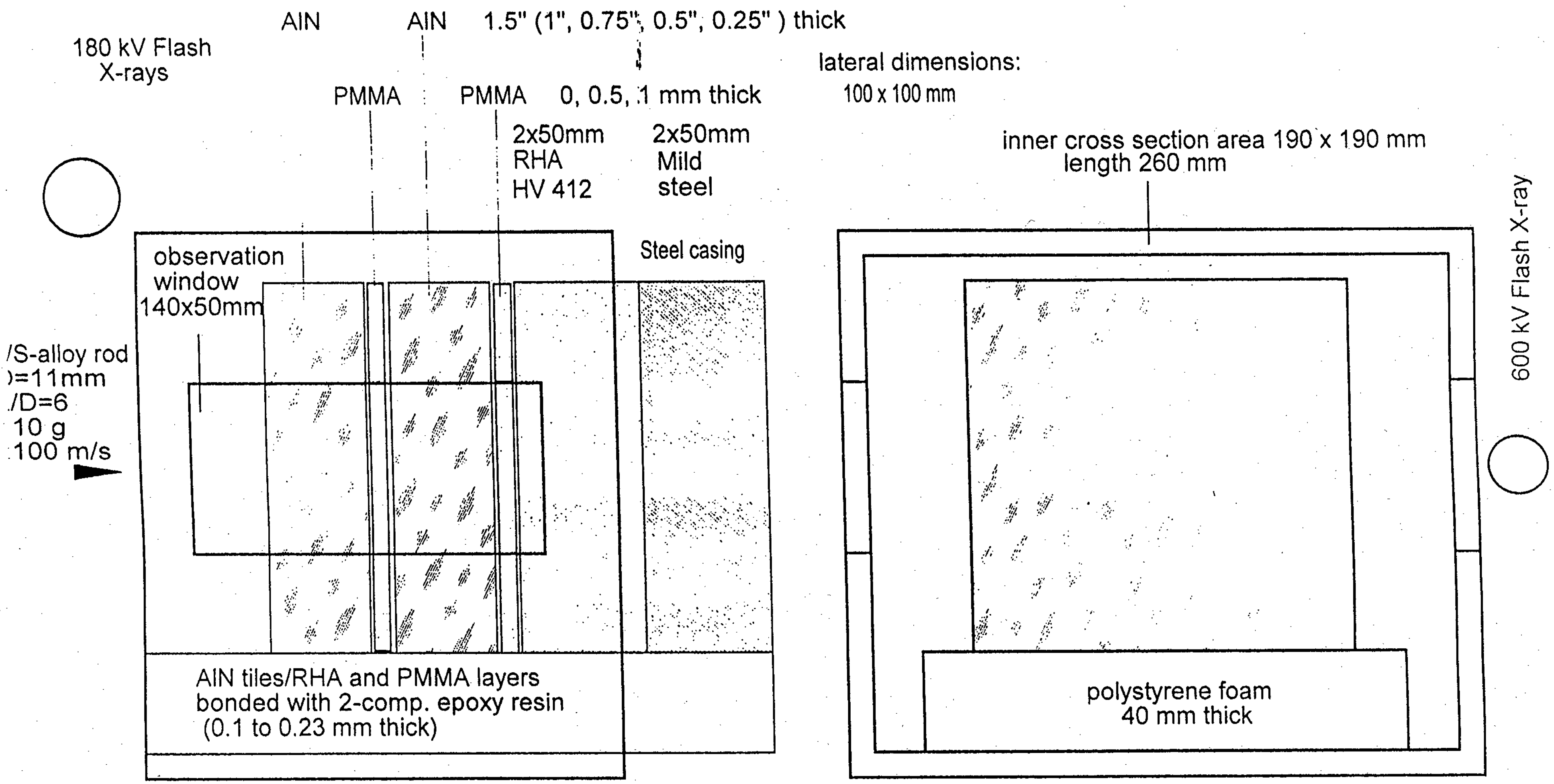

Fig. 4 Test set-up of the time-resolved observation method

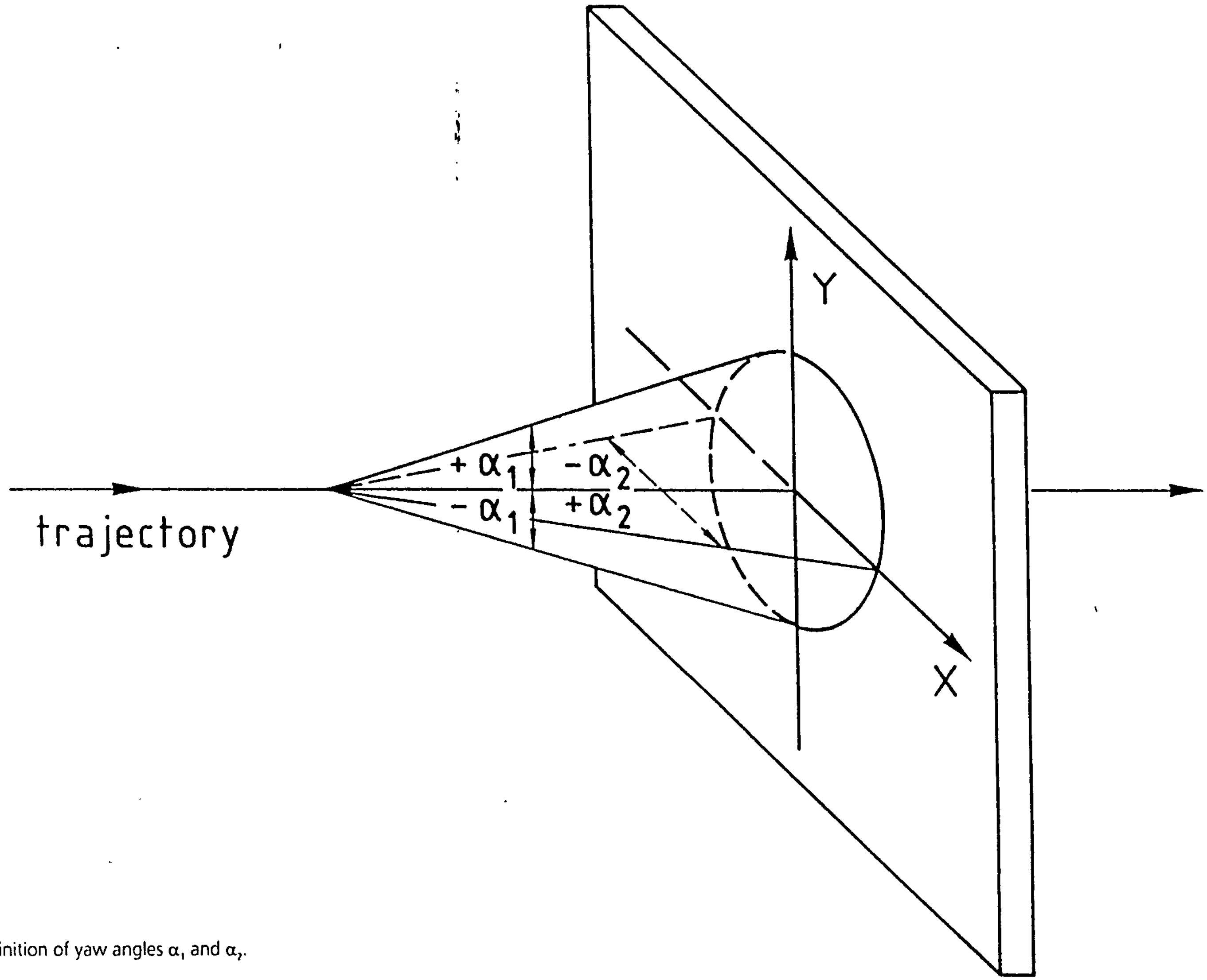

Fig. 5 Definition of yaw angles α_1 and α_2.

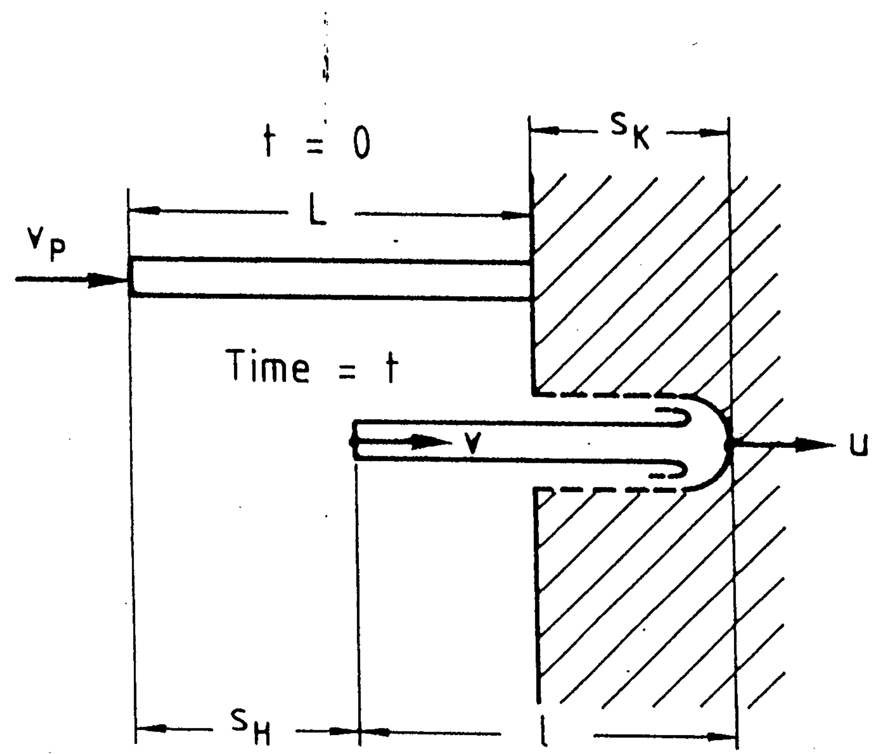

Fig. 6 Definition of parameters of time-resolved measurements

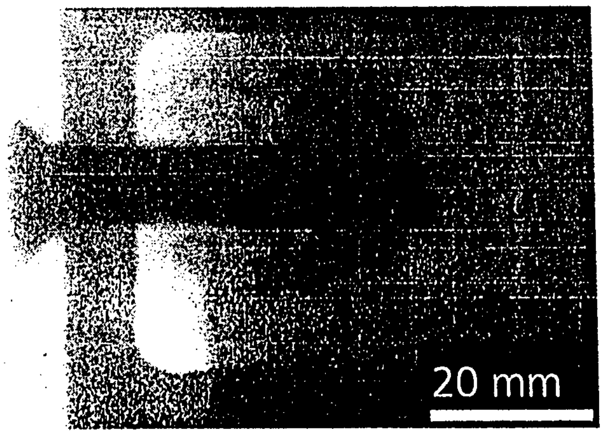

Fig. 7 600 kV flash X-Ray photograph of the WS-alloy rod penetration into the layered AlN-Target at v_p = 2116 m/s.
Target: 2 x 1.5'' AlN tiles; lateral dimensions: 100 x 100 mm; no PMMA intermediate layers; bonded with epoxy resin adhesive.

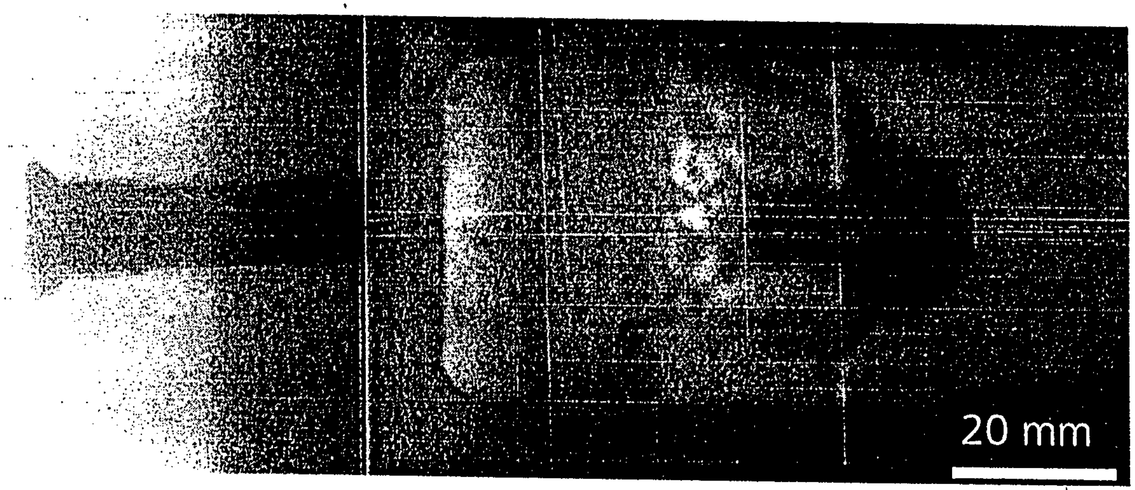

Fig. 8 600 flash X-Ray photograph of the WS-alloy rod penetration into the layered AlN-Target at v_p = 2119 m/s, taken 47.2 µs after impact. Target: 2 x 1.5'' AlN tiles; lateral dimensions: 100 x 100 mm; 1 mm thick PMMA intermediate layer; bonded with epoxy resin adhesive.

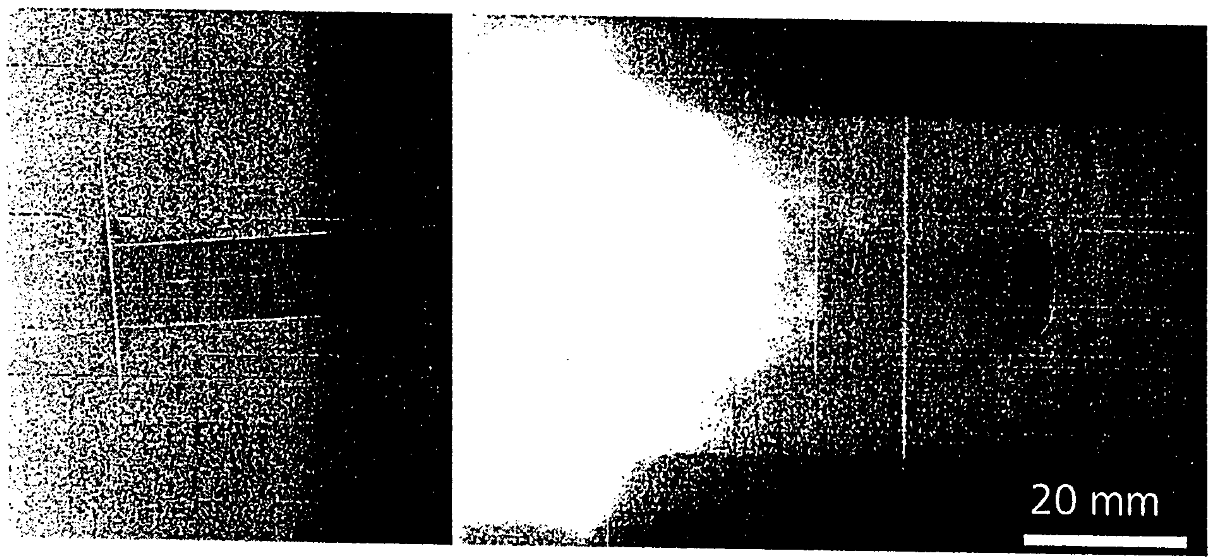

Fig. 9

600 kV flash X-Ray photograph of the WS-alloy rod penetration into a layered AlN-Target at v_p = 2123 m/s, taken 47.3 µs after impact.
Target: 12 x 0.25" AlN tiles; lateral dimensions: 100 x 100 mm; no PMMA intermediate layers; bonded with epoxy resin adhesive.

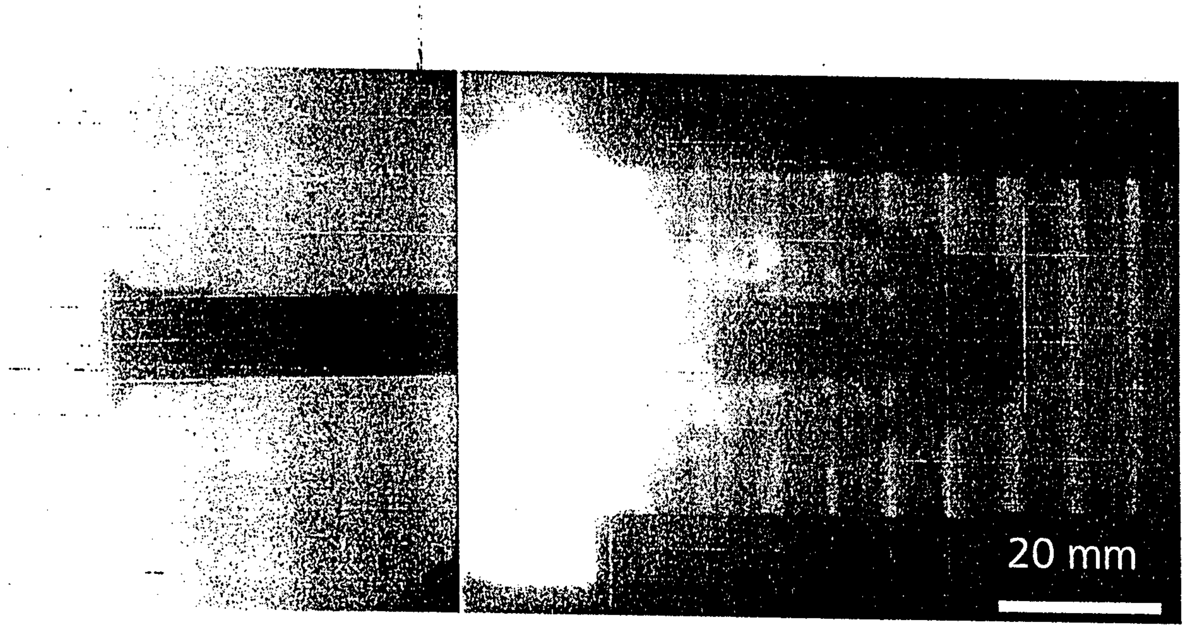

Fig. 10 600 kV flash X-Ray photograph of the WS-alloy rod penetration into the layered AlN-Target at v_r = 2108 m/s, taken 40.1 µs after impact.
Target: 12 x 0.25'' AlN tiles; lateral dimensions: 100 x 100 mm; 1 mm thick PMMA intermediate layers; bonded with eposy resin adhesive.

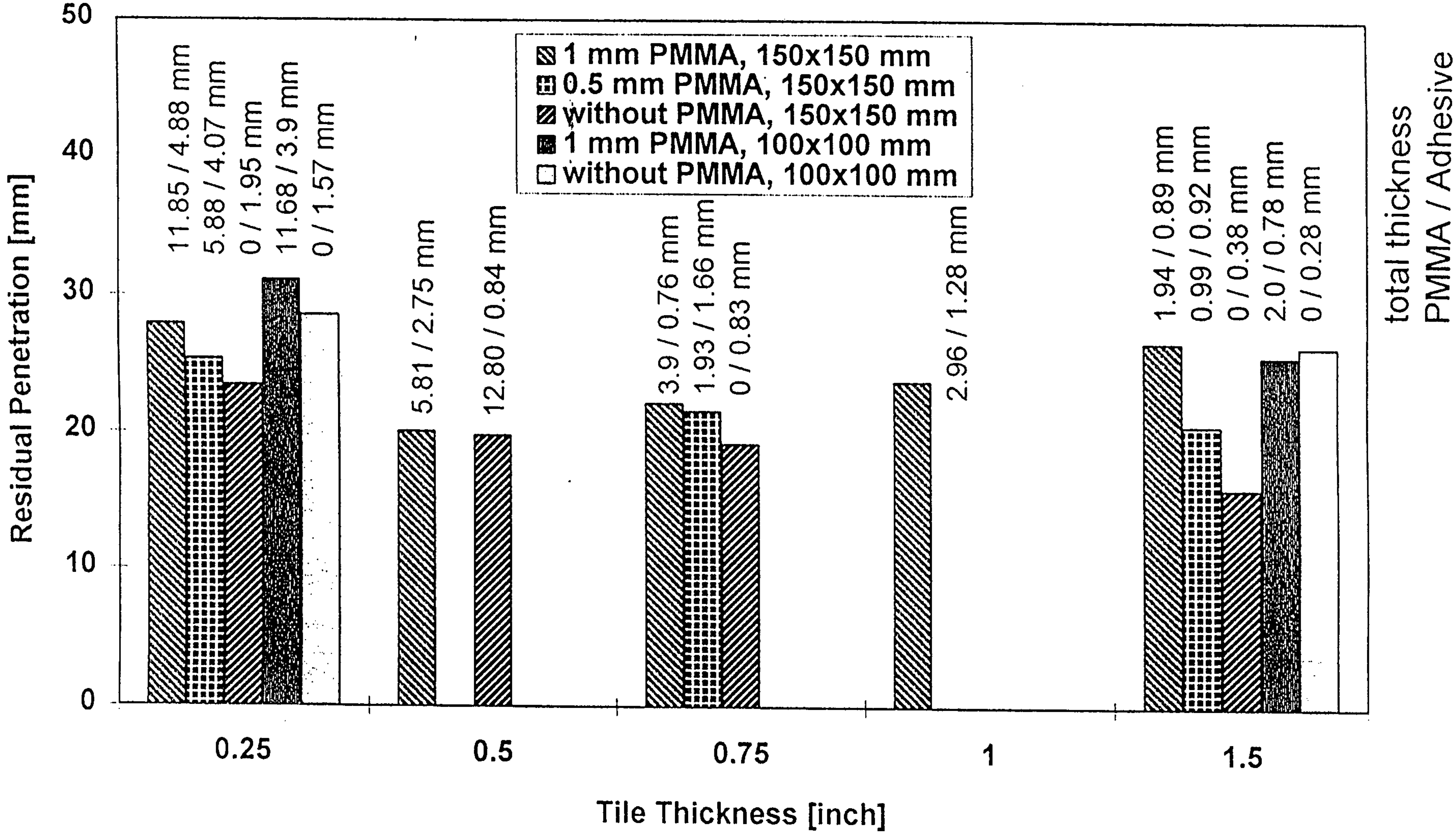

Fig. 11 Residual penetration depth versus tile thickness.

Reference [7]
Protection Efficiency of Layered AIN Ceramics Bonded with Polyurethane Films

Fraunhofer
Institut
Kurzzeitdynamik
Ernst-Mach-Institut

Protection Efficiency of Layered AlN Ceramics Bonded with Polyurethane Films

Project No. 06–275 760, DOW Subcontract Agreement No. R 097–4

Report E 19/97

Prepared by
K. Weber
V. Hohler

27. November 1997

Freiburg, Germany

Prepared by:

K. Weber

Staff Scientist - Terminal Ballistics Group

Concurred:

Dr. V. Hohler

Head of Terminal Ballistics Group

Prof. Dr. K. Thoma

Director of Ernst-Mach-Institut

Kurzfassung

Der vorliegende Bericht faßt die experimentellen Ergebnisse der Untersuchung des Einflusses der Schichtaufteilung auf die Schutzwirkung von AlN-Keramiken zusammen. Es wurden sowohl monolithische (1x1.5") als auch Zweischicht- (2x0.75") und Dreischicht-Keramikziele (3x0.5") bei einer Impaktbelastung durch einen Wolframschwermetall-Stabpenetrator (WSA, $m_P \approx 50$ g, D = 8.33 mm, L/D = 6) bei einer Auftreffgeschwindigkeit von $v_P \approx$ 1150 m/s getestet. Zur zusätzlichen Bewertung des Verdämmungseinflusses wurden drei verschiedene Versuchsaufbauten mit 1) massiver axialer und lateraler 2) schwacher axialer und massiver lateraler sowie 3) massiver axialer und schwacher lateraler Verdämmung untersucht. Die beobachtete geringere Schutzwirkung von geschichteten gegenüber monolithischen Keramikzielen wird wahrscheinlich durch die höhere Biegebelastung hervorgerufen. Der Einfluß der Biegebelastung überlagert vermutlich den Effekt der reduzierten Stoßwellenbelastung bei Schichtzielen infolge von Zwischenschichten geringer Impedanz zwischen den einzelnen Keramikkacheln. Die Versuche zeigen, daß bereits eine geringe Schwächung von axialer und lateraler Verdämmung sowohl die Kratergeometrie als auch die Resteindringtiefe (Schutzwirkung) beeinflussen.

Abstract

This report summarizes the results of the experimental investigations corresponding to the terminal ballistic protection efficiency of monolithic and layered AlN Ceramics. Monolithic (1.5") as well as multi-layer (2x0.75" and 3x0.5") ceramic targets have been investigated under impact loading by a tungsten-sinter alloy rod penetrator (WSA, $m_P \approx 50$ g, D = 8.33 mm, L/D = 6) at an velocity of $v_P \approx 1150$ m/s. Additionally, three different test set-ups have been applied with 1) strong axial and lateral 2) weak axial and strong lateral and 3) strong axial and weak lateral confinement to get information about the confinement influence. The lower protection efficiency observed for layered ceramics compared to monolithic ones may be caused by higher flexure effects. In the case of layered ceramics this effect may superpose the effect of reduced shock wave loading caused by the bonding interlayer material of low shock impedance between the tiles. It has been found that already a small weakening of the axial and lateral confinements can influence crater geometry as well as residual penetration depth (protection efficiency).

Content

1 Introduction

The report gives a summary of the experiments performed with laterally confined 6 x 6" and 4 x 4" AlN ceramic tiles to investigate the protection efficiency change of layered ceramic targets compared to monolithic tiles. In an earlier test series for laterally unconfined AlN ceramic targets it has been demonstrated that the PMMA intermediate layers reduce the ballistic protection efficiency [1]. Furthermore, the unconfined ceramic targets were totally destroyed, because of the overpower of the kinetic energy of the projectile.

In a second and third test series the lateral tile dimensions were reduced in size from 150 x 150 mm (6 x 6") to 100 x 100 mm (4 x 4") and additionally the confinement and bonding procedure of the ceramic tiles was modified. The kinetic energy of the long rod penetrator was also reduced to lower masses and velocities.

2 Experimental procedure, test set-ups and test parameters

The heavy tungsten sinter alloy (WSA) projectiles were launched with the same acceleration and sabot techniques as described in Reference [1]. For evaluation of the terminal ballistic protection efficiency of layered AlN ceramic targets the depth-of-penetration (DOP) method has been applied.

In the following the different test set-ups and test parameters will be described (Figs. 1 - 7). In test series 2 the 150 x 150 mm (6 x 6") ceramic tiles were laterally confined by a squared 16 mm thick steel tube and 8 mm steel plates in between the tube and the ceramic package. The rear and front sides of the ceramic were supported by a 50 mm thick RHA backing and a 10 mm thick front plate (with 30 mm diameter hole), respectively. The ceramic tiles were glued together with a two-component silicone rubber of a film thickness of 0.3 mm. The bonding procedure is described in Ref. [1]. For test series 2 a WSA rod projectile with hemispherical nose ($m_p \approx 70$ g, $v_p = 1550$ m/s, D = 7.87 mm, L/D = 10) was used. The AlN ceramic tiles used in test series 2 - 3 came from the same production line as those of test series 1 (Ref. [1]).

For real targets it is necessary to chose the lateral tile dimensions as small as possible. Therefore, in test series 3 (Figs. 4-6) the lateral ceramic tile size was reduced from 150 x 150 mm (6 x 6") to 100 x 100 mm (4 x 4"). The total ceramic block thickness was also reduced to 38.1 mm (1.5"). Enabling the comparison of the experimental results of EMI, Germany, and CALTECH, USA, the penetrator mass and velocity was decreased from $m_p \approx 70$ g and $v_p \approx 1550$ m/s to $m_p \approx 50$ g (D = 8.33 mm, L/D = 6; flat nose) and $v_p \approx 1150$ m/s, respectively. Instead of a 50 mm thick RHA backing an 60 mm thick aluminum backing (Al6061-T651) supported the ceramic rear side. To guarantee a homogeneous bonding between the ceramic tiles the two-component silicone rubber was replaced by a 0.25 mm (10 mil) thick Polyurethane film, heated in the oven at 190° C (375° F) over 30 minutes, pressed together by a weight of a mass of 5 kg. In test set-up 3b (Fig. 5) a 10 mm thick steel plate with a 30 mm diameter hole is added in between the ceramic rear side and the aluminum backing. Test set-up 3c (Fig. 6) corresponds to test set-up 3a with the exception that the 6 mm thick steel plates between steel tube and ceramic block are removed. The laterally remaining air gap around the ceramic block makes the lateral confinement weaker.

For approximation of real target testing experiments with the test set-up in Fig. 7 (test series 4 & 5) are planned. This test set-up corresponds to the test set-up in Fig. 6 (test series 3c) with the following differences: 1) the single aluminum block is replaced by a 15 mm aluminum / 10 mm air gap / 60 mm aluminum backing 2) the 0.25 mm thick PU film between ceramic and aluminum is substituted by a 1 mm thick soft rubber sheet.

3 Experimental results and discussion

3.1 Test series 2

A typical result of test series 2 is shown in Figs. 8 and 9. Fig. 8a depicts the crater cross section of a 150 x 150 mm (6 x 6") target consisting of a 1" (25.4 mm) in front and a 1.5" (38.1 mm) tile at the rear. Both tiles are totally cracked. In the center of the target a large crater is formed with conical entrance and exit shapes. The radial crack pattern of the target rear side is visible in Fig. 8b after removing the RHA backing plate. Quantitative results for the residual penetration depth p_R are given in Table 1 and Fig. 16. The relatively small residual penetration depth measured in the RHA backing is in the range of 9.3 mm $\leq p_R \leq$ 15 mm; the data spread was up to 0.5 D. Therefore, the improvement of the protection efficiency of the ceramic with increasing layer number indicated by the linear regression curve should be considered very carefully.

3.2 Test series 3

In Figs. 9-15 the influence of the lateral confinement and backing of the ceramic will be demonstrated for monolithic (1.5") as well as layered (2x0.75" and 3x0.5") AlN ceramic targets 100x100 mm (4x4") in size. The quantitative results of test series 3 are summarized in Table 2.

The perspective view of Fig. 9 gives an impression of the steel confinement casing after the shot. Evidence is given that it has been well designed (no strong damage and no removed casing components) for the impact loading applied in the tests.

The test results of the strongest lateral confinement and backing used are depicted in Figs. 10 and 11 for the 38.1 mm (1.5") monolithic and the 3x12.7 mm (3x0.5") layered AlN ceramic targets. From the cross sectioned targets it is clearly visible that the rod projectile is consumed by the first third of the monolithic ceramic tile; a very flat and wide crater is formed. The reminder of the ceramic tile is damaged by radial cracks initiated by shock waves propagating from the tip of the rod. The aluminum backing remains undamaged. In the case of the layered ceramic target (Fig. 11) the kinetic energy of the projectile forms a crater distinctly narrower and deeper compared to that of the monolithic ceramic. The residual penetration depth p_R is around 6 mm (Table 2). These observations and test results seem to be in contradiction to theoretical considerations carried out by analytical model calculations at the DOW Chemical Company. By means of these calculations it has been found that the PU interlayers diminish the intensity of the shock wave propagation initiated in the front layer to the subsequent ceramic tiles, i.e., pre-damaging of these layers is reduced. Because of the experimental results presented here it is supposed that in practice flexure waves dominate the damaging process of the ceramic.

This behavior of the ceramic observed in test series 3a has also been found in test series 3b and 3c with a weaker backing (air gap around shot line at the ceramic rear side) and weaker lateral confinement (air gap around the ceramic), respectively. The air gap between ceramic block and aluminum backing means a reduction of the axial confinement along the shot line. This results in the formation of an exit crater with a diameter of around the hole diameter in the steel plate (Figs. 12 and 13).

The weaker lateral confinement of test set-up 3c caused by the air gap around the ceramic block reduces the protection efficiency even stronger than the weakened axial confinement of test set-up 3b (Figs. 14 and 15). A larger crater with comminuted ceramic is formed leading to a lower protection efficiency of the monolithic as well as layered ceramic targets.

Fig. 15 represents the residual penetration depth p_R in the aluminum backing for the monolithic (1.5"), two-layered (2x0.75") and tree-layered (3x0.5") targets. The ceramic tiles with the PU bonding films presented before were heated up in the oven from 20°C to 190°C which was held constant over 30 minutes and subsequently cooled down to 20°C by natural temperature radiation. In the case of experiment nos. 8738-8740 (Fig. 15) the glued targets (PU film) were cooled down to 20°C immediately after the high temperature of 190°C has been achieved.

References

[1] K. Weber, V. Hohler and A. J. Stilp. Protection Efficiency of Layered AlN Ceramic Targets Bonded with PMMA – Terminal Ballistic Experiments. EMI-Report E 11/96

Exp. no.	m_P [g]	v_P [m/s]	α_1 [deg]	Lateral target dimensions [mm]	AlN No. of tiles	AlN tile thickness' [mm]	AlN total tile thickness [mm]	RHA thickness [mm]	p_R [mm]	p_R / D
8627	69.0	1498	-3	150 x 150	-	-		100	70.5	-
8628	69.0	1500	-3	150 x 150	-	-	-	100	72.8	-
8629	68.7	1501	-1	150 x 150	-	-	-	100	71.9	-
8630	68.8	1493	-2	150 x 150	2	38.1 + 25.4	65.15	50	12.0	1.53
8631	68.9	1554	+0.5	150 x 150	2	38.1 + 25.4	65.15	50	12.2	1.55
8632	68.9	1541	-2	150 x 150	2	38.1 + 25.4	65.15	50	15.0	1.91
8633	68.8	1543	-1	150 x 150	3	2 x 25.4 + 12.7	62.7	50	10.0	1.27
8634	68.8	1548	0	150 x 150	3	2 x 25.4 + 12.7	62.7	50	10.0	1.27
8635	69.0	1564	-1	150 x 150	4	3 x 19.05 + 6.35	64.3	50	12.7	1.61
8636	69.0	1560	-2	150 x 150	4	3 x 19.05 + 6.35	64.3	50	14.0	1.78
8637	68.8	1562	-0.5	150 x 150	5	5 x 12.7	64.0	50	9.3	1.18
8638	68.7	1543	-0.5	150 x 150	5	5 x 12.7	64.0	50	12.4	1.58
8639	68.7	1546	+1.5	150 x 150	10	10 x 6.35	65.7	50	12.5	1.59
8640	68.7	1546	+1	150 x 150	10	10 x 6.35	65.7	50	10.1	1.28

Projectile: WSA rod, D = 7.87 mm, L / D = 10; backing plate: RHA, 50 mm thick, HV20 = 280; cover plate: steel, 10 mm thick;

Table 1 Test results of test series 2

Exp. No.	Test series	v_P [km/s]	m_P [g]	AlN layers	Yaw angle [deg]	St plate thickn. [mm]	p_R [mm]
8715	3a	1223	51	Al6061-T651 5 x 40 mm	-2.0	--	123.0
8716	3a	1192	51	1 x 1.5"	0	--	0
8718	3a	1145	51	1 x 1.5"	-1.0	--	0
8717	3a	1174	51	3 x 0.5"	-1.5	--	6.2
8719	3a	1161	51	3 x 0.5"	+0.5	--	6.0
8725	3b	1167	51	1 x 1.5"	+1.0	9.75	--
8726	3b	1125	51	1 x 1.5"	+0.5	9.75	--
8724	3b	1203	51	3 x 0.5"	+3.5	9.75	8.2
8727	3b	1169	51	3 x 0.5"	-2.0	9.75	20.5
8733	3c	1130	51	1 x 1.5"	+2.0	--	6.8
8738	3c	1133	51	1 x 1.5"	+1.0	--	0
8734	3c	1140	51	2 x 0.75"	0	--	10.3
8739	3c	1182	51	2 x 0.75"	+2.0	--	26.0
8735	3c	1186	51	3 x 0.5"	-4.0	--	23.3
8740	3c	1170	51	3 x 0.5"	+0.5	--	23.5

Projectile: WSA rod, D = 8.33 mm, L / D = 6; backing plate: Al6061-T651, 60 mm thick; cover plate: steel, 10 mm thick;

Table 2 Test results of test series 3

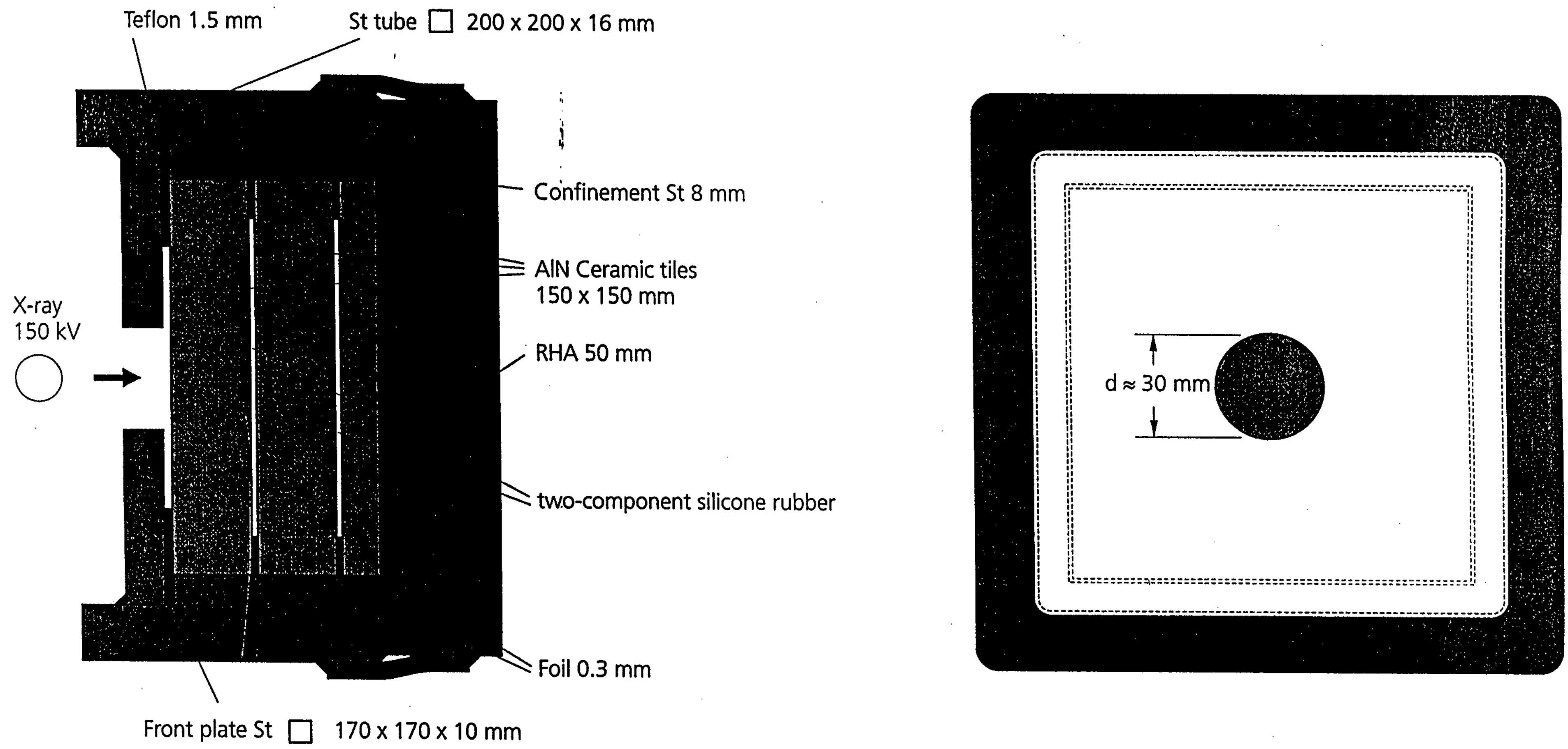

Projectile: $D = 7.87$ mm, $L/D = 10$, $m_p \approx 70$ g, $v_p = 1550$m/s, hemispherical nose

Fig. 1 Test set-up 2

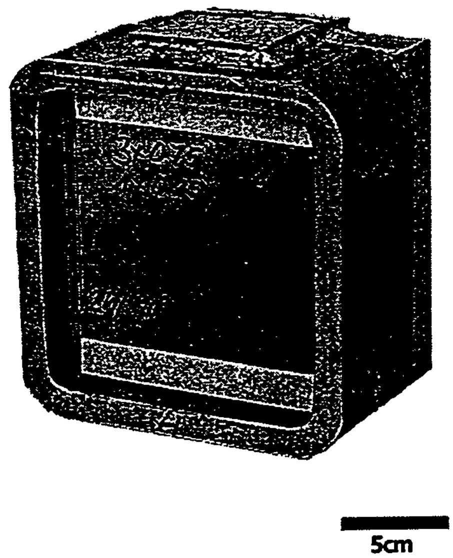

Fig. 2 AlN ceramic target assembled in steel casing with RHA backing plate; front plate removed (test series 2)

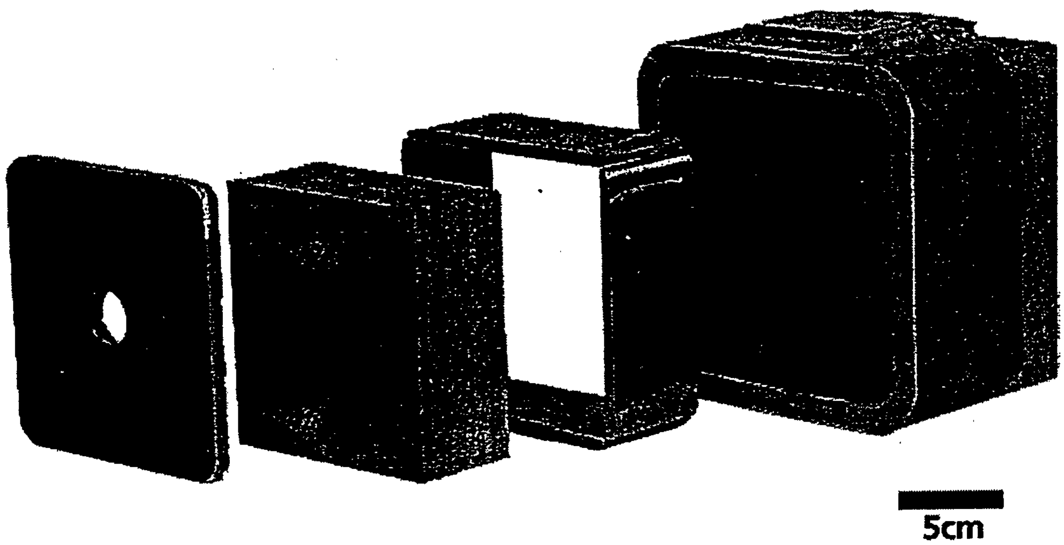

Fig. 3 Assembled AlN ceramic tiles and confinement components (test series 2)

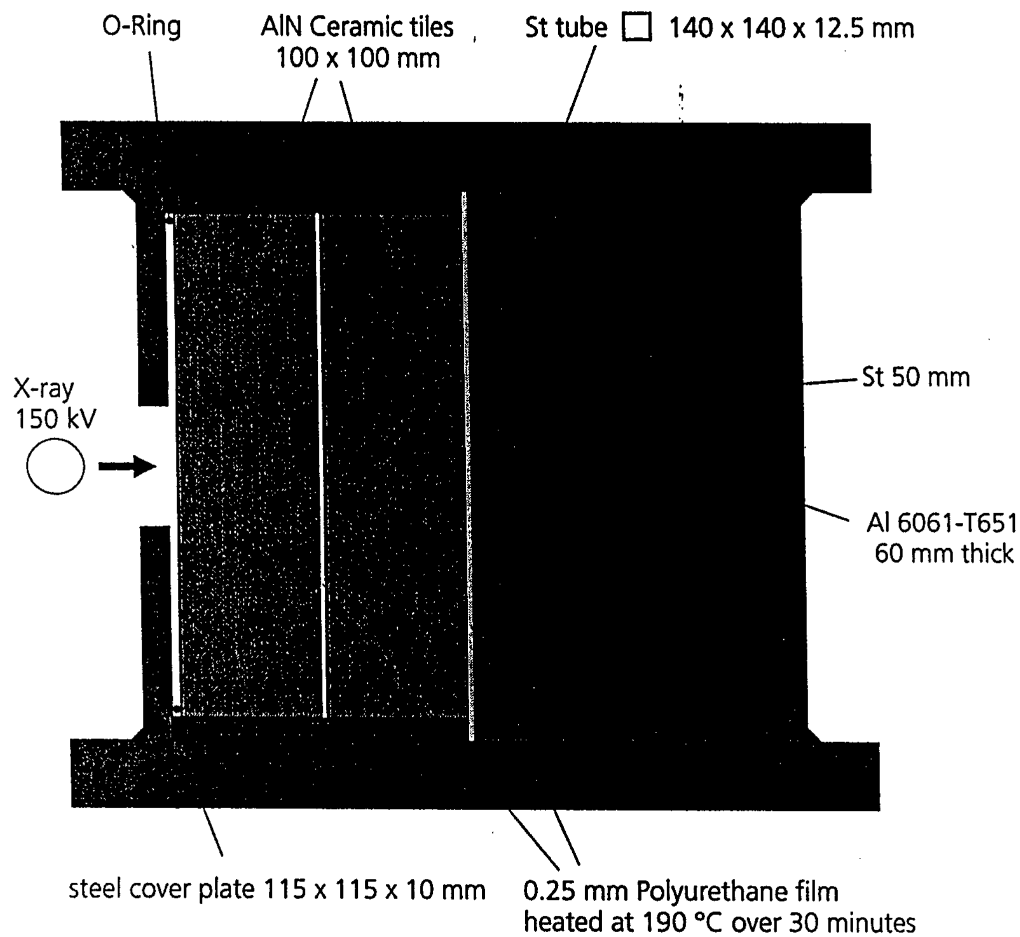

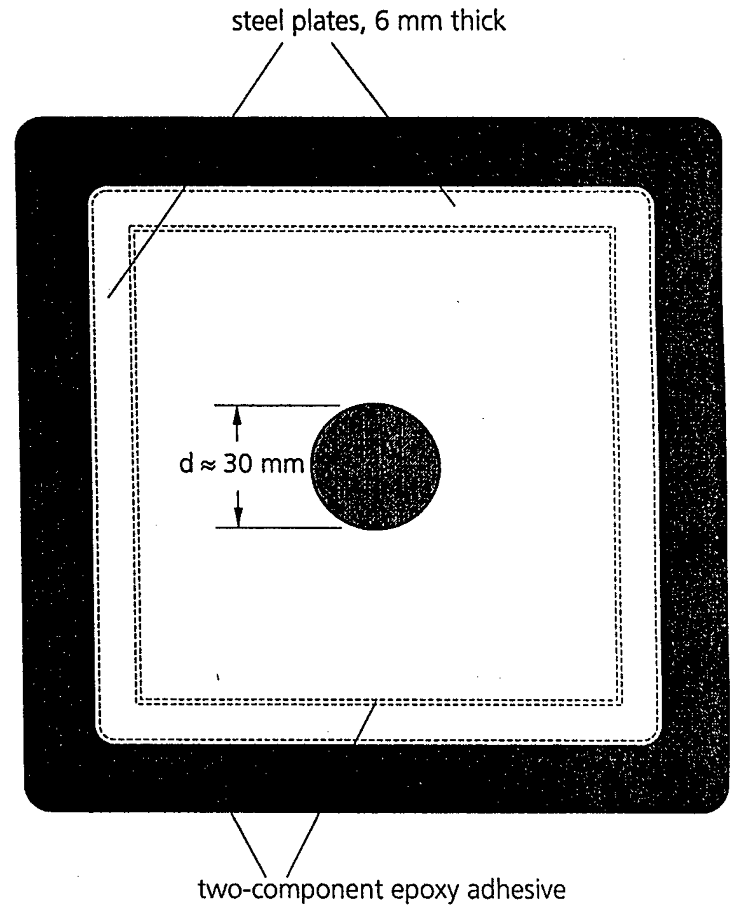

Projectile: D = 8.33 mm, L/D = 6, $m_p \approx 50$ g, $v_p = 1150$m/s, flat nose

Fig. 4 Test set-up 3a

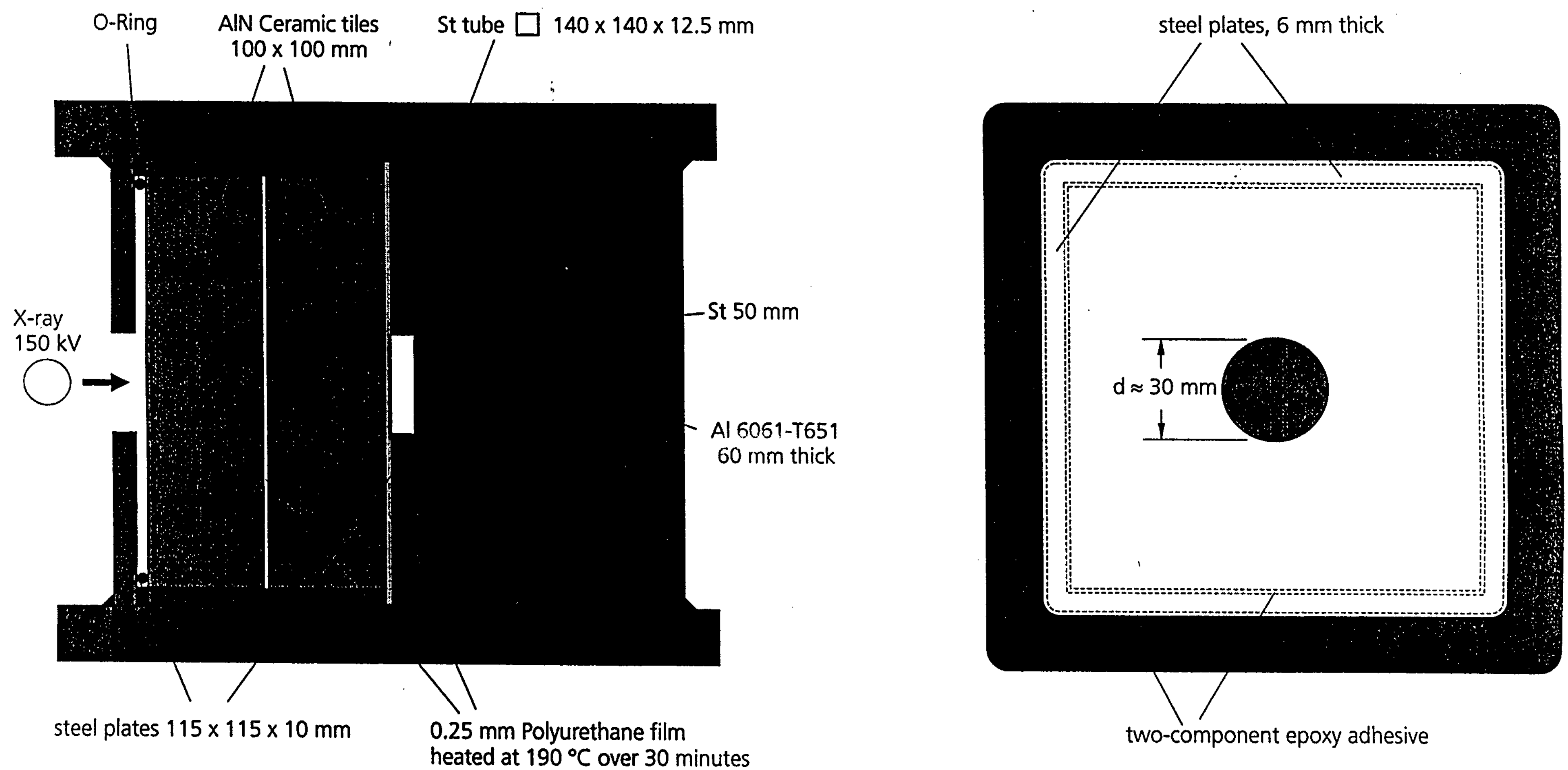

Projectile: D = 8.33 mm, L/D = 6, $m_r \approx 50$ g, $v_r = 1150$m/s, flat nose

Fig. 5 Test set-up 3b

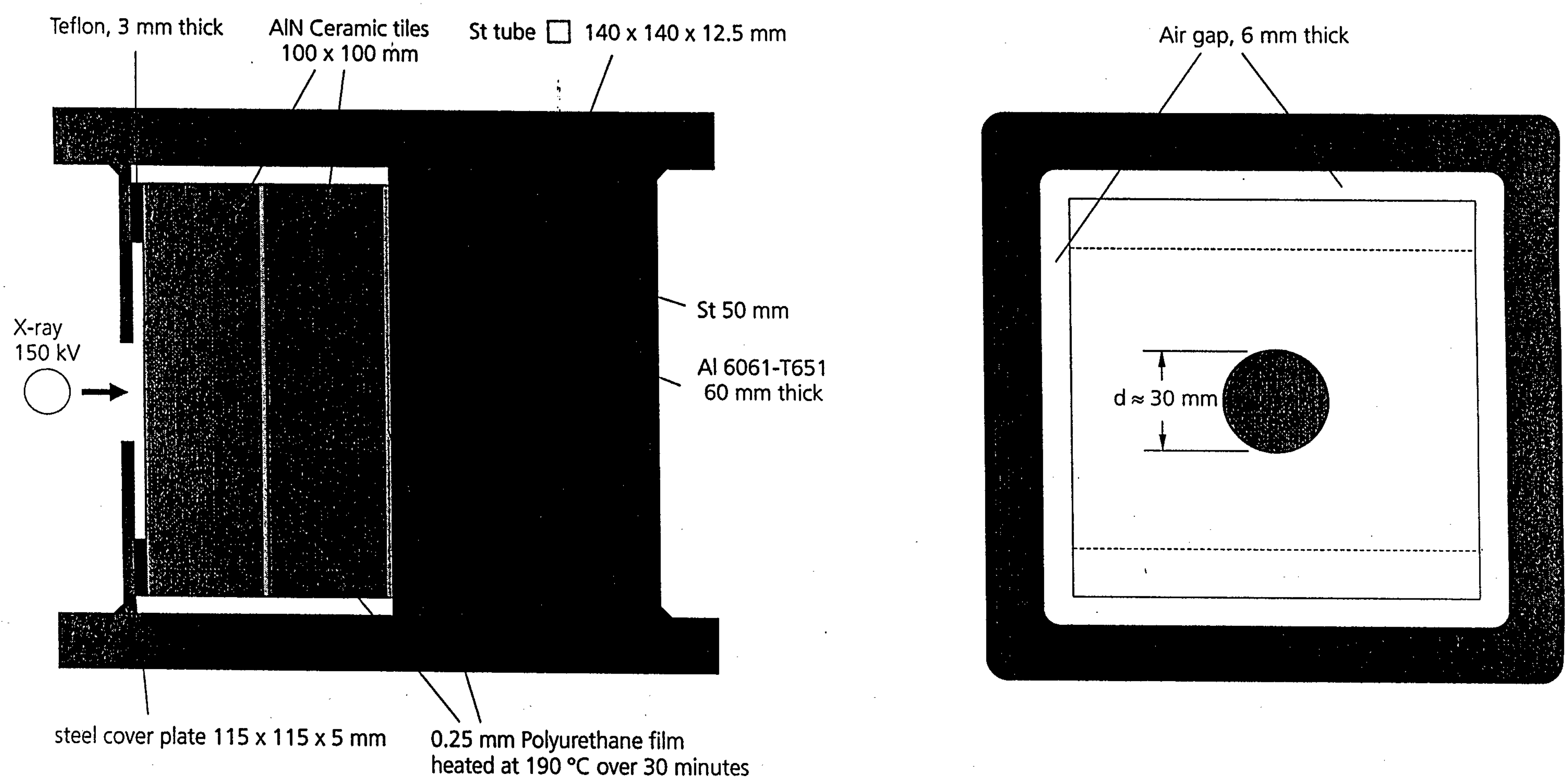

Projectile: D = 8.33 mm, L/D = 6, $m_r \approx 50$ g, $v_r = 1150$m/s, flat nose

AlN-Targets: 1) 1.5"   2) 2x0.75"   3) 3x0.5"

Fig. 6   Test set-up 3c

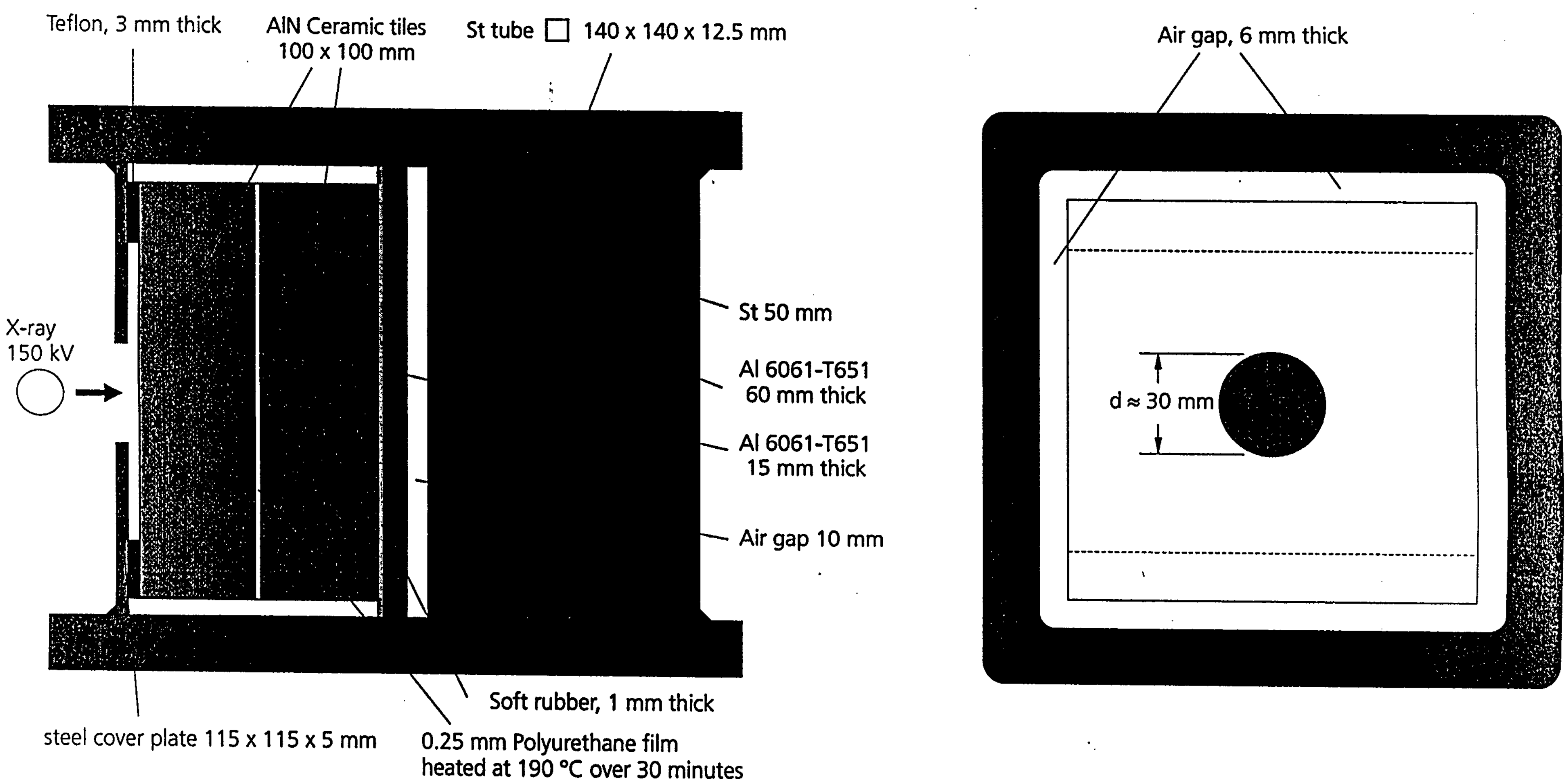

Projectile: $D = 8.33$ mm, $L/D = 6$, $m_P \approx 50$ g, $v_P = 1150$m/s, flat nose

Fig. 7 Test set-up of test series 4 & 5

Fig. 8a Crater cross section of a two layer AlN ceramic tile (6 x 6", 1" + 1.5" thick), after perforation of a WSA rod (D = 7.87 mm, L/D = 10) at v_P = 1493 m/s (Exp. 8630)

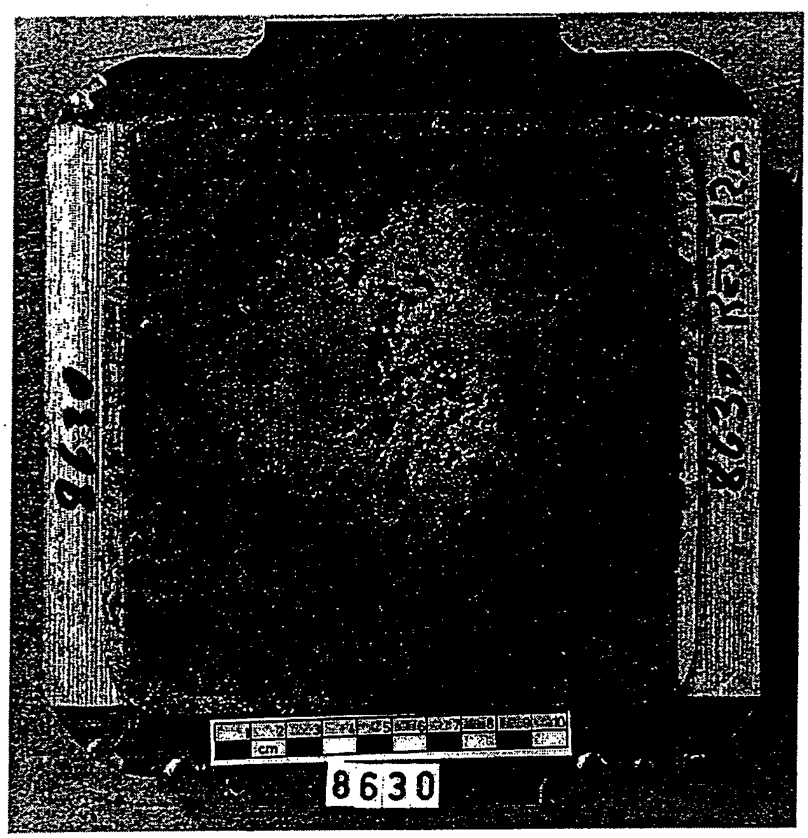

Fig. 8b AlN ceramic rear side after removal of the RHA backing plate (Exp. 8630)

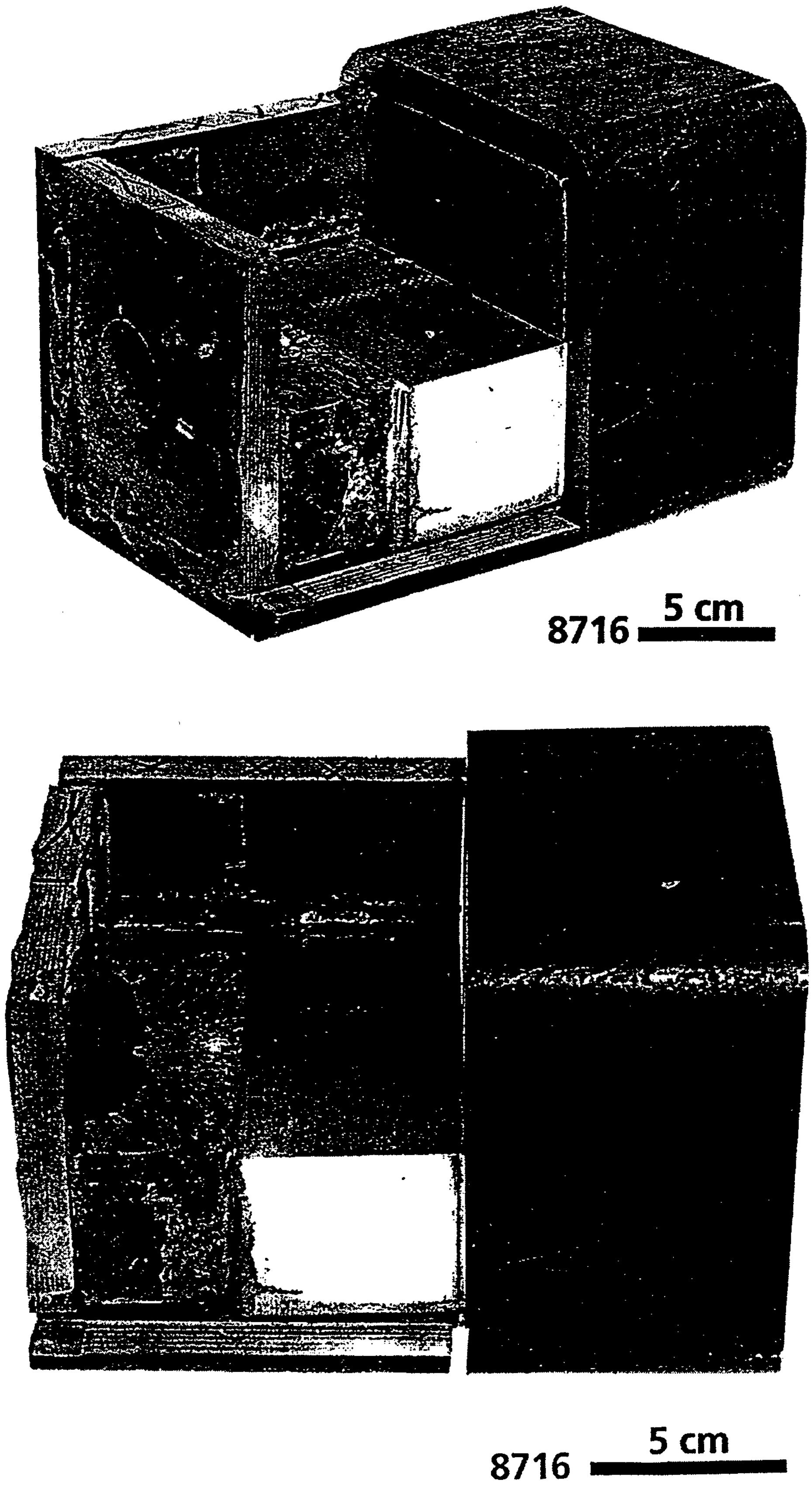

Fig. 9 Perspective views of steel casing, cross sectioned monolithic 1.5" AlN ceramic and aluminum backing (test series 3a, strong confinement) top: front view bottom: side view

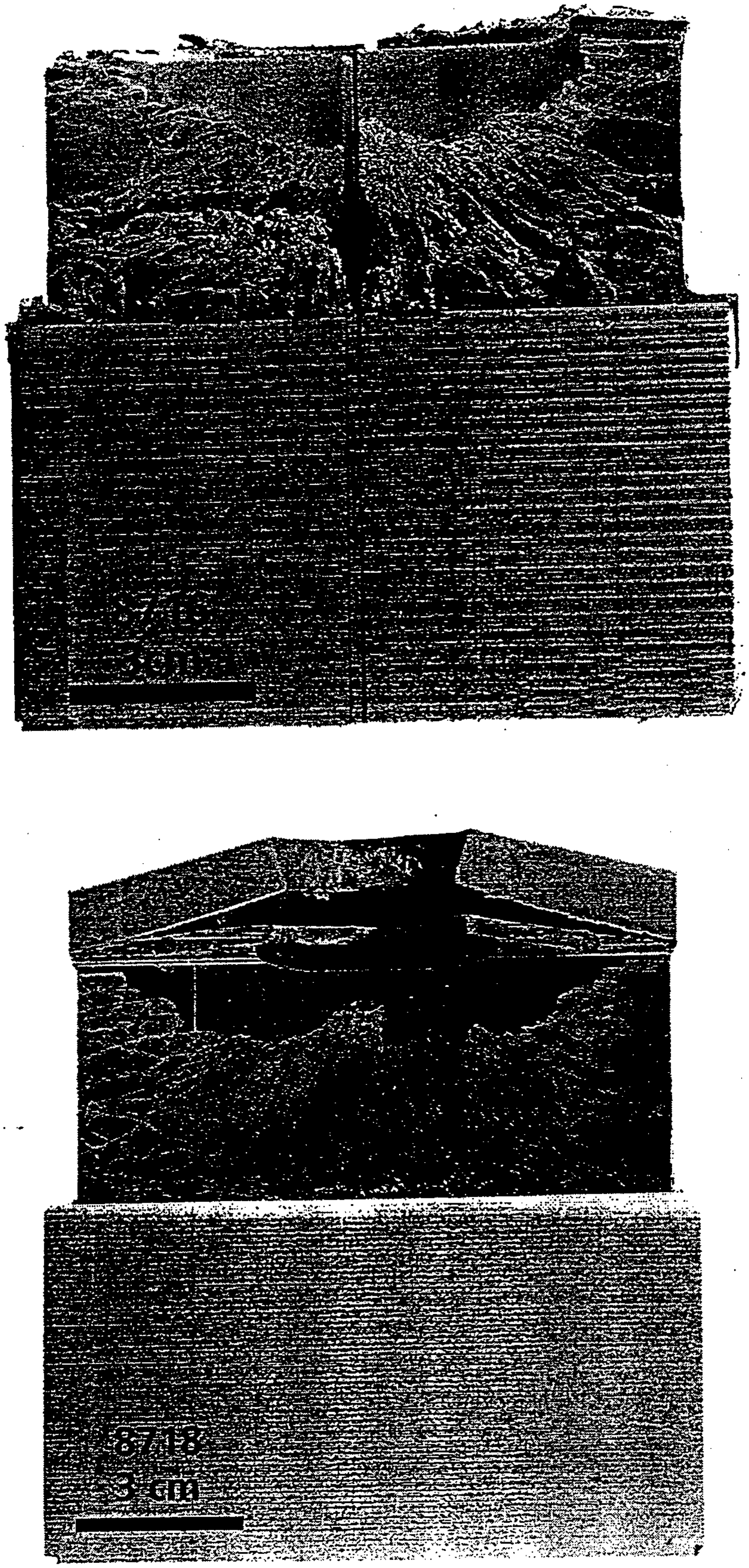

Fig. 10 Cross sections of 1.5" monolithic AlN ceramic targets with aluminum backing, (test series 3a, strong confinement).
a) Exp. 8716; v_P = 1192 m/s; (front plate removed) b) Exp. 8718; v_P = 1145 m/s

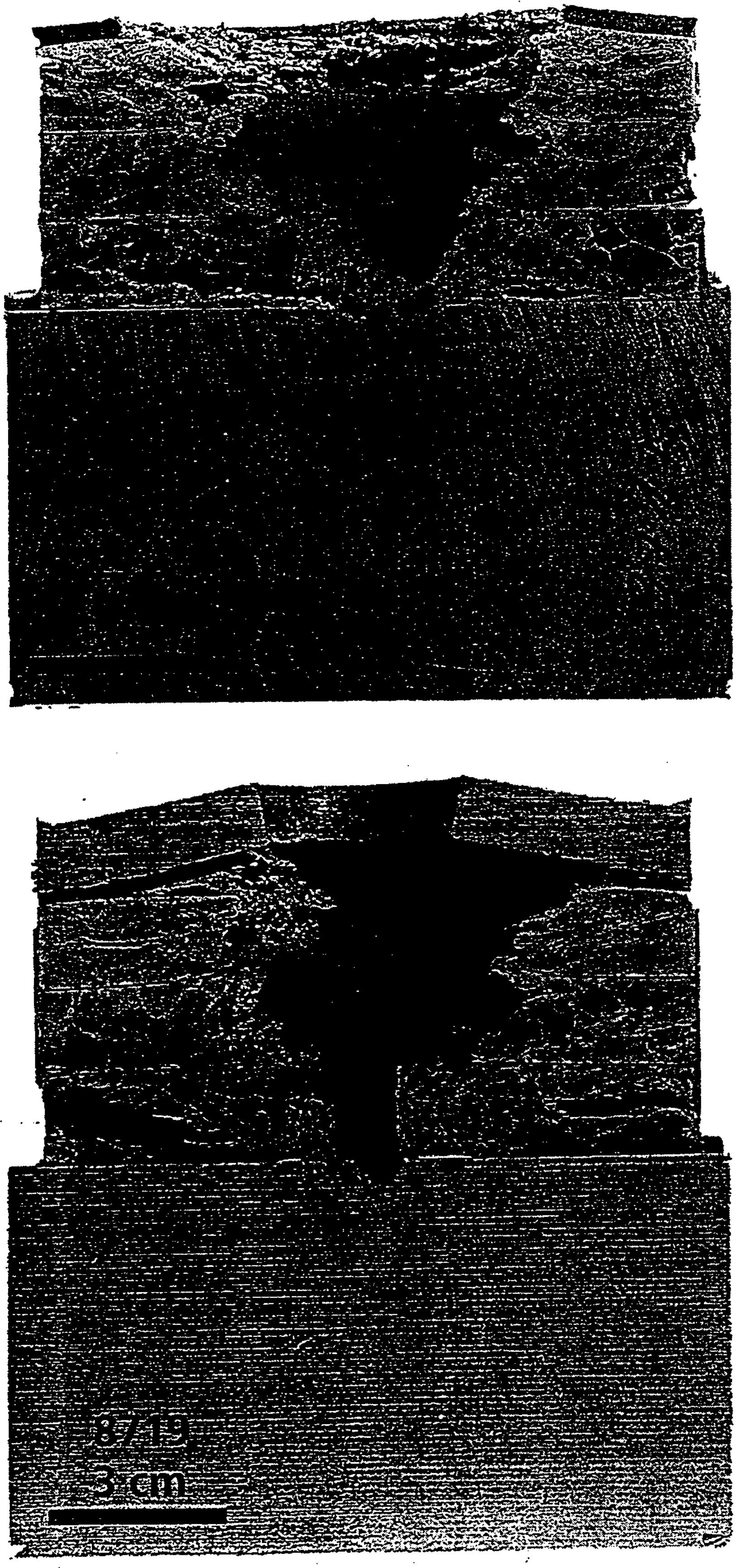

Fig. 11 Cross sections of 3x0.5" layered AlN ceramic target (front plate removed) with aluminum backing, (test series 3a, strong confinement). a) Exp. 8717; $v_P = 1174$ m/s b) Exp. 8719; $v_P = 1161$ m/s

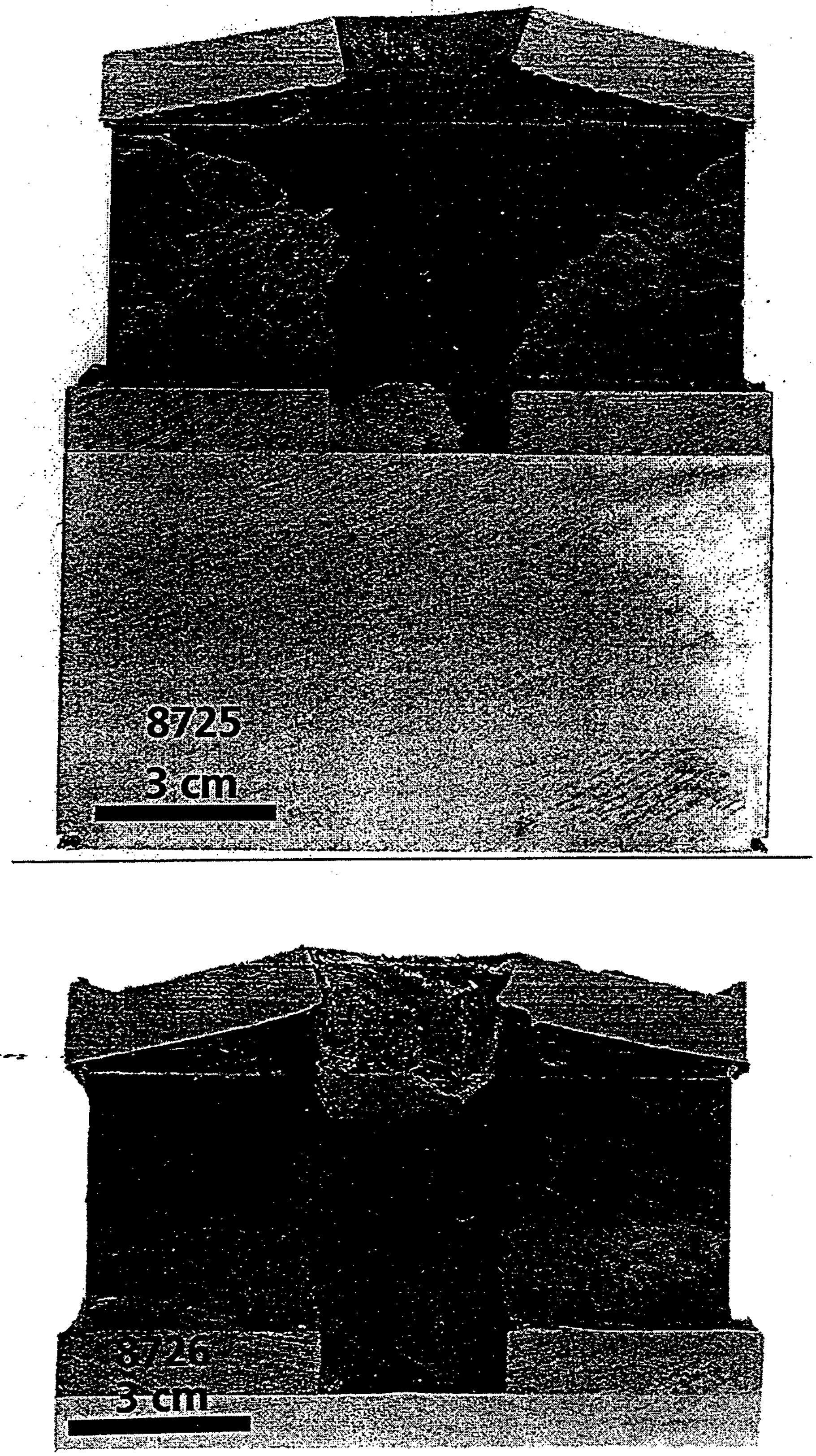

Fig. 12 Cross sections of 1.5" monolithic AlN ceramic target and steel & aluminum backing (test series 3b, weakened axial confinement); a) Exp. 8725; v_P = 1167 m/s b) Exp. 8726; v_P = 1125 m/s

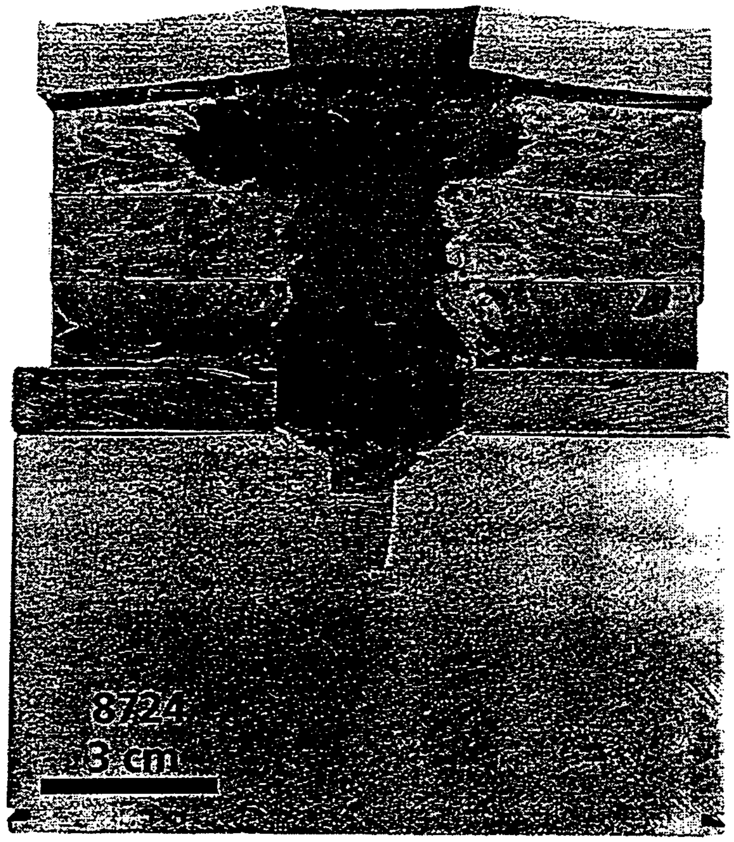

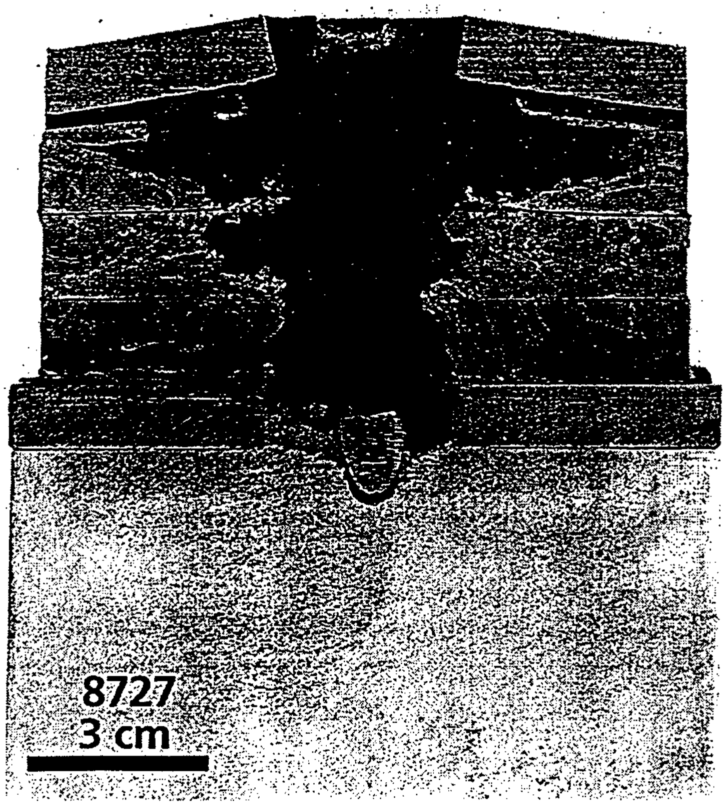

Fig. 13 Cross sections of 3 x 0.5" layered AlN ceramic target and steel & aluminum backing (test series 3b, weakened axial confinement); a) Exp. 8724; v_P = 1203 m/s b) Exp. 8727; v_P = 1169 m/s

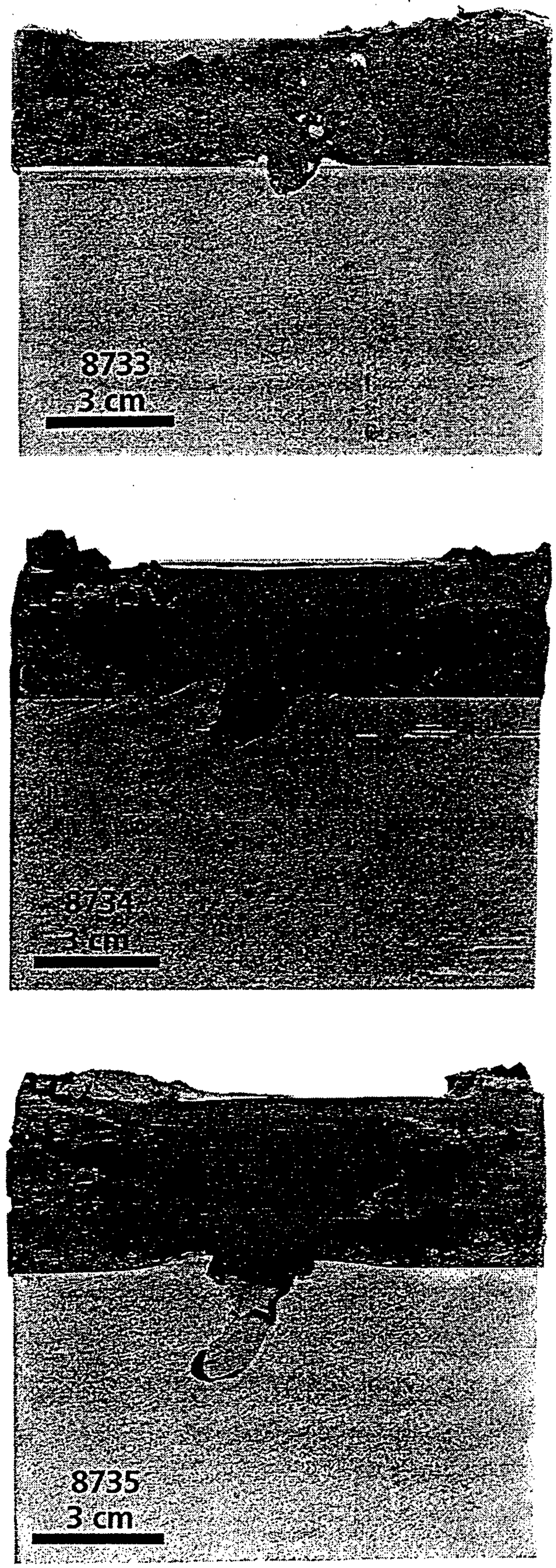

Fig. 14 Cross sections of AlN ceramic target and aluminum backing (test series 3c, weakened lateral confinement);
a) Exp. 8733; v_P = 1130 m/s; 1.5" monolithic b) Exp. 8734; v_P = 1140 m/s; 2 x 0.75" layers
c) Exp. 8735; v_P = 1186 m/s; 3 x 0.5" layers

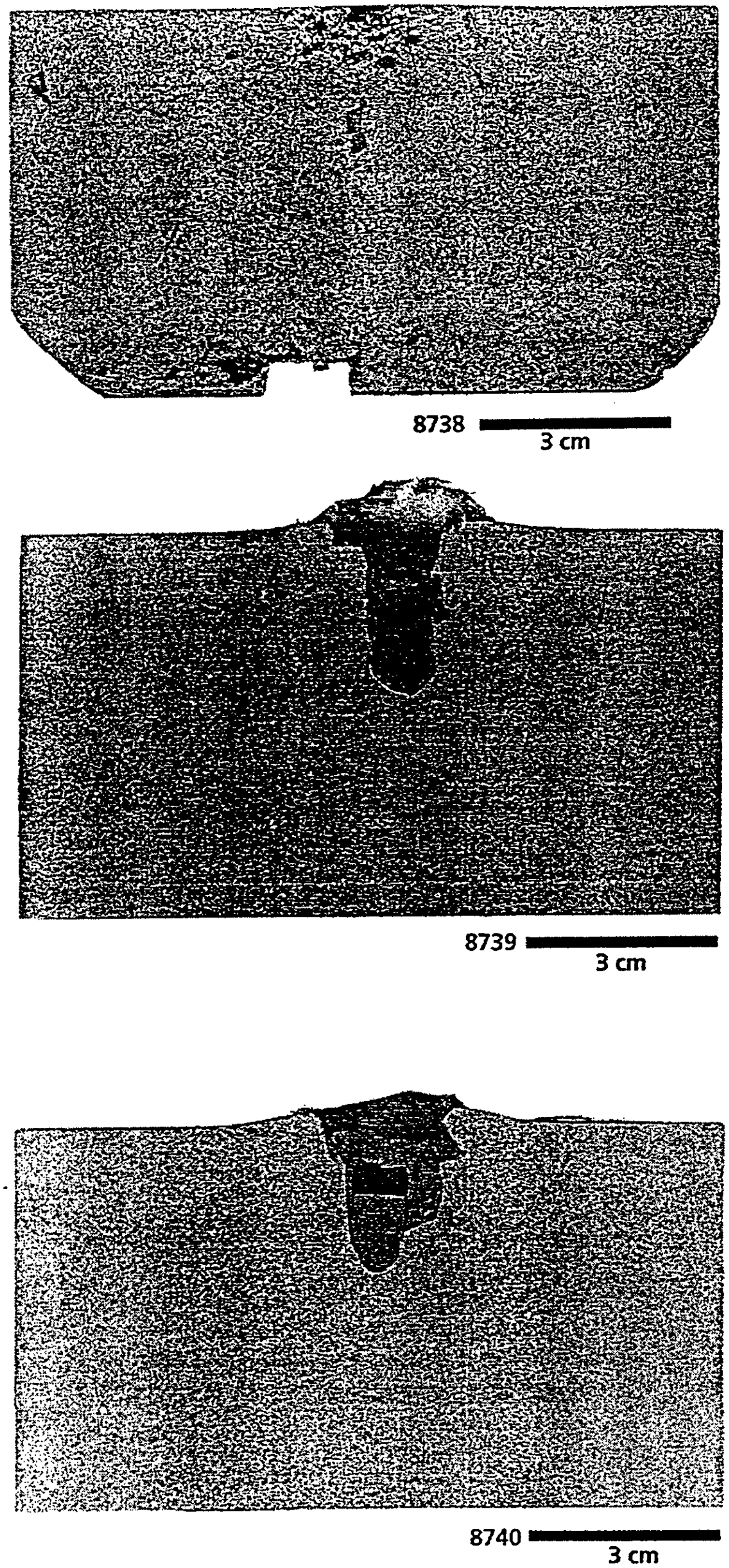

Fig. 15 Cross sections of the aluminum backing with residual projectile (test series 3c, weakened lateral confinement);
a) Exp. 8738; v_P = 1133 m/s; 1.5" monolithic b) Exp. 8739; v_P = 1182 m/s; 2 x 0.75" layers
c) Exp. 8740; v_P = 1170 m/s; 3 x 0.5" layers

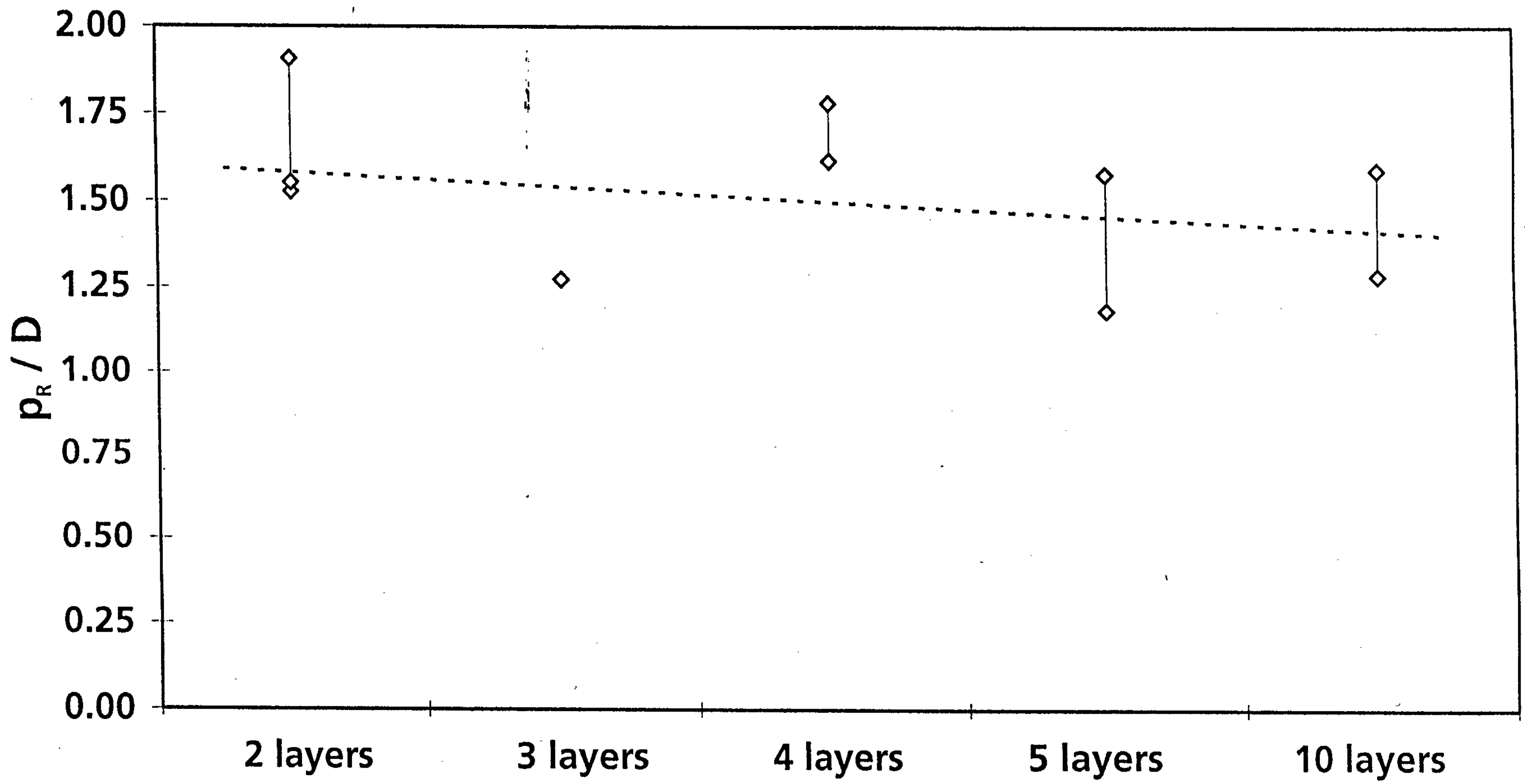

Fig. 16 Normalized residual penetration depth p_R vs. AlN layer number (test series 2)

Verteilerliste

Bericht Nr. E 19/97

Autor: K. Weber, V. Hohler
Titel: Protection Efficiency of Layered AlN Ceramics Bonded with Polyurethane Films

Interne Verteilung:
Autor(en): K. Weber
V. Hohler

Belegexemplar Bibliothek EMI-Freiburg

weitere Referate/Institute/Firmen/Personen:
Dr. El-Raheb, DOW Chemical Company, Midland, Michigan, USA (6 Exemplare)

27.11.1997

Reference [7]
Protection Efficiency of Layered AIN Ceramics Bonded with Polyurethane Films

DISTRIBUTION LIST

No. of Copies	Organization
2	Defense Technical Information Center DTIC DDA 8725 John J. Kingman Rd. Ste. 0944 Ft. Belvoir, VA 22060-6218
10	U.S. Army Tardec K. Bishnoi (5 cps) D. Templeton J. Thompson AMSTA TR R MS 263 Warren, MI 48397-5000
1	Army High Performance Computing Research Center T. Holmquist 1200 Washington Ave. S. Minneapolis, MN 55415
2	Dir. USARL AMSRL-WM-TD A. Rajendran D. Grove Aberdeen Proving Ground Aberdeen, MD 21005-5065

Reference [8]
Results of the 1998 Center and Off-Center Hitting Tests with 4 x 4″ and 6 x 6″ AlN Ceramic Targets

EMI

Fraunhofer Institut
Kurzzeitdynamik
Ernst-Mach-Institut

Fraunhofer EMI Eckerstraße 4 D-79104 Freiburg

Institutsleitung
Prof. Dr. rer. nat. Klaus Thoma

Eckerstraße 4
D-79104 Freiburg

Telefon +49 (0) 761/2714-0
Telefax +49 (0) 761/2714-316

Dr. Michael El-Raheb
The DOW Chemical Company
Central Research Engin. Lab.
Bldg. 1776

Midland, MI 48640

USA

Karl Weber
Durchwahl +49 (0) 761/2714-323
Telefax +49 (0) 761/2714-316
e-mail: weber@emi.fhg.de

Freiburg,
27. November 1998

Results of the 1998 center and off-center hitting tests with 4 x 4" and 6 x 6" AlN ceramic targets

Dear Dr. El-Raheb:

Enclosed please find the results of all the tests with monolithic and layered AlN ceramic targets carried out in 1998.

The tables and diagrams include also the data of the 1997 experiments performed with test set-up 3c (Exps. 8733 – 8740); these results were already presented in EMI report E 19/97 „Protection Efficiency of Layered AlN Ceramics Bonded with Polyurethane Films".

Don't hesitate to contact us if you have any questions.

We are looking forward to your visit at Ernst-Mach-Institut in March 8-12, 1999.

Yours sincerely,

K. Weber

K. Weber
Staff Scientist

Dr. E. Schneider
Head of the Impact Physics Division

Enclosures:

Fraunhofer Institut
Kurzzeitdynamik
Ernst-Mach-Institut

Fraunhofer EMI Eckerstraße 4 D-79104 Freiburg

Dr. Michael El-Raheb
The DOW Chemical Company
Central Research Engin. Lab.
Bldg. 1776

Midland, MI 48640

USA

Institutsleitung
Prof. Dr. rer. nat. Klaus Thoma

Eckerstraße 4
D-79104 Freiburg

Telefon +49 (0) 7 61 / 27 14-0
Telefax +49 (0) 7 61 / 27 14-3 16

Karl Weber
Durchwahl +49 (0) 761/2714-323
Telefax +49 (0) 761/2714-316
e-mail: weber@emi.fhg.de

Freiburg,
27. November 1998

Results of the 1998 center and off-center hitting tests with 4 x 4" and 6 x 6" AlN ceramic targets

Dear Dr. El-Raheb:

Enclosed please find the results of all the tests with monolithic and layered AlN ceramic targets carried out in 1998.

The tables and diagrams include also the data of the 1997 experiments performed with test set-up 3c (Exps. 8733 – 8740); these results were already presented in EMI report E 19/97 „Protection Efficiency of Layered AlN Ceramics Bonded with Polyurethane Films".

Don't hesitate to contact us if you have any questions.

We are looking forward to your visit at Ernst-Mach-Institut in March 8-12, 1999.

Yours sincerely,

K. Weber

K. Weber
Staff Scientist

Dr. E. Schneider
Head of the Impact Physics Division

Enclosures:

Test Set-Up of the Depth-of-Penetration Method (Test Series 3c)

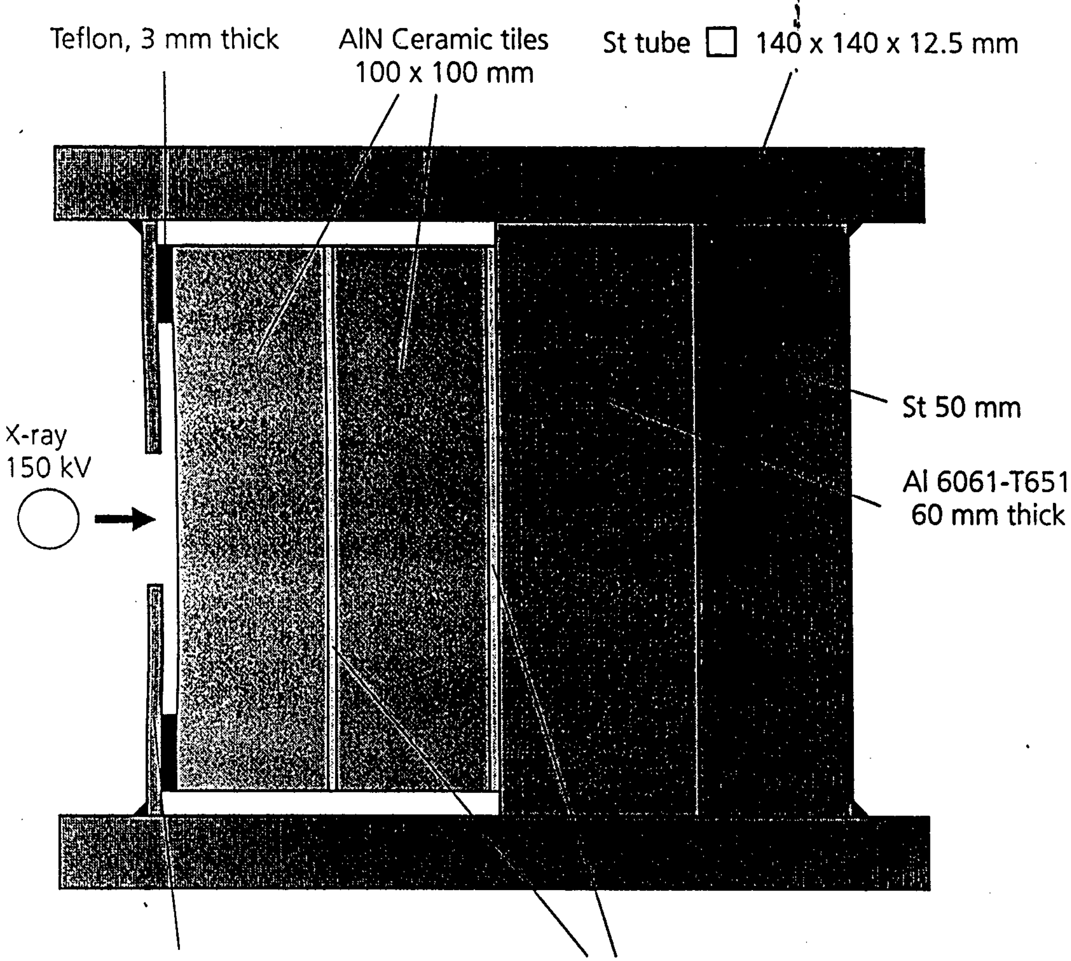

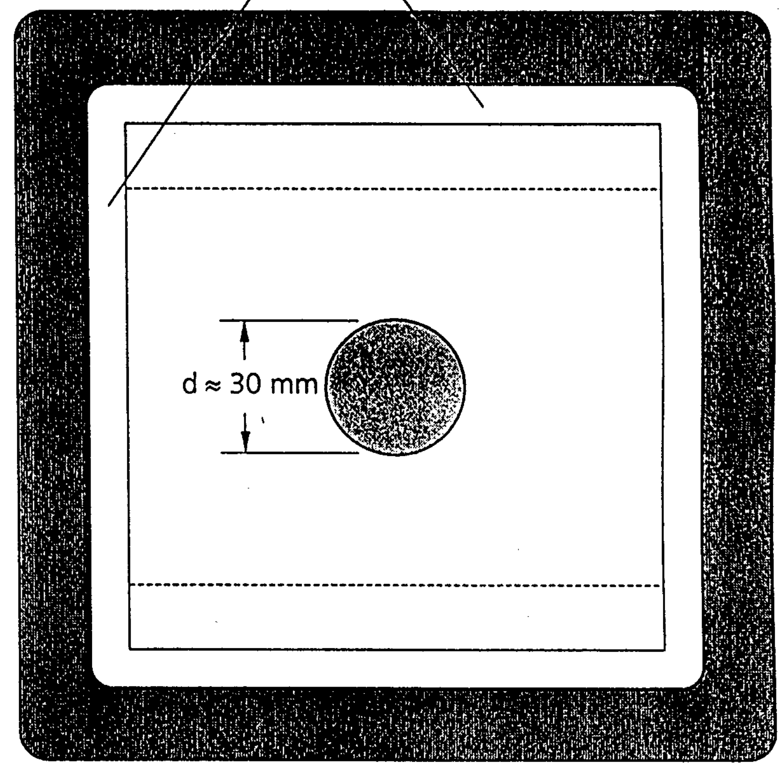

Projectile: D = 8.33 mm, L/D = 6, $m_p \approx 50$ g, $v_p = 1150$m/s, flat nose

AlN-Targets: 1) 1.5"   2) 2x0.75"   3) 3x0.5"   4) 6x0.25"

Fraunhofer Institut

Author: Karl Weber

Test Set-Up of the Depth-of-Penetration Method (Test Series 3d)

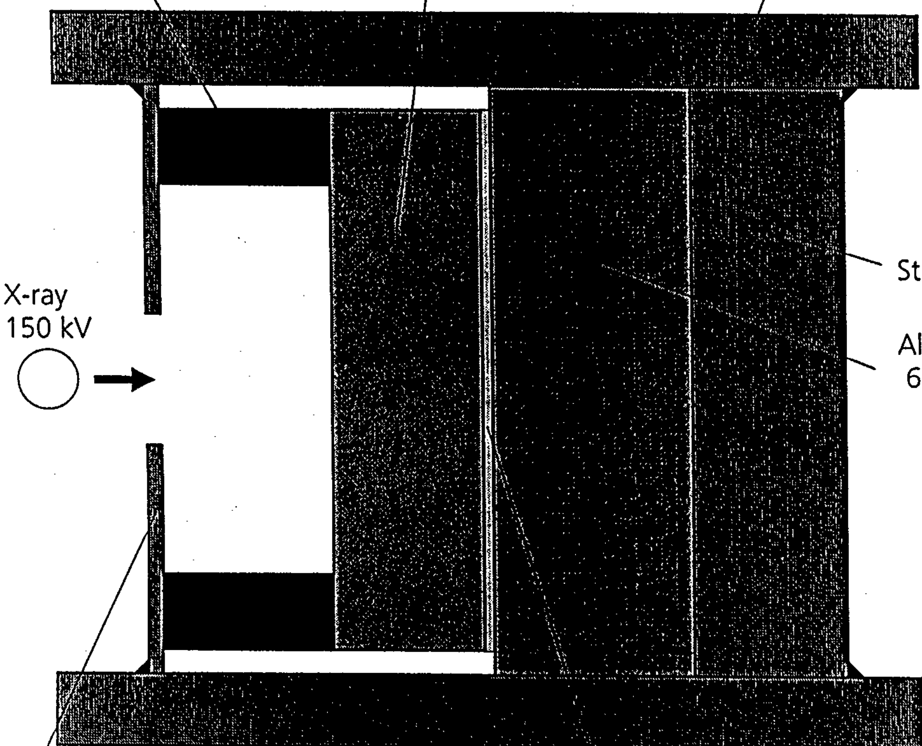

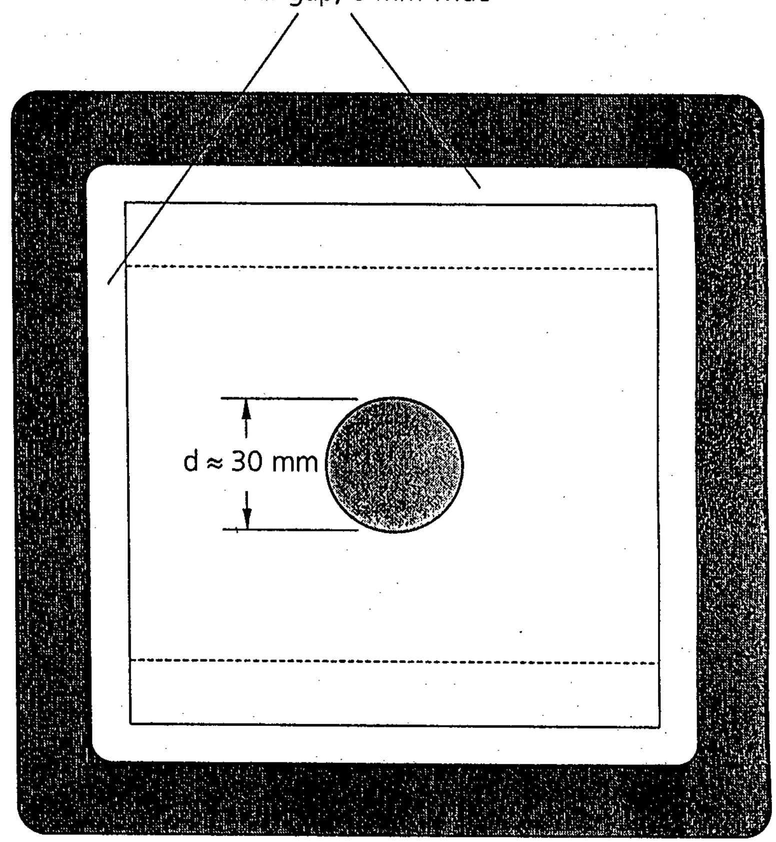

Projectile: D = 8.33 mm, L/D = 6, $m_P \approx 50$ g, v_P = 1150m/s, flat nose

AlN-Targets: 1 x 1.5" (monolith)

Fraunhofer Institut

Author: Karl Weber

Test Set-Up of the Depth-of-Penetration Method (Test Series 3e)

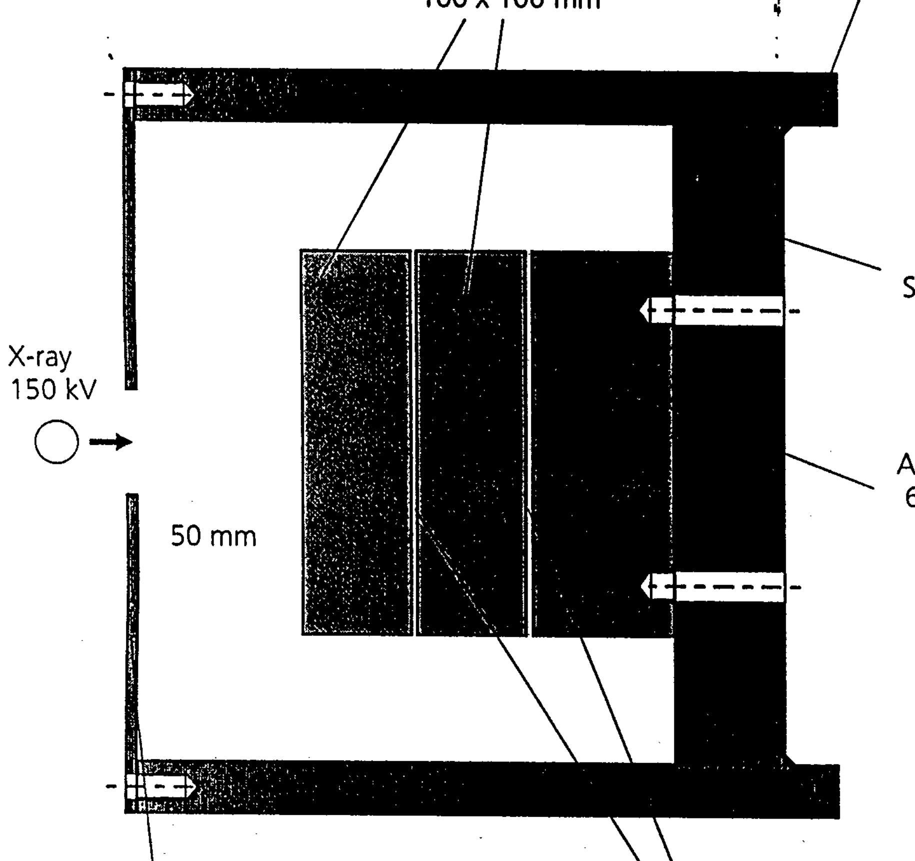

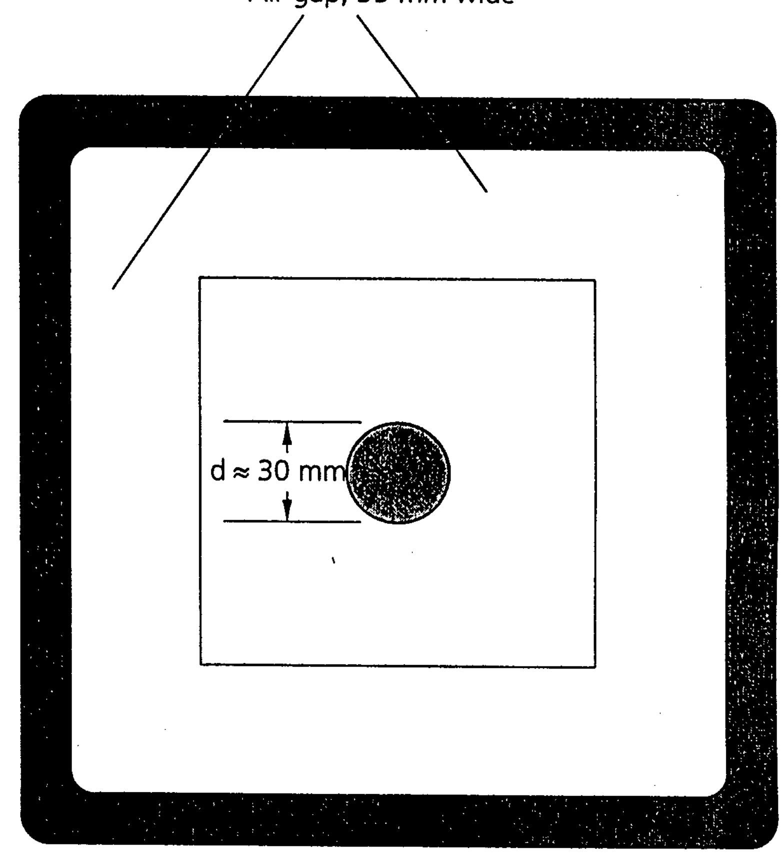

ojectile: D = 8.33 mm, L/D = 6, $m_p \approx 50$ g, $v_p = 1150$m/s, flat nose

AlN-Targets: 1) 1.5" 2) 2 x 0.75" 3) 3 x 0.5" 4) 6 x 0.25"

Fraunhofer Institut Kurzzeitdynamik Ernst-Mach-Institut

Author: Karl Weber

Test Set-Up of the Depth-of-Penetration Method (Test Series 3f)

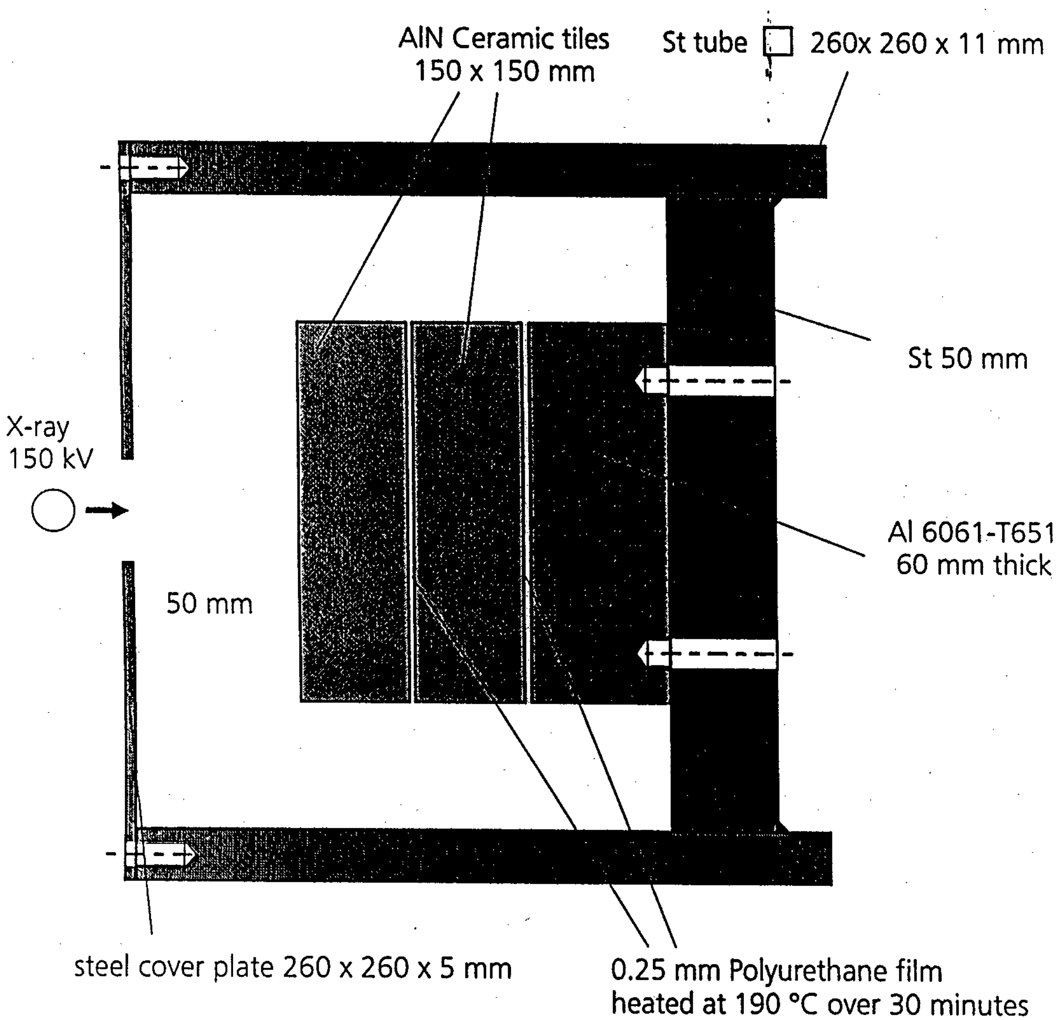

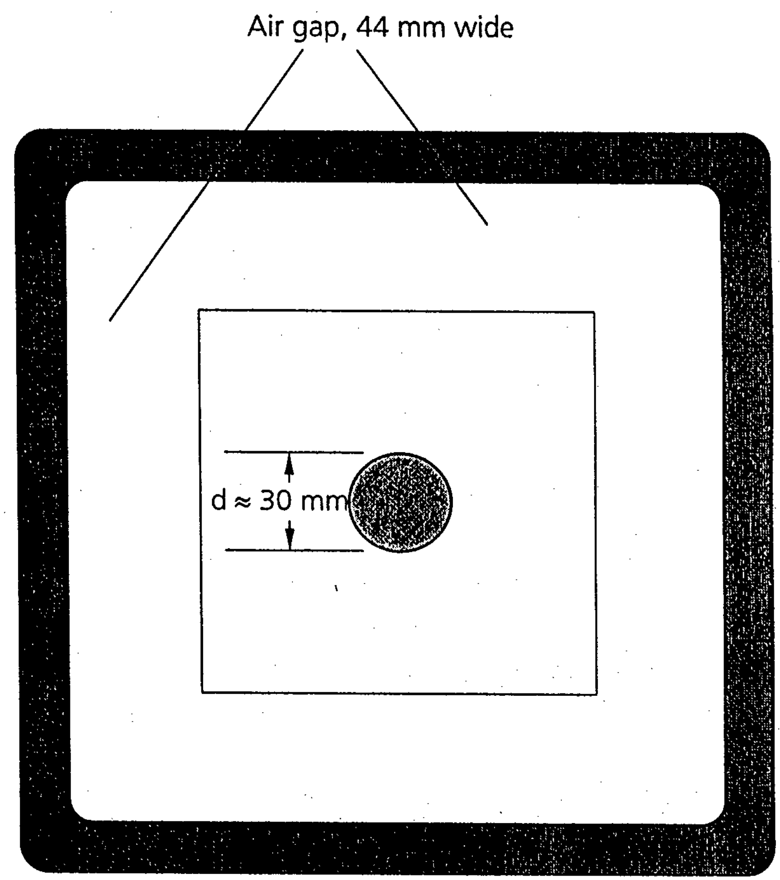

ojectile: D = 8.33 mm, L/D = 6, $m_p \approx 50$ g, $v_p = 1150$m/s, flat nose

AlN-Targets: 1) 1.5" 2) 2 x 0.75" 3) 3 x 0.5" 4) 6 x 0.25"

Test Set-Up of the Depth-of-Penetration Method (Test Series 3g-OCD)

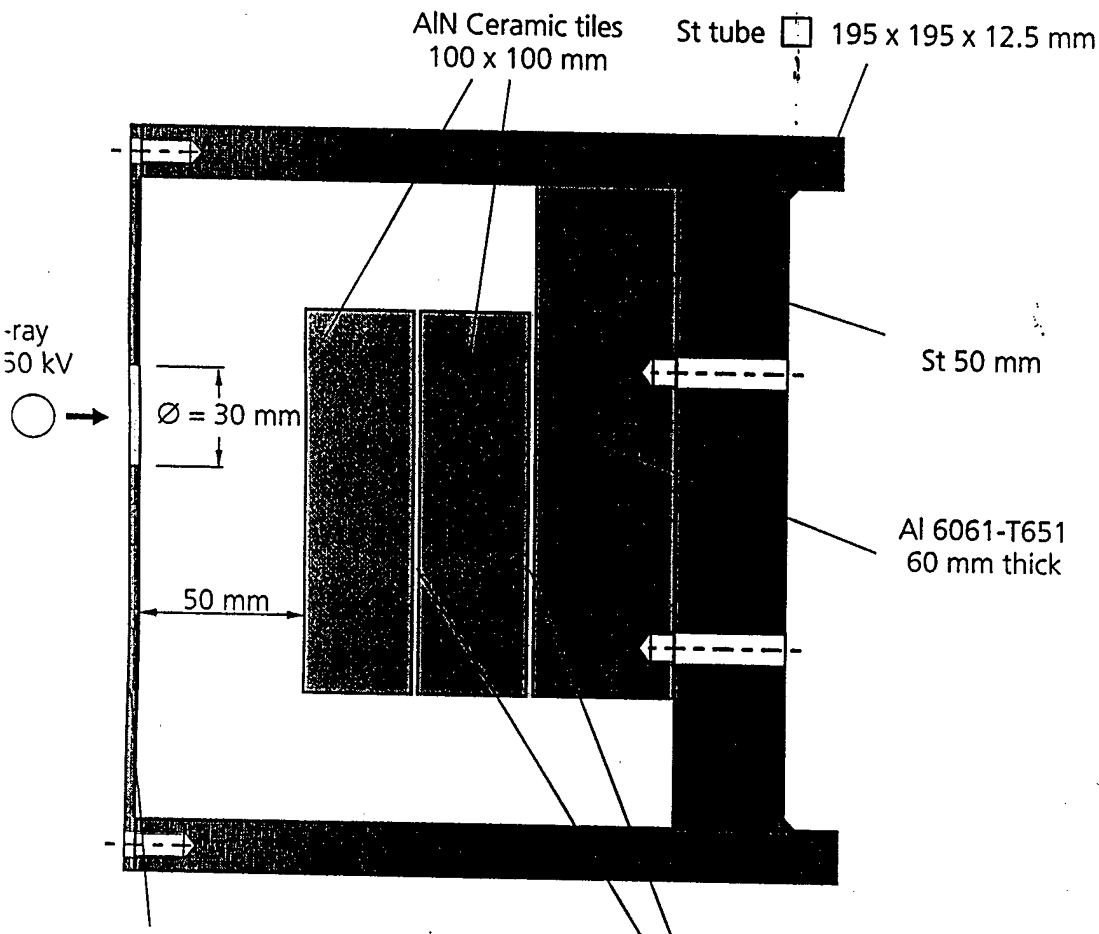

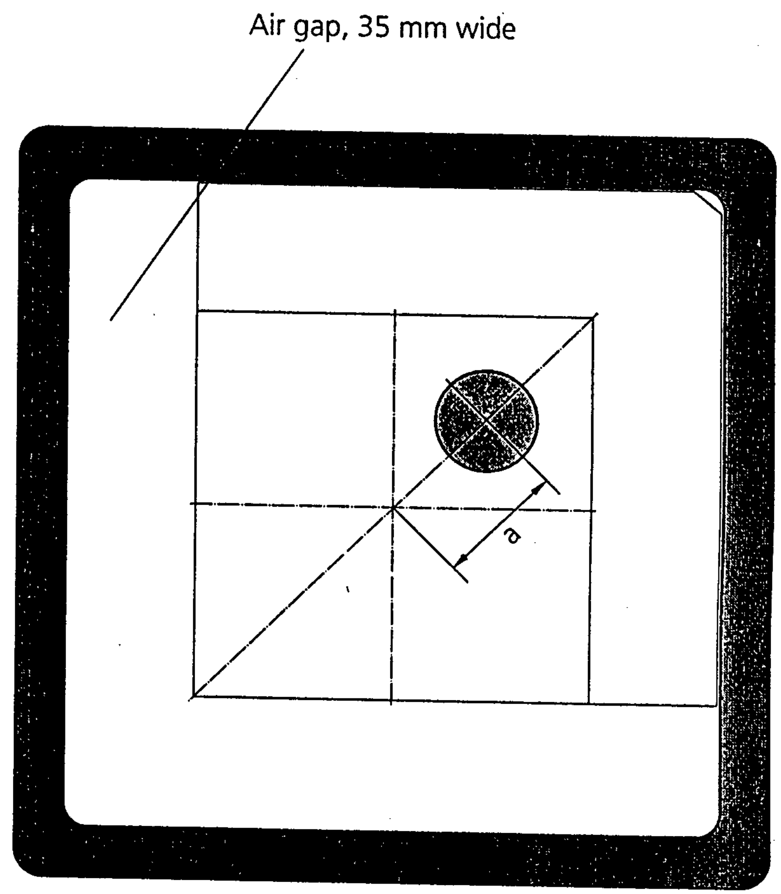

1) a = 40 mm

Projectile: D = 8.33 mm, L/D = 6, $m_p \approx 50$ g, $v_p = 1150$ m/s, flat nose

AlN-Targets: 1) 2 x 0.75"   2) 6 x 0.25"

Fraunhofer
Institut
Kurzzeitdynamik
Ernst-Mach-Institut

Author: Karl Weber

Test Set-Up of the Depth-of-Penetration Method (Test Series 3g-OCII)

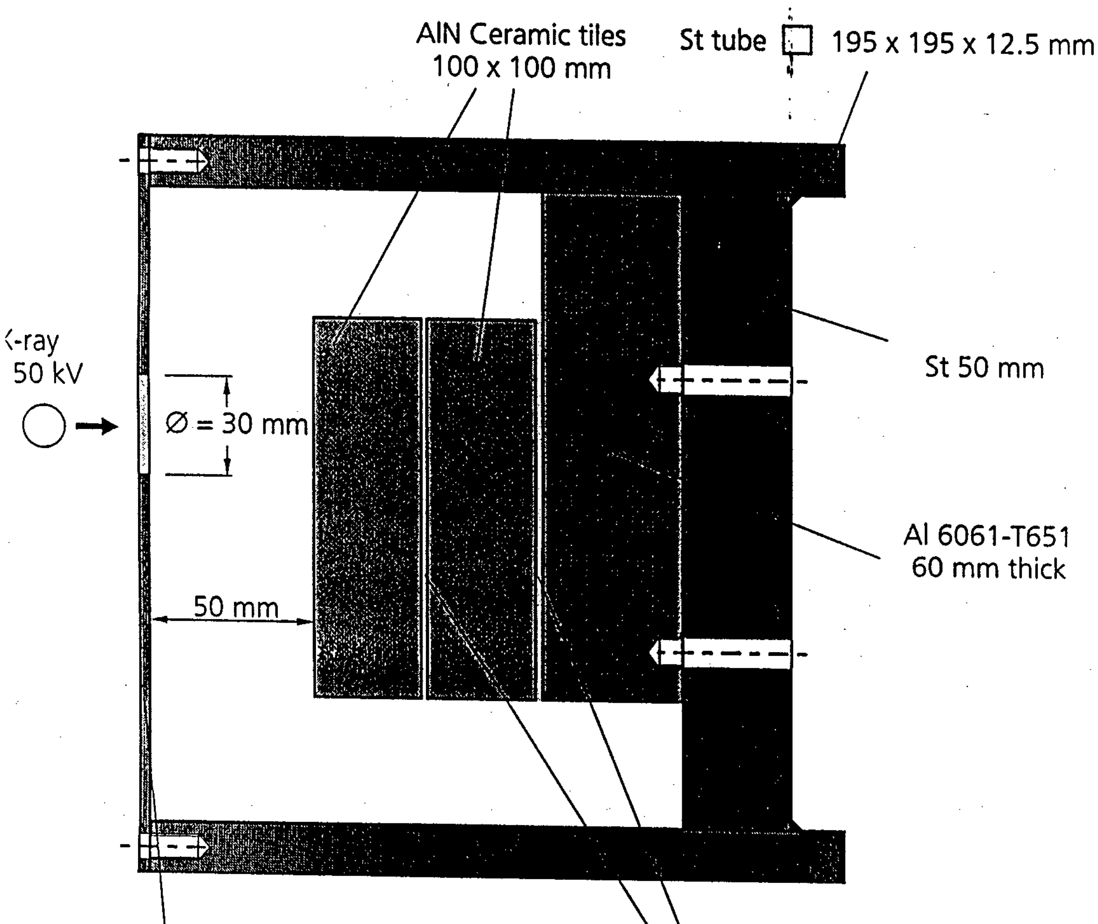

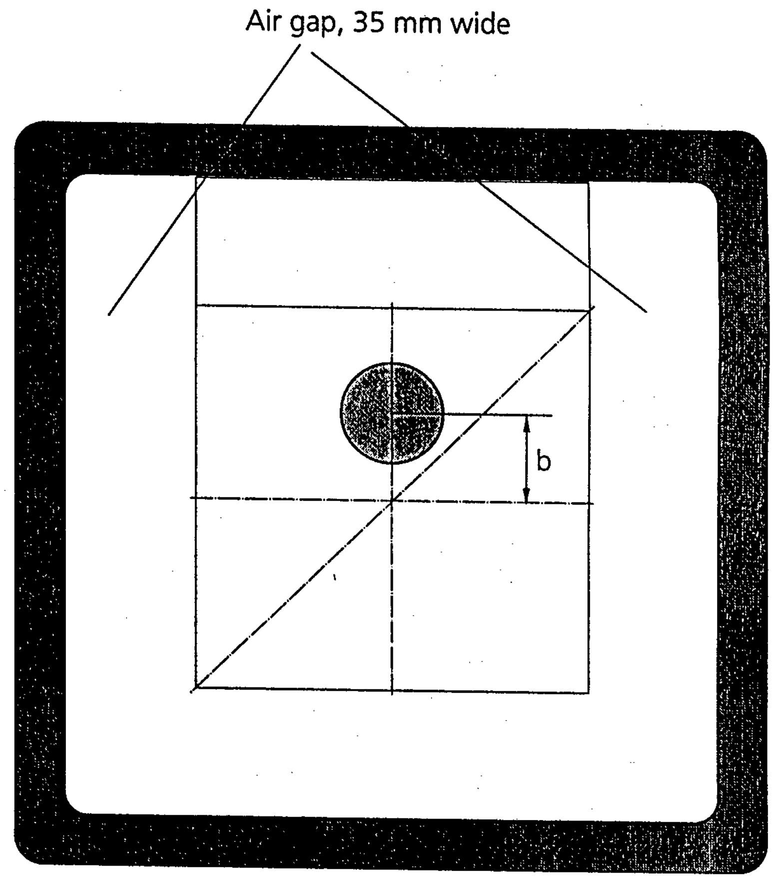

1) b = 15 mm
2) b = 30 mm

Projectile: D = 8.33 mm, L/D = 6, $m_P \approx 50$ g, $v_P = 1150$m/s, flat nose

AlN-Targets: 1) 2 x 0.75" 2) 6 x 0.25"

Fraunhofer Institut Kurzzeitdynamik EMI

Author: Karl Weber

Test Set-Up of the Depth-of-Penetration Method (Test Series 3h-OCD)

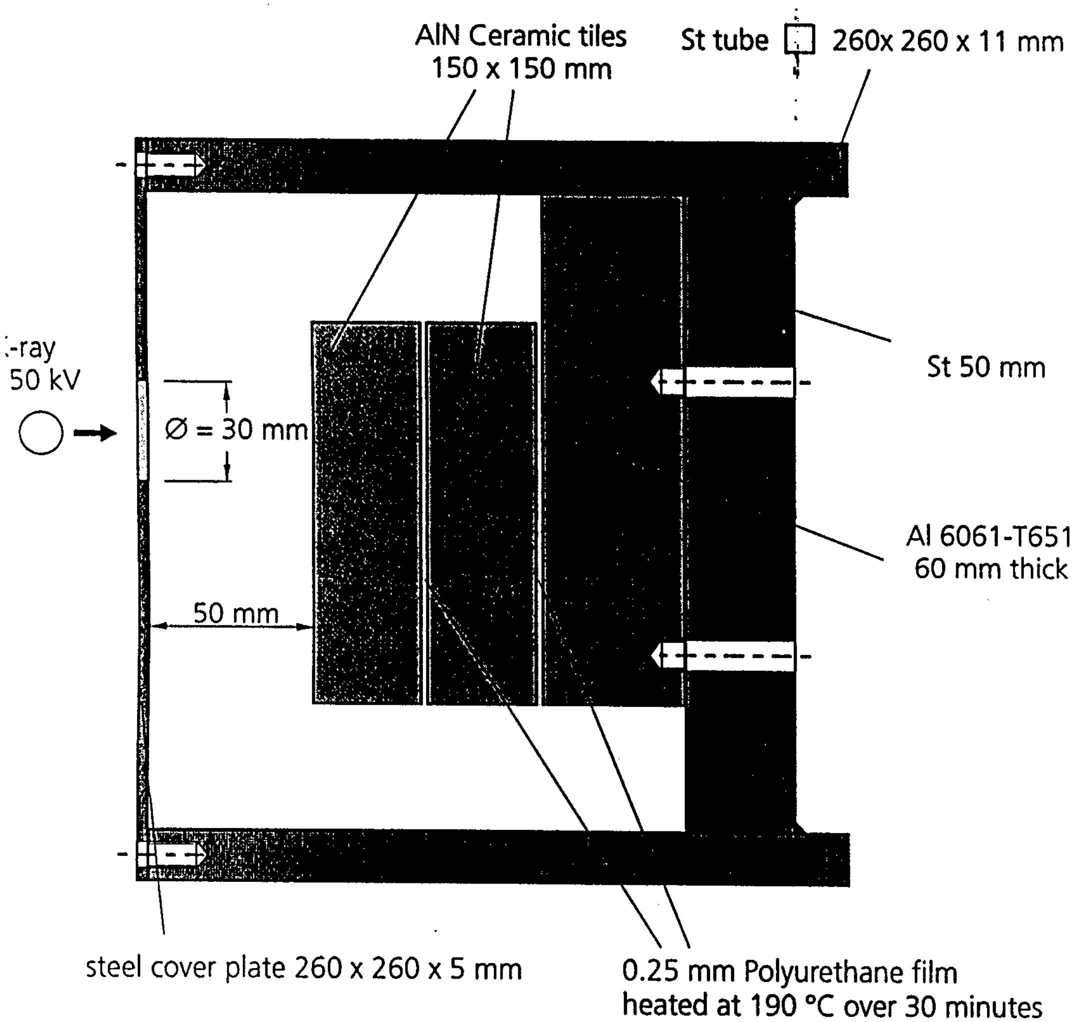

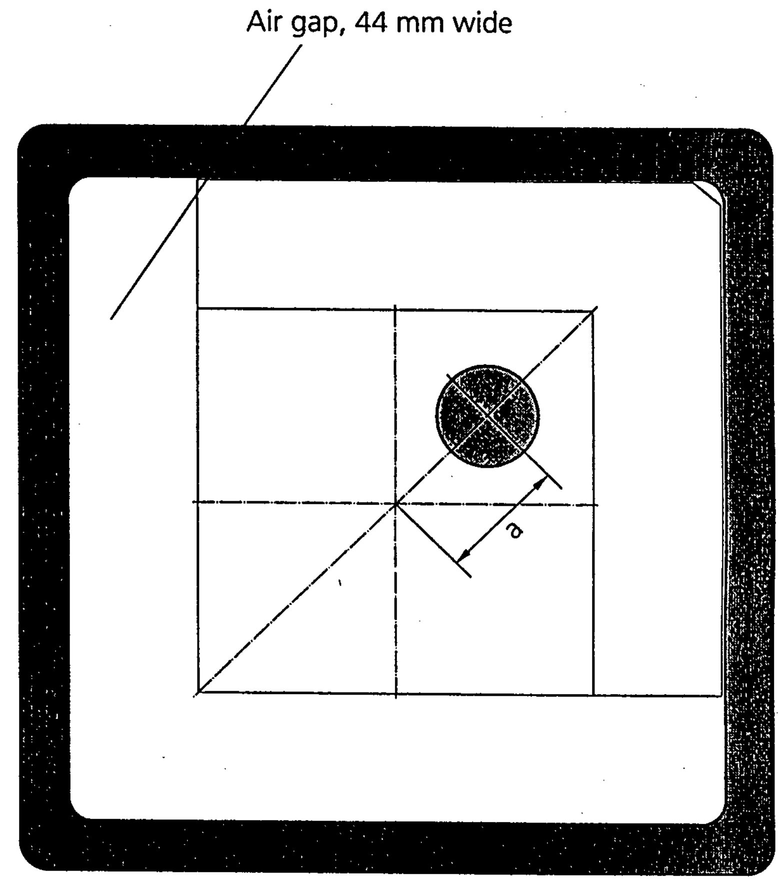

1) a = 35 mm
2) a = 70 mm

Projectile: D = 8.33 mm, L/D = 6, $m_p \approx 50$ g, $v_p = 1150$m/s, flat nose

AlN-Targets: 1) 1.5"

Fraunhofer Institut Kurzzeitdynamik Ernst-Mach-Institut

Author: Karl Weber

Test Set-Up of the Depth-of-Penetration Method (Test Series 3h-OCII)

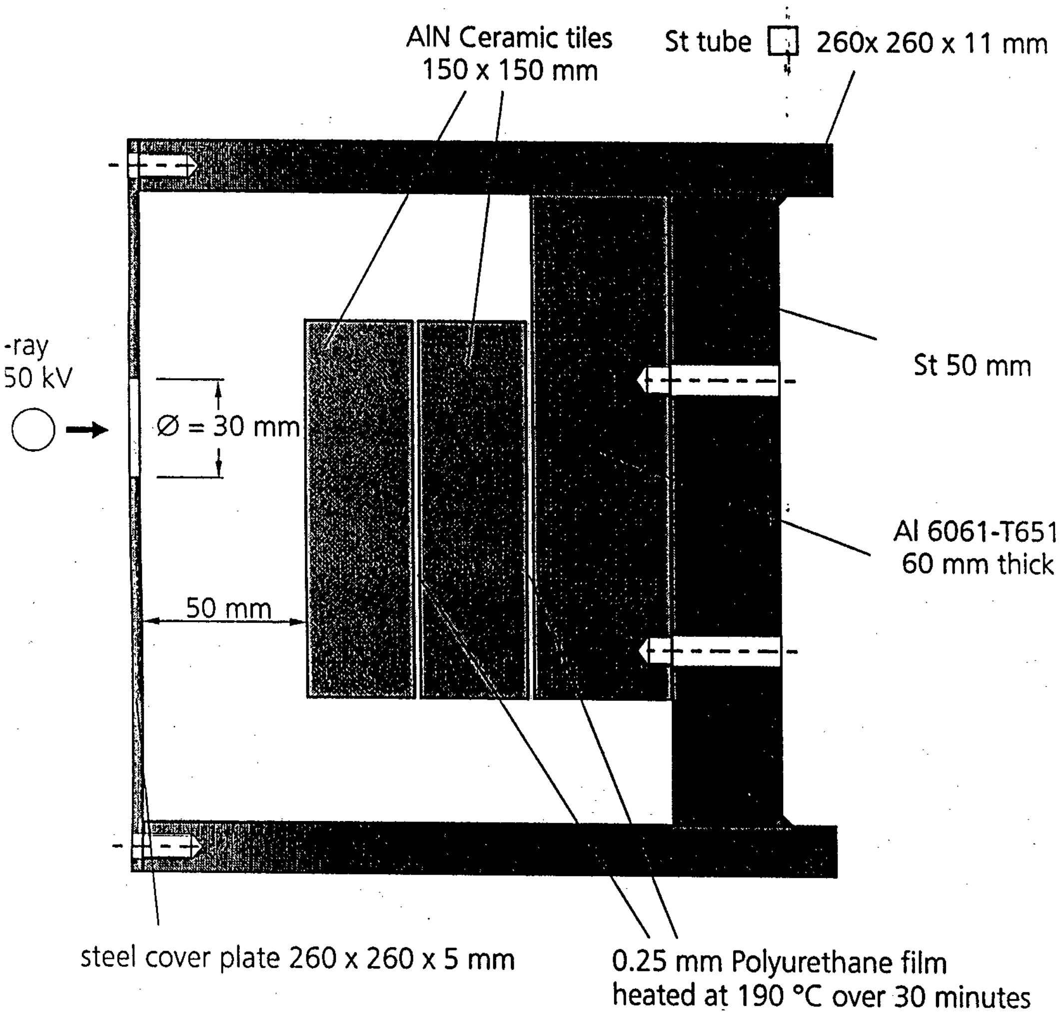

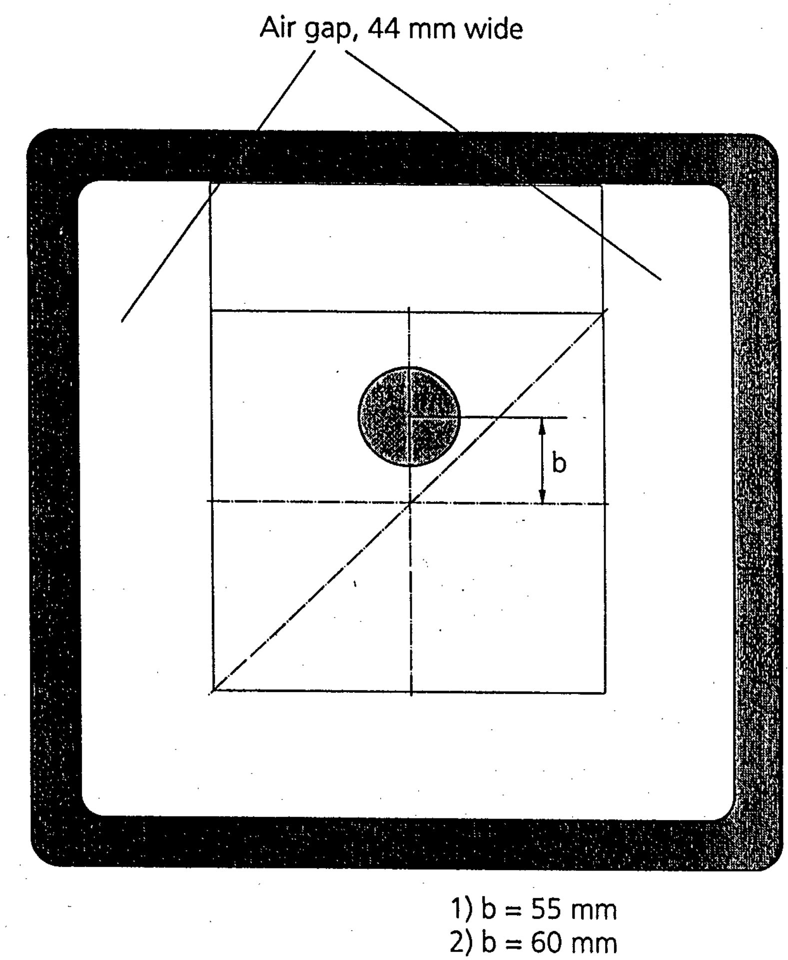

Projectile: D = 8.33 mm, L/D = 6, $m_p \approx 50$ g, $v_p = 1150$m/s, flat nose

AlN-Targets: 1) 1.5" 2) 3 x 0.5"

Fraunhofer Institut Kurzzeitdynamik EMI

Author: Karl Weber

Test Set-Up of the Depth-of-Penetration Method (Test Series 3i)

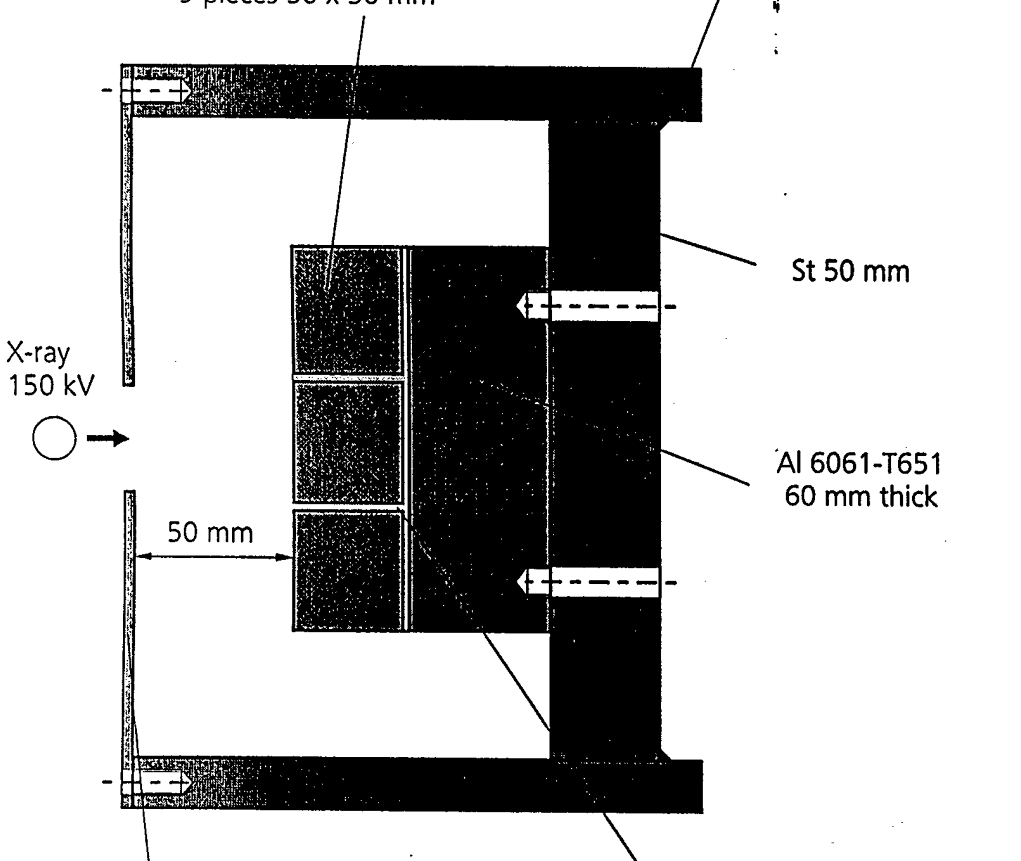

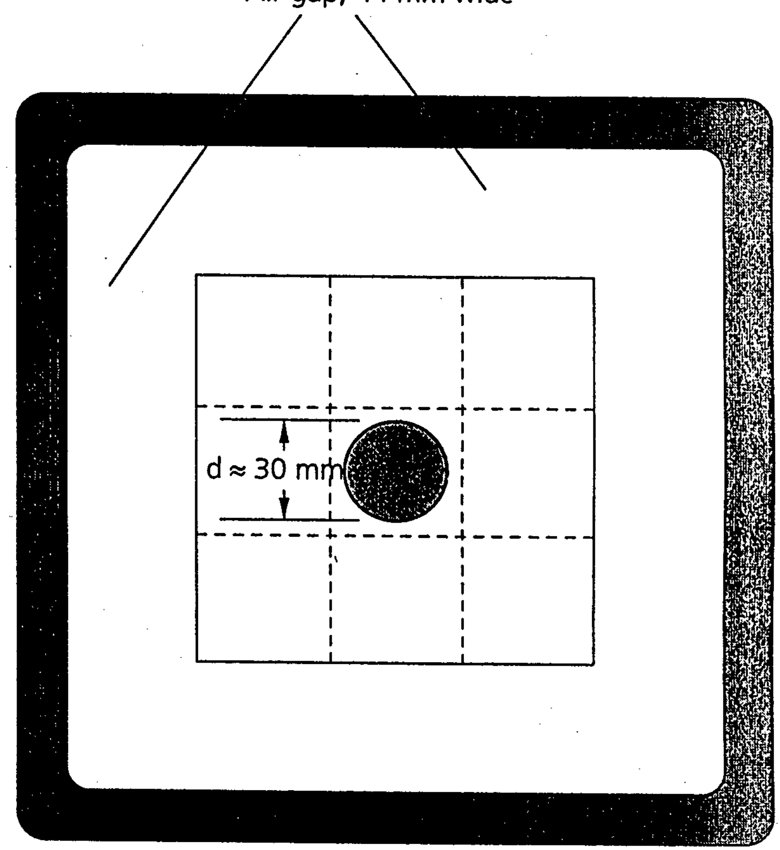

ɔjectile: $D = 8.33$ mm, $L/D = 6$, $m_p \approx 50$ g, $v_p = 1150$m/s, flat nose

Fraunhofer Institut Kurzzeitdynamik Ernst-Mach-Institut

Author: Karl Weber

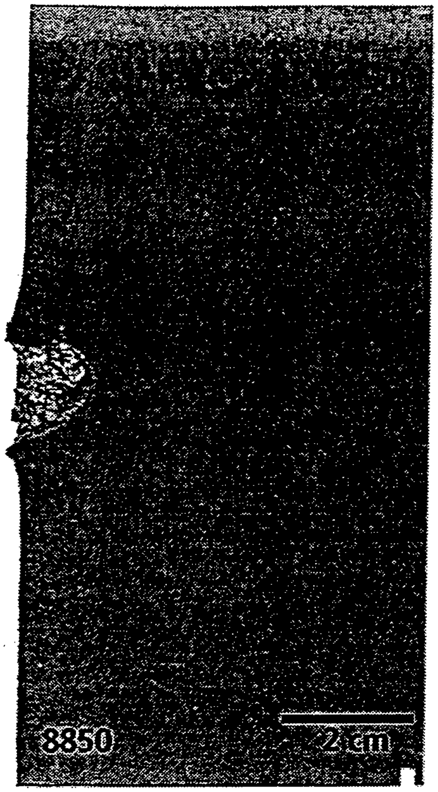
8850
2 cm

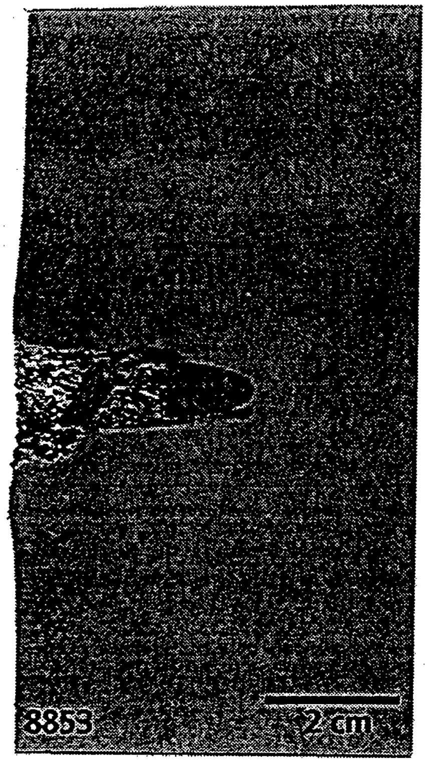
8853
2 cm

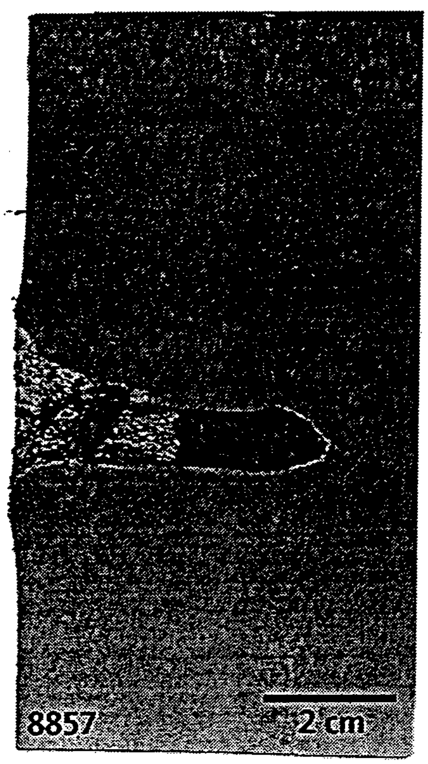
8857
2 cm

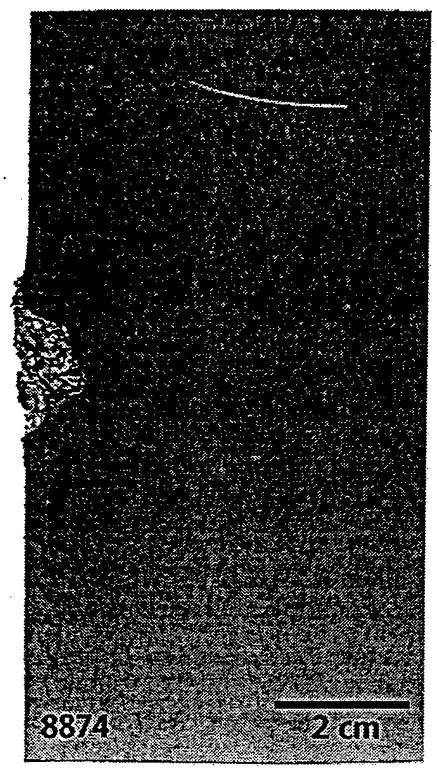
8874
2 cm

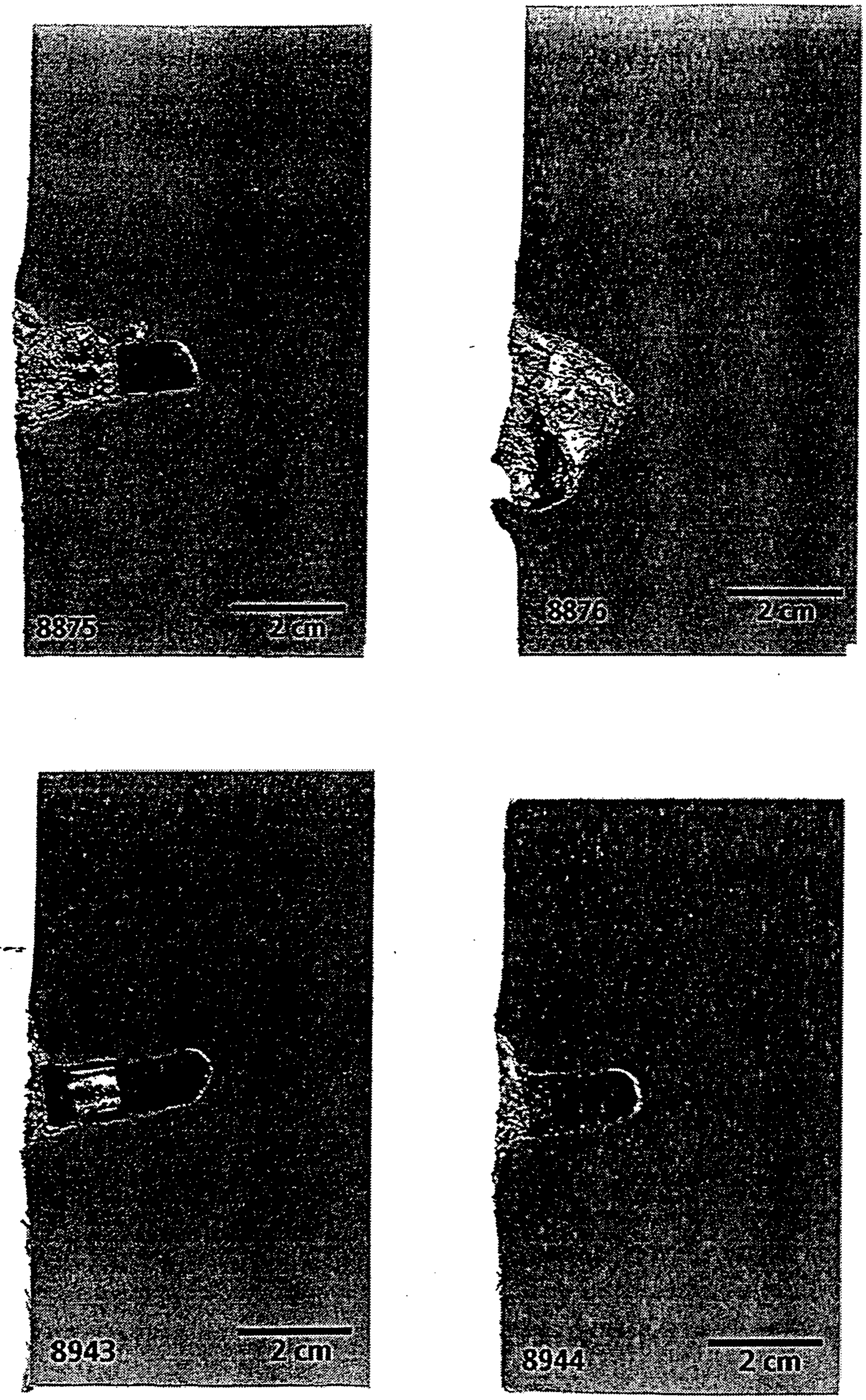

Fig 1-8: Experiments with single layer tile (1.5") 100 x 100 mm tiles


8851
2 cm

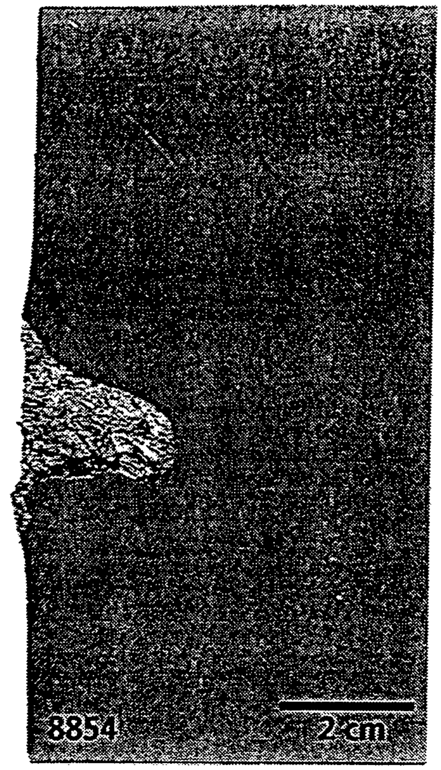
8854
2 cm

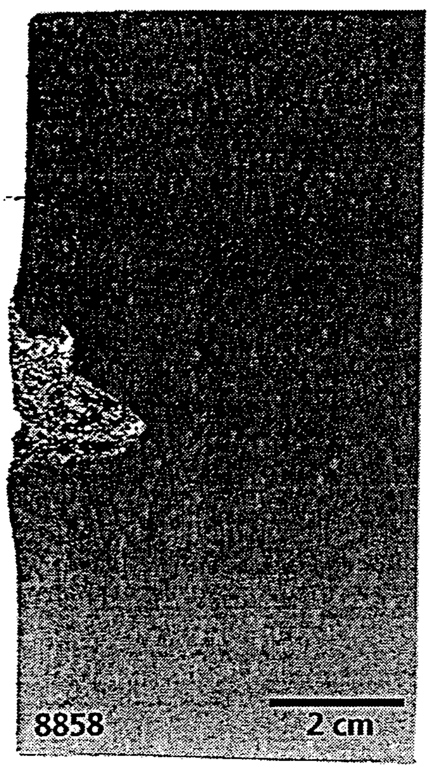
8858
2 cm

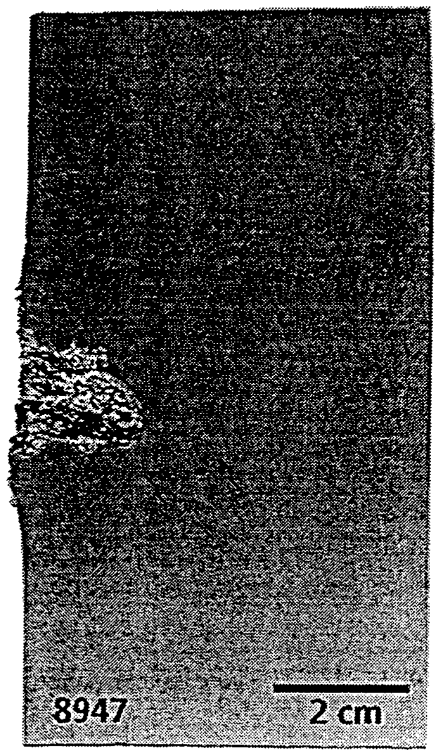
8947
2 cm

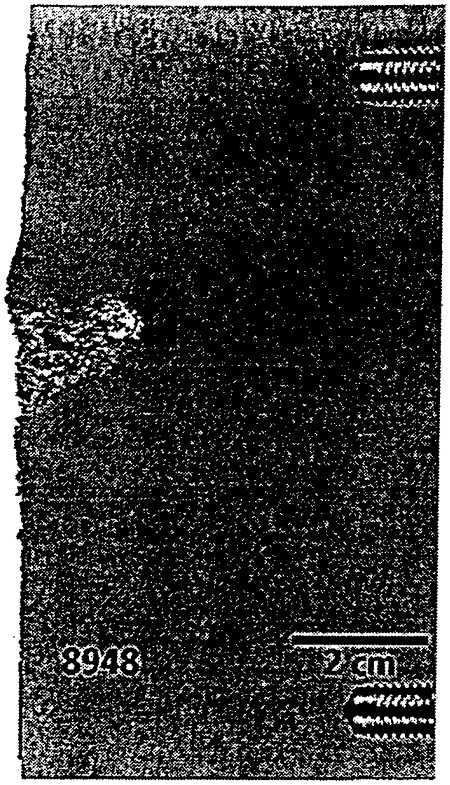

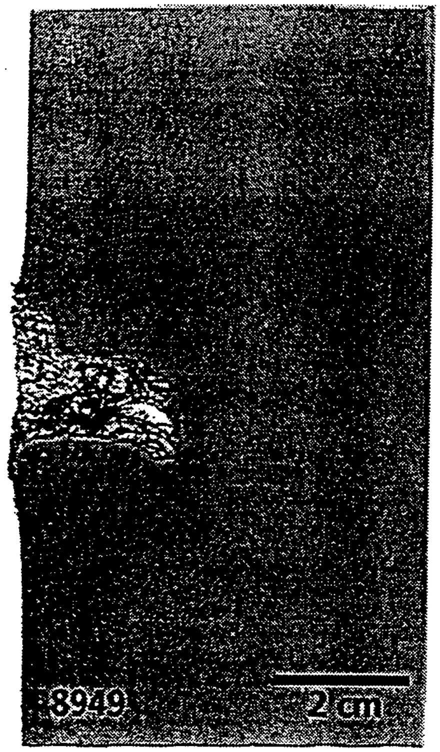

Fig. 9-14: Experiments with 2-layer tiles (2 x 0.75") 100 x 100 mm tiles

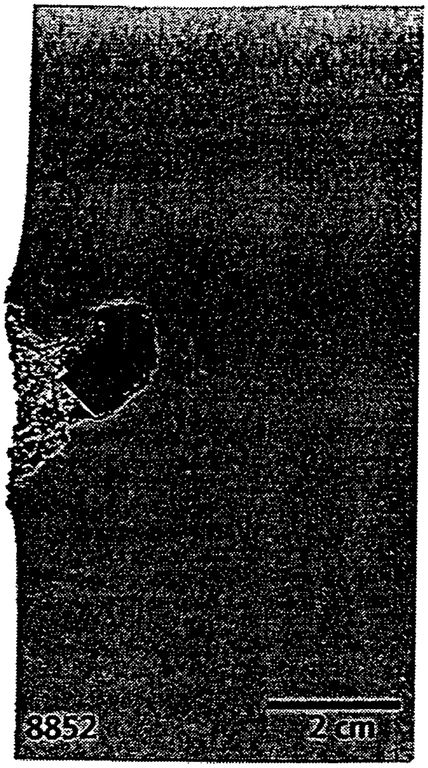
8852
2 cm

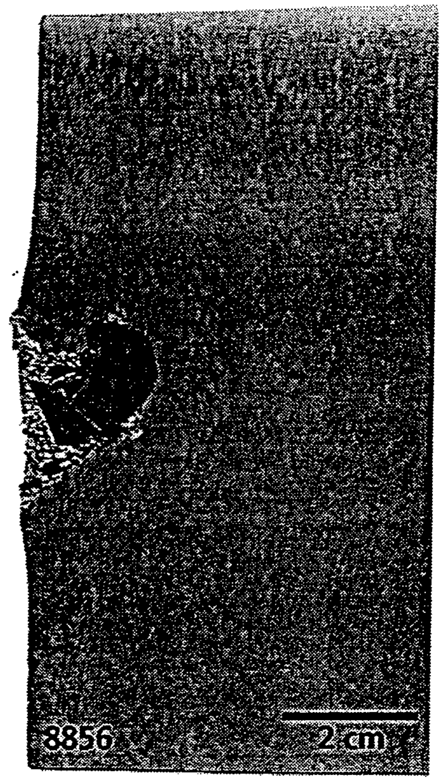
8856
2 cm

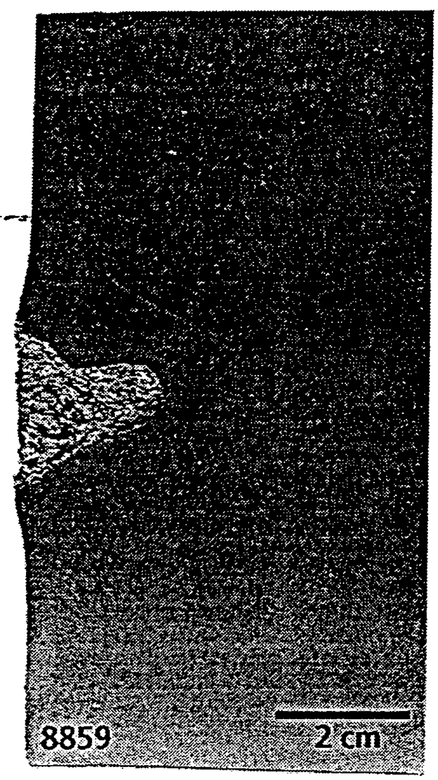
8859
2 cm


8871
2 cm

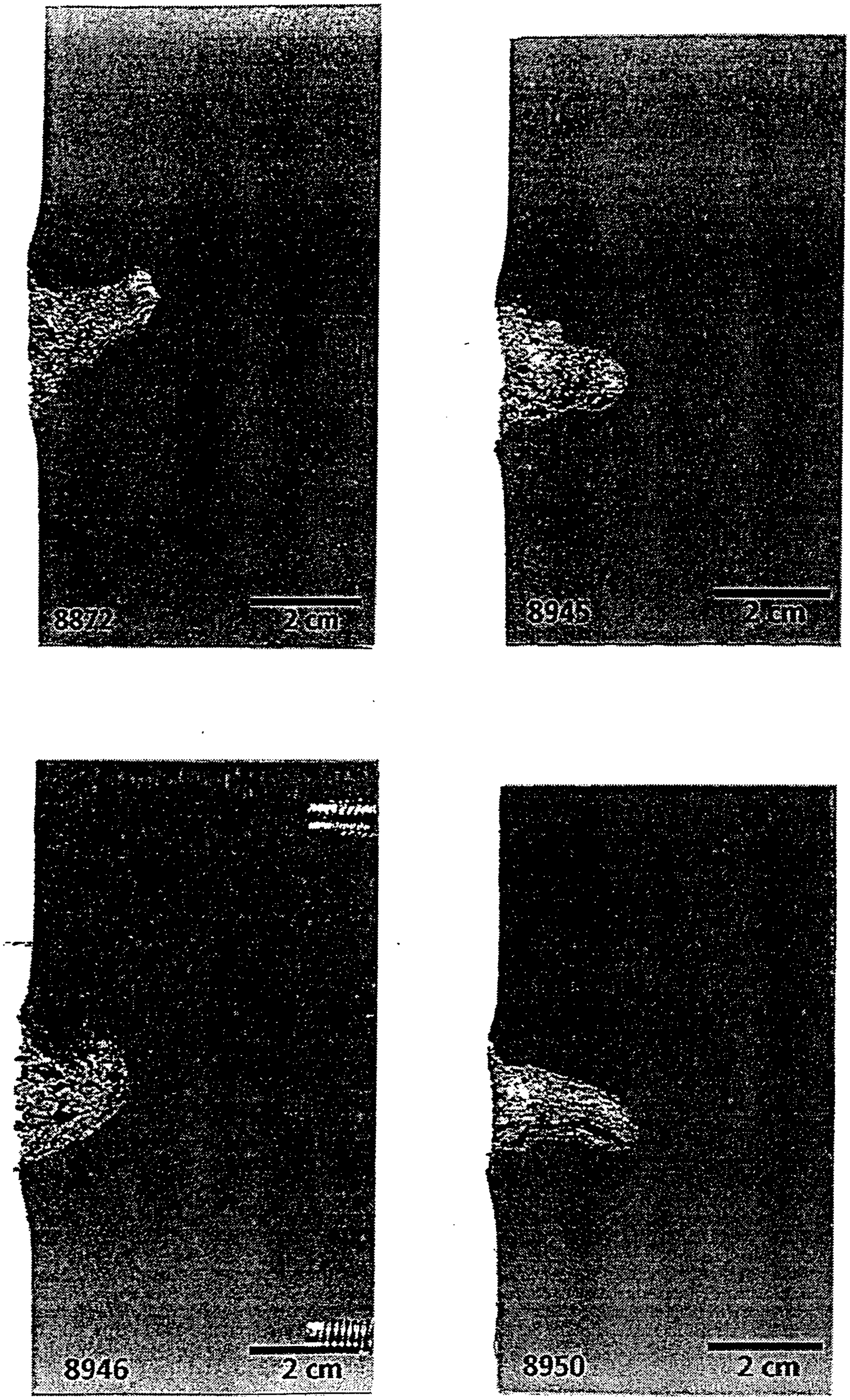

Fig. 15-22: Experiments with 3-layer tiles (3 x 0.5") 100 x 100 mm tiles

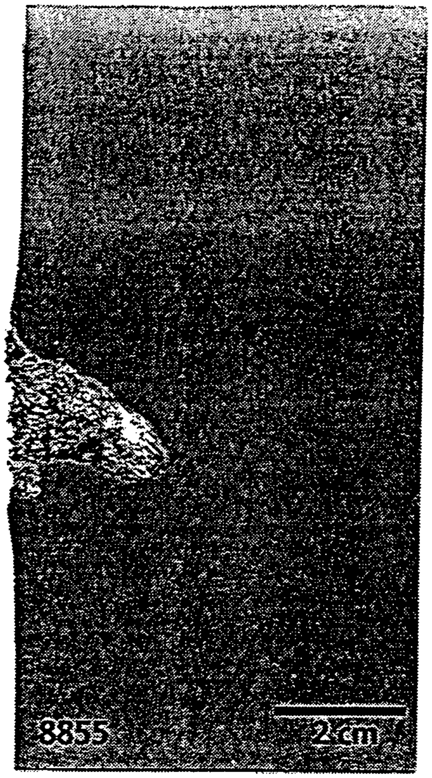
8855
2 cm

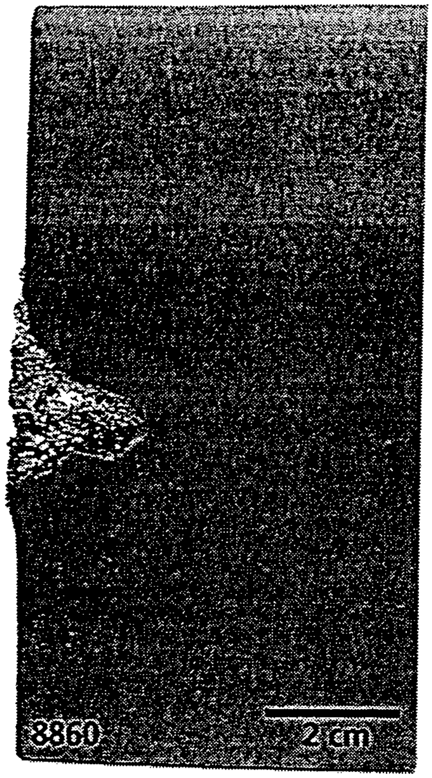
8860
2 cm


8861
2 cm


8951
2 cm

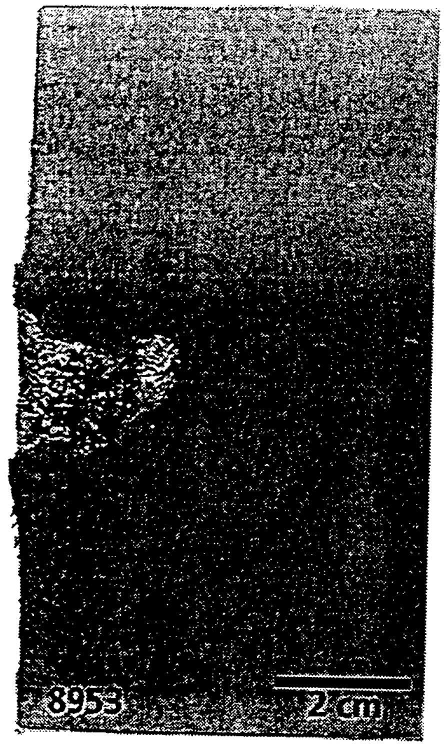

Fig. 23-28: Experiments with 6-layer tiles (6 x 0.25") 100 x 100 mm tiles

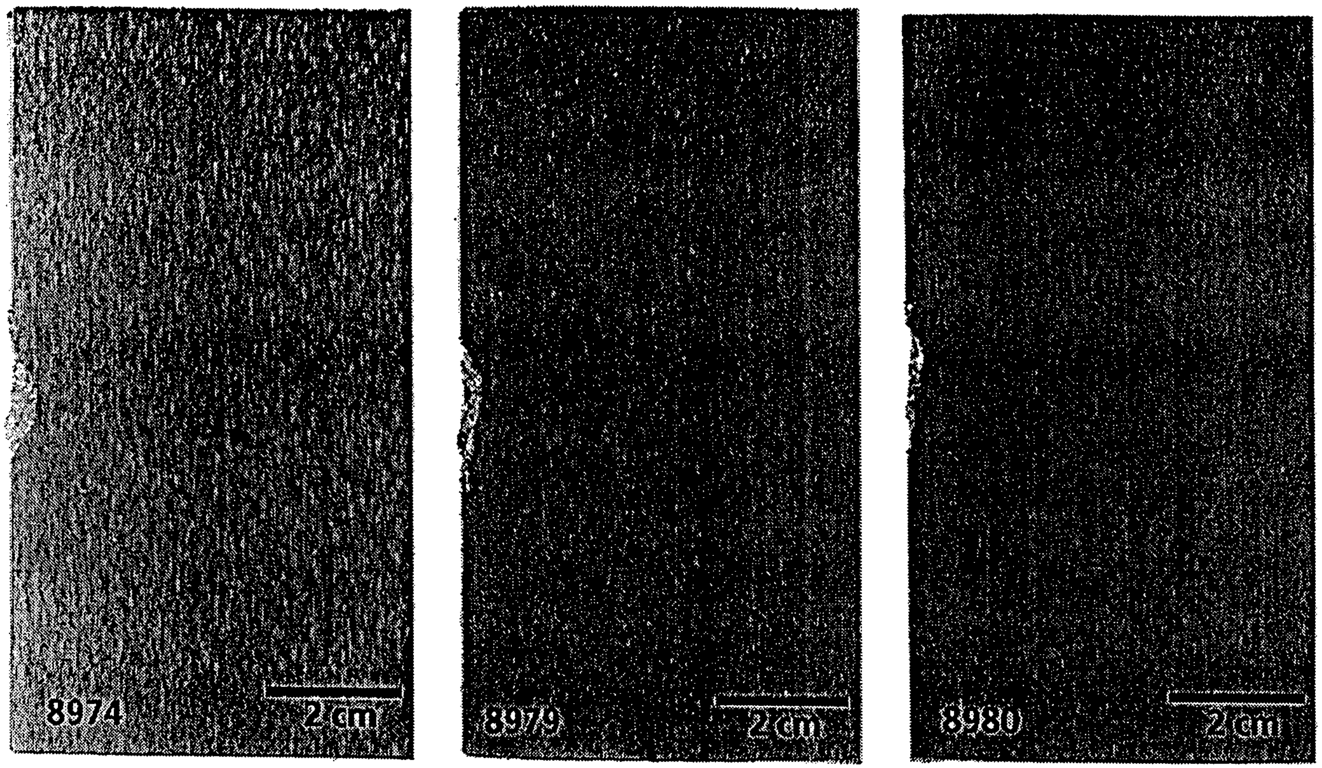

'g. 29-31: Experiments with 2-layer tiles (2 x 0.75") 150 x 150 mm tiles

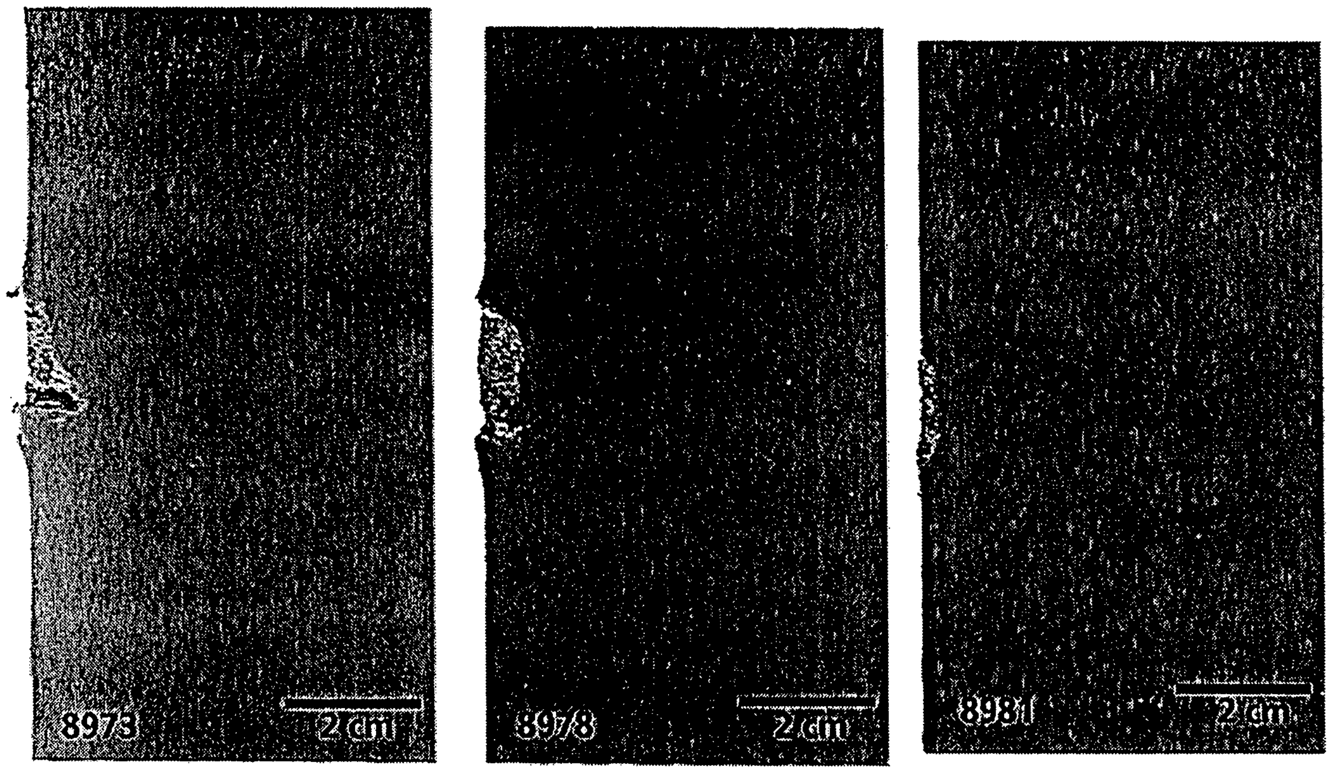

ig. 32-34: Experiments with 3-layer tiles (3 x 0.5") 150 x 150 mm tiles

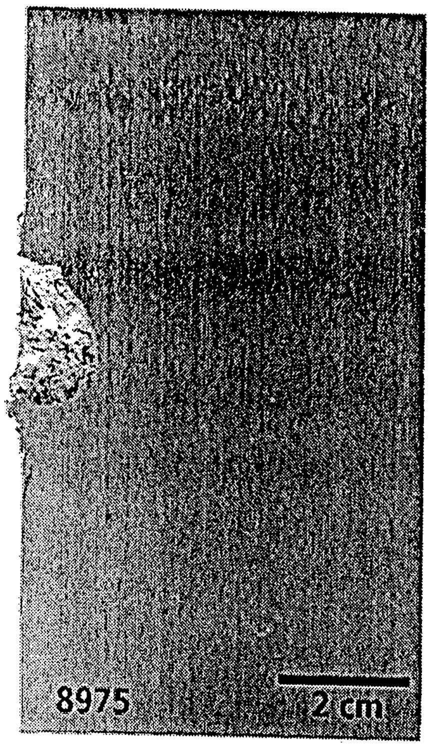

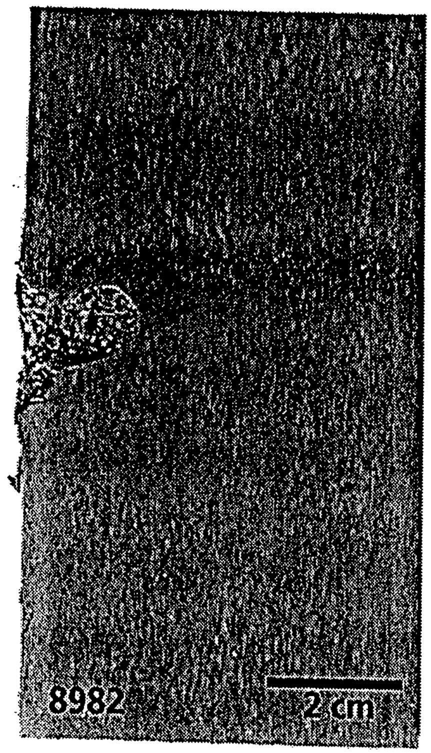

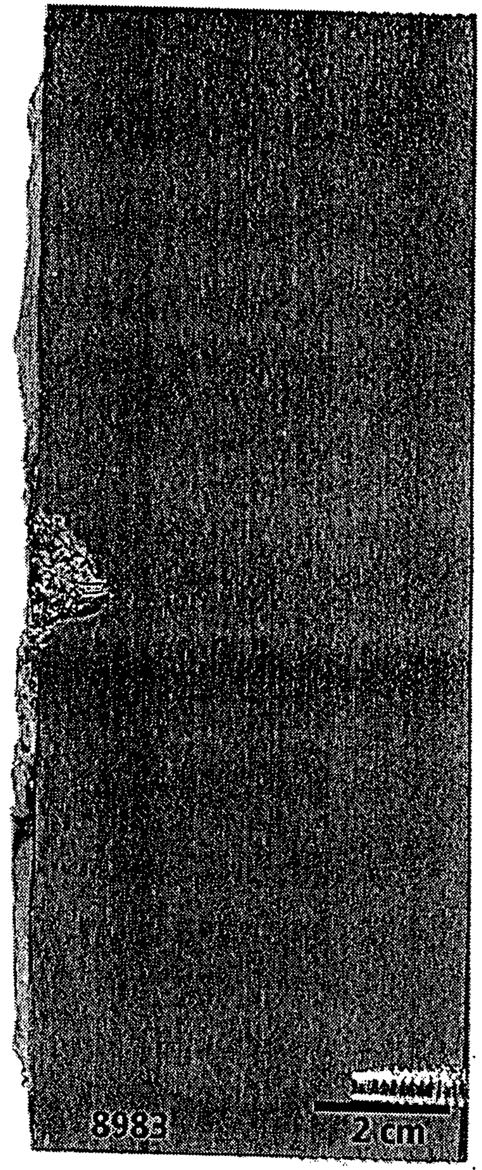

ɟ. 35-37: Experiments with 6-layer tiles (6 x 0.25") 150 x 150 mm tiles

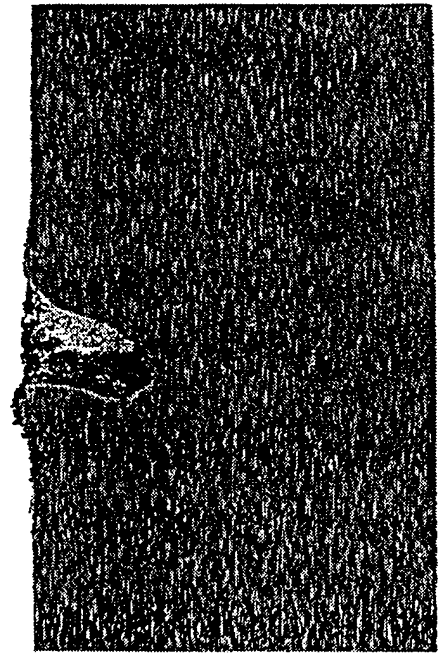

ig. 38:Experiments with 9 pieces overall 150 x 150 mm tiles

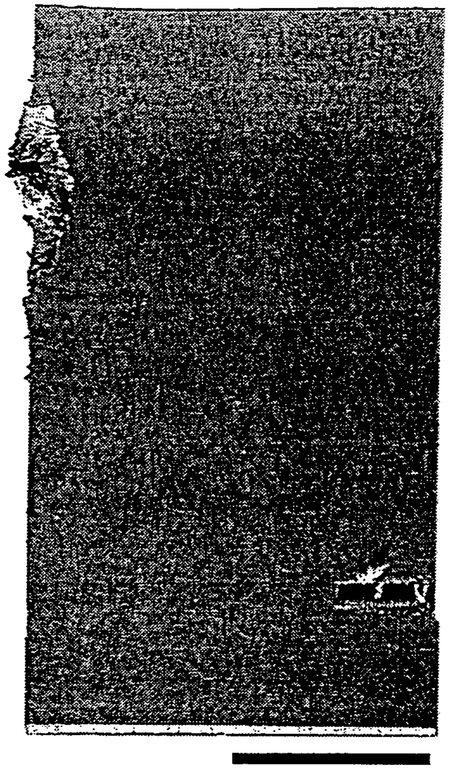

9029 3 cm

9031 3 cm

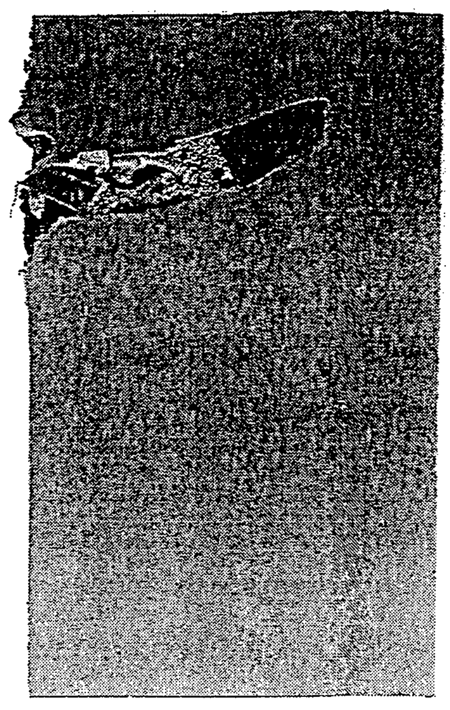

9032 3 cm

Fig. 39-41: Experiments with single-layer tile (1 x 1.5") 150 x 150 mm tile, (off-center)

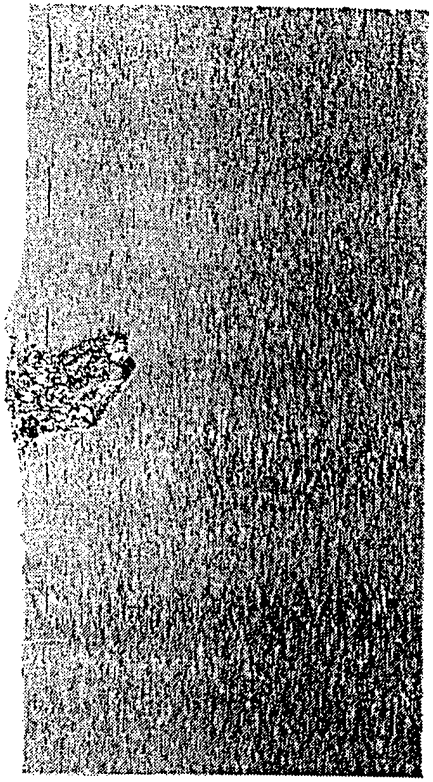

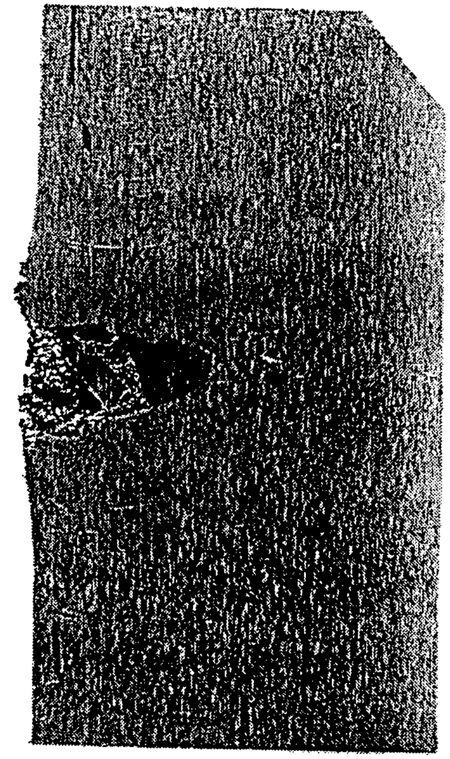

g. 42-44: Experiments with 2-layer tiles (2 x 0.75") 100 x 100 mm tiles, (off-center)

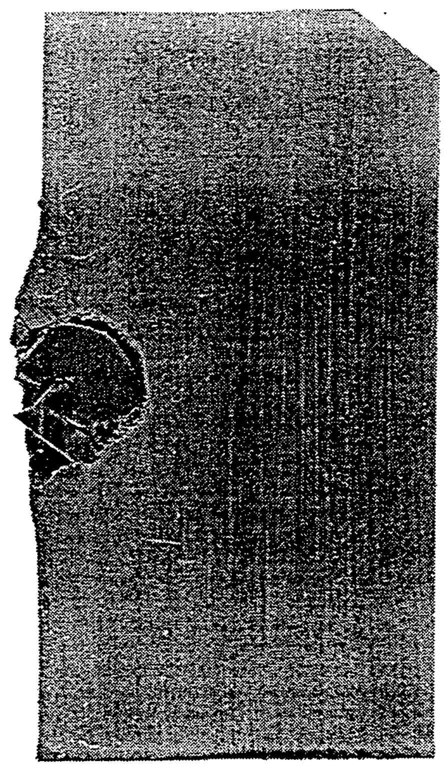

Fig. 45: Experiment with 3-layer tiles (3 x 0.5") 150 x 150 mm tiles, (off-center)

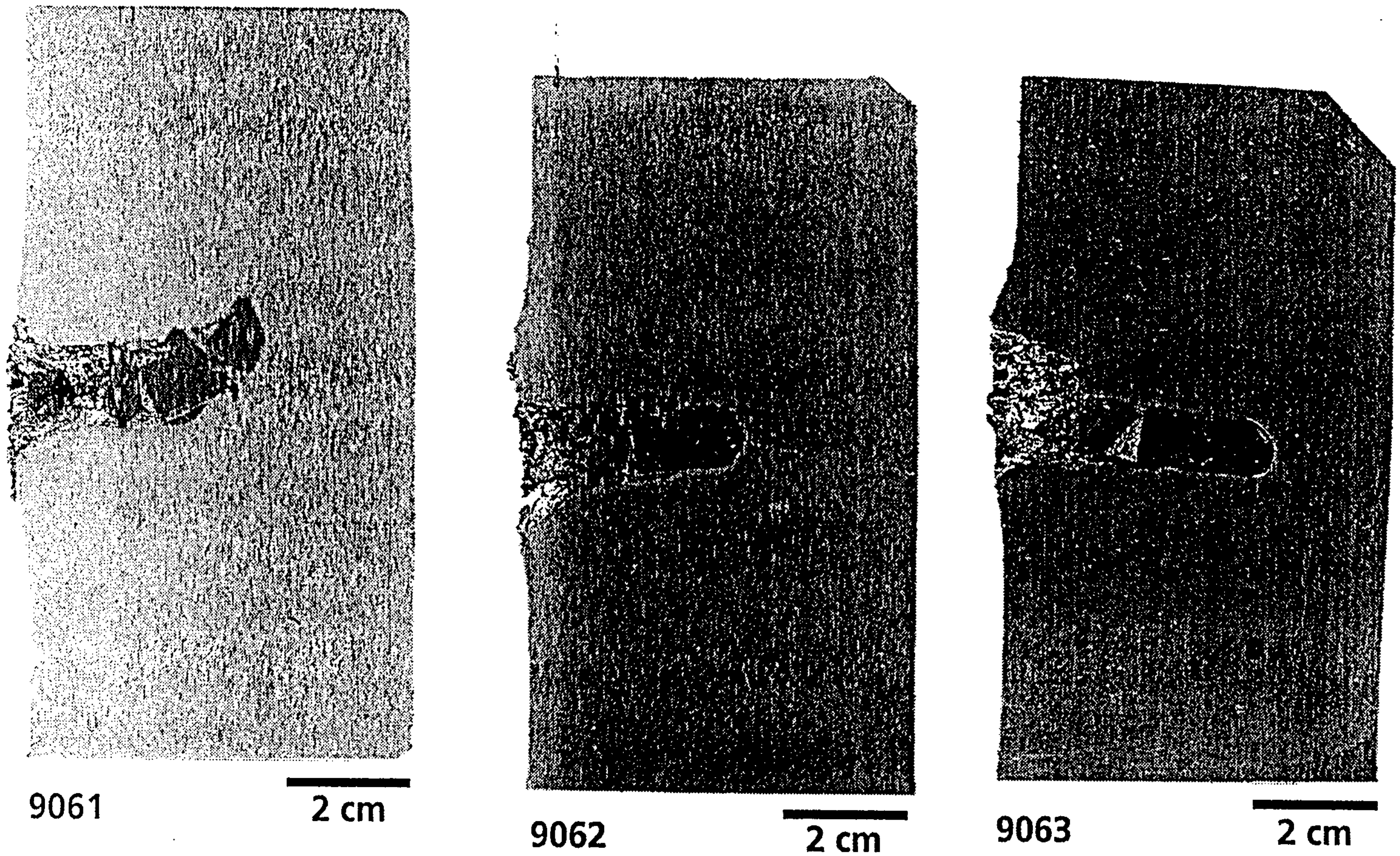

ig. 46-48: Experiments with 6-layer tiles (6 x 0.25") 100 x 100 mm tiles, (off-center)

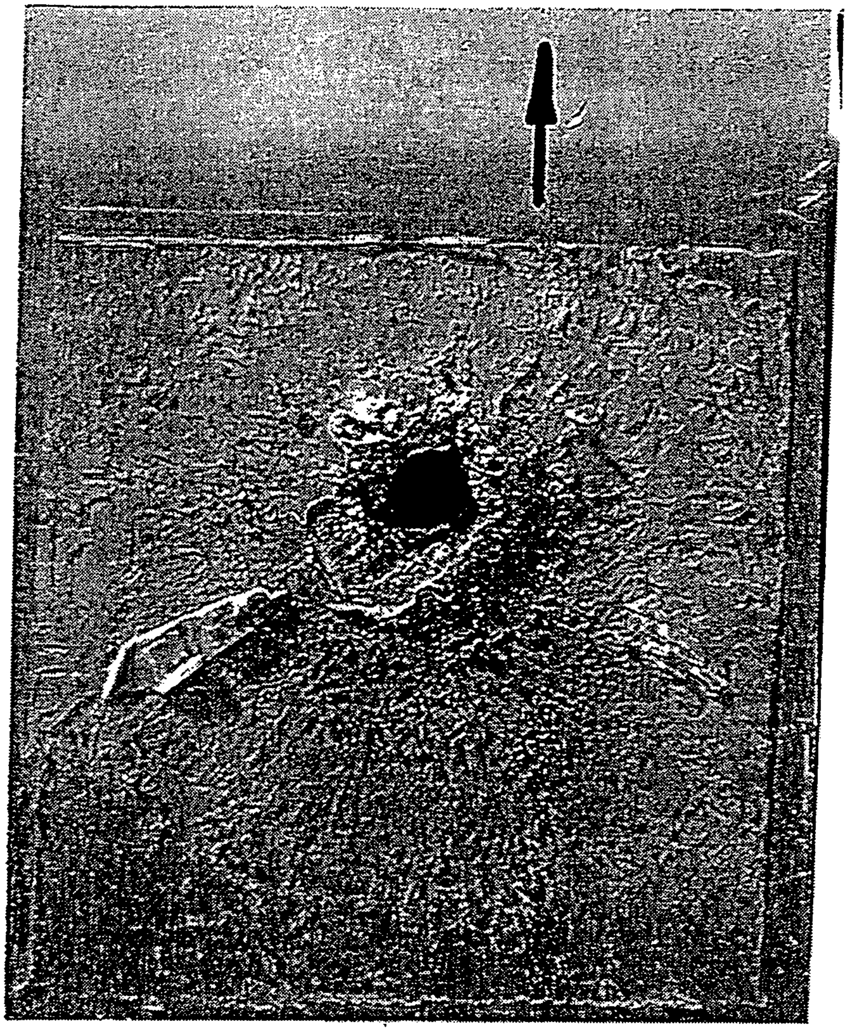

9058 2 cm

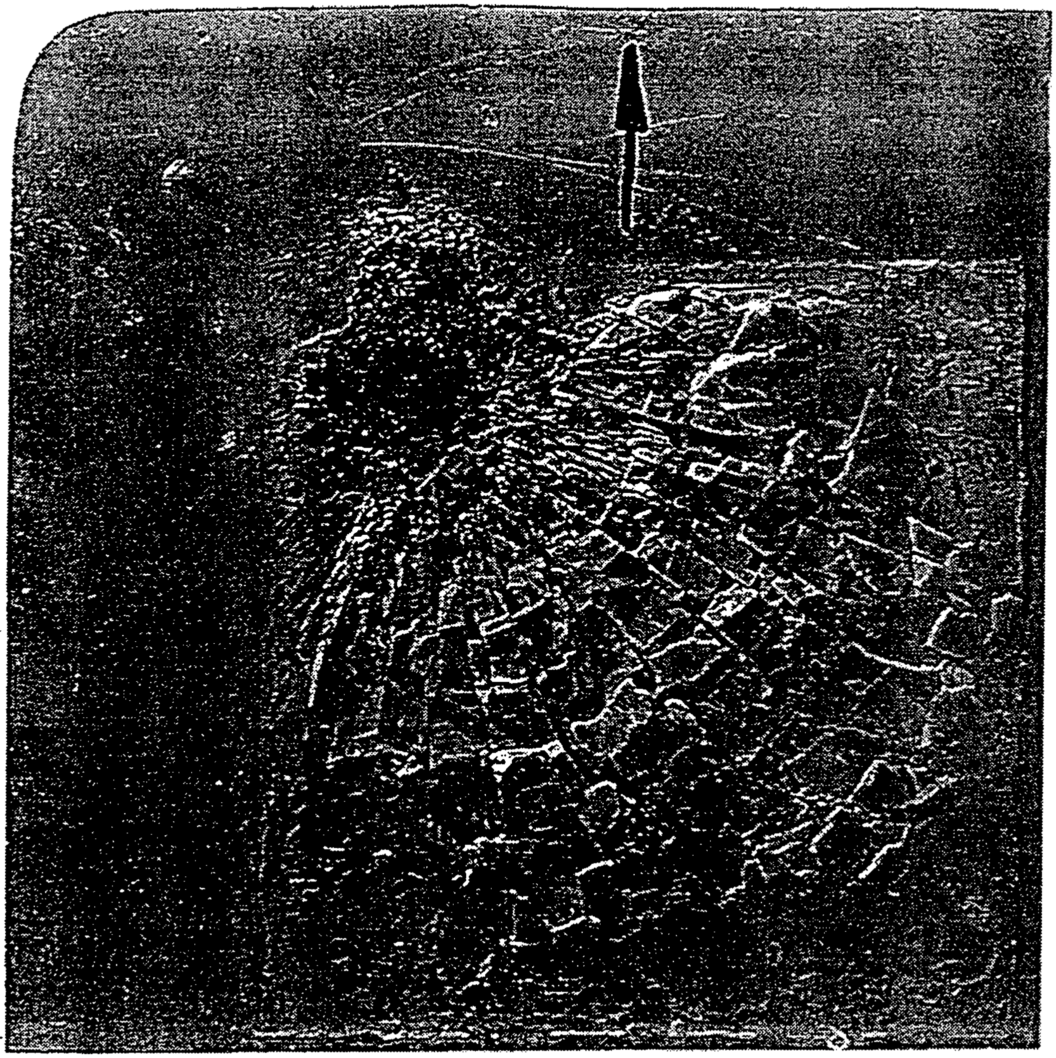

9059

2 cm

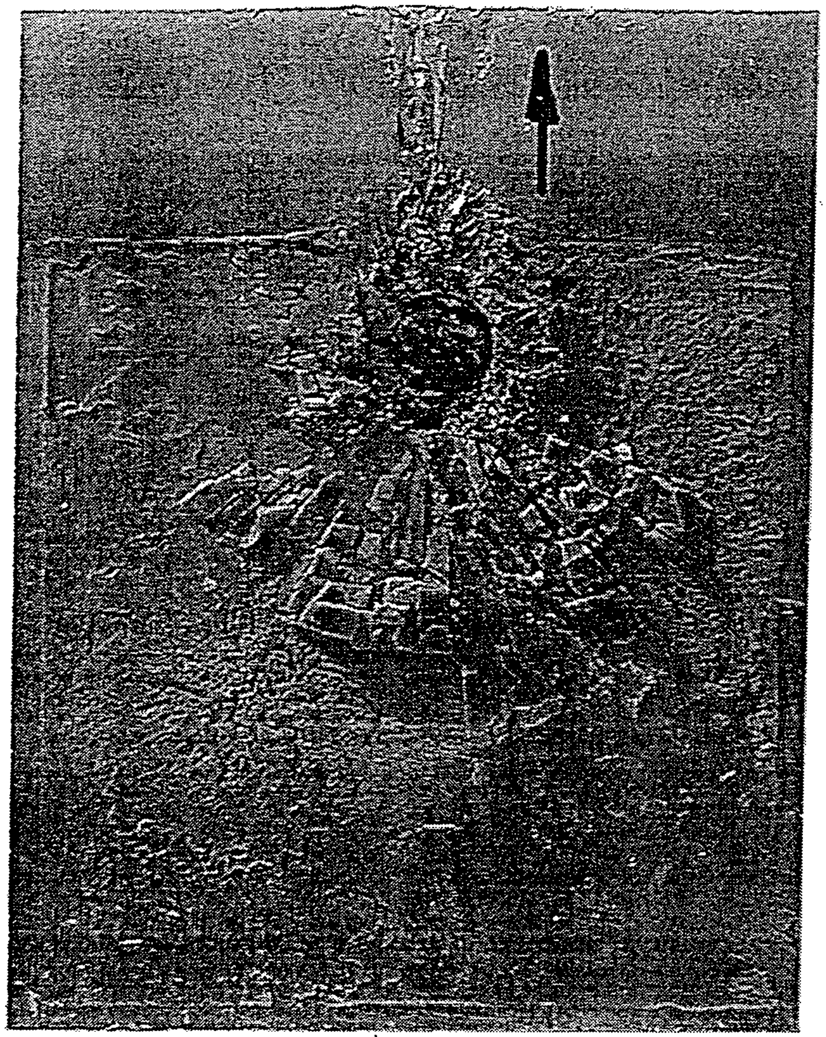

9060 2 cm

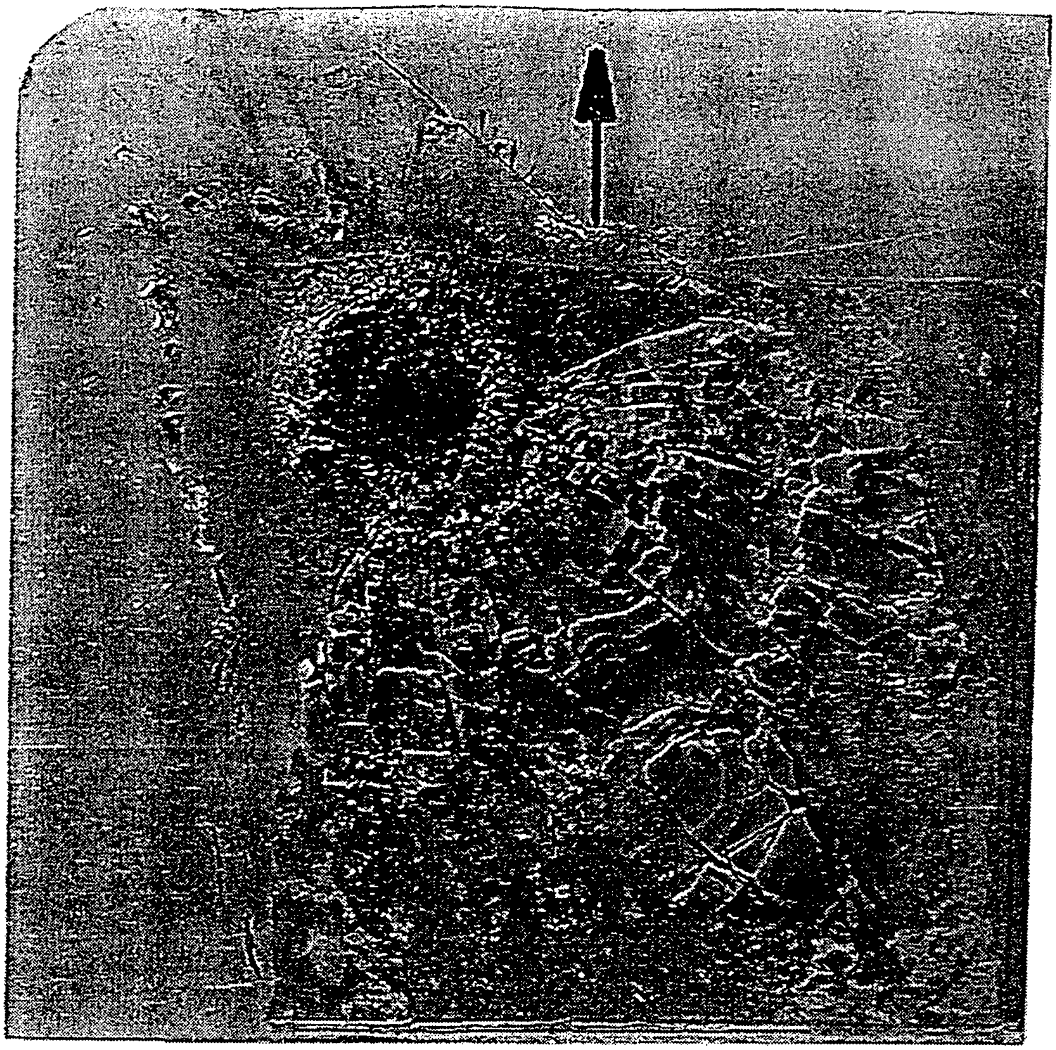

9061

2 cm

9062

2 cm

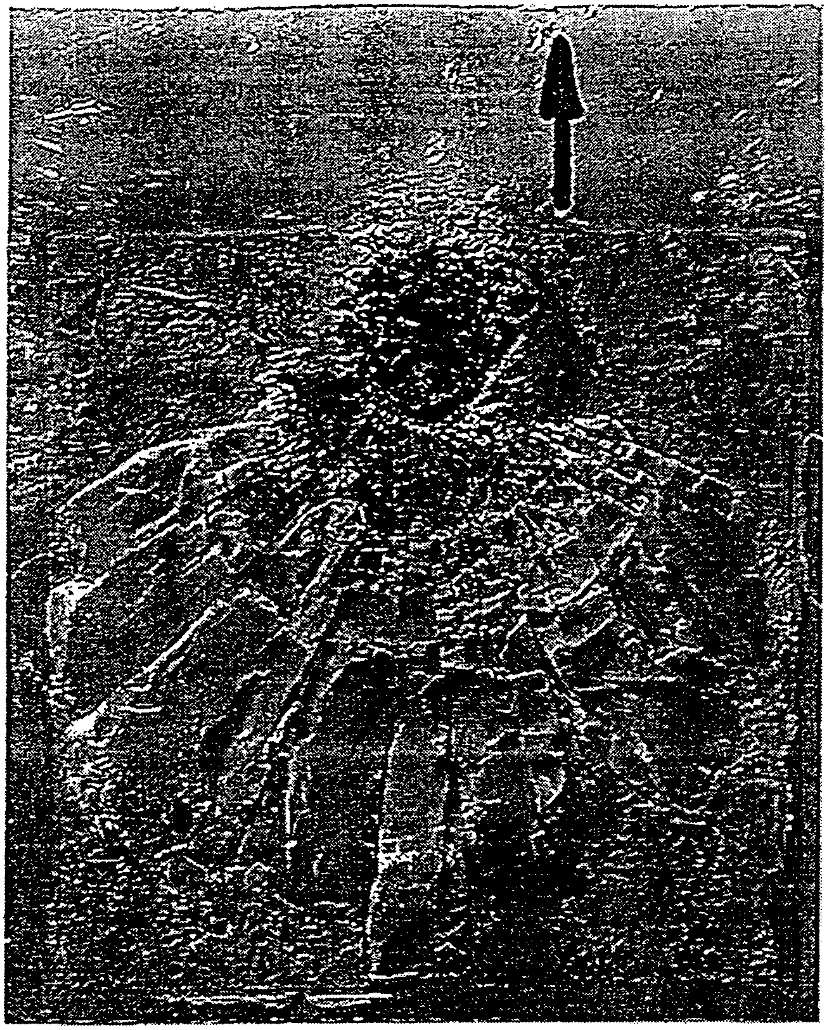

9063

2 cm

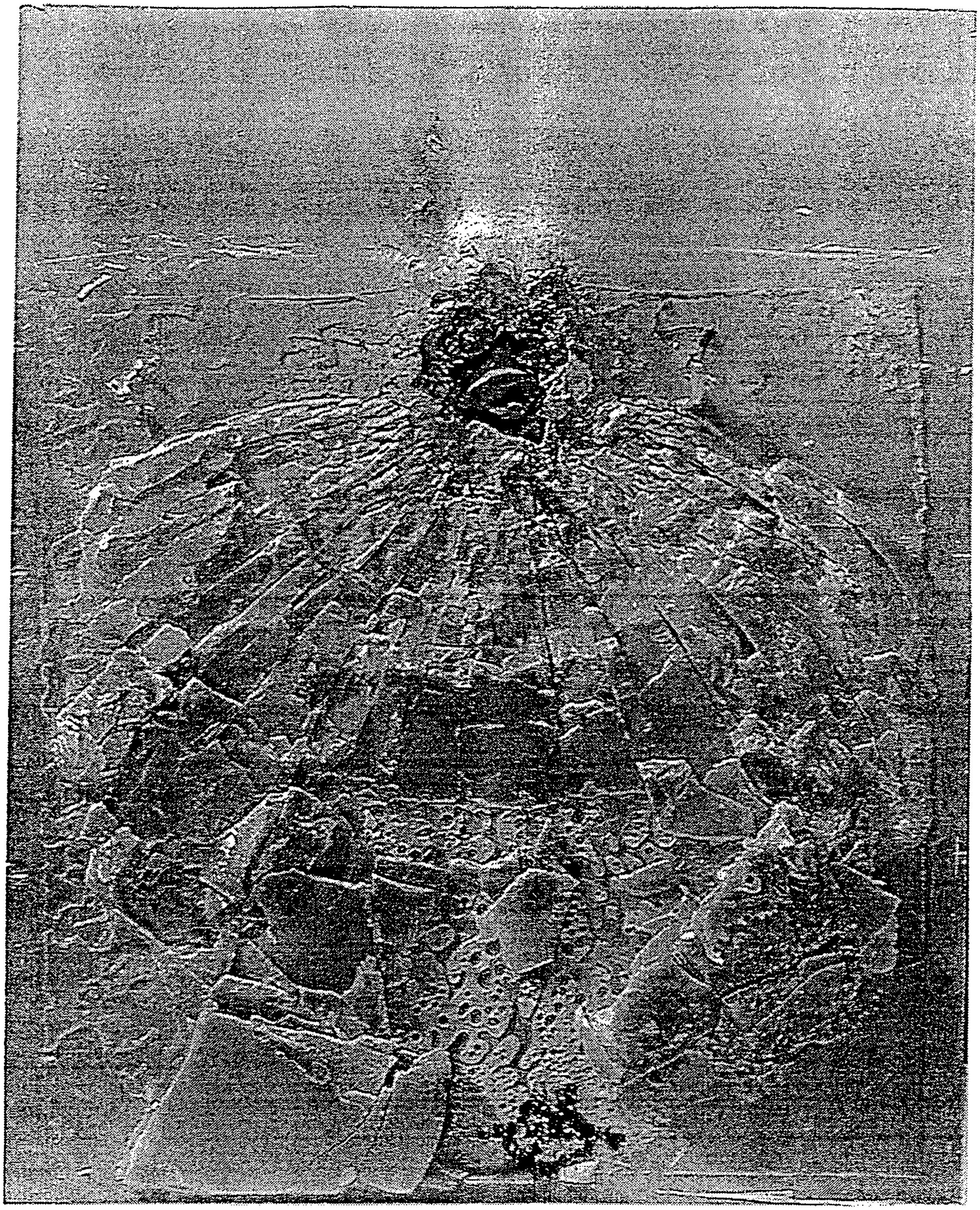

9064

2 cm

Projectile: WSA rod, D = 8.33 mm, L/D = 6, flat nose
Backing Plate: Al 6061-T651, 60 mm thick; Cover Plate: steel, 5 mm thick

Exp. no.	m_P [g]	v_P [m/s]	α_1/α_2 [deg]	Test set-up	lat. tile dim. [mm]	No. of tiles	p_R [mm]	p_{KE} [mm]	Projectile used from
8733	51	1130	+2.0/--	3c	100 x 100	1 x 1.5"	6.8	-	EMI
8738	51	1133	+1.0/--	3c	100 x 100	1 x 1.5"	0	-	EMI
8850	51	1142	0/-1	3c	100 x 100	1 x 1.5"	10.6	12.3	EMI
8853	51	1173	-4/-2	3c	100 x 100	1 x 1.5"	33.0	-	EMI
8857	51	1140	-1/-4	3c	100 x 100	1 x 1.5"	45.9	47.0	EMI
8874	53	1111	0/-1.5	3c	100 x 100	1 x 1.5"	8.5	-	CALTECH
8875	53	1105	-3/0	3d	100 x 100	1 x 1.5"	29.3	29.4	EMI
8876‡	53	1138	0/-3	3d	100 x 100	1 x 1.5"	20.5	33.8	EMI
8943	51	1190	-0.8/0	3e	100 x 100	1 x 1.5"	30.5	31.3	EMI
8944	51	1182	-1/+3	3e	100 x 100	1 x 1.5"	24.7	25.4	EMI
8734	51	1140	0/--	3c	100 x 100	2 x 0.75"	10.3	17.3	EMI
8739	51	1182	+2.0/--	3c	100 x 100	2 x 0.75"	26.0	-	EMI
8851	51	1200	-0.5/-2.5	3c	100 x 100	2 x 0.75"	20.05	22.4	EMI
8854	51	1160	+2/-1	3c	100 x 100	2 x 0.75"	21.75	24.6	EMI
8858	51	1188	+1/0	3c	100 x 100	2 x 0.75"	18.85	19.3	EMI
8947	51	1148	+1/0	3e	100 x 100	2 x 0.75"	17.6	19.2	EMI
8948	51	1166	0/0	3e	100 x 100	2 x 0.75"	16.7	18.0	EMI
8949	51	1172	-4/+3	3e	100 x 100	2 x 0.75"	23.1	26.3	EMI
8735	51	1186	-4/--	3c	100 x 100	3 x 0.5"	23.3	30.2	EMI
8740	51	1170	+0.5/--	3c	100 x 100	3 x 0.5"	23.5	-	EMI
8852	51	1179	-0.5/+3.0	3c	100 x 100	3 x 0.5"	19.8	24.8	EMI
8856	51	1187	-1/-1.5	3c	100 x 100	3 x 0.5"	18.9	24.3	EMI
8859	51	1182	-1/-3	3c	100 x 100	3 x 0.5"	19.9	19.9	EMI
8871	53	1179	-1/+0.5	3c	100 x 100	3 x 0.5"	22.0	22.4	CALTECH
8872	53	1156	+0.5/0	3c	100 x 100	3 x 0.5"	20.5	23.0	CALTECH
8945	51	1186	0/0	3e	100 x 100	3 x 0.5"	21.4	22.2	EMI
8946	51	1145	-5/+2.2	3e	100 x 100	3 x 0.5"	17.2	19.5	EMI
8950	51	1165	0/-2	3e	100 x 100	3 x 0.5"	24.7	27.4	EMI
8855	51	1140	-1/-1	3c	100 x 100	6 x 0.25"	22.5	24.8	EMI
8860	51	1138	-1.5/-1.5	3c	100 x 100	6 x 0.25"	19.0	-	EMI
8861	51	1158	+0.5/+0.5	3c	100 x 100	6 x 0.25"	23.0	23.6	EMI
8951	51	1130	-2/-1.5	3e	100 x 100	6 x 0.25"	25.2	27.4	EMI
8952	51	1141	+3/-3	3e	100 x 100	6 x 0.25"	20.1	27.2	EMI
8953	51	1161	-2/-6	3e	100 x 100	6 x 0.25"	22.6	24.2	EMI

1997 experiments: 8733-8740; 1998 experiments: 8850-8861, 8943-8953

‡ In Experiment 8876 strong deflection of the residual projectile during the penetration into the ceramic; therefore, ricocheting of the rod in the Al backing plate.

Projectile: WSA rod, D = 8.33 mm, L/D = 6, flat nose
Backing Plate: Al 6061-T651, 60 mm thick; Cover Plate: steel, 5 mm thick

Exp. no.	m_P [g]	v_P [m/s]	α_1/α_2 [deg]	Test set-up	lat. tile dim. [mm]	No. of tiles	p_R [mm]	p_{KE} [mm]	Projectile used from
8972	51.06	1131	0/0	3f	150 x150	1 x 1.5"	0	-	EMI
8976	51.03	1155	0/0	3f	150 x150	1 x 1.5"	0	-	EMI
8977	50.96	1155	0/0	3f	150 x150	1 x 1.5"	0	-	EMI
8974	51.08	1157	0/0	3f	150 x150	2 x 0.75"	3.9	-	EMI
8979	51.08	1135	0/0	3f	150 x150	2 x 0.75"	3.1	-	EMI
8980	51.06	1163	0/0	3f	150 x150	2 x 0.75"	2.9	-	EMI
8973	51.05	1164	0/0	3f	150 x150	3 x 0.5"	8.6	9.3	EMI
8978	51.12	1186	-0.5/0	3f	150 x150	3 x 0.5"	8.3	-	EMI
8981	51.09	1156	0/0	3f	150 x150	3 x 0.5"	4.9	-	EMI
8975	51.20	1161	1/-3.5	3f	150 x150	6 x 0.25"	11.3	12.6	EMI
8982	51.06	1166	0/0	3f	150 x150	6 x 0.25"	16.8	16.9	EMI
8983	51.15	1120	0/0	3f	150 x150	6 x 0.25"	10.3	-	EMI

Projectile: WSA rod, D = 8.33 mm, L/D = 6, flat nose
Backing Plate: Al 6061-T651, 60 mm thick; Cover Plate: steel, 5 mm thick

Exp. no.	m_P [g]	v_P [m/s]	α_1/α_2 [deg]	Test set-up	lat. tile dim. [mm]	AlN layers	p_R [mm]	p_{KE} [mm]	hit-point
9058	50.98	1120	0/0	3g-OCII	100 x100	2 x 0.75"	17.1	17.8	15 mm OCII
9059	50.97	1170	0/0	3g-OCD	100 x100	2 x 0.75"	36.6	36.8	40 mm OCD
9060	50.90	1147	0/0	3g-OCII	100 x100	2 x 0.75"	25.6	26.6	30 mm OCII
9061	51.08	1105	0/0	3g-OCD	100 x100	6 x 0.25"	38.6	40.9	40 mm OCD
9062	51.08	1157	0/0	3g-OCII	100 x100	6 x 0.25"	33.7	34.9	15 mm OCII
9063	51.16	1112	0/0	3g-OCII	100 x100	6 x 0.25"	41.6	43.5	30 mm OCII
9028	51.10	1158	0/0	3h-OCD	150 x150	1 x 1.5"	0	-	35 mm OCD
9029	50.87	1155	0/0	3h-OCD	150 x150	1 x 1.5"	5.7	-	70 mm OCD
9031	51.19	1157	1/-1.5	3h-OCII	150 x150	1 x 1.5"	-	-	60 mm OCII
9032	51.15	1153	0/0	3h-OCII	150 x150	1 x 1.5"	43.8	46.2	55 mm OCII
9064	50.91	1146	0/0	3h-OCII	150 x150	3 x 0. 5"	16.9	26.4	55 mm OCII
9030	51.22	1140	0/0	3i	9 x(50 x50)	1 x 1.5"	19.3	19.7	center

OCD: off-center, along diagonal   OCII: off-center, parallel edge

Residual Penetration Depth vs. AlN Layer Numbers
Tile Dimension 100 x 100 mm

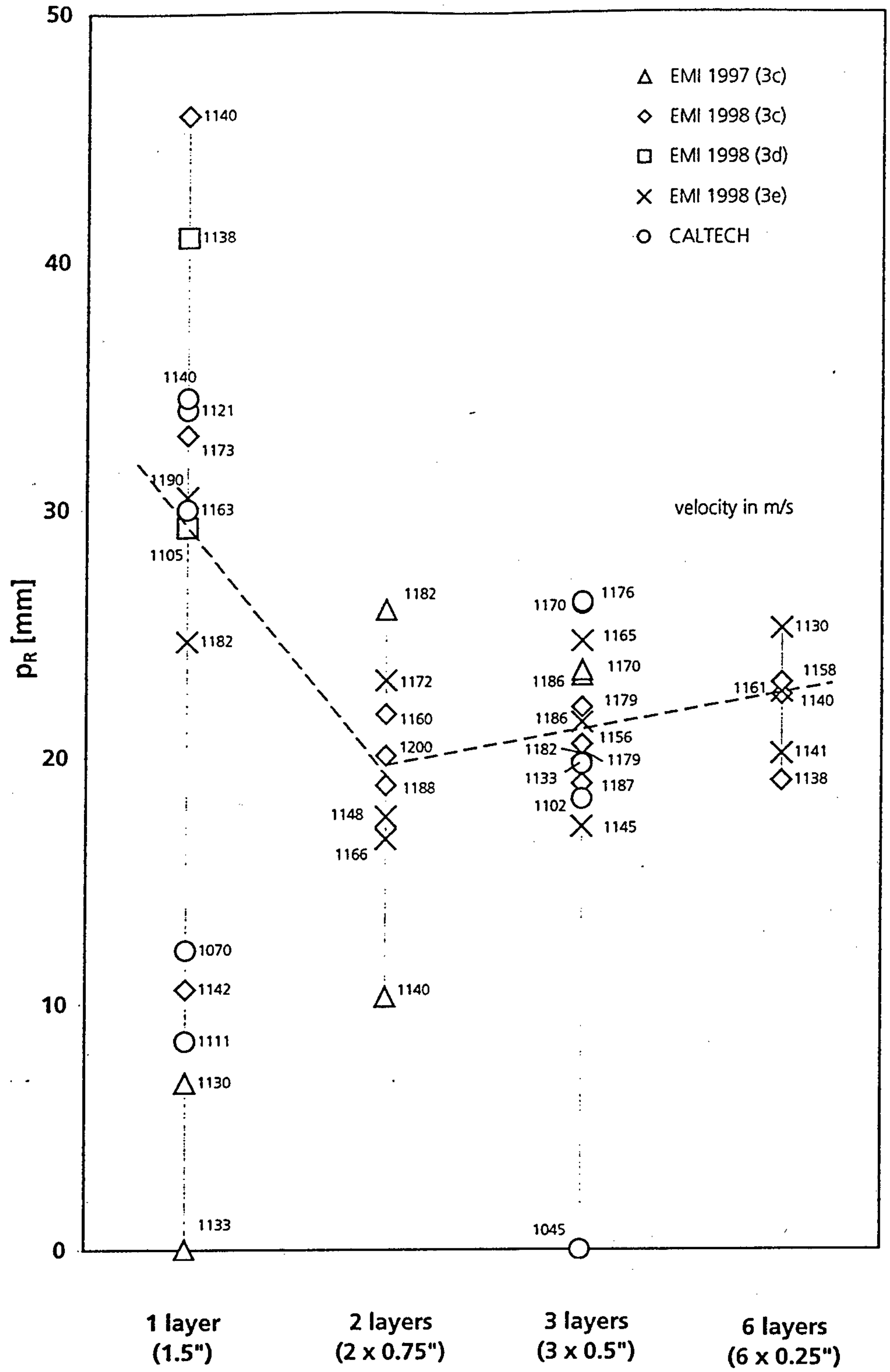

27.11.1998

Fraunhofer
Institut
Kurzzeitdynamik
Ernst-Mach-Institut

Residual Penetration Depth vs. AlN Layer Numbers
Kinetic Energy Line (100 x100 mm Tiles)

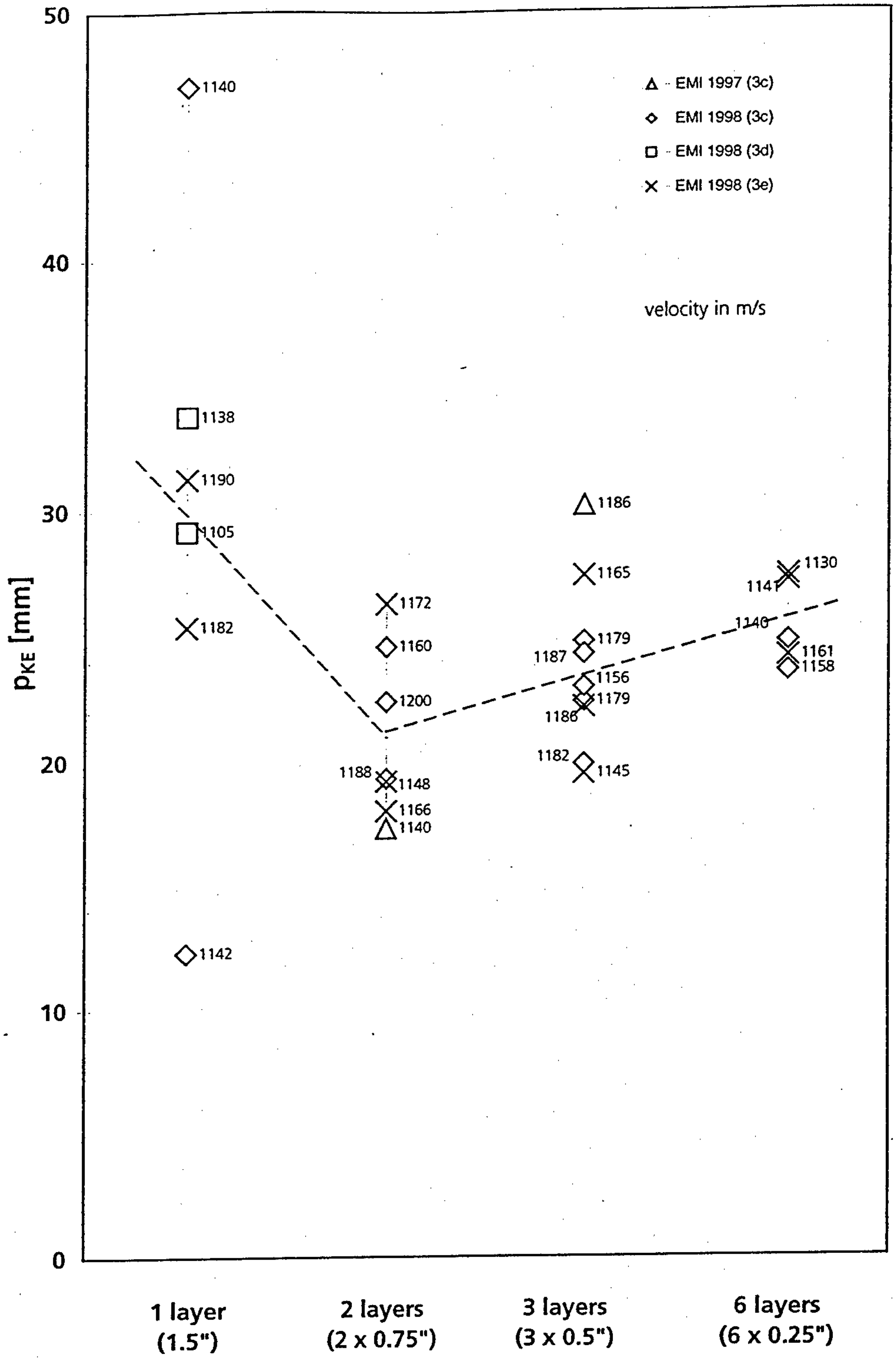

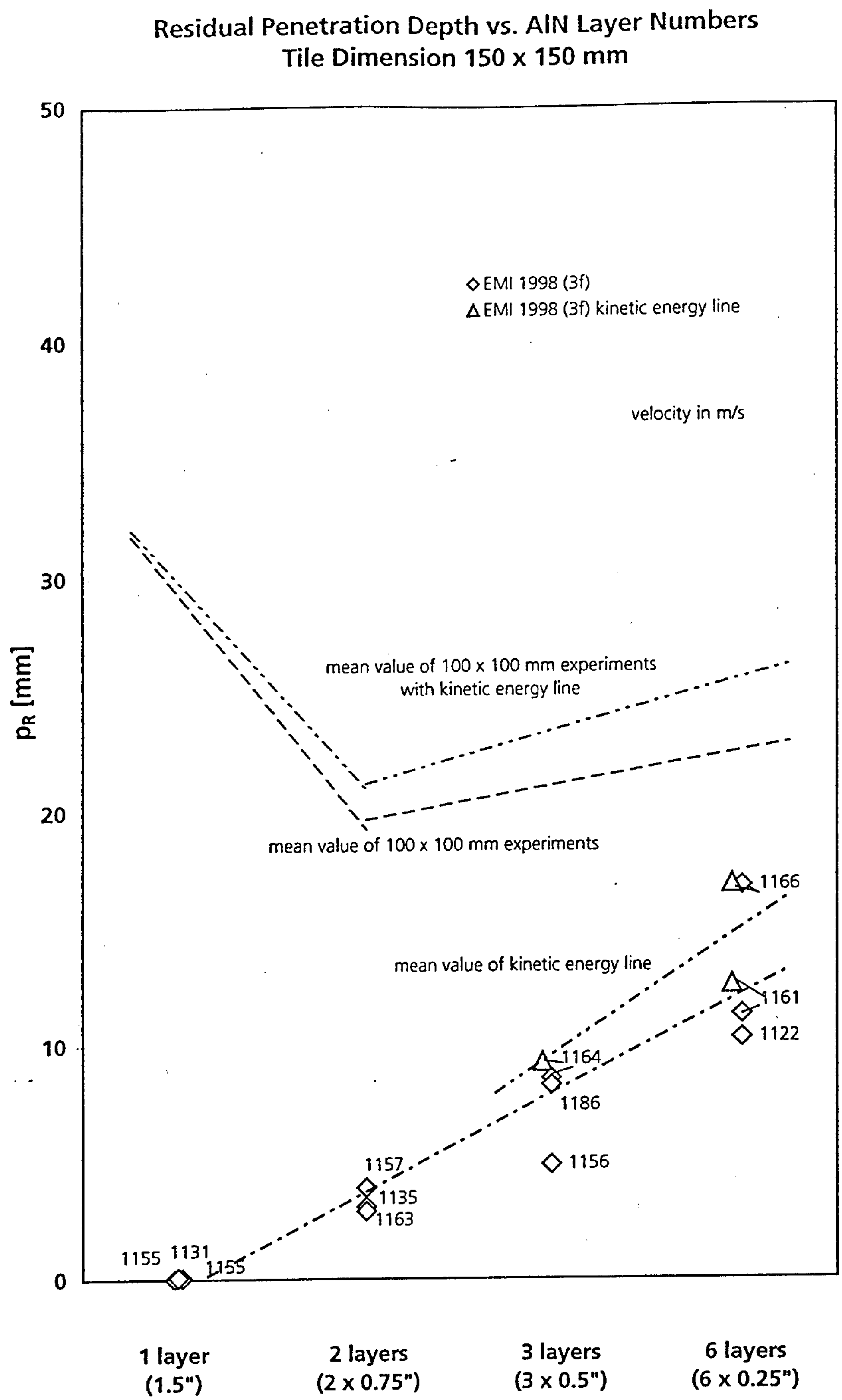

27.11.1998

Fraunhofer
Institut
Kurzzeitdynamik
Ernst-Mach-Institut

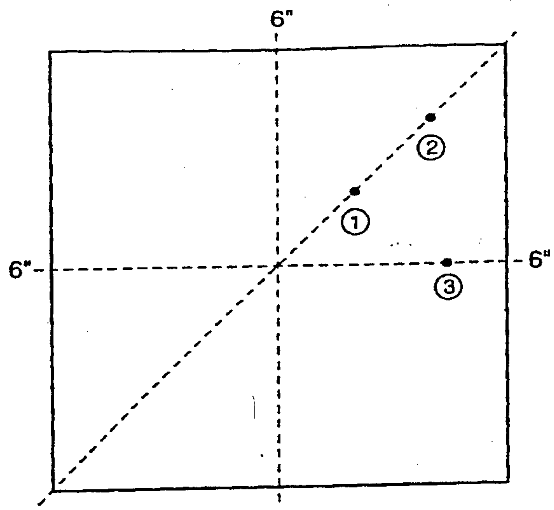

stack	pos.	r(mm)	DOP(mm)
1 x 1.5"	①	35	0
1 x 1.5"	②	70	5.7
1 x 1.5"	③	55	43.8
3 x .5"	③	55	16.9

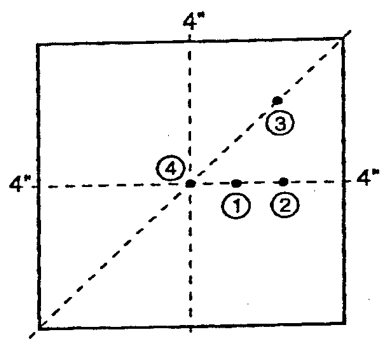

stack	pos.	r(mm)	DOP(mm)
2 x 3/4"	①	15	17.1
2 x 3/4"	②	30	25.6
2 x 3/4"	③	40	36.6
2 x 3/4"	④	0	$10 \leq DOP \leq 23$
6 x 1/4"	①	15	33.7
6 x 1/4"	②	30	41.6
6 x 1/4"	③	40	38.6
6 x 1/4"	④	0	$19 \leq DOP \leq 25$

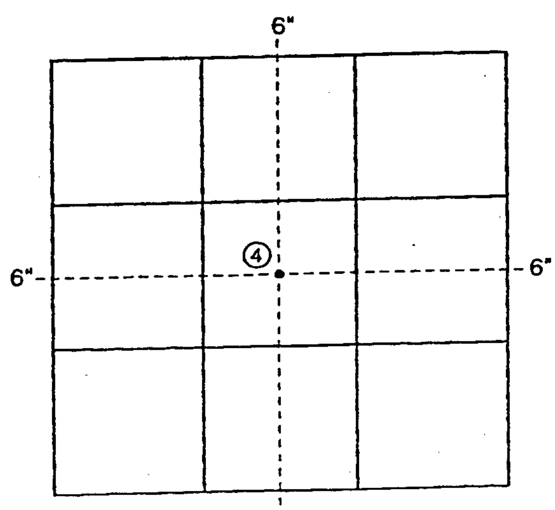

stack	pos.	DOP(mm)
1 x 1.5"	④	19.8

8441 GWLJ 10/22/98

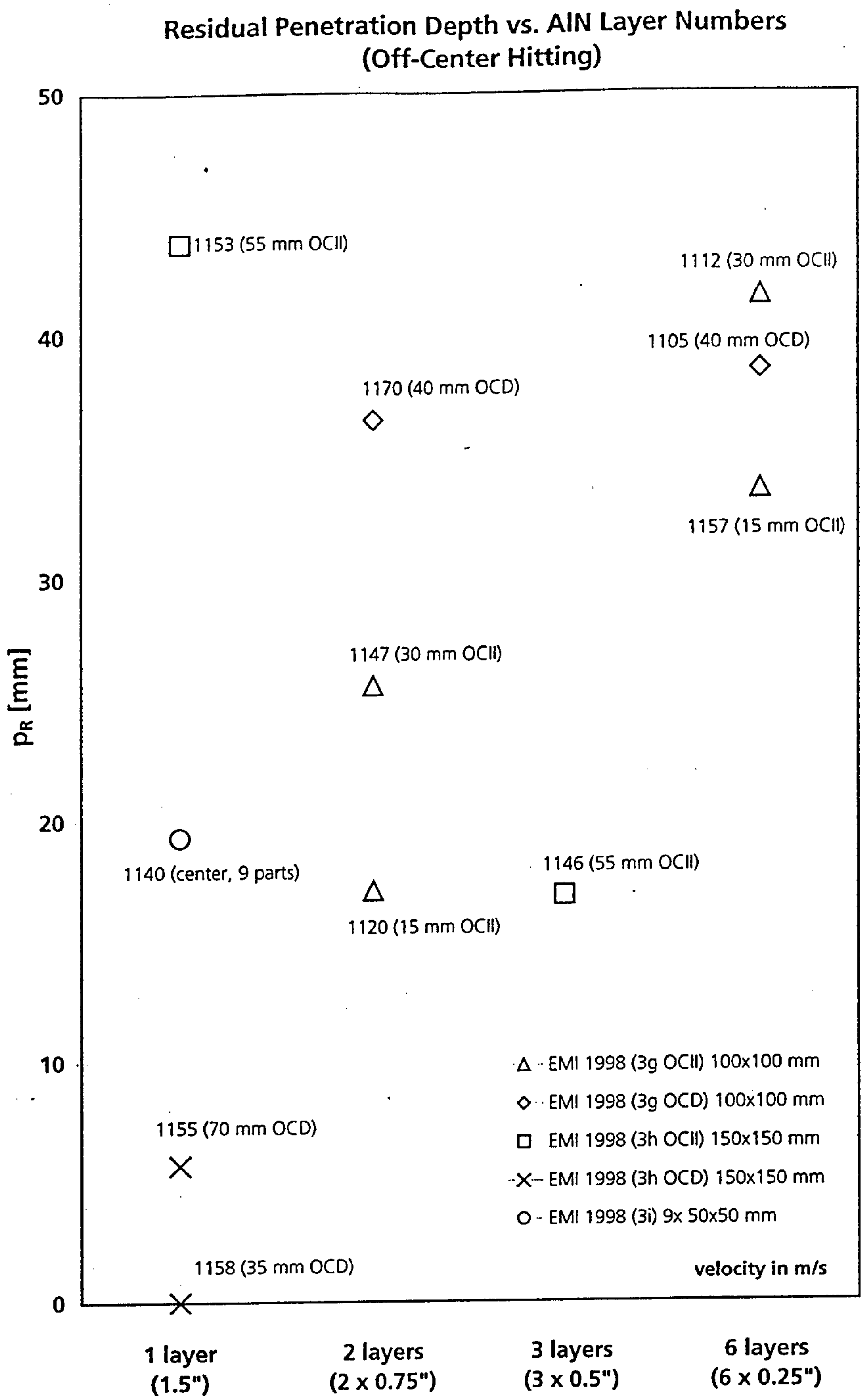

Residual Penetration Depth vs. AlN Layer Numbers
(Off-Center Hitting)
50
40
30
20
10
0
p_R [mm]
1153 (55 mm OCII)
1112 (30 mm OCII)
1105 (40 mm OCD)
1170 (40 mm OCD)
1157 (15 mm OCII)
1147 (30 mm OCII)
1140 (center, 9 parts)
1146 (55 mm OCII)
1120 (15 mm OCII)
1155 (70 mm OCD)
1158 (35 mm OCD)
EMI 1998 (3g OCII) 100x100 mm
EMI 1998 (3g OCD) 100x100 mm
EMI 1998 (3h OCII) 150x150 mm
EMI 1998 (3h OCD) 150x150 mm
EMI 1998 (3i) 9x 50x50 mm
velocity in m/s
1 layer (1.5")
2 layers (2 x 0.75")
3 layers (3 x 0.5")
6 layers (6 x 0.25")

Residual Penetration Depth vs. AlN Layer Numbers
Kinetic Energy Line (Off-Center Hitting)

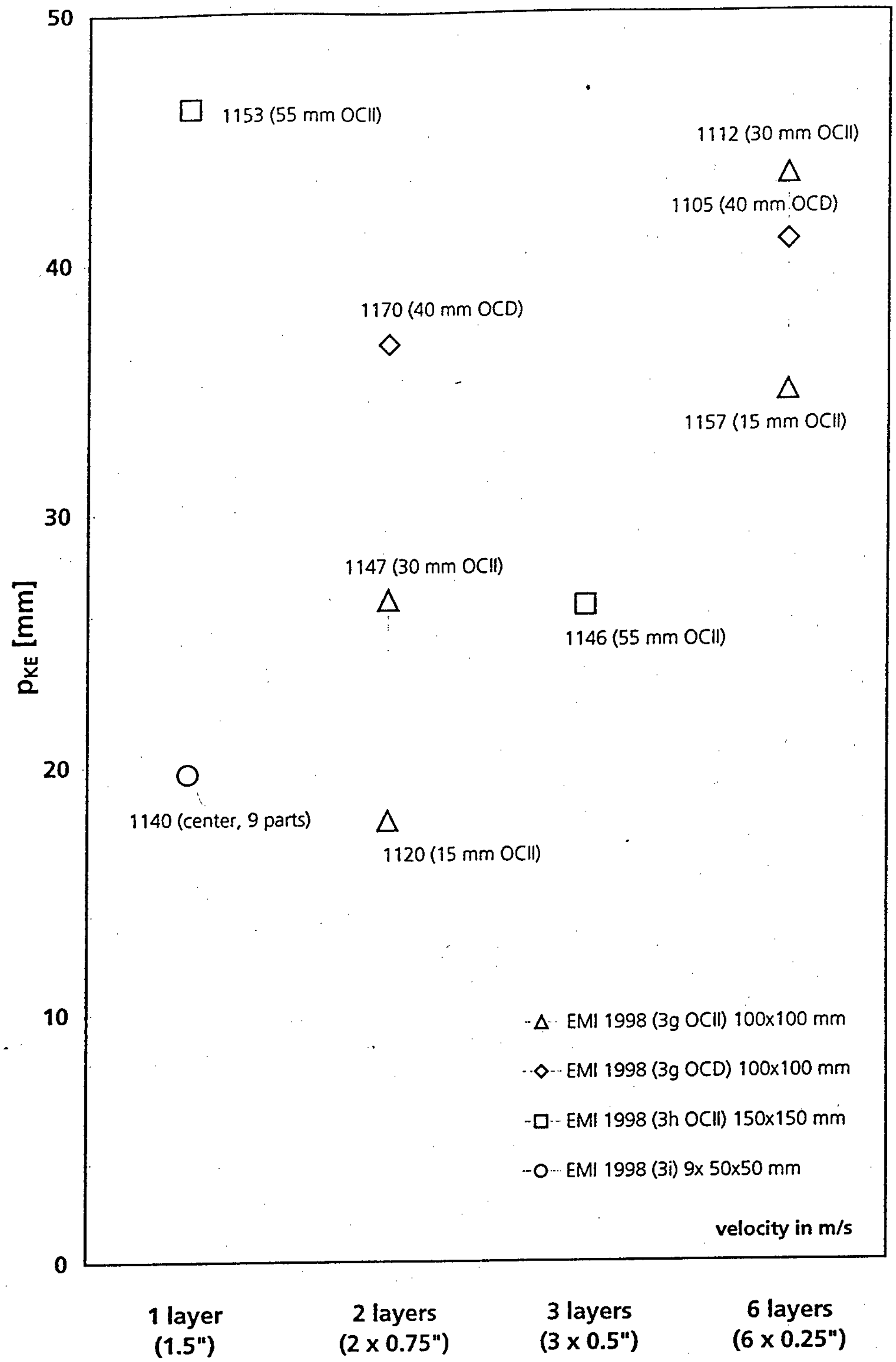

Residual Penetration Depth vs. AlN Layer Numbers

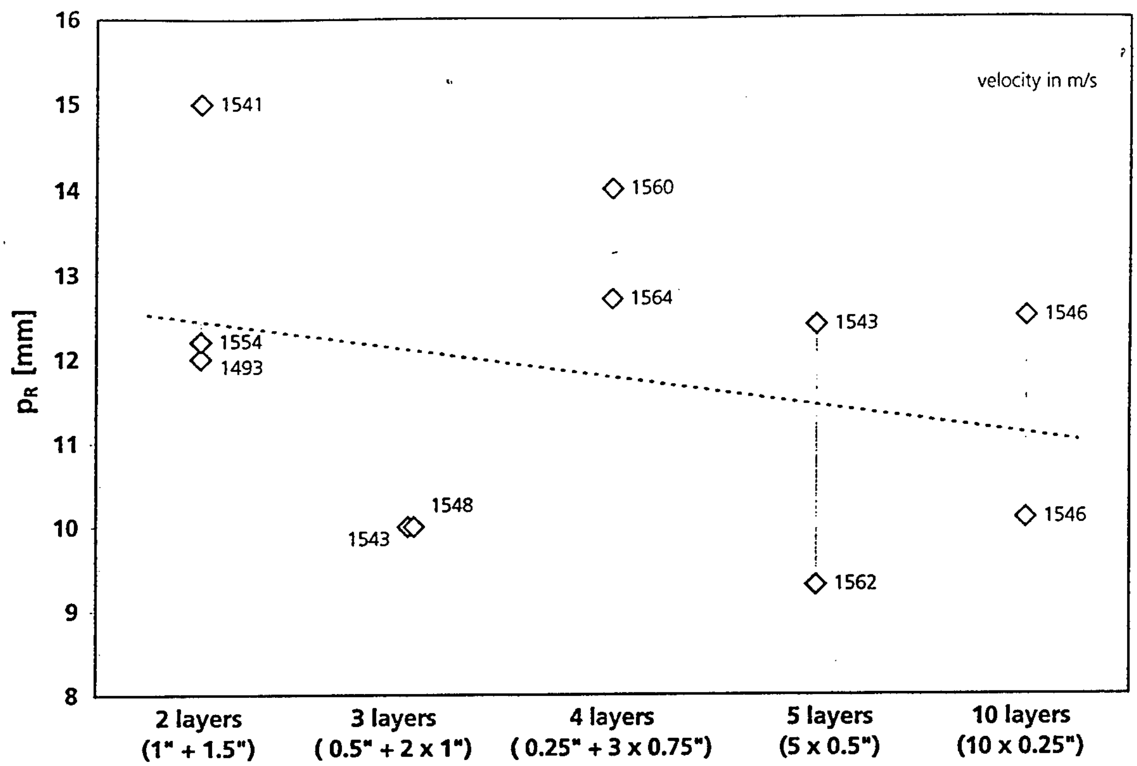

Normalized Residual Penetration Depth vs. AlN Layer Numbers

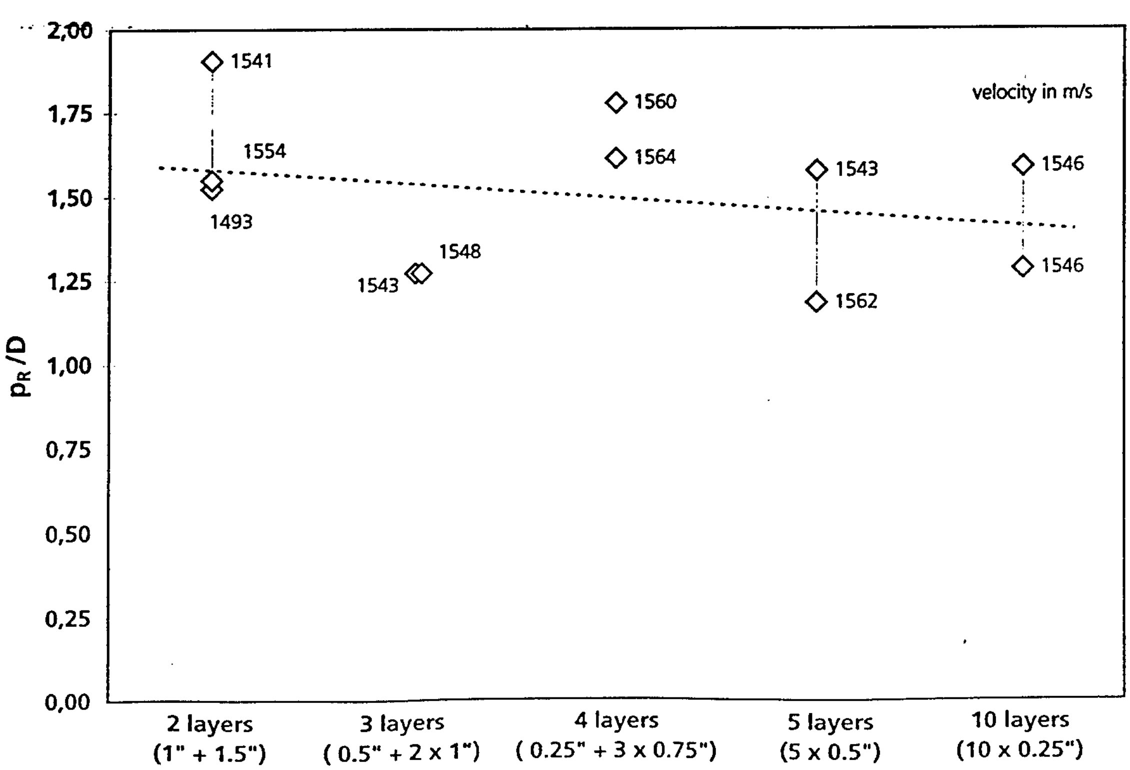

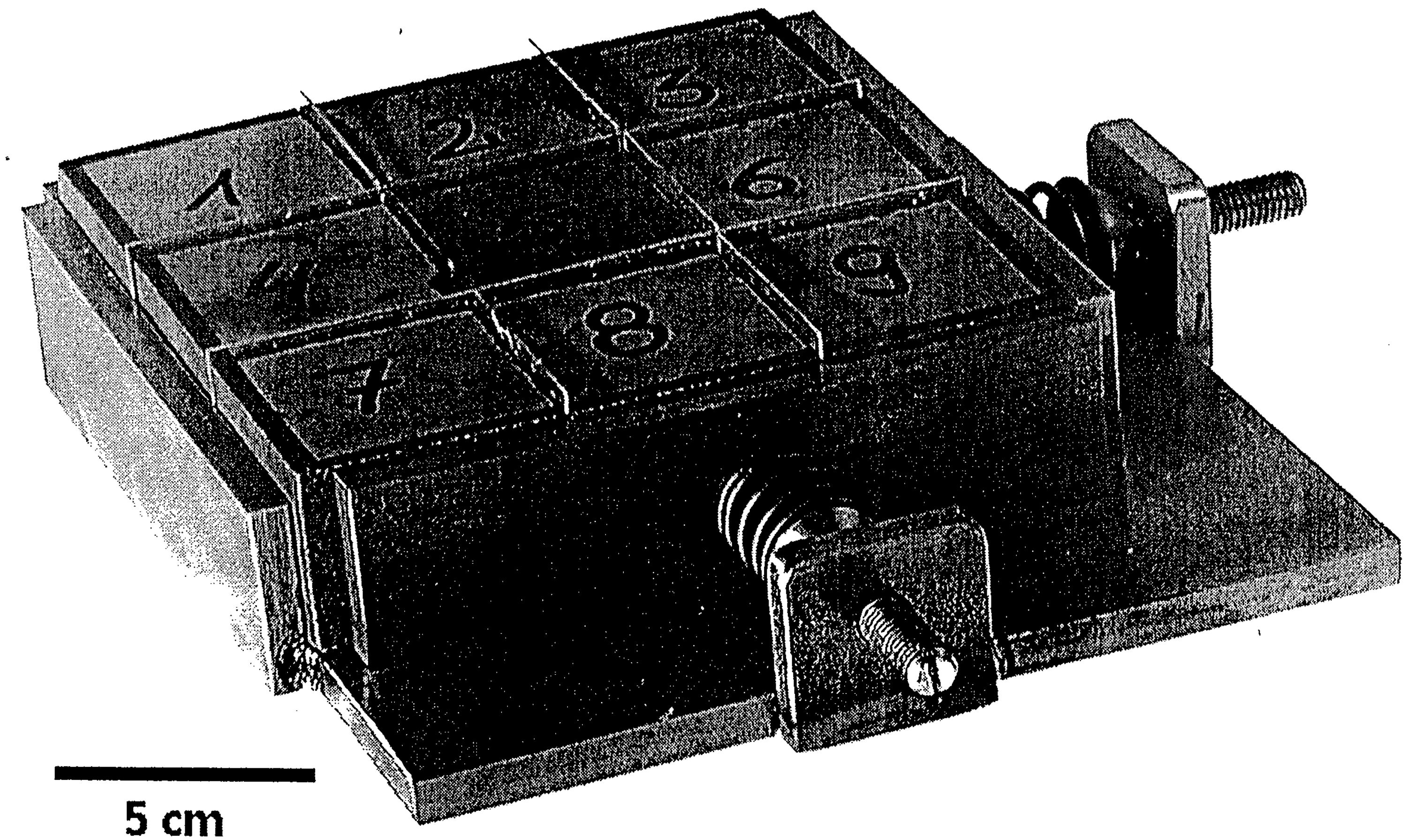

periment 9030: 9 x 50 x 50 mm tiles, single layer

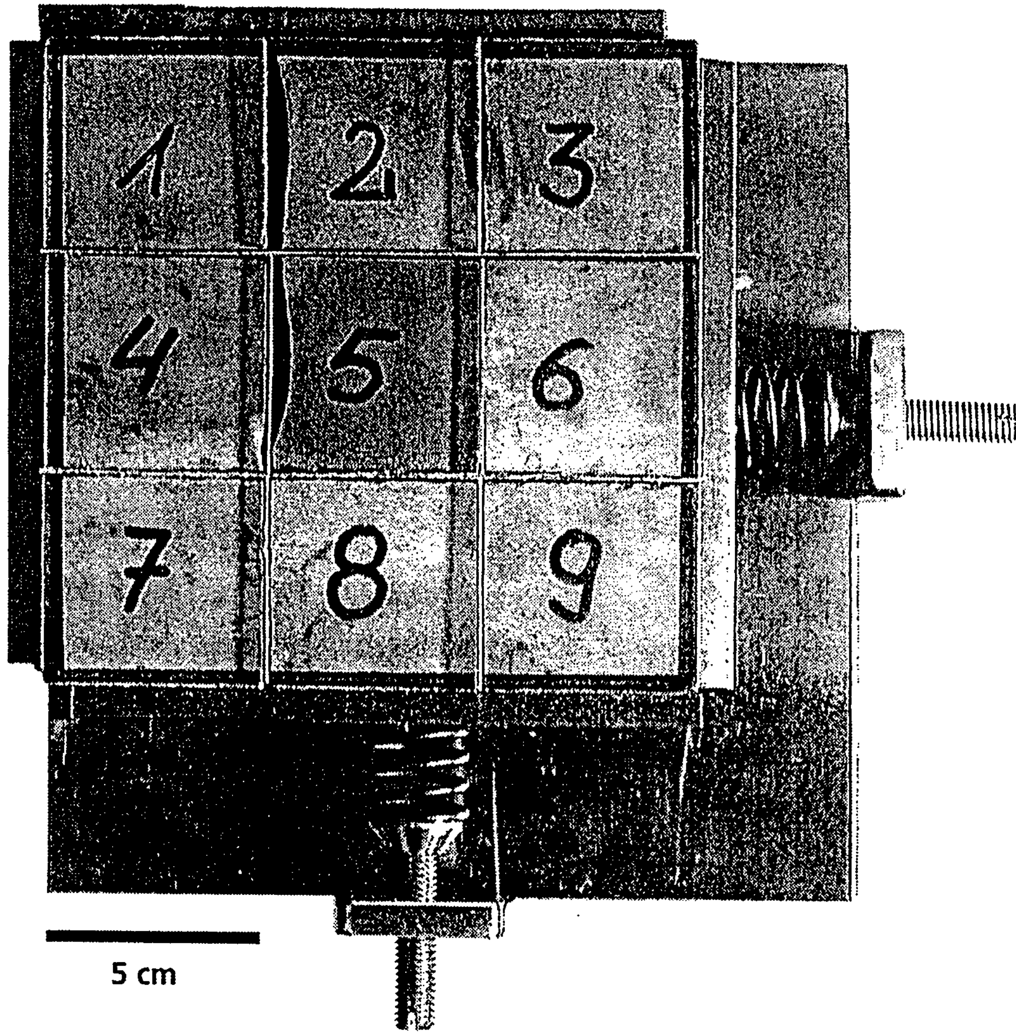

periment 9030: 9 x 50 x 50 mm tiles, single layer

DISTRIBUTION LIST

No. of Copies	Organization
2	Defense Technical Information Center DTIC DDA 8725 John J. Kingman Rd. Ste. 0944 Ft. Belvoir, VA 22060-6218
10	U.S. Army Tardec K. Bishnoi (5 cps) D. Templeton J. Thompson AMSTA TR R MS 263 Warren, MI 48397-5000
1	Army High Performance Computing Research Center T. Holmquist 1200 Washington Ave. S. Minneapolis, MN 55415
2	Dir. USARL AMSRL-WM-TD A. Rajendran D. Grove Aberdeen Proving Ground Aberdeen, MD 21005-5065